

# **Development of Polymeric Nano-Composite Fiber Based Structures for Acoustics and Filtration Applications**

by

Utkarsh

A thesis submitted to the  
School of Graduate and Postdoctoral Studies in partial  
fulfillment of the requirements for the degree of

**Doctor of Philosophy in Mechanical Engineering**

Department of Mechanical and Manufacturing Engineering/Faculty of Engineering and  
Applied Science

University of Ontario Institute of Technology (Ontario Tech University)

Oshawa, Ontario, Canada

August 2021

© Utkarsh, 2021

## THESIS EXAMINATION INFORMATION

Submitted by: **Utkarsh**

### Doctor of Philosophy in Mechanical Engineering

Thesis title: Development of Polymeric Nano-Composite Fiber Based Structures for Acoustics and Filtration Applications

An oral defense of this thesis took place on August 16, 2021 in front of the following examining committee:

#### Examining Committee:

Chair of Examining Committee	Dr. Martin Agelin-Chaab
Research Supervisor	Dr. Remon Pop-Iliev
Research Co-supervisor	Dr. Ghaus Rizvi
Examining Committee Member	Dr. Sayyed Ali Hosseini
Examining Committee Member	Dr. Shaghayegh Bagheri
University Examiner	Dr. Yuping He
External Examiner	Dr. Simon S. Park, Dept. of Mechanical & Manufacturing Engineering, Schulich School of Engineering, University of Calgary, Canada

## ABSTRACT

Electrospinning lab-scale experimental set-up was developed for manufacturing polymeric nanofiber composites for acoustics and filtration applications. In this study, nanofiber membranes were fabricated using two types of polymer materials: Polyvinylpyrrolidone (PVP) and Polyvinylidene Fluoride (PVDF). The control parameters of the electrospinning process, including polymer concentration, voltage input, flow rate, needle to collector surface distance, and collector rotational speed, were studied and optimized using Taguchi's experimental design methodology. The parametric study was performed to investigate the effect of varying the electrospinning variables on the fiber diameter, thickness, and weight of nanofiber membranes, respectively. Statistical models were developed for modeling and optimization of electrospinning parameters using Analysis of Variance (ANOVA), Response Surface Methodology (RSM), and Genetic Programming (GP). The experimental work examined and proposed in this thesis involves developing nanofiber membrane composites from a pure polymeric base, fillers, and layers for two different objectives, including low-frequency sound absorption and filtration applications.

Experimental results show that polymer concentration and voltage input were the two most significant parameters that regulate the fiber diameter, thickness, and weight of PVP and PVDF fiber membranes at high significance levels greater than or equal to 95%. Mathematical models developed using RSM show high average accuracies greater than 80% for the respective output responses. Empirical models developed using GP show higher accuracy than RSM models for all three responses generated from the electrospinning of PVP and PVDF fibers. The acoustic performance of the pure polymeric nanofiber composites with micro-scale thickness shows high sound absorption coefficient values close to one at different Back Cavities (BC's) in the frequency range of 200-300Hz. Filler infused polymeric nanofiber composites show high coefficient values greater than 0.9 at even reduced thickness, compared to pure polymer fiber composites, in the frequency range of 300-500Hz at different BC's. Electro-spun nanofiber membranes were developed from PVDF polymeric base and anti-viral /bacterial fillers for filtration applications. The layering of these nanofiber composites with surgical masks shows better particle filtration

efficiency in the particulate size ranging from 0.3 $\mu$ m to 10.0 $\mu$ m with equivalent pressure drop level of N-95 masks.

**Keywords:** Electrospinning; Sound Absorption; Nanofibers; Filtration; Pressure Drop;



## **AUTHOR'S DECLARATION**

I hereby declare that this thesis consists of original work of which I have authored. This is a true copy of the thesis, including any required final revisions, as accepted by my examiners.

I authorize the University of Ontario Institute of Technology (Ontario Tech University) to lend this thesis to other institutions or individuals for the purpose of scholarly research. I further authorize University of Ontario Institute of Technology (Ontario Tech University) to reproduce this thesis by photocopying or by other means, in total or in part, at the request of other institutions or individuals for the purpose of scholarly research. I understand that my thesis will be made electronically available to the public.

Utkarsh

---

## STATEMENT OF CONTRIBUTIONS

The experimental work carried out in Chapter four was performed at the Fluid-Structure Interaction and Noise Control Laboratory, Faculty of Engineering and Applied Science - Ontario Tech University, Oshawa, ON, Canada using the Impedance Tube Experimental Set-up under the supervision of Dr. Atef Mohany.

I performed majority of the experimental work towards preparing and calibrating the equipment for acoustic characterization of nanofiber-based specimens. The manufacturing of experimental samples and acoustic data analysis have been conducted by me.

The part of the work described in Chapter three has been published as:

Utkarsh, Hegab, Hussien, Muhammad Tariq, Nabeel Ahmed Syed, Ghaus Rizvi, and Remon Pop-Iliev, "Towards Analysis and Optimization of Electrospun PVP (Polyvinylpyrrolidone) Nanofibers." *Advances in Polymer Technology* 2020 (2020).

I performed the majority of the fabrication, testing of membrane materials, and writing of the manuscript.

The part of the work described in Chapter four has been under consideration for publication as:

Utkarsh, Nabeel Ahmed Syed, Muhammad Tariq, Atef Mohany, Remon Pop-Iliev, Ghaus Rizvi, "Experimental Investigation of Low-Frequency Sound Absorption Characteristics of Electro-spun Polyvinylpyrrolidone (PVP) Nanofiber Membranes." *Polymer*.

I performed the majority of the fabrication, testing of membrane materials, and writing of the manuscript.

## ACKNOWLEDGEMENTS

First of all, I would like to thank my supervisors Professor Ghaus Rizvi and Professor Remon Pop-Iliev, for their continuous support and guidance throughout the thesis work. Over the last four years, their trust, patience, and assistance uplifted me in carrying out my research successfully. I would also like to express my immense gratitude to my supervisors for my selection into the graduate study program and their kind approval in pursuing this research area. I am deeply grateful to my supervisors for providing financial support for my research project and attending several North America conferences as a presenter.

I am deeply thankful to Dr. Atef Mohany for his continuous support and technical guidance in carrying out the acoustics laboratory experiments. I am also grateful to Dr. Carlos Quijano-Solis for providing training on equipment for polymer characterization. I am also greatly obliged to my colleagues in Dick McLaughlin Manufacturing Design Lab, Isha Raktim, Nabeel Ahmed Syed, Muhammad Tariq Abdul Samad, Pedram Karimipour Fard, Wing Yi Pao, and Ashique Baten, for their continuous support and help in research activities.

Finally, I am very thankful to my parents, Dr. Rakesh Saxena and Dr. Sunita Saxena, and my fiancé Shubhangi Sharma for being patient with me throughout my research work. Their trust, confidence, support, and encouragement helped me a lot in my career endeavors life-long.

## TABLE OF CONTENTS

<b>Thesis Examination Information.....</b>	<b>ii</b>
<b>Abstract.....</b>	<b>iii</b>
<b>Author’s Declaration .....</b>	<b>v</b>
<b>Statement of Contributions .....</b>	<b>vi</b>
<b>Acknowledgements .....</b>	<b>vii</b>
<b>Table of Contents .....</b>	<b>viii</b>
<b>List of Tables .....</b>	<b>xv</b>
<b>List of Figures.....</b>	<b>xvii</b>
<b>List of Abbreviations and Symbols .....</b>	<b>xxvi</b>
<b>Chapter 1. Introduction.....</b>	<b>1</b>
1.1 Preamble.....	1
1.2 Problem Statement .....	2
1.2.1 Need for Research Focusing in Acoustics Applications.....	2
1.2.2 Need for Research Focusing in Filtration Applications .....	3
1.3 Motivation .....	4
1.4 Thesis Objectives .....	5
1.5 Thesis Methodology .....	6
1.6 Targeted Main Contributions of the Thesis.....	8
1.7 Thesis Outline .....	9
 <b>Chapter 2. Theoretical Background and Literature Review .....</b>	 <b>11</b>
2.1 Nanotechnology and Nanofibers .....	11
2.2 Nanofiber Fabrication Techniques .....	12
2.2.1 Drawing Technique .....	12
2.2.2 Self-Assembly Technique.....	13
2.2.3 Template-Based Synthesis Technique.....	13
2.2.4 Phase Separation Technique .....	14
2.2.5 Electrospinning Technique .....	15
2.3 Electrospinning process and parameters affecting the process .....	18

2.4 Sound Waves and Noise Control .....	25
2.4.1 Sound Absorption Coefficient ( $\alpha$ ) .....	27
2.4.2 Sound Reflection Coefficient (R) .....	28
2.4.3 Acoustic Impedance (Z) .....	29
2.4.4 Factors Influencing Acoustic Behavior of Passive Materials .....	31
2.4.5 Low-Frequency Sound Waves.....	34
2.4.6 Sound Absorption of Low-Frequency Waves .....	34
2.4.7 Sound Absorptive Nanofiber Materials .....	38
2.5 Filtration .....	45
2.5.1 Filtration Mechanisms .....	45
2.5.1.1 Particle Capture Mechanism by Single Fiber .....	45
2.5.1.2 Particle Capture Mechanism by Single Pore .....	48
2.5.2 Filtration Performance Tests.....	49
2.5.2.1 Filtration Efficiency .....	49
2.5.2.2 Pressure Drop Measurement .....	50
2.5.3 Effect of Nanofiber Properties on Filtration Performance .....	52
2.5.4 Viruses and Pollutants .....	53
2.5.5 Electro-spun Nanofibers as Filter Media.....	55
2.6 Literature Review Summary and Knowledge Gap .....	58
<b>Chapter 3. Experimental Methodology .....</b>	<b>61</b>
3.1 Experimental Materials .....	61
3.2 Electrospinning Experimental Set-up.....	63
3.3 Material or Specimen Preparation .....	64
3.3.1 Polymeric Solution Preparation .....	64
3.3.2 Polymeric-Filler Solution Preparation .....	65
3.4 Thermal, Mechanical, and Morphological Characterization.....	67
3.4.1 Thermo-gravimetric Analysis (TGA) .....	67
3.4.2 Differential Scanning Calorimetry (DSC) .....	67
3.4.3 Dynamic Mechanical Analysis (DMA) .....	68
3.4.4 Scanning Electron Microscopy (SEM).....	69
3.4.5 Digital Microscope (DM) .....	70

3.5 Acoustic Characterization of Nanofiber Membranes and Composites .....	70
3.5.1 Introduction.....	70
3.5.2 Impedance Tube Experimental Set-up.....	71
3.5.3 Impedance Tube Validation Study .....	75
3.6 Filtration Characterization.....	75
3.6.1 Introduction.....	75
3.6.2 Differential Pressure Measurement Experimental Set-Up .....	76
3.7 Modelling and Optimization of Electrospinning Parameters for Manufacturing of PVP Fibers.....	78
3.7.1 Introduction.....	78
3.7.2 Experimental Methodology .....	79
3.7.3 Results and Discussion .....	80
3.7.3.1 Morphological Characterization of Electro-Spun PVP Fibers.....	80
3.7.3.2 Design of Experiments (DOE) Using Orthogonal Array .....	81
3.7.3.3 Evaluation of Electrospinning Parameters: ANOVA Study .....	83
3.7.3.5 Electrospinning Process Modelling Using RSM .....	87
3.7.3.6 Electrospinning Process Modelling Using GP.....	89
3.7.4 Conclusions .....	91
3.8 Modelling and Optimization of Electrospinning Parameters for Manufacturing of PVDF Fibers.....	92
3.8.1 Introduction.....	92
3.8.2 Experimental Methodology .....	92
3.8.3 Results and Discussion .....	93
3.8.3.1 Morphological Characterization of Electro-Spun PVDF Fibers.....	93
3.8.3.2 Design of Experiments (DOE) Using Orthogonal Array .....	95
3.8.3.3 Evaluation of Electrospinning Parameters: ANOVA Study .....	97
3.8.4.4 Effect of Electrospinning Designed Parameter on Fiber Diameter, Weight and Thickness of Electro-Spun Membrane.....	99
3.8.3.5 Electrospinning Process Modelling Using RSM .....	101
3.8.3.6 Electrospinning Process Modelling Using GP.....	103
3.8.4 Conclusions .....	105

<b>Chapter 4. Sound Absorption Performance of Nanofiber Composites.....</b>	<b>106</b>
4.1 Introduction .....	106
4.2 Sound Absorption Characteristics of PVP Fibers and Its Composites.....	106
4.2.1 Acoustic Sample Formulation .....	106
4.2.2 Sound Absorption Performance (SAP) of Single PVP Fiber Membrane .....	107
4.2.3 SAP of Multiple Layers of PVP Membrane at 3 Discrete BC .....	108
4.2.3.1 SAP of Two Layers.....	108
4.2.3.2 SAP of Four Layers .....	109
4.2.3.3 SAP of Eight Layers .....	109
4.2.3.4 SAP of Sixteen Layers .....	110
4.2.3.5 SAP of Twenty Layers .....	111
4.2.3.6 Sound Absorption Coefficient Variation with Change in Thickness at Different Frequency Bands (1/3 Octave Plots) .....	112
4.3 Sound Absorption Characteristics of PVDF Fibers and Its Composites.....	113
4.3.1 Acoustic Sample Formulation .....	113
4.3.2 SAP of Single PVDF Fiber Membrane at Three Discrete BC.....	113
4.3.3 SAP of Multiple Layers of PVDF Membrane at Three Discrete BC .....	114
4.3.3.1 SAP of Two Layers.....	114
4.3.3.2 SAP of Four Layers .....	115
4.3.3.3 SAP of Eight Layers .....	116
4.3.3.4 SAP of Sixteen Layers .....	117
4.3.3.5 SAP of Twenty Layers .....	118
4.3.3.6 Sound Absorption Coefficient ( $\alpha$ ) Variation with Change in Thickness at Different Frequency Bands (1/3 Octave Plots) .....	118
4.4 Sound Absorption Characteristics of Combined PVP and PVDF Composites.....	119
4.4.1 Acoustic Sample Formulation .....	119
4.4.2 SAP of Alternate Layers of PVP and PVDF Membrane at Three Discrete BC .....	120
4.4.2.1 SAP of Two Layers.....	120
4.4.2.2 SAP of Four Layers .....	121
4.4.2.3 SAP of Eight Layers .....	121
4.4.2.4 SAP of Sixteen Layers .....	122
4.4.2.5 SAP of Twenty Layers .....	123

4.4.2.6 Sound Absorption Coefficient ( $\alpha$ ) Variation with Change in Thickness at Different Frequency Bands (1/3 Octave Plots) .....	123
4.5 Sound Absorption Characteristics of Filler Infused PVP Fibers and Its Composites .....	124
4.5.1 Acoustic Sample Formulation .....	124
4.5.2 SAP of Multiple Layers of Filler Infused PVP Membranes at 3 Discrete BC	125
4.5.2.1 SAP of CNT Based Layers.....	125
4.5.2.2 SAP of GN Based Layers.....	126
4.5.2.3 SAP of FS Based Layers .....	127
4.5.2.4 SAP of FG Based Layers .....	127
4.5.2.5 SAP of MC Based Layers .....	128
4.5.2.6 Sound Absorption Coefficient ( $\alpha$ ) Variation with Change in Thickness at Different Frequency Bands (1/3 Octave Plots) .....	129
4.5.3 SAP of Combined Layers of Filler Infused PVP at Varying BC .....	130
4.5.3.1 SAP of progressive layering of filler infused PVP membrane at discrete BC's .....	130
4.5.3.2 Sound Absorption Coefficient ( $\alpha$ ) Variation with Change in Thickness at Different Frequency Bands (1/3 Octave Plots) .....	131
4.6 Sound Absorption Characteristics of Filler-Infused PVDF Fibers and Its Composites .....	132
4.6.1 Acoustic Sample Formulation .....	132
4.6.2 SAP of Multiple Layers of Filler Infused PVDF Membranes at 3 Discrete BC .....	132
4.6.2.1 SAP of CNT Based Layers.....	133
4.6.2.2 SAP of GN Based Layers.....	134
4.6.2.3 SAP of FS Based Layers .....	135
4.6.2.4 SAP of FG Based Layers .....	135
4.6.2.5 SAP of MC Based Layers .....	136
4.6.2.6 Sound Absorption Coefficient ( $\alpha$ ) Variation with Change in Thickness at Different Frequency Bands (1/3 Octave Plots) .....	137
4.6.3 SAP of Combined Layers of Filler Infused PVDF at Varying BC.....	138
4.6.3.1 SAP of progressive layering of filler infused PVDF membrane at discrete BC .....	138
4.6.3.2 Sound Absorption Coefficient ( $\alpha$ ) Variation with Change in Thickness at Different Frequency Bands (1/3 Octave Plots) .....	139



4.7 Summary and Conclusions.....	140
<b>Chapter 5. Filtration Characteristics of Electro-Spun Nanofiber Composites ....</b>	<b>144</b>
5.1 Introduction .....	144
5.2 Experimental Methodology.....	144
5.2.1 Filtration-Ready Specimen Formulation .....	144
5.2.2 Fabrication of Filter-Ready Electro-Spun Samples.....	145
5.2.3 Characterization and Testing of Filter Media.....	146
5.3 Results and Discussion.....	146
5.3.1 Morphological Characterization of Electro-Spun Filter Samples .....	146
5.3.2 Pressure Drop ( $\Delta P$ ) Measurements of Conventional Masks .....	151
5.3.3 Effect of Polymer Concentration on $\Delta P$ Measurements of Nanofiber Samples .....	152
5.3.4 Effect of Filler Infusion on $\Delta P$ Measurements of Nanofiber Samples.....	155
5.3.5 Effect of Electrospinning Time on $\Delta P$ Measurements of Nanofiber Samples to Reach N-95 Equivalency .....	159
5.3.6 Effect of Electro-Spun Membrane Layering on $\Delta P$ Measurements of Surgical Masks (SM) .....	159
5.3.7 Particle Filtration Efficiency (PFE) of Electro-Spun Membrane Layered SM's .....	162
5.4 Summary and Conclusions.....	164
<b>Chapter 6. Conclusions, Contributions, and Future Recommendations .....</b>	<b>166</b>
6.1 Summary .....	166
6.2 Thesis Contributions .....	166
6.3 Future Recommendations.....	169
<b>References.....</b>	<b>170</b>
<b>Appendices.....</b>	<b>183</b>
Appendix A .....	183
A1. TGA thermograph of pure PVP powders. ....	183
A2. TGA measurements of PVP-based specimens.....	183
A3. TGA thermograph of pure PVDF pellets.....	184

A4. TGA measurements of PVDF-based specimens.....	184
Appendix B .....	185
B1. DSC thermograph of pure PVP powders. ....	185
B2. DSC measurements of PVP-based specimens. ....	185
B3. DSC thermograph of pure PVDF pellets. ....	186
B4. DSC measurements of PVDF-based specimens. ....	186
Appendix C .....	187
C1. DMA of pure PVP nanofiber membrane. ....	187
C2. DMA measurements of PVP-based specimens.....	187
C3. DMA of pure PVDF nanofiber membrane. ....	188
C4. DMA measurements of PVDF-based specimens.....	188
Appendix D .....	189
D1. Three-dimensional surface and contour plots demonstrating the effect of significant design parameters on fiber diameter, thickness, and weight of PVP nanofiber membranes using RSM models. ....	189
D2. Three-dimensional surface and contour plots demonstrating the effect of significant design parameters on fiber diameter, thickness, and weight of PVP nanofiber membranes using GP models. ....	190
D3. Three-dimensional surface and contour plots demonstrating the effect of significant design parameters on fiber diameter, thickness, and weight of PVDF nanofiber membranes using RSM models. ....	191
D4. Three-dimensional surface and contour plots demonstrating the effect of significant design parameters on fiber diameter, thickness, and weight of PVDF nanofiber membranes using GP models. ....	192
Appendix E.....	193
E1. Modelling and Optimization Criteria for Electrospinning of Polymeric Materials .....	193
E2. Signal-to-Noise (S/N) ratio .....	194
E3. Signal-to-Noise (S/N) ratio and confirmation study for PVP .....	195
E4. Signal-to-Noise (S/N) ratio and confirmation study for PVDF .....	196
Appendix F.....	197
F1. Rights and permissions for the figures used in the thesis.....	197

## LIST OF TABLES

### CHAPTER 2

Table 2.1: Description of parametric effect on the morphology and structure of electro-spun fibers. ....	21
Table 2.2: Relationship between low-frequency sound wave (Hz), wavelength (m), and associated material thickness (m) required to absorb low-frequency sound [105].....	34

### CHAPTER 3

Table 3.1: Description of different polymeric, filler materials, and solvents used for various applications. ....	63
Table 3.2: Tabular description of polymer solution concentration range (wt.%). ....	65
Table 3.3: Tabular description of polymer-filler concentration range (wt.%). ....	66
Table 3.4: Description of coefficient measurement frequency range. ....	73
Table 3.5: Electrospinning control factors and levels.....	79
Table 3.6: SEM images to study fiber morphology at different parametric levels. ....	81
Table 3.7: Experimental plan for parametric analysis of PVP nanofibers using L27 Orthogonal array. ....	82
Table 3.8: Fiber diameter ANOVA results .....	83
Table 3.9: Thickness ANOVA results .....	84
Table 3.10: Weight ANOVA results.....	84
Table 3.11: Electrospinning process parameters at different control levels. ....	93
Table 3.12: SEM micro-graphs of PVDF nanofibers fabricated at different levels. ....	95
Table 3.13: Experimental scheme for parametric analysis following Taguchi's orthogonal array (L-27) configuration. ....	96
Table 3.14: ANOVA study for fiber diameter measurements. ....	97
Table 3.15: ANOVA study for average thickness measurements. ....	98
Table 3.16: ANOVA study for membrane weight (g) measurements. ....	99

## CHAPTER 4

Table 4.1: Percentage increase data for different frequency bands (1/3 - Octave plot)..	112
Table 4.2: Percentage increase data for different frequency bands (1/3 - Octave plot)..	119
Table 4.3: Percentage increase data for different frequency bands (1/3 - Octave plot)..	124
Table 4.4: Percent increase data for different frequency bands (1/3-Octave plot) 3cm BC. .....	130
Table 4.5: Percent increase data for different frequency bands (1/3-Octave plot) 3cm BC. .....	132
Table 4.6: Percent increase data for different frequency bands (1/3-Octave plot) 3cm BC. .....	137
Table 4.7: Percent increase data for different frequency bands (1/3-Octave plot) 3cm BC. .....	140
Table 4.8: Maximum $\alpha$ -values at respective frequencies for PVP nanocomposites.....	141
Table 4.9: Maximum $\alpha$ -values at respective frequencies for PVDF nanocomposites....	141
Table 4.10: Maximum $\alpha$ -values for combined PVP and PVDF nanocomposites.....	142
Table 4.11: Maximum $\alpha$ -values for PVP-Filler-based composites.....	143
Table 4.12: Maximum $\alpha$ -values for PVDF-Filler-based composites.....	143

## CHAPTER 5

Table 5.1: Description of various filtration-ready specimens.....	145
Table 5.2: Detailed description of masks represented by symbols (A-F).....	151
Table 5.3: $\Delta P$ measurements with the electro-spun time of nanofiber layered SM's.....	162
Table 5.4: PFE measurements of nanofiber layered SM's.....	163

## LIST OF FIGURES

### CHAPTER 2

Figure 2.1: Nanofiber drawing process (Step-wise methodology) [26].	12
Figure 2.2: Self-assembly process and nanofiber arrangement [26].	13
Figure 2.3: Template-assisted Nanofiber synthesis [26].	14
Figure 2.4: (a) SEM of anodic aluminum template structure, (b) Nano-fibrous surface, and (c) Cross-sectional appearance of nanofibers. Rep. with permission [30].	14
Figure 2.5: Schematics of nanofiber synthesis from phase separation technique [26].	15
Figure 2.6: Schematic description of the vertically positioned electrospinning apparatus. Rep. with permission [20].	16
Figure 2.7: (a) Schematic description of the horizontally positioned electrospinning set-up. Rep. with permission [38], and (b) Description of the Taylor cone generation with the SEM micrograph of nanofiber mat produced Rep. with permission [37].	18
Figure 2.8: Sound wave perseverance through human body reaction path (Extra aural) Rep. with permission [94].	26
Figure 2.9: Schematics of the sound wave path through the sound absorptive porous material.	28
Figure 2.10: Incident and reflected sound pressure wave at the material surface.	31
Figure 2.11: Graphical description of fiber-based acoustic absorber various design properties; (a) $\epsilon=2$ – represented by the dashed line and $\epsilon=6$ – represented by the dotted line on the graph. Rep. with permission [104].	33
Figure 2.12: (a) Manufacturing process for Porous Laminated Composite Material (PLCM); Sound absorption coefficient of various laminated structures composed of; (b) Four layers, and (c) Five layers [106].	35
Figure 2.13: Schematic description of resonant absorber; (a) Helmholtz and (b) Membrane or panel-based, and (c) Acoustic performance of porous mineral wool absorber and perforated sheet covered mineral wool layer. Rep. with permission [108].	36
Figure 2.14: Three samples with Hole Diameter (HD) of; (a) 0.5mm, (b) 0.8mm, and (c) 0.8-0.5mm; (d) Acoustic Performance of samples; (A: Dash, B: Dot, and C: Solid) . Rep. with permission [117]; and (e) Graphical representation of sound absorption coefficient	

measurements of MPP specimens (Solid - 0.4mm D   0.4mm T, Dotted – 0.4mm D   10mm T, and Dashed – 4mm D   10mm T) [113].	37
Figure 2.15: SEM micrographs of; (a) PAN nanofibers, (b) Average fiber diameter distribution, (c) PAN nanofiber thicknesses manufactured from varying electrospinning time; (d) 10 min., (e) 30min., and (f) 60 min . Rep. with permission [118].	38
Figure 2.16: (a) Perforated panel layering with PAN nanofiber membranes, Acoustic performance of layered composite at different back cavities: (b) 10 mm, (c) 20mm, and (d) 30mmm. Rep. with permission [118].	39
Figure 2.17: (a) Conventional material with PAN nanofiber membranes; Acoustic performance of layered composite in following order (no back cavity): (b) BASF foam, (c) Glass fiber, and (d) Polypropylene fiber-based. Rep. with permission [118].	40
Figure 2.18: SEM images of PVA nanofibers manufactured; With water vapor action for – (a) 0 sec., (b) 60 sec., (c) 120 sec. and with water action for – (d) 60 sec.; Acoustic ready specimens of e) Fiber-based films and f) Polymer-based films [119].	41
Figure 2.19: Acoustic Performance of; (a) PVA nanofiber membrane (black curve) and polymeric foil (grey curve) and (b) PVA nanofiber layers with times water vapor action in grey line-30 seconds, grey line (dashed) 90seconds, and black line-120 seconds [119].	41
Figure 2.20: SEM images of electro-spun nanofibers of: (a) PAN, (b) TPU and (c) TPEE [120].	42
Figure 2.21: Sound absorption coefficient of; (a) Nickel plate perforated panel, (b) PAN nanofibers, (c) TPU nanofibers, and (d) TPEE nanofibers [120].	42
Figure 2.22: Acoustic-ready specimens of; (a) PVDF nanofibers, (b) PVA nanofibers, (c) Non-stretched PVDF nanofibers, and (d) Stretched PVDF nanofiber membrane; (e) Sound absorption coefficients of PVDF specimens. Rep. with permission [121].	43
Figure 2.23: Acoustic ready specimens composed of; (a) PP and PET-based non-woven traditional material, (b) Layered composite of PVDF-Graphene electro-spun membrane and nonwoven material, and (c) Acoustic performance of respective PVDF composite specimens. Rep. with permission [121].	43
Figure 2.24: Acoustic performance of; (a) PVC nanofiber specimens (Thickness: S-0.183in, T-0.288in, and U-0.710in) compared with Melamine foam specimens (1in and	

2in thick), (b) PVC nanofiber specimens compared (Thickness: P-0.325in, Q-0.512in, and R-0.719in) with Melamine foam specimens (1in and 2in thick), and (c) PVP nanofiber specimens compared (Thickness: M-0.441in, N-0.737in, and O-0.807in) with Polyimide foam specimens (1in and 2in thick) [122].	44
Figure 2.25: SEM micro-graphs of; PVC nanofibers (fabricated at – 20KV, 25cm distance, and 3.5ml/hr. feed rate) taken at – (a) 3000X and (b) 2000X; PVP based nanofibers (fabricated at – 20KV, 25cm distance, and 3.5ml/hr. feed rate) taken at – (c) 500X and (d) 2000X [122].	45
Figure 2.26: Schematic illustration of various filtration mechanisms through a single unique fiber; (a) Sieving, (b) Fluid flow description near fiber surface, (c) Interception, (d) Inertial impaction, (e) Diffusion, (f) Deposition (Gravitational), and (g) Electrostatic attraction.	47
Figure 2.27: Schematic illustration of various filtration mechanisms through a single unique pore; (a) Description of fluid flow lines through pores, (b) Sieving, (c) Interception, (d) Inertial Interception, (e) Diffusion, and (f) Deposition (Gravitational).	48
Figure 2.28: Schematic description of; a) Coronavirus attachment with aerosol size structure of 60nm, and b) Coronavirus attachment with higher size aerosol of 100-300nm. Rep. with permission [17].	54
Figure 2.29: PVC-PU nanofiber membrane structure with many flow channels loaded in the network. Rep. with permission [135,154].	55
Figure 2.30: SEM micro-graphs of Polysulfone (PSF) based membrane structure modified with TiO <sub>2</sub> nanoparticles in varying concentrations of: (a) 2.5wt.%, (b) 5wt.%, (c) 7.5 wt.%, and (d) 10wt.% . Rep. with permission [135,155].	56
Figure 2.31: Sand witching of PA-6 and PAN nanofiber membrane explaining the filtration technique through the structures. Rep. with permission [135,156].	57
Figure 2.32: (a) Silver nanoparticles (Ag Nps) action on the bacteria [135,158], (b) Silk fibers loaded with Ag to prevent the diffusion of smoke, and c) TEM image of silver nanoparticles doped on the silk nanofiber structure. Rep. with permission [135,161].	58

### CHAPTER 3

Figure 3.1: (a) Schematic description of the electrospinning set-up and (b) Laboratory-scale unit. ....	65
Figure 3.2: Step-by-Step description electro-spun nanofiber membrane fabrication process.....	66
Figure 3.3: Thermo-gravimetric Analyzer - TGA (Q series – Q50).....	67
Figure 3.4: Differential Scanning Calorimeter - DSC (Q series – Q20).....	68
Figure 3.5: Dynamic Mechanical Analyzer - DMA (Q series – Q800).....	69
Figure 3.6: Scanning Electron Microscope – SEM (FlexSEM 1000).....	69
Figure 3.7: Digital Microscope – DM (VHX – 1000). ....	70
Figure 3.8: (a) Impedance tube experimental set-up schematics and (b) Pictorial demonstration of laboratory-scale set-up.....	72
Figure 3.9: a) Lab-view software for pressure signal measurement and b) MATLAB software for pressure signal and absorption coefficient measurement. ....	74
Figure 3.10: Comparison of the reflection coefficient experimental value with the theoretical value for open-end test for validation. ....	75
Figure 3.11: Experimental set-up for differential pressure ( $\Delta P$ ) measurement; (a) Schematic description and (b) Laboratory-scale set-up with exploded view of sample holder and mask placement between the mold. ....	77
Figure 3.12: SEM image of the PVP nanofibers at (a) 5000X (Scale: 5 $\mu$ m) and (b) 50000X (Scale: 0.5 $\mu$ m). ....	81
Figure 3.13: Graphical representation of main effects of electrospinning control factors on fiber diameter. ....	86
Figure 3.14: Graphical representation of main effects of electrospinning control factors on membrane thickness.....	86
Figure 3.15: Graphical representation of main effects of electrospinning control factors on nanofiber weight. ....	87
Figure 3.16: Mathematical model validation with experimental results for fiber diameter measurements.....	88
Figure 3.17: Mathematical model validation with experimental results for thickness measurements.....	88



Figure 3.18: Mathematical model validation with experimental results for membrane weight measurements. ....	89
Figure 3.19: Experimental values of fiber diameter versus modeled value using GP at 27 experimental runs. ....	90
Figure 3.20: Experimental values of PVP fiber membrane thickness versus modeled value using GP at 27 experimental runs. ....	90
Figure 3.21: Experimental values of PVP membrane weight versus modeled value using GP at 27 experimental runs. ....	91
Figure 3.22: SEM micro-graphs (Scale 10 $\mu$ m at 5000X) of: (a) PVDF based electro-spun nanofibers and (b) Fiber diameter measurements. ....	93
Figure 3.23: Microscopic images of; (a) Membrane sample, (b) Thickness calculation at different spots, and (c) Exploded view of measurements. ....	93
Figure 3.24: Significant effect of electrospinning process variables on average fiber diameter. ....	100
Figure 3.25: Significant effect of electrospinning process variables on the average thickness. ....	100
Figure 3.26: Significant effect of electrospinning process variables on PVDF nanofiber membrane. ....	101
Figure 3.27: Mathematical model validation with experimental results for PVDF nanofiber diameter measurements. ....	102
Figure 3.28: Mathematical model validation with experimental results for PVDF membrane thickness measurements. ....	103
Figure 3.29: Mathematical model validation with experimental results for PVDF membrane weight measurements. ....	103
Figure 3.30: Experimental fiber diameter value versus modeled value at 27 trials. ....	104
Figure 3.31: Experimental thickness value versus modeled value at 27 trials. ....	104
Figure 3.32: Experimental weight value versus modeled value at 27 trials. ....	105

## CHAPTER 4

Figure 4.1: a) PVP membrane layering order and b) Schematics of layering pattern. ...	106
---	-----

Figure 4.2: a) Sound absorption coefficient of single PVP fiber membrane at three discrete BC's and b) Schematics of layering configuration.....	107
Figure 4.3: a) Sound absorption coefficient of two layers of PVP fiber membranes at three discrete BC's and b) Schematics of layering configuration.....	108
Figure 4.4: a) Sound absorption coefficient of four layers of PVP fiber membranes at three discrete BC's and b) Schematics of layering configuration.....	109
Figure 4.5: a) Sound absorption coefficient of eight layers of PVP fiber membranes at three discrete BC's and b) Schematics of layering configuration.....	110
Figure 4.6: a) Sound absorption coefficient of sixteen layers of PVP fiber membranes at three discrete BC's and b) Schematics of layering configuration.....	111
Figure 4.7: a) Sound absorption coefficient of twenty layers of PVP fiber membranes at three discrete BC's and b) Schematics of layering configuration.....	111
Figure 4.8: Sound absorption coefficient percent increase with thickness variation at discrete BC's for PVP layers. ....	112
Figure 4.9: a) PVDF membrane layering order and b) Schematics of layering pattern. ....	113
Figure 4.10: a) Sound absorption coefficient of single PVDF fiber membrane at three discrete BC's and b) Schematics of layering configuration.....	114
Figure 4.11: a) Sound absorption coefficient of two layers of PVDF fiber membranes at three discrete BC's and b) Schematics of layering configuration.....	115
Figure 4.12: a) Sound absorption coefficient of four layers of PVDF fiber membranes at three discrete BC's and b) Schematic of layering configuration. ....	116
Figure 4.13: a) Sound absorption coefficient of eight layers of PVDF fiber membranes at three discrete BC's and b) Schematics of layering configuration.....	116
Figure 4.14: a) Sound absorption coefficient of sixteen layers of PVDF fiber membranes at three discrete BC's and b) Schematics of layering configuration.....	117
Figure 4.15: a) Sound absorption coefficient of twenty layers of PVDF fiber membranes at three discrete BC's and b) Schematics of layering configuration.....	117
Figure 4.16: Sound absorption coefficient percent increase with thickness variation at discrete BC's for PVDF layers. ....	119
Figure 4.17: a) PVP and PVDF membrane layering order and b) Schematics of layering pattern. ....	120

Figure 4.18: a) Sound absorption coefficient of two alternate layers of PVP and PVDF fiber membranes at three discrete BC's and b) Schematics of layering configuration...	120
Figure 4.19: a) Sound absorption coefficient of four alternate layers of PVP and PVDF fiber membranes at three discrete BC's and b) Schematics of layering configuration...	121
Figure 4.20: a) Sound absorption coefficient of eight alternate layers of PVP and PVDF fiber membranes at three discrete BC's and b) Schematics of layering configuration...	122
Figure 4.21: a) Sound absorption coefficient of sixteen alternate layers of PVP and PVDF fiber membranes at three discrete BC's and b) Schematics of layering configuration...	122
Figure 4.22: a) Sound absorption coefficient of twenty alternate layers of PVP and PVDF fiber membranes at three discrete BC's and b) Schematics of layering configuration...	123
Figure 4.23: Sound absorption coefficient percent increase with thickness variation at discrete BC's for PVP and PVDF combined layers.....	124
Figure 4.24: Filler infused PVP membranes layering blocks. ....	125
Figure 4.25: Sound absorption coefficient of CNT infused PVP membrane layers at different BC's: a) 3cm and b) 5cm; and c) Schematics of layering configuration. ....	126
Figure 4.26: Sound absorption coefficient of GN infused PVP membrane layers at different BC's: a) 3cm and b) 5cm; and c) Schematics of layering configuration. ....	126
Figure 4.27: Sound absorption coefficient of FS infused PVP membrane layers at different BC's: a) 3cm and b) 5cm; and c) Schematics of layering configuration. ....	127
Figure 4.28: Sound absorption coefficient of FG infused PVP membrane layers at different BC's: a) 3cm and b) 5cm; and c) Schematics of layering configuration. ....	128
Figure 4.29: Sound absorption coefficient of MC infused PVP membrane layers at different BC's: a) 3cm and b) 5cm; and c) Schematics of layering configuration. ....	128
Figure 4.30: Sound absorption coefficient percent increase with thickness variation at discrete BC's for filler-infused PVP membrane layers.....	129
Figure 4.31: Sound absorption coefficient of filler-infused PVP membranes multiple layers at BC's: a) 0cm, b) 3cm, and c) 5cm; and d) Schematics of layering configuration. ....	131
Figure 4.32: Sound absorption coefficient percent increase with thickness variation at discrete BC's for filler-infused PVP membrane multiple layers. ....	132
Figure 4.33: Filler infused PVDF membranes layering blocks. ....	133

Figure 4.34: Sound absorption coefficient of CNT infused PVDF membrane layers at different BC's: a) 3cm and b) 5cm; and c) Schematics of layering configuration. ....	134
Figure 4.35: Sound absorption coefficient of GN infused PVDF membrane layers at different BC's: a) 3cm and b) 5cm; and c) Schematics of layering configuration. ....	134
Figure 4.36: Sound absorption coefficient of FS infused PVDF membrane layers at different BC's: a) 3cm and b) 5cm; and c) Schematics of layering configuration. ....	135
Figure 4.37: Sound absorption coefficient of FG infused PVDF membrane layers at different BC's: a) 3cm and b) 5cm; and c) Schematics of layering configuration. ....	136
Figure 4.38: Sound absorption coefficient of MC infused PVDF membrane layers at different BC's: a) 3cm and b) 5cm; and c) Schematics of layering configuration. ....	136
Figure 4.39: Sound absorption coefficient percent increase with thickness variation at discrete BC's for filler-infused PVDF membrane layers.....	137
Figure 4.40: Sound absorption coefficient of filler-infused PVDF membranes multiple layers at BC's: a) 0cm, b) 3cm, and c) 5cm; and d) Schematics of layering configuration. ....	139
Figure 4.41: Sound absorption coefficient percent increase with thickness variation at discrete BC's for filler-infused PVDF membrane multiple layers. ....	140

## CHAPTER 5

Figure 5.1: Demonstration of the time-controlled electrospinning process for manufacturing of filtration-ready nanofiber membranes. ....	145
Figure 5.2: (a) Filter-ready nanofiber membrane samples with dotted red circles representing testing locations, and Pressure drop testing of single specimen at spot 1 (b), spot 2 (c), and spot 3 (d). ....	146
Figure 5.3: SEM micrographs with fiber diameter and distribution for samples; PVDF 20wt.% (a-b), PVDF 22wt.% (c-d), and PVDF 25wt.% (e-f).....	148
Figure 5.4: SEM micrographs with fiber diameter and distribution for samples; CNT 0.25wt.% (a-b), GN 0.25wt.% (c-d), TiO <sub>2</sub> 0.25wt.% (e-f), and CuNP's 0.25wt.% (g-h). ....	150
Figure 5.5: Description of the various conventional mask samples. ....	151
Figure 5.6: Average pressure drop measurements of various conventional masks. ....	152

Figure 5.7: SEM micrographs and $\Delta P$ measurements at different electrospinning times for configurations; PVDF 20wt.% (a-b), PVDF 22wt.% (c-d), and PVDF 25wt.% (e-f). ...	154
Figure 5.8: Variation in the specific weight of PVDF nanofiber membrane at different electrospinning times for varying polymeric concentrations. ....	154
Figure 5.9: Fiber diameter versus pressure drop of nanofiber membranes produced at different electrospinning times and concentrations. ....	155
Figure 5.10: SEM micrographs and $\Delta P$ measurements at different electrospinning time for configuration; CNT 0.25wt.% (a-b), GN 0.25wt.% (c-d), TiO <sub>2</sub> 0.25wt.% (e-f), and CuNP's 0.25wt.% (g-h).....	157
Figure 5.11: Specific weight of filler infused membranes produced at different electrospinning times. ....	158
Figure 5.12: Fiber diameter versus pressure drop of filler infused nanofiber membranes produced at different electrospinning times.....	158
Figure 5.13: Electrospinning time required to reach the N-95 $\Delta P$ equivalency. ....	159
Figure 5.14: Step-wise nanofiber layering methodology on SM; a) Layer-wise dismantling of SM, b) Membrane handling, c) Nanofiber membrane sandwiching; and d) Placement of sandwiched layer for final testing. ....	160
Figure 5.15: $\Delta P$ measurements of SM's and respective nanofiber layered configurations. ....	161
Figure 5.16: PFE measurements of SM's and respective nanofiber layered configurations at particulate size of 0.3, 0.5, 1.0, 2.5, 5.0, and 10 $\mu$ m. ....	163
Figure 5.17: PFE measurements of SM's and respective nanofiber layered configurations at particulate size of 0.3 $\mu$ m. ....	163

## LIST OF ABBREVIATIONS AND SYMBOLS

AgNPs	Silver Nano-particles
ANOVA	Analysis of Variance
ASTM	American Society for Testing and Materials
BC	Back Cavity (cm)
CuNPs	Copper Nano-particles
DAQ	Data Acquisition System
DM	Digital Microscope
DMA	Dynamic Mechanical Analyzer
DMF	N,N-Dimethylformamide
DSC	Differential Scanning Calorimetry
EN	European Standards
FD	Fiber Diameter
FG	Fiber Glass
FS	Fumed Silica
GN	Graphene
GP	Genetic Programming
LPM	Liters Per Minute
MPP	Micro-Perforated Panel
MWCNTs	Multi-Walled Carbon Nanotubes
PA-6	Polyamide-6
PAN	Polyacrylonitrile
PEO	Polyethylene Glycol
PLCM	Porous Laminated Composite Material
PLCM	Porous Laminated Composite Material
PLCM	Porous Laminated Composite Material
PLLA	Polylactic Acid
PSF	Polysulfone

PVA	Polyvinyl Alcohol
PVC	Polyvinyl Chloride
PVDF	Polyvinyl Difluoride
PVP	Polyvinylpyrrolidone
RPM	Revolutions Per Minute
RSM	Response Surface Methodology
SAP	Sound Absorption Performance
SARS-CoV-2	Severe Acute Respiratory Syndrome Coronavirus-2
SEM	Scanning Electron Microscope
SM	Surgical Mask
TGA	Thermogravimetric Analyzer
TPEE	Thermoplastic Polyester Elastomer
TPU	Thermoplastic Polyurethane
TiO <sub>2</sub>	Titanium Dioxide
$\alpha$	Sound absorption coefficient
R	Sound reflection coefficient
Z	Acoustic impedance
Z <sub>s</sub>	Surface impedance
Z <sub>c</sub>	Characteristic impedance
H <sub>12</sub>	Transfer function between mic 1 and mic 2
H <sub>I</sub>	Transfer function of incident wave
H <sub>R</sub>	Transfer function of reflected wave
f	Sound wave frequency (Hz)
f <sub>l</sub>	Low frequency range (Hz)
f <sub>u</sub>	High range (Hz)
$\Delta P$	Pressure drop (Pa)
s	Spacing between microphones (cm)
c	Speed of sound (m/s)

$R_{th}$	Theoretical value of reflection coefficient
$I_r$	Sound intensity of reflected wave
$I_i$	Sound intensity of incident wave
$P_r$	Pressure amplitude of reflected wave
$P_i$	Pressure amplitude of incident wave
$\rho_o$	Density of air
$\alpha_\infty$	Tortuosity
$\phi$	Porosity
$\sigma$	Static air flow resistivity
$d$	Material thickness (m)
$\varepsilon$	Matching ratio
$\lambda$	Wavelength
QF	Quality Factor
$\omega$	Angular frequency
$t$	Time (s)
$d$	Tube diameter (m)
$a$	Radius of pipe
$Q$	Air flow rate
$U$	Face velocity



# **Chapter 1. Introduction**

## **1.1 Preamble**

Over the years, nanotechnology has emerged as one of the most interesting and encouraging fields of science and engineering. It represents the foundation for a wide variety of technological advancements in different areas. Different related terminologies like nanofibers, nanocomposites, nanotubes, etc., are associated with nanotechnology. Compared to microscale particles, nanoscale particles (1-100nm) offer a wide variety of advantages in terms of physical and chemical properties [1]. Products and devices fabricated at this scale find different and unprecedented industrial applications. The significance of nanomaterials can be gauged by the recent sharp increase of published research works in this field that mainly focuses on developing unique and different methods for fabricating nanostructured materials [2,3].

Fibers having diameters less than 1000nm are known as nano-fibers. They can be produced by various manufacturing processes such as: phase separation, drawing, self-assembly, electrospinning, template synthesis, etc. [4,5]. Nanofibers offer exceptional advantageous properties, including lightweight, high surface area to volume ratio, low thickness, high porosity, better aspect ratio, flexibility, etc., making them better substitutes for various industrial applications. Typical industrial applications involve filtration mediums, bone/tissue engineering, sound absorption, medical and health care, electronic and piezo sensors, energy generation, and energy storage [6,7].

The electrospinning technique, used in the fabrication of micro/nano-scaled fibers, is well-instituted. The electrospinning process of manufacturing fibers is carried out by applying electric potential using a high voltage source that stretches the extruded polymer strand into a thin fibrous structure. These fibers can be electro-spun from various materials, including polymer, ceramic, and metallic base materials [8,9]. The electrospinning process is governed by a set of controllable processing variables, including physical parameters: electric voltage, solution flow, needle to collector distance, and collector geometry as well as solution conditions: concentration, additives, and type of solvent. The successful optimization of these process control variables results in an effective electrospinning process to achieve application-based nanofiber-based structures [10,11].

## **1.2 Problem Statement**

### **1.2.1 Need for Research Focusing in Acoustics Applications**

Noise pollution is the third-largest source of pollution in the world and has a detrimental effect on health, according to World Health Organization (WHO) [12,13]. The generation of high or low-frequency sound waves from a wide variety of sources like railway locomotives, transport buses, trucks, aircraft's engines, air conditioning units (public and residential, industrial units, heavy machinery, electronic gadgets, worship places, electricity transmission wires, etc. are the primary sources of noise pollution. Therefore, to reduce the detrimental effects of noise, an acoustic material of exceptional absorption behavior becomes necessary to develop for a wide variety of volume restricted applications [12,13].

The noise can be attenuated by different methodologies, which include active noise control and passive noise control. Passive noise control is the most reliable and easy method compared to active noise control, including the assembly of various sensors and algorithms. The passive noise control method involves applying passive media, a solid medium prone to modifications, for energy interaction wherein the sound waves interact with the material. It attenuates the noise by energy conversion to heat. Different types of porous/fibrous materials are traditionally used as a passive medium for noise control, and these include conventional foams, panels, and fibrous sheets. These traditional materials offer better sound absorptive behavior in high-frequency zones but exhibit very low absorption in low and medium frequency zones. The size of the pores/fibers in these materials usually range in a few micrometers, but the fibers obtained from electrospinning have diameter sizes in nanoscale, which offers high specific area, porosity, reduced thickness, and moldability. The reduced size and enhanced features of nanofibers exhibit better sound absorption behavior in low and medium frequency zone [14,15].

Low-frequency noise attenuation is a significant consideration in the aircraft, automotive, manufacturing, and transportation industry. Moreover, low-frequency noise reduction is the biggest challenge encountered by these industries. The conventional foam or micro-fibrous materials exhibit the best acoustic performance in absorbing high-frequency noise (more than 1000Hz) but are not capable enough to absorb the noise of

lower frequencies at feasible thickness. The wavelengths at lower frequencies (20-200Hz) reach the room dimensions that result in resonance inside the room. Consequently, it is harder to absorb the low-frequency noise except by using thicker absorbing materials. The thickness should be about the quarter of a wavelength that can go up to meters in thickness. Therefore, the material volume required for low-frequency noise reduction is relatively larger and is not viable for applications where space and cost are major considerations. In order to mitigate the low-frequency noise, it is essential to develop the acoustic material structure that overcomes the limitations of cost & thickness and offers better sound absorption performance.

### **1.2.2 Need for Research Focusing in Filtration Applications**

Severe Acute Respiratory Syndrome Coronavirus-2 (SARS-CoV-2/COVID-19) has been recently articulated as a global pandemic in March-2020 by World Health Organization (WHO). The novel SARS-CoV-2/COVID-19 virus has reported average size of 100nm with a mean aerosol size  $\leq$  of 100nm [16]. When fused with a virus, particulates from contaminated human body discharge (nasal droplets/saliva) make it airborne. Filtration test standards have not been developed to trap such viruses. The test standards established by the National Institute for Occupational Safety (NIOSH) are limited to the aerosol size of 300nm, wherein the conventional fiber-based masks like N95 and N99 are standardized for respective particle size protection at 95% and 99% efficiency at nominal pressure drops of 350Pa (approx.) [17]. The carrier virus/bacteria or any pollutant aerosol can transform itself into floaty particles, mists, extremely thin or thick droplets, and mixed surrounding particulate of any shape and size. The aerosols generated from various pollutants like fuel emissions bear a typical standard size of 10-100nm. These pollutant aerosols can also enter the bloodstream through different organ passages and badly affect our nervous system, leading to severe brain damage [18]. The prevention against nano-scale virus/bacteria through the application of face masks also applies to these pollutant aerosols originating from fuel emissions, industrial units, and factories. The filtration medium composed of non-woven materials is considered the most favorable media for face protection and other industrial filtration-based protection. The traditional microfiber-based non-woven filters are limited to several micrometers of fiber diameter size (10-15 $\mu$ m).

Therefore, the filters composed of nanofibers manufactured using the electrospinning process could offer promising protection against nano-aerosols due to associated nanoscale diametric size and porosity of electro-spun fibers (100-600nm).

Protection against the novel coronavirus, other viruses/bacteria, and pollutants is one of the major challenges faced by medical professionals, front-line workers, industrial engineers, and the general public. The conventional face mask protection protects us from micro-sized particulates and aerosol but limits itself to nano-scale viruses or pollutants. The best-known NIOSH standardized mask prevents the aerosols of 300nm with 95-99% filtration efficiency with a pressure drop less than equal to 344Pa at 8LPM airflow. These masks are well suited for various industrial-grade pollutants and several viral or bacterial infections to date. These high-grade masks (N-95) were very limited during the pandemic and are currently provided only to medical professionals. On the other hand, the surgical face masks are economical and readily available masks with a very low-pressure drop of 200Pa (at 8LPM airflow) due to thick micro-scale fibers and a large air gap. Breathability or pressure drop is one of the significant considerations in mask selection. The mask with dense layers of fibers provides breathing discomfort and hypoxia (caused due to lack of oxygen supply to body parts).

### **1.3 Motivation**

Electro-spun nanofibers offer alternate technological solutions by their unique properties such as the high surface area to volume ratio, high porosity, lower thickness, high tortuosity, flexibility, and lightweight.

These properties are an essential factor for improvement in the sound absorption performance of acoustic materials. The sound waves interact with the material's structures, and energy transfer takes place between them. The interaction between the sound waves and the nano-sized fiber-loaded membrane is higher because of the large surface area exposed in a given volume. In this context, these membranes can help minimize the thickness and maximize the absorption of low-frequency noise. The thermal, mechanical, and acoustic properties of these membranes can be modified using different types of fillers. Different combinations of nanofiber membranes were layered together to enhance the low-

frequency absorption. The layering arrangements include the following; single membranes made from pure polymers, a single membrane made from filler addition, multi-layering of the single material-based membrane, multi-layering of two material-based membranes, multi-layering of filler-based membranes, membrane layering on different conventional materials.

On the other hand, electro-spun nanofibers possess lower weight, lower thickness, nano-scale fiber diameters, and air gap dimensions which is significantly important in providing protection against nano-sized aerosols with pressure drop compared to conventional N-95's.

Prevention against aerosols of size less than 300nm (average) can be provided with multiple layers of microfibers or thick layers of nanofibers, but the breathability should not be compromised. The filtration medium developed from electro-spun nanofibers was characterized by analyzing the morphological attributes (fiber diameter and distribution), air gaps, specific weight, and pressure drop measurements. The filtration test set-up measurements were validated with the conventional N-95 masks available in the market. The single layer of electro-spun fibers was fabricated at different concentrations, different electrospinning times, various anti-viral/anti-bacterial fillers, and membrane layering on surgical masks to achieve pressure drop level comparable to medical-grade N-95 masks (currently used in SARS-CoV-2/COVID-19 emergency ward by front-liners).

#### **1.4 Thesis Objectives**

The purpose of the experimental study in this thesis is to develop nanofiber-based electro-spun composites for various industrial applications utilizing the electrospinning process. The developed nanofiber membrane composites produced from the different polymeric bases, fillers, and layers are used for specific industrial applications, including low-frequency sound absorption and filtration. The experimental work, proposed and studied in detail in this study, is divided into two different categories;

- a) Developing technologies for manufacturing sound absorptive nanofiber membranes and their composites by implementing the electrospinning process.**

The strategy includes the production of pristine polymeric fiber membranes and the inclusion of micro/nano-sized fillers like FG, FS, MWCNTs, GN, and MC on pure polymeric fiber structures in varying concentrations to study its effect on the acoustic performance of nanocomposites. The acoustic ready nanocomposites were developed in the following arrangements, PVP-based multi-layering combinations, PVDF-based multi-layering combinations, PVP-PVDF-based multi-layering combinations, PVP-Filler based multi-layering combinations, and PVDF-Filler based multi-layering combinations. The acoustic performance of these arrangements was investigated to study the effect of varying material composition on low-frequency sound absorption.

**b) Developing technologies for manufacturing filtration nanofiber membranes and their composites by implementing the electrospinning process.**

The strategy includes the production of pristine polymeric fiber membranes and the addition of micro/nano-sized fillers like MWCNTs, GN, TiO<sub>2</sub>, and CuNP on pure polymeric fiber structures to study its effect on the filtration property (pressure drop) of nanofiber composites. The study involves the development of a pressure drop measurement system to study the effect of varying pure polymer concentration, varying filler material, electrospinning time, and electrospun membrane layering on filtration characteristics of nanofiber composites.

## **1.5 Thesis Methodology**

The development of smart nanofiber material structures for different industrial applications was carried out using various polymeric and nano/micro filler materials. The sound-absorbing nanofiber membranes were fabricated using two polymeric materials: PVP and PVDF. The polymers were dissolved in a suitable solvent (ethanol for PVP solution and DMF for PVDF solution) by continuous stirring at an elevated temperature of 60°C to 75°C for 4-6 hours, followed by electrospinning. Five electrospinning control parameters were varied at different levels to optimize the corresponding fiber diameter, thickness, and weight measurements of nanofiber membrane. The sound absorption performance of the resulting nanofibers was investigated for different combinations of polymer nanofiber membranes at different back cavities. The thermal, mechanical, and morphological characterization of the samples was carried out using Thermogravimetric

Analyzer (TGA), Differential Scanning Calorimetry (DSC), and Dynamic Mechanical Analyzer (DMA), Digital Microscope (DM), and Scanning Electron Microscope (SEM). The acoustic characterization was carried out on circular-cut samples of 10cm diameter in an impedance tube using the transfer function method.

The PVDF nanofiber-based filtration composites were manufactured utilizing the methodology described above. The parametric study was also carried out using statistical tools for optimizing the electrospinning parameters to achieve minimum fiber diameter. The smooth, homogenous, and thin nanofibers were manufactured using these optimum values. Furthermore, the nanofiber composites were fabricated by adding various fillers like MWCNTs, GN, TiO<sub>2</sub>, and CuNPs. The pressure drop measuring apparatus was assembled and validated with the pressure drop measurements of known conventional masks. The breathability characterization of nanofiber composites was carried out in the following patterns: a) Pure polymer nanofiber membrane with different fiber diameter and distribution, b) Filler modified membranes, c) Different electrospinning timed membrane, and d) Membrane layering on surgical grade masks. The filtration test was designed to achieve the breathability (pressure drop) level of medical grade N-95 masks with nanofiber infusion. These thin nano-fibrous membranes were produced at different fiber diameter sizes and distribution (by varying concentration), different electrospinning times, different filler materials, and different layering patterns with conventional surgical masks to achieve an N-95 level of protection and breathability.

The experimental study deals with nanofiber mat manufacturing using an electrospinning process from different polymer materials for sound absorption and filtration-based industrial applications. The morphological characterization of these electro-spun nanofiber membranes was carried out utilizing SEM and DM. The SEM and DM micrographs were further used in statistical analysis of the electro-spun nanofiber structures to optimize the average fiber diameter with its distribution, average thickness, and weight. The electrospinning process parametric modeling and optimization was carried out using the statistical study of Taguchi's design, Analysis of Variance (ANOVA), Response Surface Methodology (RSM), and Genetic Programming (GP). The nanofiber membranes were further modified with different types of nano/micro filler materials to

study the effect on absorption coefficient and pressure drop. The thermal and mechanical characterization of the samples was carried out using TGA, DSC, and DMA. The acoustic characterization of the nanofiber membrane composites was investigated at different back cavities using impedance tube on various sample combinations, including; single membrane (with and without filler), multi-layering combinations (with and without fillers), and membrane layering with conventional material. The filtration performance of the nanofiber composites was performed on a laboratory scale pressure drop measurement set-up. The fiber diameter, air gap, thickness, and pressure drop of the filter media were characterized using SEM, DM, Differential Pressure Measurement setup. The filtration characterization was carried out on various nanofibers-based samples such as single membrane (with and without filler), conventional masks pressure drop validation, membrane layering on traditional medical masks, and different electro-spin timed samples to reach pressure drop of N-95 but with thin nanofibers.

## **1.6 Targeted Main Contributions of the Thesis**

The envisioned main contributions of the research work presented in this thesis can be outlined as follows:

- ❑ Development of statistical models for evaluating effects of five electrospinning process parameters on production of PVP and PVDF nanofiber membranes utilizing ANOVA, RSM, and GP.
- ❑ Development of multi-layered pure polymeric nanofiber-based composites in various combinations/patterns including different materials to enhance low frequency sound absorption with the incorporation of three different back cavities.
- ❑ Development of multi-layered filler based polymeric nanofiber-based composites in various combinations/patterns including different materials to enhance low frequency sound absorption with the incorporation of three different back cavities.
- ❑ Development of thin and lightweight nanofiber-based filtration mediums in several configurations to achieve pressure drop barrier level of medical grade N-95 masks (344Pa approx.). The developed filter materials were configured in several patterns: single electrospun layer with pure polymer and anti-viral/bacterial filler induced membranes, varying electro-spun timed membranes, and electro-spun membrane



layering on conventional masks to improve filtration characteristics in terms of fiber size and pressure drop barrier level.

## **1.7 Thesis Outline**

Chapter one introduces the basics of nanofibers, nanotechnology, the electrospinning process, and its applications, low-frequency problem statement, nanofibers as a solution, conventional surgical mask and its limitations, and nanofiber membrane filtration potential. Further, thesis motivation, objective, methodology, targeted main contributions, and outline is also described in this chapter.

Chapter two provides the theoretical background and a thorough review of the nanotechnological advancements, nanofibers, different nanofiber manufacturing technologies, electrospinning process, the effect of electrospinning control parameters on the production of nanofibers, and various electrospinning techniques. In addition, a detailed study on noise control fundamentals, low-frequency problems, sound absorption and reflection coefficient measurement method, filtration mechanism, conventional mask filtration standard limitations, energy wastage, and its harvesting is presented in this chapter. A review of the previous research studies undertaken in the past concerning nanofibers as the sound absorptive material medium and filtration media membranes are also presented in this chapter. The chapter concludes with a summary of the literature survey conducted, limitations of the traditional manufacturing techniques, and experimental research requirements.

Chapter three provides the detailed explanation of the experimental technique used in this work to develop nanofiber membranes for different industrial applications with the description of the characterization techniques. The experimental methodologies include; material type and properties, electrospinning set-up used in nanofiber manufacturing, instruments and mechanisms used for material characterization (thermal, mechanical, morphological, acoustic, filtration, piezoelectric), and pressure drop measurement set-up. The effect of electrospinning parameters on the production of PVP and PVDF fibers by utilizing statistical analysis tools (Taguchi's design, ANOVA, RSM, and GP) is investigated in this chapter. The effect of controlling processing variables of the

electrospinning process on the morphological attributes of the produced nanofibers, associated fiber diameter, thickness, and weight (output responses) are also presented in this chapter. The statistical and modeling study of five chosen electrospinning parameters explains the significance of each processing variable involved in regulating the output response of different fiber materials.

Chapter four describes the acoustic performances of pure polymeric nanofiber membranes and their composites manufactured by different layering arrangements. The acoustic characterization of nanocomposites carried out at different back cavities is presented in this chapter in the following manner; effect of single nanofiber membrane layer (pristine polymer), multi-layering of PVP-based membranes, multi-layering of PVDF based membranes, and multi-layering of PVP-PVDF based membranes. The multi-layered composites were stacked in the following order in this study; two layers, four layers, eight layers, sixteen layers, and twenty layers. In addition, the acoustic performances of five filler-based polymeric nanofiber membranes and their composites manufactured by different layering arrangements are described here. The acoustic characterization of nanocomposites carried out at different back cavities is presented in this chapter in the following manner: effect of two, three, and four filler-based fiber membrane layers (progressive layering of CNT, GN, FS, FG, and MC in three varying concentrations), multi-layering of PVP-Filler based membranes, and multi-layering of PVDF-Filler based membranes. The multi-layered filler composites were stacked in the following order in this study; seven layers, ten layers, thirteen layers, and sixteen progressive layers from each filler configuration.

Chapter five investigates the filtration characteristics (fiber diameter size, distribution, basis weight, and pressure drop) of the nanofiber-based electro-spun layers. The filtration performance of the pure polymer-based nanofiber layer with varying fiber diameter, filler infused polymeric nanofiber membrane, different electro-spun timed membrane, and layered nanofiber membrane on surgical masks is presented in this section.

Chapter six provides a summary of the experimental investigations carried out in this work. The chapter is finally concluded with the significant research contributions of the study followed by recommendations for future research work.

## **Chapter 2. Theoretical Background and Literature Review**

### **2.1 Nanotechnology and Nanofibers**

Nano-technology is the term derived from the word Nano and technology where the Greek word “Nano” means “dwarf,” and the study of small/dwarf particles is known as Nano-technology. The study of tiny particles applies to science and technology, including physics, materials sciences, chemistry, engineering, and biology. Nanotechnology is the study that regulates or handles the particulate matter of size that varies from 1 to 100 nanometers, and it also elucidates the quantum realm scale and its effects [7,19,20]. Nanomaterials encapsulate an extensive range of materials, metallic, ceramic, polymeric, etc., that possess exceptional thermal, physical, mechanical, and chemical properties. The material with these outstanding properties includes nano-particles, nano-rods, nano-sheets, nano-wires, nano-tubes, and nanofibers. Among all other nanomaterials, Nanofibers are considered one of the most exceptional and robust candidates for various advanced industrial applications [3,21].

Polymeric fibers produced from different technologies like drawing or spinning result in fiber diameter sizes ranging from 10-100 $\mu$ m, commonly known as microfibers. On the other hand, polymeric fibers with a diameter ranging less than 1 $\mu$ m are known as nanofibers. Nanofibers are one-dimensional nano-sized materials with outstanding properties for a wide range of industrial applications such as filtration, energy generation, energy storage, medical treatment, water treatment, sound absorption, biomedical research, and electronics. The nanofiber diametric range from several hundred to thousands of nanometers offers several properties like the high surface area to volume ratio, lower weight, flexibility, tortuosity, better porosity, added surface functions, and lower thickness compared with traditional fibers. Nanotechnology in nanofiber manufacturing has emerged as the most prominent technology that permits a broad spectrum of materials polymeric materials, natural fibers, composite materials, carbon-based material, clays, etc., spun in the form of nanofibers. Polymeric nanofibers, membranes, mats, and applications have recently gained significant attention in several technical research and scientific developments in the past several years [22–24].

## 2.2 Nanofiber Fabrication Techniques

Several processing methods currently in use for the manufacturing of nanofibers include nanofiber drawing, template-assisted synthesis, phase separation, nanofiber/nanostructure self-assembly, and electrospinning. The synthesis techniques are also associated with various drawbacks or issues in processing method or fiber structure like non-continuity in fiber length or diameter, higher fiber production time, low fiber density or collection, fibers with bead defects, etc. A comprehensive review provides the discussion of these methods in detail with the associated drawbacks.

### 2.2.1 Drawing Technique

The process of nanofiber drawing is often referred to as the dry spinning process carried out at the molecular level. The drawing methodology is limited to viscoelastic polymeric materials that experience extreme buckling or shape deformations with sufficient cohesive force to handle stresses generated during fiber pulling. Ondarcuhu et al. [25] and Ramakrishna et al. [26] described the production of fibers using a micropipette dipped in a sodium citrate solution and chloroauric acid by the drawing process. As shown in Figure 2.1, the pipette was submerged in the material solution droplet on the contact line by a micromanipulator. Then it was pulled out from the droplet at an approximate speed of  $1 \times 10^{-4}$  m/s. The fibers were stretched from the liquid and accumulated with the pipette surface contact. The viscosity of the material and the evaporation of the solvent play an essential role in regulating the fiber diameter value and the continuous drawing of the fibers. The nanofiber drawing process is a laboratory-scale easy process that includes few components like the material solution, micro-pipette, and  $\text{SiO}_2$  base. Still, it limits itself to fiber production one at a time [25].

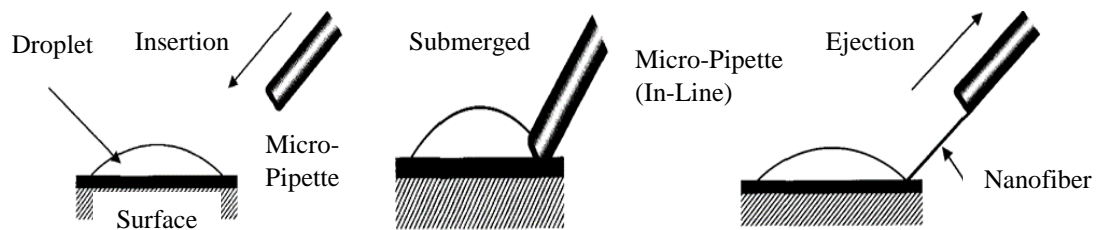


Figure 2.1: Nanofiber drawing process (Step-wise methodology) [26].

### 2.2.2 Self-Assembly Technique

The process of self-assembly is the reflexive autonomous arrangement of nano-scale components into different structures. Guodong et al. [27] described self-assembly as the process of building up the nanoscale fibers in specific arrangements or blocks with small nano-sized components or fillers such as nano-particles. These particles were arranged in an orderly fashion to build various structures such as monolayers, tubes, and honey comb structures. Ramakrishna et al. [26] explained the self-assembly process from the study of Hartgerink et al. [28] through an easy schematic shown in Figure 2.2, where the small nanoscale particle was arranged concentrically with bonding in a similar pattern. The pattern normal to the plane in longitudinal direction formed a cylindrical shape with an arranged cluster of nanofibers. According to their studies, the intermolecular force of attraction is an essential factor in bonding the nanoparticles together, which controls the nanofiber assembly's overall shape. The self-assembly process is a laboratory-scale complex method that involves the exquisite requirement of standard laboratory instruments and is limited to concrete polymeric materials. The theory of self-assembly technique has been used progressively in various disciplines and areas [29].

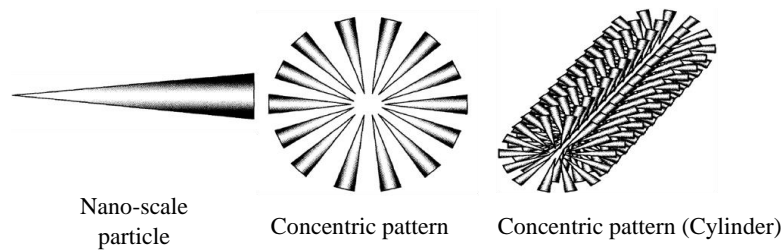


Figure 2.2: Self-assembly process and nanofiber arrangement [26].

### 2.2.3 Template-Based Synthesis Technique

The template-assisted method fabricates nanofibers from very few fixed or particular materials through nano-scale pores of porous membranes. The membranes have uniform diametric pores of the cylindrical structure, and these pores extend to the uniform depth ranging from 5-50 millimeters. The cylindrical shape of the pores produces nano-cylindrical structures of preferred materials. The template technique produces the nanofibrils and nano-tubular structures of metallic, polymeric, and carbon compounds. Ramakrishna et al. [26] defined template-based synthesis as the process that molds the

material in desired nano-structural shape by a template holding nano-pores [Figure 2.3]. The synthesis of PAN nanofibers involved using an anodic aluminum oxide template with an array of 13mm diameter and 60μm thickness channels by Feng et al. [30]. The polymeric solution of PAN extrusion through the template under pressure resulted in an aligned nanofibrous structure of different pore sizes. Figure 2.4 (a) shows the SEM representation of an anodic aluminum oxide template with a structured arrangement of pores in a hexagonal pattern of 102.4nm pore diameter and  $6.43 \times 10^3$  pores/cm<sup>2</sup>. As shown in Figure 2.4 (b), the solidified nanofibers, after extruding out from the template, mimicked the aligned pattern and reached the diameter value of 104.6nm close to the template pore size. The approach resulted in an aligned 10.7μm long nanofiber surface with air present in between pores which was evident in the cross-sectional SEM in Figure 2.4 (c). The template-assisted methodology is a laboratory-scale simple process that involves standard laboratory supplies and instruments. It can regulate the fiber diameter of the produced structures by utilizing different size templates and is limited to quite a few polymeric materials [31].

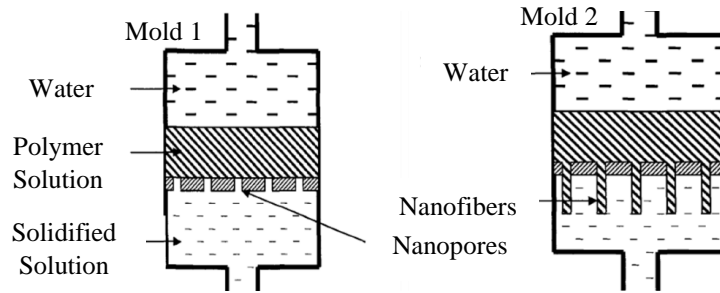


Figure 2.3: Template-assisted Nanofiber synthesis [26].

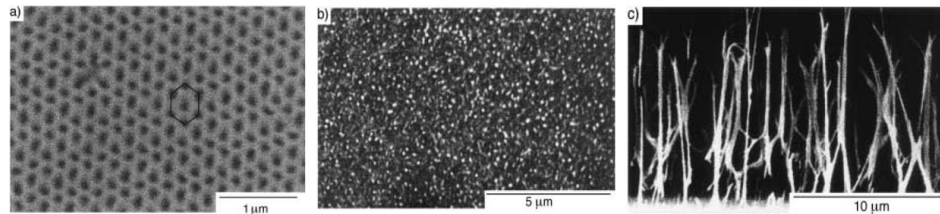


Figure 2.4: (a) SEM of anodic aluminum template structure, (b) Nano-fibrous surface, and (c) Cross-sectional appearance of nanofibers. Rep. with permission [30].

## 2.2.4 Phase Separation Technique

The phase separation process involves accidental separation of the polymer substance from the homogenous solution mixture of polymer and solvent. The separation of polymer-rich and poor phases from the solution or mixture is typically carried out by incorporating

some non-miscible solvent or reducing the temperature of the solution. The porous structures are produced by quenching the polymer-solvent mixture below the solvent freezing range [32]. Peter X et al. [33] provided a detailed study on a five-step nanofiber synthesis process from PLLA - poly (L-lactic) acid. In the study, the first step involved polymer dissolution, where PLLA was added in THF – Tetrahydrofuran in 1 – 15% w/v by continuous stirring at 60°C for 2 hours. The second step was gelation, where the as-prepared solution (2ml at 50°C) was poured on Teflon and then was cooled to -18 to 45°C - Gelation temperature for 2 hours. The third step of solvent extraction was carried out for two days by immersing the gel in the distilled water, which was changed at least three times per day. The fourth step involved the freezing of gel at -18°C for 2 hours after removing it from water. The final step involved the freezing and drying of as-prepared frozen gel at -55° in a vacuum for seven days. The complete process is explained by the schematic shown in Figure 2.5 provided by Ramakrishna et al. [26]. The phase separation laboratory-scale method is simple and involves standard laboratory instruments and freezing dryer and refrigerator, but the process is limited to a discrete material range.

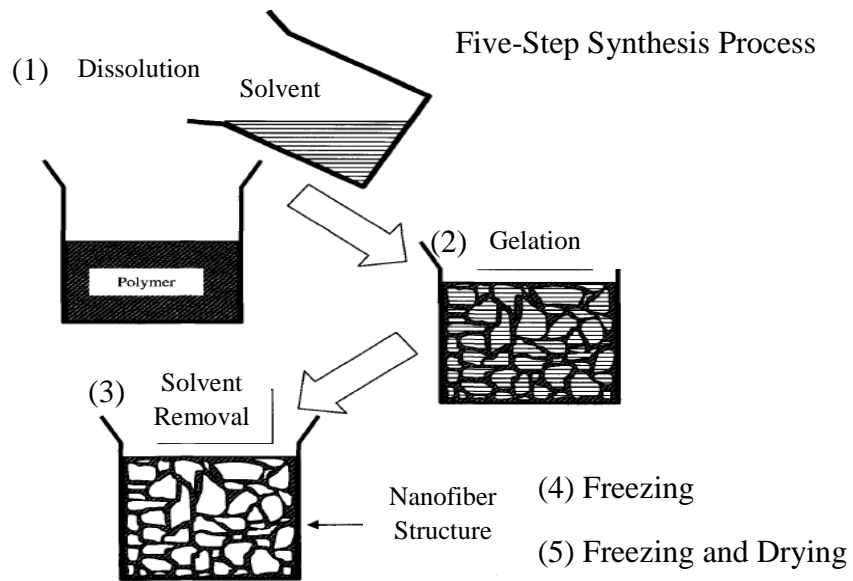


Figure 2.5: Schematics of nanofiber synthesis from phase separation technique [26].

### 2.2.5 Electrospinning Technique

In general, the process of electrospinning is the stretching of polymeric solution/melt under the action of electrostatic force. Electrospinning is derived from the word

electrostatic spinning, and its fundamental roots date back to the early '90s. The first observed phenomenon of electrostatic attraction of a liquid substance was dated back to 1600 [34]. The technological advancements in nanotechnology have led to the foundation for developing the nano-sized material structure that can substitute the conventional industry-based material for specific applications. A detailed study on the electrospinning process and its applications are provided in the following section.

Fibers are categorized as nanofibers when the diameter values are less than 1000nm. It can be produced by different manufacturing techniques like drawing, template-based synthesis, self-assembly, phase separation, electrospinning, etc. Among all the manufacturing techniques discussed, Electrospinning is the most simple, flexible, and reliable method of producing long continuous nanofibers from a wide variety of polymeric materials. The electrospinning produces fibers with the following properties: extended length, smaller in diameter (nano-scaled), porosity control, and high surface area to volume ratio offers distinctive properties for various industrial and research applications [35].

Anthony [10] reviewed the basic pre-requisites for carrying out the electrospinning process in a laboratory-scale setup, including the following:

- a) Polymeric solution/melt.
- b) Hollow tube/solid structure acting as an electrode that holds the polymer solution.
- c) High voltage DC power supply.
- d) Grounded Collector for nanofiber collection.

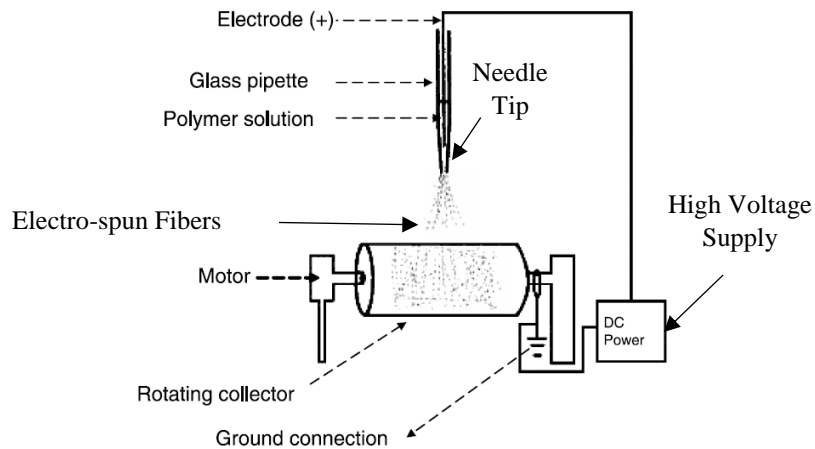


Figure 2.6: Schematic description of the vertically positioned electrospinning apparatus. Rep. with permission [20].



As shown in Figure 2.6, the electrospinning setup consists of a needle or a glass pipette that holds the viscous polymer solution or melts with varying concentrations. The polymer solutions are prepared by dissolving the polymer material into the appropriate solvent at specific concentrations (E.g., Polystyrene dissolved in methylene chloride at 20% w/w concentration). In order to avoid polymer solution dripping from a vertically positioned electrode, the viscosity maintained should be sufficient enough to hold the solution inside. The tubular electrode is placed 6-10 inches far from the grounded collector (metal drum/sheet). An electrode with polymer solution is connected to the positive side of a DC high voltage supply by wiring. As the DC power supply is powered with voltage control of 10-20KV, the polymer droplet stretches out in cone shape from the tube/needle/pipette and move towards the grounded drum/plate. The jet of polymer coming out is nanofibers of that solution which are hardly visible. Renekar et al. [36] observed that the nanofiber spraying from a single droplet appeared to be divided into multiple spray patterns, but when observed with a high-speed camera, it was a single nanofiber spinning out with fast movements. Long strands of nanofibers were collected on the collector drum surface randomly, and it was hard to visualize the ends of fibers in microscopic images. The solvent plays a vital role as the solution contains 80% of it, and it evaporates quickly from the sprayed jet while spinning. The selection of solvent, electrode-collector distance, and temperature confirmed the fabrication of dry nanofibers at the collector. The grounded collector ensured the dissipation of the residual charge on the produced nanofiber mats, which can be removed from the drum easily.

The electrospinning method involves applying an electric charge to the polymer solution, and the solution jet stretches in a high electric field to produce nanofibers. Figure 2.7 (a) explains the basic methodology of the electrospinning process, where the basic components in the setup include: High voltage power supply, needle, and grounded collector. The polymer solution flows out from the needle with a constant flow rate maintained by a syringe pump. The high voltage is supplied by a DC power supply and is connected to the needle to provide an electrical charge to the material flowing out the needle. When the electric charge intensity increases, the fluid coming out stretches and elongates itself to a conical shape at the end, which is known as the Taylor cone [Figure 2.7 (b)]. The polymer solution droplet crosses the surface tension with increasing electric

field, and the charged polymer jet extrudes out by electrostatic force between them. Due to the movement of the polymer jet towards the collector, it undergoes several bending instabilities that lead to looping, whipping motion, and elongation. The fiber diameter of the solidified jet reduces due to plastic stretching caused by repulsive charges to reduce the bending instabilities [37–39]. The electrospinning technique is a relatively cost-efficient and straightforward approach wherein the smooth, long, and continuous fibers of different materials can be produced at a laboratory scale and industrial scale. Production of aligned nanofibers with better repeatability is possible with electrospinning methodology.

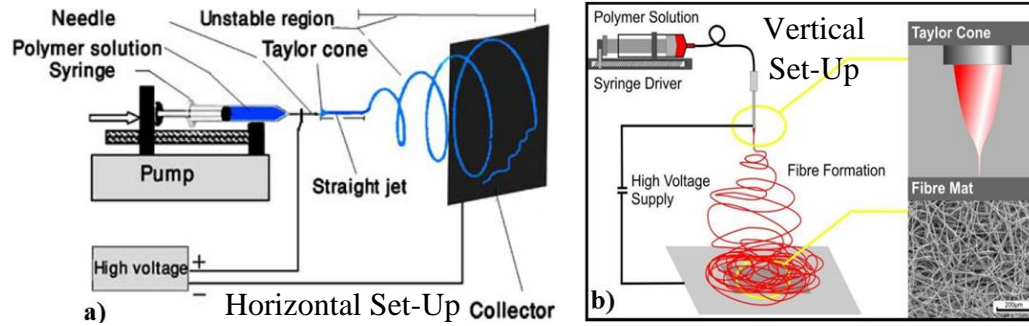


Figure 2.7: (a) Schematic description of the horizontally positioned electrospinning set-up. Rep. with permission [38], and (b) Description of the Taylor cone generation with the SEM micrograph of nanofiber mat produced Rep. with permission [37].

### 2.3 Electrospinning process and parameters affecting the process

The dominant attributes of the process that fabricates micro/nano fibers from an electro statistically induced polymeric solution jet or melt are as follows; a) The high voltage power source should supply sufficient power to subjugate the surface tension and viscoelastic force of the polymeric solution in order to extrude the liquid in form of jet from needle tip, b) An appropriate choice of solvent that is capable of liquefying the polymer material, c) Solvent properties like surface tension and viscosity should not be too high as the polymer will not extrude out in form of jet from the needle or should not be too low as the polymeric solution will leak out from the needle, d) Solvent vapor pressure should be appropriate enough that evaporates rapidly to maintain fiber structure near the collector end but it should not be too fast that the fiber solidifies before stretching in form of nanofibers, and e) Distance between the needle tip and collector should not be too small as it can lead to spark generation but it should be sufficiently far for the solvent drying to create fibers in nanoscale [22,40].

Formhals [41] successfully produced fibers from the liquid polymer material using an electric field and invented the first electrospinning set-up in 1934. Fiber collection was the main issue encountered by researchers as the wet fibers adhered to each other because of improper solvent drying. Formhals solved solvent drying by introducing distance variation between the collector surface and needle tip to increase the solvent drying time [42]. Taylor carried out the polymer jet and droplet structure study under the influence of the applied electric field in 1960 and 1969. The polymer solution extruded out from the needle tip in the shape of a conical structure, and the droplet from the cone stretched out further to form a jet that flew out towards the collector. This conical structure is commonly known as the Taylor cone structure. In his studies on electrospinning with different polymeric materials, Taylor observed that the cone angle of  $49.3^\circ$  was the optimum balance of polymeric surface tension under the applied electric field [43]. The polymer jet was generated near the tip of the Taylor cone, where the solution surpassed its surface tension force. The jet travel further towards the unstable zone often referred to as bending instabilities. Three different models demonstrate the instabilities; Axisymmetric instabilities (influenced by high electric power), Rayleigh instabilities (influenced by low electric fields), and Whipping instabilities (influenced by variation in mutual charges present in solution). The polymer jet stretching, bending, and elongation are observed due to the bending instabilities [44]. In his studies, Baumgarten [45] successfully produced fibers in the diameter range of 0.05 to  $1.10\mu\text{m}$  from the acrylic solution utilizing an electrospinning process modified with infusion pump place of needle tube to achieve a constant solution flow rate. Simons [45] introduced the revised concept of electrospinning wherein the positive terminal of the electrode was dipped into the polymer solution, and the other side was connected to a belt on which the fibers were accumulated. He observed lower fiber diameter and short fiber structures with the lower viscosity of the solution. The electrospinning process has been used to achieve the ultrafine polymeric nano-fibrous structures [4]. Lorrondo et al. [46] built the melt electrospinning set-up wherein the material placed in a temperature-controlled barrel was heated (for melting) and pushed forward using a piston. The extruded polymer droplet was stretched in the form of fibers. Wannatong et al. [47] investigated the effect of six acting forces responsible for the generation of fibers. These forces include; a) electrostatic force which is responsible for pushing the jet from needle point to collector

surface, b) body force or gravitational pull, c) coulombic stretching force, which is responsible for stretching of polymer jet flying towards the collector screen due to mutual polarity of charges, d) surface tension which is responsible for stretching of polymeric jet, e) viscoelastic force which is responsible for stretching prevention of polymeric jet, and f) drag forces that generate because of the friction between the moving jet and ambient air. Drozin [42] investigated the generation of polymeric streams and extruded droplets under the action of electric field applied. The study examined the co-relationship between the electric field required concerning the radius of polymer droplet and dielectric constant of liquid coming out from needle. Optimum parametric limits of factors like refractive index, conductivity, and dipole moment were defined in the study.

The fiber morphology and structure depend on the viscosity of the solution predominantly. Lower solution viscosity often leads to the production of non-smooth fibers with defects. On the contrary, highly viscous polymer solution makes the liquid extrusion harder when it pushed through the pipette. In order to obtain the smooth and homogenous fibers, an appropriate solution viscosity is required which can be tuned by varying the polymer concentration in the solution. The effect of critical limits of solution viscosity of PAN fibers produced from 1.3wt.% and 15wt.% polymer concentration was studied where the solution-based factors like concentration, viscosity, and molecular weight are inter-dependent to each other and can be tuned with the variation of one of the mentioned factors. With the lower solution viscosities, surface tension of liquid plays an important role and the fibers manufactured in this case comprises of bead defects [48,49]. Fong et al. [50], in his studies, investigated the effect of viscosity variation on the electro-spun Polyethylene Oxide (PEO) nanofibers. They investigated a suitable range of viscosity for smooth and uniform generation of nanofibers and concluded the optimum viscosity range from 1 to 20poise. The polymer solution experiences higher duration of stress relaxation during electrospinning process which in turn escapes the breaking of polymer streams extruding out from the droplet. Higher viscosity of the solution mixture often results in higher measurements of uniform fiber diameters.

Several parameters can affect the fabrication of nanofibers produced from electrospinning of the polymer liquid solution, and these control parameters are categorized

further in three sections in the following manner; a) Solution-based factors (such as polymer solution concentration, solution conductivity, the viscosity of the solution, molecular weight of solution, surface tension, type of solvent), b) Processing based factors (such as high voltage supply, needle tip to collector surface distance, solution flow rate, collector geometry and rotational speed, and needle design), and c) Surrounding factors (such as ambient temperature, pressure, and humidity). The condensed discussion of all electrospinning control parameters and their effect on morphological attributes of fibers and associated diameter is described briefly in Table 2.1.

Table 2.1: Description of parametric effect on the morphology and structure of electro-spun fibers.

<b>Electrospinning control parameters</b>	<b>Parametric effect on fiber morphology and structure</b>	<b>References</b>
<b>Solution Based Factors</b>		
Polymer solution concentration	High polymer concentration: Higher fiber diameter values.  Low polymer concentration: Bead formation on fiber structure and the possibility of electro-spraying increases.	[48,51–55]
Solution conductivity	High Conductivity: Uniform smooth fibers, bead-less structure, and lower fiber diameter values.	[56–58]
Solution viscosity	High viscosities: Fiber diameter value increases, bead defects reduction, and uniform fiber structures.	[48–50,54]
Solution molecular weight	High molecular weight: Production of fibers with very less bead defects and droplet-free fiber accumulation.	[48,59,60]

Solution surface tension	High surface tension: Instability of polymer stream increases and electro-spraying phenomenon.  Indecisive inter-relationship established between fiber morphology and surface tension.	[38,53,54,58,61,62]
Solvent type	Depends on the dielectric constant and evaporation rate.  High dielectric properties: Smooth fiber with no beads on the structure and reduced fiber diameter measurements.	[58,63–65]
<b>Processing Based Factors</b>		
High voltage supply	High voltage intensity: Lower diameter values, better solvent evaporation, and quick solvent drying.  Indecisive relationship between the voltage intensity and fiber diameter measurements.	[26,56,66–71]
Needle tip to collector distance	Very high and low distances: Generation of beads on fiber structure. The optimum distance is required for the generation of smooth fibers.  High distances: Longer elongation time and lower diameter values.	[67,70,72]
Solution feed rate	Low feed rates: High stretching time and low fiber diameter values.	[70,73]

	High feed rates: Bead defect generation and insufficient fiber drying.	
Collector geometry and rotational speed	<p>Metal collectors: Smooth fiber structures</p> <p>Rotating cylindrical drum collector: Aligned fiber structures, yarn type or braid type fiber structure produced.</p> <p>Zero RPM collectors: High fiber diameter value.</p>	[54,74–83]
Needle design	<p>Low needle diameter: Low fiber diameter values and extruded droplet size reduction.</p> <p>Co-axial and twin capillary needles: Fiber production from different polymer blends and hollow fiber structure.</p>	[84,85]
<b>Surrounding (Ambient) Factors</b>		
Temperature	High-temperature input: Low fiber diameter value and low solution viscosity.	[62,86,87]
Pressure	<p>Very low-pressure environment:</p> <p>Bubbling of polymeric solution from needle tip or impossible electrospinning, optimum pressure required, and indecisive morphological effect relation with pressure.</p>	[26]
Humidity	High humidity environment: A higher number of circular-shaped pores on fiber structure.	[88]

---

Very high humidity: Amalgamation of pores, non-circular structures, and high fiber diameter values

---

The electrospinning process has been utilized in wide variety of industrial applications including textiles, filtration, energy generation, medical treatment, sound absorption, biomedical research, and electronics [22–24]. However, these applications require further investigations and extensive research to fully commercialize the electro-spun products which further demands for the high capacity volume production of the process. A straightforward and easy technique to elevate the rate of production involves application of multiple needles or additional nozzles in the existing polymeric solution injection unit. The multiple nozzles or needles can be mounted in circular and uniaxial configurations and the approach is useful for improving the process through-output and thickness of electro-spun membranes. The major drawback associated with this approach is transfiguration of electrostatic forces in the polymer jet induced by the jet coming from the multiple needle tips [89,90]. Krishnamoorthy et al. [91] investigated the electrospinning configuration of 24 nozzles arranged in 8X3 matrix arrangement for high scale ceramic fiber production. The nozzle design, in his study, was capable of incorporating various sizes with easy installation and replacement. Wang et al. [92] investigated the electrospinning process with three needles wherein each needle was fabricating unique fiber of different material and the membrane was further combined with conveyor belt to produce composite membrane films with higher mechanical strength. Huang et al. [93] established an electrospinning set-up with two rotating nozzles placed opposite to each other to produce nanofiber-based scaffold composites with adjustable pore dimensions of the fibers. The multi-nozzle technology provides advantage over conventional single needle electrospinning in terms of time, thickness, and productivity but requires additional components.



## 2.4 Sound Waves and Noise Control

Sound waves are vibrations that propagate through different mediums, solid, liquid, and gas. When the sound wave propagates, the mechanical vibration of the waves is detected by the human eardrum, which converts it into electrical signals, and we perceive it as sound. The sound wave frequency range from 20Hz to 20000Hz is the limit of detection for humans. The perception of sound depends on a sound source that generates the sound, a transmitting media, and a receiver or the observer. Sound pressure waves travel in different frequencies, and the limits to these frequencies decide the comfortability of the receiver's perseverance [94].

Noise is defined as the type of sound elucidated as distressing, non-pleasant, and disturbing to human individuals. These sound waves obstruct human hearing making a person very uncomfortable as a receiver. Noise is a form of sound pollution that is caused by human-made activities and daily life routine. Low or high-frequency sound waves can be generated from various sources; railway trains, public buses, cars, motorbikes, airplanes; Air cooling and heating systems in residential and public properties, factory sites, construction sites, industrial plants, concerts areas, restaurants, hotels, shopping complexes, movie theatres, worship areas, etc. The attenuation of such noise sources is significant for better quality of life standards and, most prominently, for human health. An extreme noise level can affect human health detrimentally and influence human behavior and concentration, making an individual less energetic. According to several studies, it has been reported that excessive exposure to noise can adversely affect human health in terms of fatigue, headache, backache, digestive disorders, asthma, hearing loss, and cardiovascular losses. As shown in Figure 2.8, the sound wave perseverance through the human ear travels through many sensory nerves that follow specific paths and affect the human body in different ways [94–96].

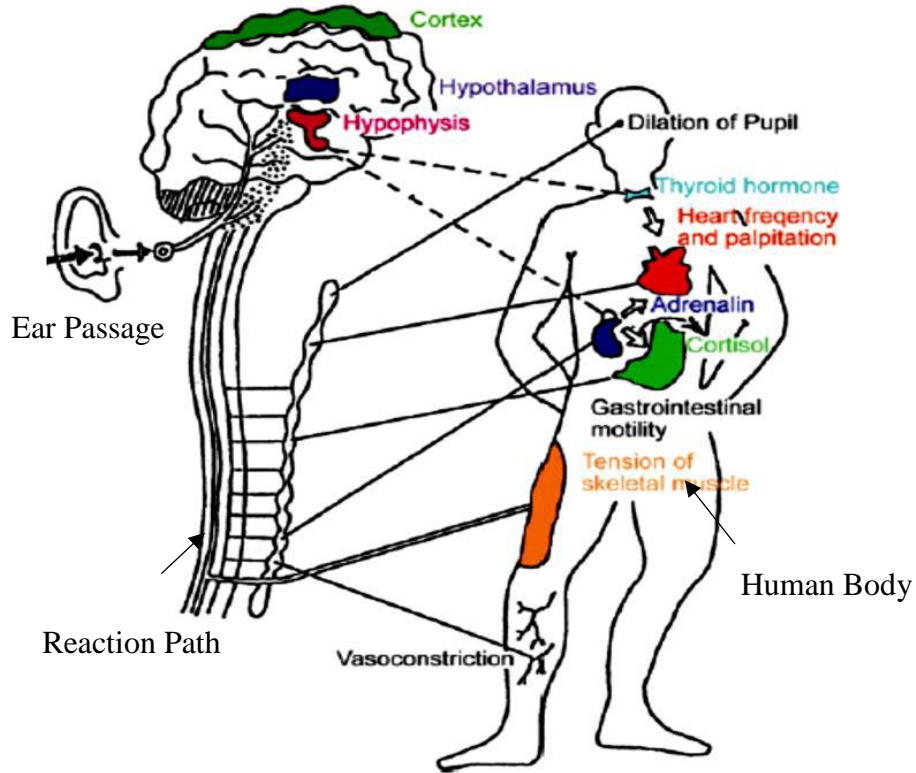


Figure 2.8: Sound wave perseverance through human body reaction path (Extra aural)  
Rep. with permission [94].

The noise pollution can be regulated by implementing various noise attenuation methodologies, essentially noise attenuation at the sound source, attenuation at the transference trajectory (obstructing the waves in their transmission route), and attenuation at the receiver's end (by muffling the receiver from noise). Noise attenuation at the source can be performed in several ways, including modification of machines, volume reduction from the source, complete change of noisy machinery, and repair of the equipment at the source. The noise control in the transmission route can be carried out by assembling soundproofing materials, insulation, enclosures, and other blocking structures. The noise control at the receiver's end requires ear muffs or hearing safety gears [97].

Two existing methodologies of noise control can eliminate the problem of noise; active control and passive control. Active noise control methodology includes an external energy source such as several electronic components like sensors, actuators, vibration-meters, different control systems, and associated algorithms. These components favor eliminating noise or associated vibrations, but any component failure or calibration error

will lead to the entire noise control system breakdown. On the contrary, the passive noise control methodology is the more responsible and secure way to attenuate the noise. The passive control deals with the inclusion of a passive solid medium produced from a different source of material wherein the material structure attenuate the noise by converting sound wave energy into heat. The noise attenuation by various passive mediums is directly dependent on the frequency of a sound wave (low, medium, or high). The passive solid medium can be tuned by changing the material, structure, dimension, and morphology to regulate the acoustic absorption at different frequencies [98–100]. Traditional acoustic porous materials absorb high-frequency sound waves due to an adiabatic energy interaction resulting in heat energy loss because of friction through the pores or fibers. These conventional passive medium structures include; micro-scaled cellular structure foams, thick fiber-based blankets, metal panels (perforated type), acoustic films or membranes. The commercially used fibrous matrix can be fabricated from a wide variety of base materials like natural (straw, wool, plant-based fibers, etc.), polymer materials, metals, and other synthetic sources [101,102].

#### 2.4.1 Sound Absorption Coefficient ( $\alpha$ )

As shown in Figure 2.9, when the plane sound waves of power ( $W_i$ ) incidents on a sound absorptive porous media supported by a solid surface of the thickness ( $d$ ). The part of the incident power is reflected ( $W_r$ ), transmitted past the material ( $W_t$ ), converted into structural vibrations ( $W_s$ ), and converted into heat or absorbed because of air friction ( $W_\alpha$ ) [103]. The incident power is the summation of all these conversions of power according to the energy conservation principle, i.e.;

$$W_i = W_r + W_t + W_s + W_\alpha \quad (2.1)$$

Sound absorption coefficient is defined as the performance index or the measuring quantity for sound energy absorption efficiency analysis of fibrous material or polymeric open cell structured foam. The sound absorption coefficient is represented as ( $\alpha$ ) and is the ratio of sound energy not reflected back to the ambient environment to the incident sound energy which is given by [103];

$$\alpha = \frac{W_t + W_s + W_\alpha}{W_i} = \frac{W_i - W_r}{W_i} = 1 - \frac{W_r}{W_i} = 1 - \frac{I_r}{I_i} \quad (2.2)$$

Where  $I_i$  and  $I_r$  are the sound intensities of reflected and incident sound waves.

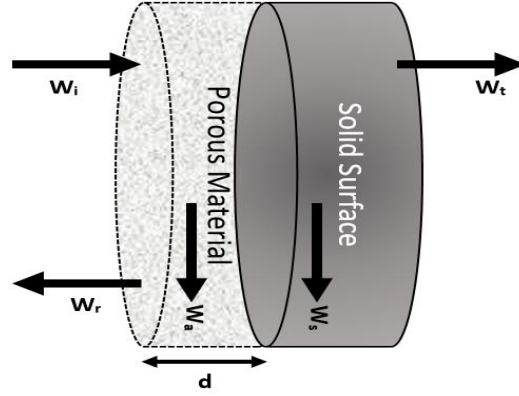


Figure 2.9: Schematics of the sound wave path through the sound absorptive porous material.

#### 2.4.2 Sound Reflection Coefficient (R)

The acoustic performance of the sound-absorbing media can also be determined by measuring the sound reflection coefficient (R). The coefficient value is calculated as the ratio of reflected sound plane wave pressure amplitude to the incident sound (plane wave) pressure amplitude and is defined as [103];

$$R(\omega) = \frac{p_r}{p_i} \quad (2.3)$$

Wherein, angular frequency is denoted as  $\omega$ , reflected plane sound wave is represented as  $p_r$ , and the incident plane sound wave is denoted as  $p_i$ . The sound reflection coefficient is given by a complex equation where a phase term expresses the phase lag of the two pressure sound waves, reflected and incident. The co-relationship between the intensities of sound and pressure amplitudes is given by Equations 2.4 and 2.5 [103];

$$I_i = \frac{p_i^2}{\rho_0 c_0} \quad (2.4)$$

$$I_r = \frac{p_r^2}{\rho_0 c_0} = \frac{|R|^2 p_i^2}{\rho_0 c_0} \quad (2.5)$$

The speed of sound in ambient air is denoted as  $c_0$ , and the air density is represented as  $\rho_0$ . The co-relationship between sound absorption coefficient and sound reflection coefficient was given by substituting the value of  $I_r$  and  $I_i$  in Equation 2.2 [103];

$$\alpha(\omega) = 1 - \frac{|R|^2 \frac{p_i^2}{\rho_o c_o}}{\frac{p_i^2}{\rho_o c_o}} \quad (2.6)$$

$$\alpha(\omega) = 1 - |R|^2 \quad (2.7)$$

### 2.4.3 Acoustic Impedance (Z)

When the plane sound waves travel between different mediums, it reflects these surfaces, and the reflection of the waves depend on the acoustic impedance difference of these mediums. Acoustic impedance (specific to the medium) is generally determined as the ratio of pressure amplitude to the velocity of surrounding particle in that medium and is given by Equation 2.8 [103];

$$Z(x, t) = \frac{p(x, t)}{v(x, t)} \quad (2.8)$$

$$Z(x, t) = Z' + jZ'' \quad (2.9)$$

In the above equation, acoustic pressure amplitude is denoted as p, the velocity of surrounding particle in a medium is denoted as v, and the acoustic impedance is denoted as Z. The acoustic impedance is defined by two components; real part (Z') and imaginary part (Z''). This complex terminology expresses the resistance of sound waves traveling through the real medium part. The imaginary part gives the phase lag of acoustic pressure amplitude and velocity of the surrounding particle in a medium. Both pressure and velocity remains in phase as the plane sound wave propagation is a realistic approach, and the corresponding air impedance is given by [103];

$$Z_c = \rho_o c_o \quad (2.10)$$

The above equation gives characteristic impedance as  $Z_c$ , which is calculated as (at normal ambient conditions);

$$Z_c = \rho_o c_o = 1.21 \left( \frac{Kg}{m^3} \right) \times 344 \left( \frac{m}{s} \right) \quad (2.11)$$

$$Z_c = 416.24 Pa.s.m^{-1} \quad (2.12)$$

The acoustic impedance determined between the interface of two different media is known as the surface impedance, denoted as ( $Z_s$ ). The surface impedance of the acoustic

material depends on several factors, namely; a) Material dependent impedance factors: Tortuosity, porosity, flow resistivity, and characteristic length (viscous and thermal); b) External factors: Sound wave incidence angle, assembly conditions, and thickness of the material. The sound wave reflection coefficient ( $R$ ) and surface impedance ( $Z_s$ ) can be correlated with the consideration of plane propagation in the x-direction at the interface of acoustic material [Figure 2.10]. The stand wave generation takes place due to the intervention of incident sound wave and reflected sound wave through which the resultant pressure is determined by Equation 2.13 (utilizing superposition theory) [103];

$$p(x, t) = p_i + p_r \quad (2.13)$$

$$p(x, t) = P_i e^{j(\omega t - \bar{k}x)} + R P_i e^{j(\omega t + \bar{k}x)} \quad (2.14)$$

In the above equation, incident sound wave pressure amplitude is denoted as  $P_i$ ; incident sound wave pressure is represented as  $p_i$ , reflected sound wave pressure is indicated as  $p_r$ , the distance between the incident wave and the surface is given by  $x$ , time is given as  $t$ , sound wavenumber is denoted as  $\bar{K}$  which is calculated as;  $\bar{K} = \left(\frac{\omega}{c_0}\right) = \left(\frac{2\pi}{\lambda}\right)$ . The angular frequency is  $\omega = 2\pi f$ , the frequency of the sound wave is  $f$ , and wavelength is given by  $\lambda$ . The following equation determines the velocity of the surrounding particle in the medium [103];

$$v(x) = \frac{p(x)}{Z_c} \quad (2.15)$$

$$v(x) = \frac{P_i}{Z_c} e^{j(\omega t - \bar{k}x)} - \frac{R P_i}{Z_c} e^{j(\omega t + \bar{k}x)} \quad (2.16)$$

The pressure amplitude and velocity of the particle at the acoustic material surface is given as follows;

$$p(0) = (1 + R) P_i e^{j\omega t} \quad (2.17)$$

$$v(0) = (1 - R) \frac{P_i}{Z_c} e^{j\omega t} \quad (2.18)$$

The respective surface impedance value ( $Z_s$ ) is given by;

$$Z_s = \frac{p(0)}{v(0)} \quad (2.19)$$

$$Z_S = \frac{(1+R)P_i e^{j\omega t}}{(1-R)\frac{P_i}{Z_C} e^{j\omega t}} \quad (2.20)$$

$$Z_S = Z_C \frac{(1+R)}{(1-R)} \quad (2.21)$$

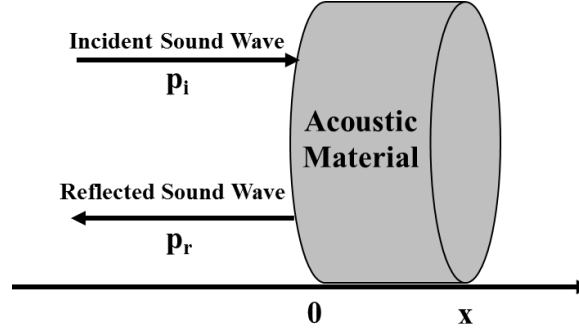


Figure 2.10: Incident and reflected sound pressure wave at the material surface.

The sound reflection and absorption coefficient can be determined concerning surface impedance of acoustic material by;

$$R(\omega) = \frac{Z_S - Z_C}{Z_S + Z_C} \quad (2.22)$$

$$\alpha(\omega) = 1 - |R|^2 \quad (2.23)$$

By substituting  $R(\omega)$  in terms of surface impedance in Equation 2.23;

$$\alpha(\omega) = \frac{4Z'_S Z_C}{(Z'_S + Z_C)^2 + Z''_S{}^2} \quad (2.24)$$

The sound absorption coefficient in relation to the surface impedance of the material surface deduced in the above equation demonstrates the significance of acoustic impedance on acoustic material surface and is also known as the matching law [103].

#### 2.4.4 Factors Influencing Acoustic Behavior of Passive Materials

The acoustic performance of the sound-absorbing medium can be determined by characterizing the material properties in terms of tortuosity ( $\alpha_\infty$ ), porosity ( $\phi$ ), static airflow resistivity ( $\sigma$ ), and surface impedance ( $Z_S$ ). Concerning these parameters, the surface impedance can be determined by Equation 2.25 [104];

$$Z_S = Z_C \frac{\sqrt{\alpha_\infty}}{\phi} \sqrt{1 - j \frac{\phi \sigma}{2\pi f \rho_0 \alpha_\infty}} \quad (2.25)$$

For the acoustic material with extremely high thickness, the airflow resistivity is very small and can be neglected, which further reduces the equation to the following;

$$\sigma \ll 2\pi f \rho_0 \quad (2.26)$$

$$Z_S = Z_C \frac{\sqrt{\alpha_\infty}}{\phi} \quad (2.27)$$

$$\alpha = \frac{4}{2 + \frac{\phi}{\sqrt{\alpha_\infty}} + \frac{\sqrt{\alpha_\infty}}{\phi}} \quad (2.28)$$

In the above equation,  $\phi \approx \alpha_\infty \approx 1$ , for the passive materials, which will result in an absorption coefficient value of unity as the air impedance is equaled to surface impedance. In the scenario, where zero reflection takes place at the surface of the material, the sound waves (plane) is exposed to exponential dissipation that reduces with exponent denoted as ( $\mu$ ) [104];

$$\mu \sim \sqrt{\frac{\phi \alpha_\infty}{\rho_0 c_0^2} f} \quad (2.29)$$

The equation deduced above explains the frequency decrease with decrease in exponent value ( $\mu$ ). The frequency reduction demonstrates that a higher thickness of sound-absorbing material is essentially required for noise attenuation at lower frequencies. On a realistic note, the current sound-absorbing mediums used for acoustic applications have finite dimensions. The airflow resistivity and thickness of the material ( $d$ ) are the two parameters taken into consideration while selecting an acoustic material. The dissipation of sound wave energy through viscoelastic losses increases with an increase in either of the two factors. The maximum acoustic performance of a material can be achieved by finding the optimum limits of the two factors as the surface impedance also increases with its increment. The critical points of the two factor can be determined by Equation 2.30 [104];

$$2 < \varepsilon = \frac{\sigma d \phi}{\rho_0 c_0 \sqrt{\alpha_\infty}} < 6 \quad (2.30)$$



In the above equation, the matching ratio is defined by ( $\varepsilon$ ) and with the considered assumption for passive materials ( $\phi \approx \alpha_\infty \approx 1$ ), the deduced equation was given by equation 2.31 [104];

$$800 < \sigma d < 2400 \text{ (Pa.s.m}^{-1}\text{)} \quad (2.31)$$

Figure 2.11 shows the design consideration of homogenous sound absorbers. It was examined that sound waves of higher wavelength (low frequency) impinging on the material of low thickness penetrates through the material and are not absorbed. To reach a sound absorption coefficient value of 0.8, the thickness of the absorber material should be one-eighth of the incident wavelength ( $\lambda/8$ ). On the other hand, the sound absorption coefficient of 0.9 can be achieved by a minimum of a quarter of a wavelength of the incident sound wave ( $\lambda/4$ ). For better sound absorption, sound waves have to reach the material at a higher velocity that leads to higher friction dissipation losses, but the maximum velocity is achieved at a distance of  $\lambda/4$ . It means that the low-frequency sound waves can only be absorbed with high thickness material, which is not desirable for acoustic application with space constraint and weight considerations [104].

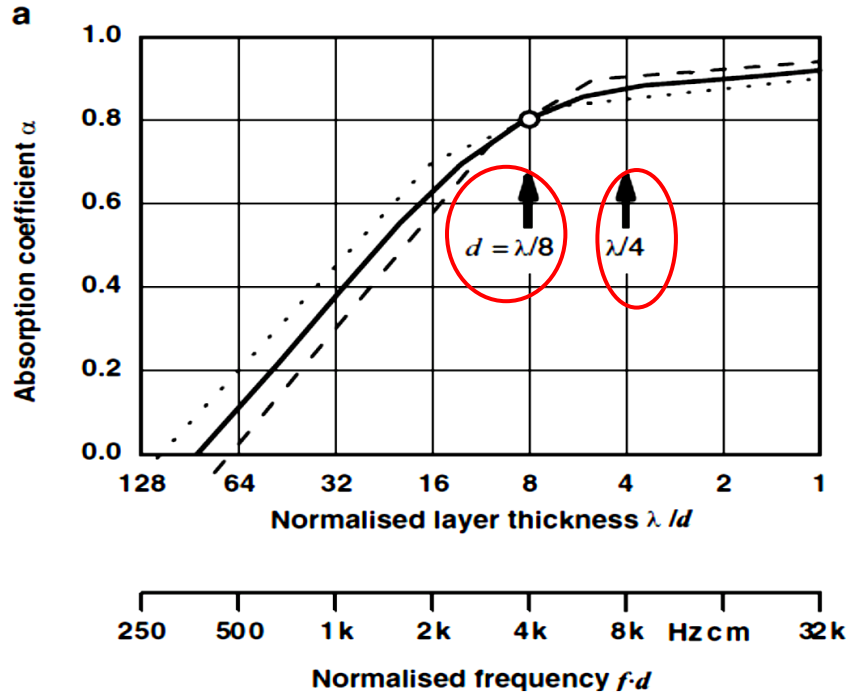


Figure 2.11: Graphical description of fiber-based acoustic absorber various design properties; (a)  $\varepsilon=2$  – represented by the dashed line and  $\varepsilon=6$  – represented by the dotted line on the graph. Rep. with permission [104].

### 2.4.5 Low-Frequency Sound Waves

The low-frequency sound waves range between (20-200Hz), and they can travel longer distances, which can also pierce through thicker walls. The continuous exposure to these low-frequency sound waves can lead to sleep problems, concentration issues, irritation, tiredness, and anxiety because of constant humming noise. The sound velocity ( $c$ ) is the product of wavelength ( $\lambda$ ) and frequency (Hz), and the relationship between the thicknesses of the materials required with corresponding sound frequency and wavelength for maximum sound absorption in the low-frequency zone is tabulated in Table 2.2. It was observed that for 90% sound absorption, the thickness of the material reaches several materials, and it is not possible to absorb it with a material of lower thickness [105,106].

Table 2.1: Relationship between low-frequency sound wave (Hz), wavelength (m), and associated material thickness (m) required to absorb low-frequency sound [105].

Frequency (Hz)	1	10	25	50	100	150	200
Wavelength (m)	340.00	34.00	13.60	6.80	3.40	2.27	1.70
Approx. thickness - d (m)	85.00	8.50	3.40	1.70	0.85	0.57	0.43

The low-frequency noise can be generated from various sources, including; diesel/gasoline engines, electric or mechanical pumps, compressors, fans or rotor blades, ships, winds, air disturbance, combustion, and so on. The low-frequency noise is also generated through structure-borne associated vibrations. For instance, the low-frequency noise originating in a close neighborhood can penetrate concrete walls, and the walls block the high-frequency waves entirely. The noise reduction in ambient air increases with sound wave frequency squares (in Hz), resulting in extremely low absorption at lower frequencies. Different structures containing single or multiple partitions are used to reduce low-frequency sound waves. The concrete or other room walls or buildings have very poor acoustic performance against lower frequency sound waves. Therefore, low-frequency sound absorption requires extremely thick material, which is not feasible for practical applications [105].

### 2.4.6 Sound Absorption of Low-Frequency Waves

A novel structure known as Porous Laminated Composite Material (PLCM) was developed to solve the low-frequency sound absorption problem. PLCM is composed of

laminates or layers of polymeric material, metallic fibers, and polymeric fiber structures. The fabrication process includes several steps; premixing of materials, preheat process, lamination of structures, and molding [Figure 2.12 (a)]. The resultant laminated composites possess higher sound absorption in the 500Hz to 2000Hz frequency range. The design consideration of the laminates has to meet the acoustic impedance values similar to air impedance and the impedance rise in proximity with the surface of layers. When the plane sound propagates via different layers, there should be the least amount of sound reflection to increase the sound wave dissipation throughout the wave trajectory. The laminated porous structures generally experience disintegration of different layers at an elevated ambient temperature. The graphical representation of the acoustic performance of these novel laminated structure-based composites is demonstrated in Figure 2.12 (b-c) [106].

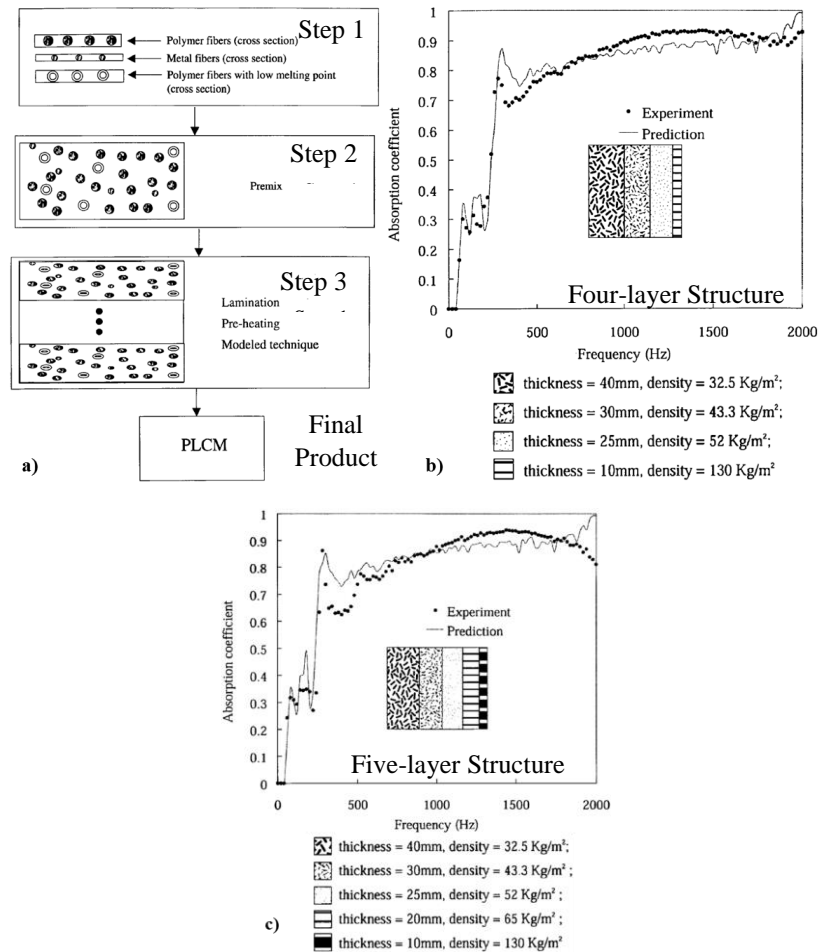


Figure 2.12: (a) Manufacturing process for Porous Laminated Composite Material (PLCM); Sound absorption coefficient of various laminated structures composed of; (b) Four layers, and (c) Five layers [106].

Several attempts have been made in the past by different researchers for low-frequency sound absorption with the utilization of resonance-based devices or membranes [107]. The resonating absorber devices work on the vibrating mass and spring-based system, which transforms pressure disturbances into the resonance at room conditions. These resultant resonances are further reduced by the application of different passive sound-absorbing materials like fiber-based or polymeric foam-based structures. The resonant sound absorbers are segregated into two distinct categories based on a design consideration, i.e., a) Helmholtz resonant absorber and b) Membrane or panel-based resonant absorber [Figure 2.13 (a) and (b)]. The Helmholtz resonant absorber comprises air plugs (mass) located at the opening or perforations of a sheet. The resonances are generated on the same principle of air blowing through the bottle opening. Passive devices further dampen these resonances. The membrane-based resonant absorbers comprise panels/sheet of different materials (mostly rubber or wood), which acts as vibrating mass. The spring action is demonstrated by the air trapped in a small cavity. The variation in mass and air cavity spring action (with stiffness variation) favors the adjustment of resonant frequencies of absorbing devices which in turn will result in higher absorption at their respective resonant frequencies [108–110]. The graphical description of a comparative analysis of the sound absorption coefficient of the mineral wool absorber and perforated sheet layered Helmholtz absorber is provided in Figure 2.13 (c) [108].

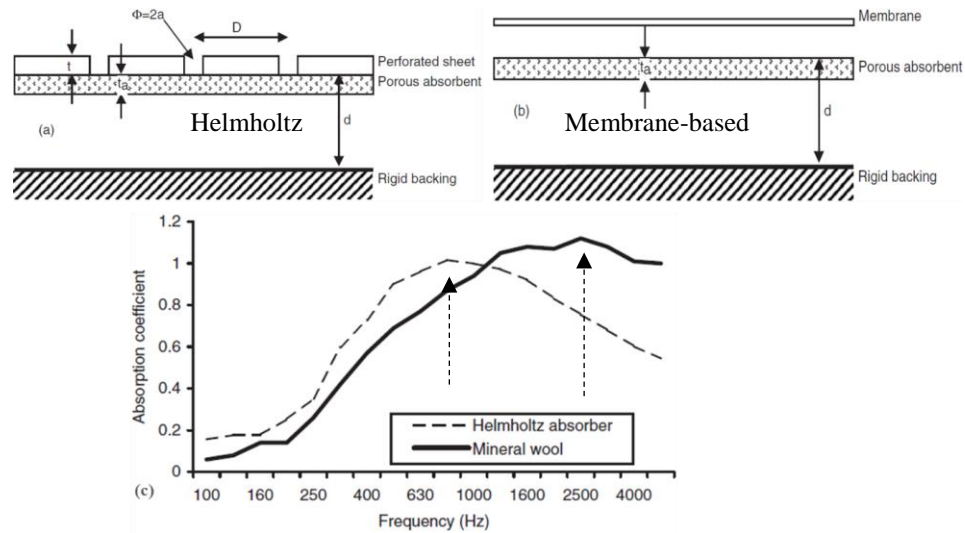


Figure 2.13: Schematic description of resonant absorber; (a) Helmholtz and (b) Membrane or panel-based, and (c) Acoustic performance of porous mineral wool absorber and perforated sheet covered mineral wool layer. Rep. with permission [108].

Low-frequency noise attenuation by Micro-Perforated Panel (MPP) based absorbers has been studied in several research works due to its straightforward and economical approach of enclosing porous materials in the assembly [111–113]. The MPP's enclosure consisting of arrays of perforations when exposed to incident plane sound waves; the energy transformation takes place (from acoustic energy to heat) because of friction losses between air molecules in motion and panel surface. These perforations are generally in the shape of slots or holes drilled as a single resonant source where the porous medium is enclosed for noise attenuation [96,114]. Dah-you Maa first demonstrated the working principle of MPP's in 1970, and further, Maa's MPP theory was improved and developed in 1997 [115,116]. MPP's are traditionally manufactured from a polycarbonate-based polymeric material drilled with perforations or holes in specific structures or patterns. In order to initiate the frictional losses due to energy transfer, the drilled hole diameter should be similarly close to the thickness of the formed boundary layer. The sound energy dissipation can be improved with thickness measurements designed similarly close to the hole diameters. The description of a transparent MPP specimen designed with a thickness of 10mm and different hole diameters is shown in Figure 2.14 (a-c). The sound absorption coefficient values of individual samples are demonstrated in the graphical representation provided in Figure 2.14 (d) [117]. The acoustic performance of MPPs with higher thickness computed by Maa's approach is demonstrated in Figure 2.14 (e) [113,116].

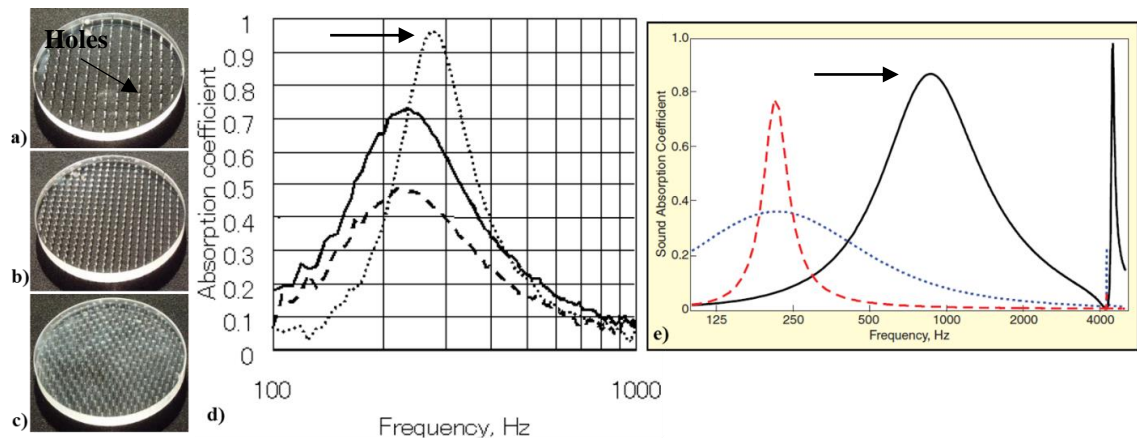


Figure 2.14: Three samples with Hole Diameter (HD) of; (a) 0.5mm, (b) 0.8mm, and (c) 0.8-0.5mm; (d) Acoustic Performance of samples; (A: Dash, B: Dot, and C: Solid) . Rep. with permission [117]; and (e) Graphical representation of sound absorption coefficient measurements of MPP specimens (Solid - 0.4mm D | 0.4mm T, Dotted – 0.4mm D | 10mm T, and Dashed – 4mm D | 10mm T) [113].

### 2.4.7 Sound Absorptive Nanofiber Materials

Low-frequency sound absorption utilizing conventional materials and methodologies requires very thick materials (in several meters). The higher thickness and weight of the material provides a limitation on commercial applications where space or large surface cover and weight is the most significant consideration. Applying these thicker materials requires more handling and maintenance attention and is still not viable for low-frequency noise attenuation. The development of lightweight smart material with very thin geometric dimensions is required to attenuate the low-frequency sound for such applications. The development of sound absorptive nanofibers in the field of acoustic science is fairly state-of-the-art. There are relatively fewer studies performed in the recent past to study the acoustic behavior of nanofibers in the high and low-frequency range. Consequently, the application of nanofibers in low-frequency sound absorption demands a considerable amount of attention for more profound and better cognizance of nanofiber developments in the acoustics field.

Xiang et al. [118] investigated the acoustic performance of Polyacrylonitrile (PAN) nanofiber-based membranes manufactured at different electrospinning times, resulting in different thicknesses. The polymeric concentration of 8wt.% was used in the study by dissolving in DMF, and the solution was electro-spun at 10, 30, and 60 minutes running time. The average diameter of the electro-spun fibers was observed to be  $333 \pm 58 \text{ nm}$ , and the fiber was distributed in a very narrow range, as shown in Figure 2.15 (a-b). The average thickness of the nanofiber samples was observed to be  $17 \pm 03 \mu\text{m}$ ,  $38 \pm 03 \mu\text{m}$ , and  $205 \pm 04 \mu\text{m}$  [Figure 2.15 (c-e)].

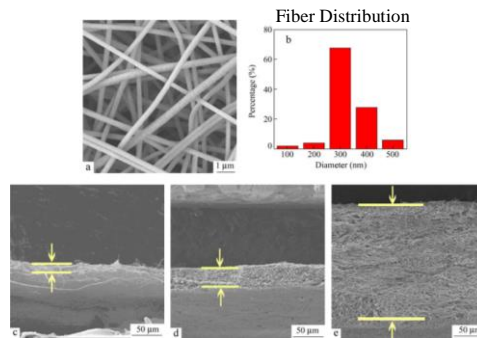


Figure 2.15: SEM micrographs of; (a) PAN nanofibers, (b) Average fiber diameter distribution, (c) PAN nanofiber thicknesses manufactured from varying electrospinning time; (d) 10 min., (e) 30min., and (f) 60 min . Rep. with permission [118].

The sound absorption coefficient value of different combinations of layered electro-spun PAN membranes was investigated in this study at various back cavities of 0mm, 10mm, 20mm, and 30mm. The PAN electro-spun membranes manufactured at different times were denoted as M1, M2, and M3. The absorption coefficient values of all these specimens were observed to be less than 0.1 at 0mm back cavity, but the absorption trend increased with higher back cavity inputs. Lower coefficient values (less than 0.6) were observed with no additional layering of materials. The addition of a perforated panel on the nanofiber membrane specimens was tested acoustically at different back cavities. The sound absorption coefficient values improved with panels and higher values of membrane thickness and back cavity. The sound absorption peak reached the maximum value of 0.9 for some samples at specific frequencies and moved towards the lower frequency region at higher back cavity inputs [Figure 2.16 (a-d)] [118].

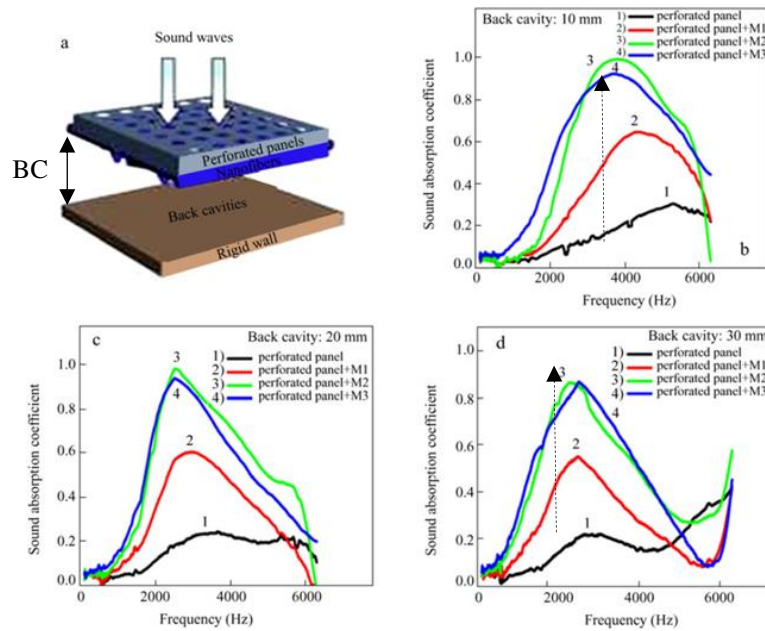


Figure 2.16: (a) Perforated panel layering with PAN nanofiber membranes, Acoustic performance of layered composite at different back cavities: (b) 10 mm, (c) 20mm, and (d) 30mm. Rep. with permission [118].

The acoustic behavior of the electro-spun time membranes was determined at zero back cavity by layering the membrane specimens on the traditional acoustic material like BASF foam layer, glass fiber layer, and Polypropylene (PP) based fiber layer. The sound absorption coefficient values increased much higher than the conventional materials [118]. The study was carried out with a varying thickness of the same material with a single



concentration. The higher absorption values were achieved at a higher thickness of material (when layered with conventional material). These composites achieved maximum absorption in higher frequency ranges but limited themselves to lower frequency and polymeric material variation for layering [Figure 2.17 (a-d)].

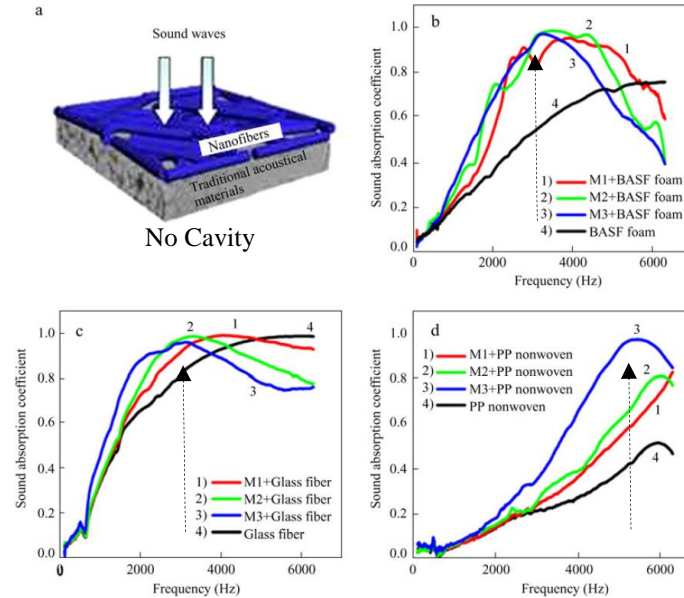


Figure 2.17: (a) Conventional material with PAN nanofiber membranes; Acoustic performance of layered composite in following order (no back cavity): (b) BASF foam, (c) Glass fiber, and (d) Polypropylene fiber-based. Rep. with permission [118].

Mohrova J. et al. [119] studied the sound absorption coefficient of electro-spun PVA nanofibers backed up by the aluminum sheet. The membrane resonance concept was introduced to explain the sound absorptive behavior of nanofiber membranes. The nanofiber membrane structure influenced by the morphology of fibers (smooth/rough) is the most significant factor for sound energy absorption. The material structure of the water-soluble PVA can be modified by the action of the water vapors on nanofiber layers [Figure 2.18 (a-d)]. The circular frame supported acoustic ready specimens of polymeric fiber-based films, and polymer-based films are demonstrated in Figure 2.18 (e-f). The maximum sound absorption coefficient of 0.58 was reported for PVA nanofiber without any water vapor action. On the other hand, the maximum sound absorption coefficient of 0.7 was reported with the water vapor modified nanofiber membrane, which confirms that the sound absorption characteristics are influenced by material structure [Figure 2.19 (a) and (b)] [119]. The study has been carried out in a frequency range of 100-6000Hz, which is



limited to PVA nanofibers fabricated from the same concentration. The study limits itself with the sound absorption in the high-frequency range.

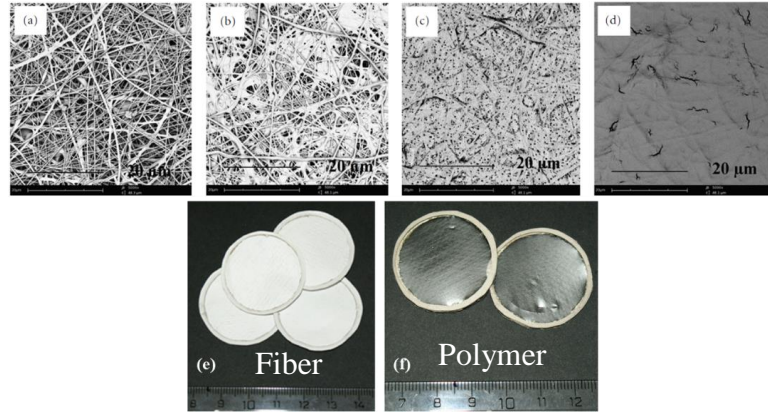


Figure 2.18: SEM images of PVA nanofibers manufactured; With water vapor action for – (a) 0 sec., (b) 60 sec., (c) 120 sec. and with water action for – (d) 60 sec.; Acoustic ready specimens of e) Fiber-based films and f) Polymer-based films [119].

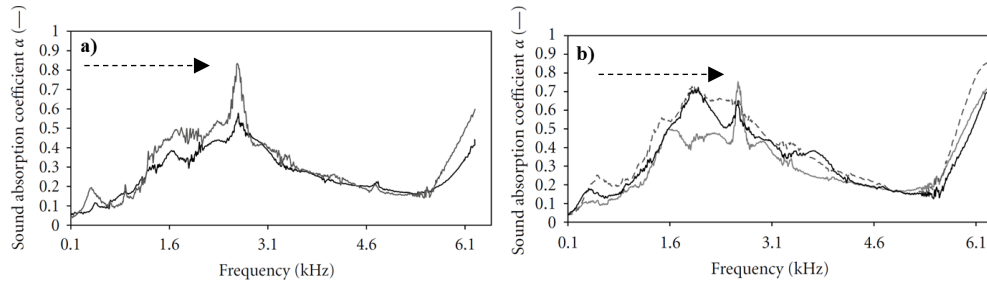


Figure 2.19: Acoustic Performance of; (a) PVA nanofiber membrane (black curve) and polymeric foil (grey curve) and (b) PVA nanofiber layers with times water vapor action in grey line-30 seconds, grey line (dashed) 90seconds, and black line-120 seconds [119].

Liu H. et al. [120] studied the sound absorption characteristics of micro/nanofibers manufactured from three different materials; Polyacrylonitrile (PAN), Thermoplastic Polyurethane (TPU), and Thermoplastic Polyester Elastomer (TPEE) with an average fiber diameter of 400nm, 1000nm and 1000nm [Fig. 2.20 (a-c)]. The study was carried out with different back cavities of 10mm, 30mm, and 50mm. It was observed that the PAN fibers have higher absorption coefficient values from 100-2500Hz frequency compared to TPU and TPEE fibers. The sound absorption curves for TPU and TPEE moved to lower frequency with an increase in the back cavity and exhibited better sound absorption in low and medium frequencies [Figure 2.21 (a-d)]. The effect of electrospinning parameters that control the fiber morphology, which affects the sound absorption properties of nanofiber membranes, has not been studied in this work.

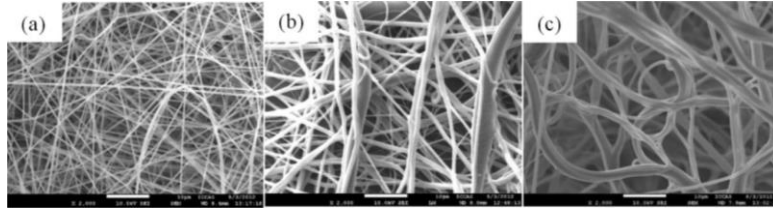


Figure 2.20: SEM images of electro-spun nanofibers of: (a) PAN, (b) TPU and (c) TPEE [120].

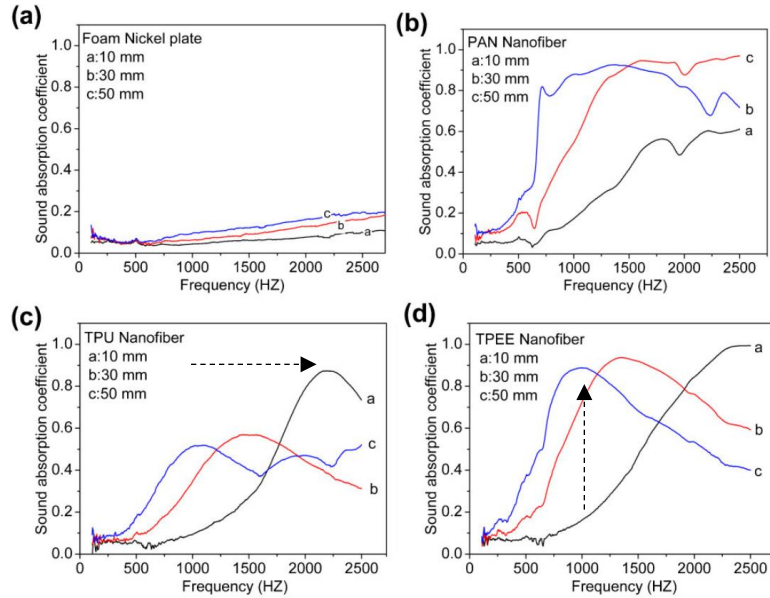


Figure 2.21: Sound absorption coefficient of; (a) Nickel plate perforated panel, (b) PAN nanofibers, (c) TPU nanofibers, and (d) TPEE nanofibers [120].

Wu C.M. et al. [121] investigated the acoustic performance of electro-spun nanofiber membranes of PVDF and Graphene (GN) added PVDF. The comparison of the absorption coefficient of conventional PVDF films (stretched/Non-stretched), electro-spun PVDF (With/Without GN), and electro-spun PVA has been carried out in the frequency range of 100-1000Hz [Figure 2.22 (a-e)]. It was observed that the electro-spun fiber of PVDF with GN has the maximum sound absorption in the low-frequency zone because of the increased surface area that enhances the energy interaction of sound waves. In addition, the PVDF nanofibers, when layered with the conventional acoustics non-woven, improved the sound absorption in the medium and high-frequency range, i.e., it reached the value of 0.8 & 0.9 at 1000Hz & 4000Hz [Figure 2.23 (a-c)] [121]. The study concluded higher absorption coefficient peaks of 0.87 and 0.95 in the frequency range of 1000Hz and 4000Hz with the

inclusion of PVDF-Graphene electro-spun membrane with PP nonwoven sample [121]. The acoustic performance of the PVDF electro-spun specimen (layered or non-layered) resulted in high absorption (greater than 0.8) in the high-frequency range of 1000Hz and limits itself to the even lower frequency range of 100-500Hz. Layering the electro-spun sample with the conventional material improves the thickness but also increased the relative thickness.

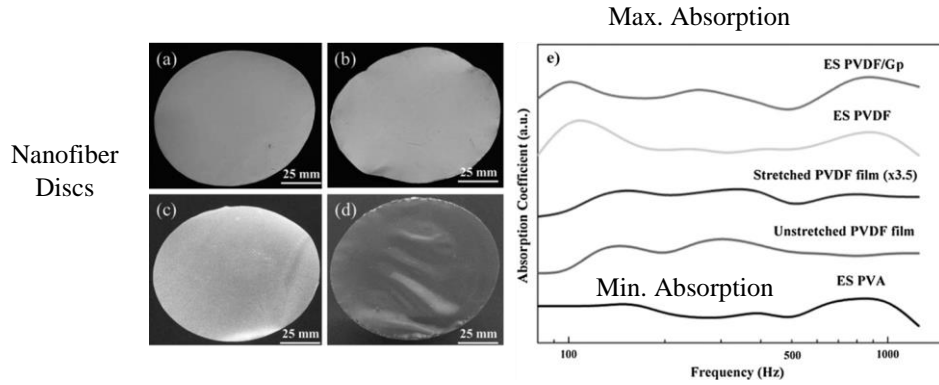


Figure 2.22: Acoustic-ready specimens of; (a) PVDF nanofibers, (b) PVA nanofibers, (c) Non-stretched PVDF nanofibers, and (d) Stretched PVDF nanofiber membrane; (e) Sound absorption coefficients of PVDF specimens. Rep. with permission [121].

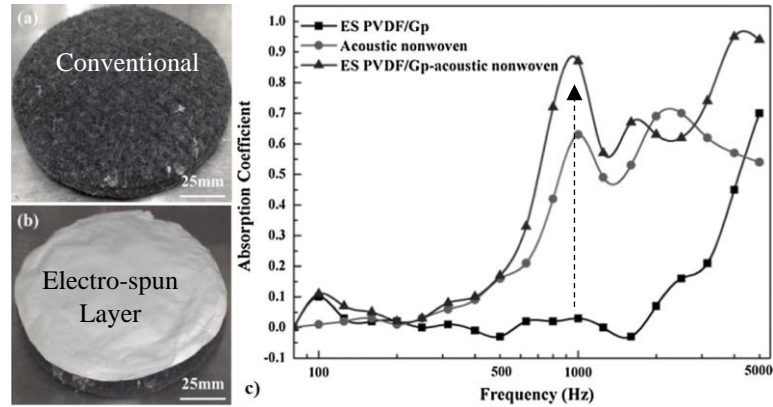


Figure 2.23: Acoustic ready specimens composed of; (a) PP and PET-based non-woven traditional material, (b) Layered composite of PVDF-Graphene electro-spun membrane and nonwoven material, and (c) Acoustic performance of respective PVDF composite specimens. Rep. with permission [121].

Khan et al. [122] studied the acoustic behavior of nanofiber membranes produced from different polymer materials like Polyvinylchloride (PVC) and Polyvinylpyrrolidone (PVP) at different electrospinning parameters. The average fiber diameter for the PVC nanofibers lay in the range of 200nm to 500nm, whereas the fiber diameter values for PVP lay between 04μm to 05μm [Figure 2.25 (a-d)]. The acoustic behavior of these membranes (fabricated

at different weight and thickness) were investigated in comparison with the melamine and polyimide foams (1in and 2in thick). It was observed that the light-weight PVC nanofiber samples had higher absorption than melamine specimens. The absorption coefficient peaks of PVC nanofibers moved towards a lower frequency range with an increase in the weight of the specimens [Figure 2.24 (a)]. The PVC-based nanofibers' acoustic performance improved with higher absorption with an increase in nanofiber weight [Figure 2.24 (b)]. The PVP microfibers also showed better acoustic performance with higher weight, and the absorption coefficient was observed to be higher than melamine foam specimens [Figure 2.24 (c)]. Morphological characterization of fibers, structure and various layering combinations of membranes was not focused in the experimental work carried out in this study.

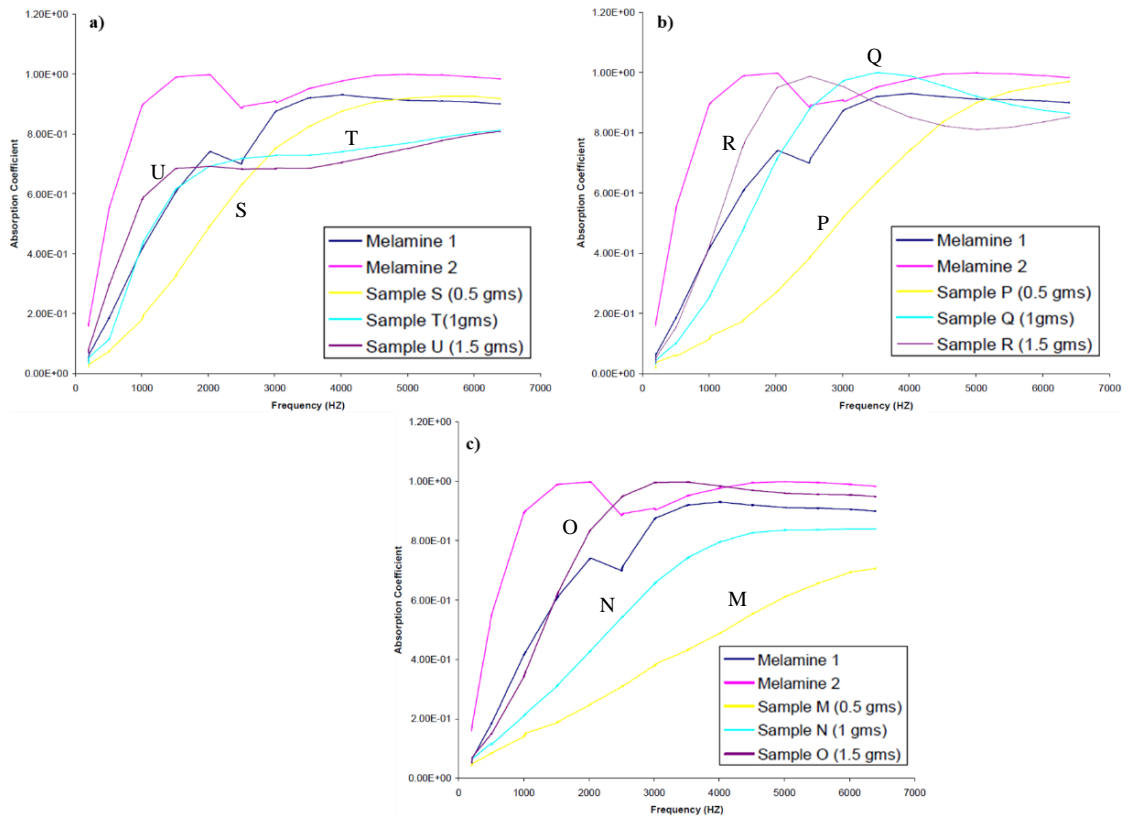


Figure 2.24: Acoustic performance of; (a) PVC nanofiber specimens (Thickness: S-0.183in, T-0.288in, and U-0.710in) compared with Melamine foam specimens (1in and 2in thick), (b) PVC nanofiber specimens compared (Thickness: P-0.325in, Q-0.512in, and R-0.719in) with Melamine foam specimens (1in and 2in thick), and (c) PVP nanofiber specimens compared (Thickness: M-0.441in, N-0.737in, and O-0.807in) with Polyimide foam specimens (1in and 2in thick) [122].

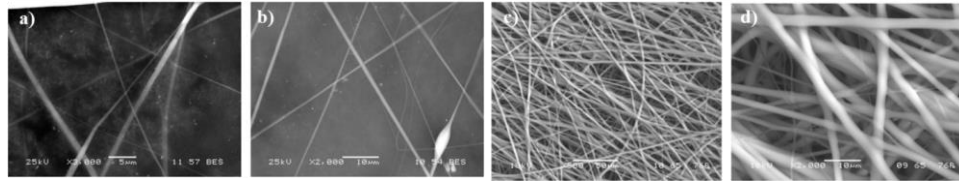


Figure 2.25: SEM micro-graphs of; PVC nanofibers (fabricated at – 20KV, 25cm distance, and 3.5ml/hr. feed rate) taken at – (a) 3000X and (b) 2000X; PVP based nanofibers (fabricated at – 20KV, 25cm distance, and 3.5ml/hr. feed rate) taken at – (c) 500X and (d) 2000X [122].

## 2.5 Filtration

The dissociation of particles from the fluid media with the porous medium is referred to as filtration. The process of sieving is among the various filtration mechanisms that separate particles from fluid media using filters. These filter sieves in the process of filtration encounter extreme clogging and offer higher resistance to fluid flow through the filtration channel [Figure. 2.26 (a)] [123]. The development of several industrial-grade gas filtration apparatuses has taken place in the past to separate particulate matter from gaseous medium. These filters were loaded with a pore of size greater than the particulate matter captured. Various engineers have successfully developed several theories to examine particle entrapment (other than the sieving mechanism) by different mechanisms. These theories helped in the estimation of filter effectiveness in particle extraction. The advancements in the development of filtration theories might help in the manufacturing of biological filters [123].

### 2.5.1 Filtration Mechanisms

The development of filtration technique involves three significant factors: a) fluid media, b) scattered particles, and c) filtration device (filter). The characterization of the factors helps in the estimation of the capture mechanism of particles. The analysis of the mechanism study depends on the assumption that particles are spherical and will stick to the filter on surface contact [123].

#### 2.5.1.1 Particle Capture Mechanism by Single Fiber

The capture mechanism of particles by a unique single fiber can be explained graphically by velocity field lines illustrations (in the direction of flow) around the fiber

surface [Figure. 2.26 (b)]. The unique single fiber is assumed to be cylindrical with its longitudinal axis aligned in the direction normal to the flow. The sequence of the streamlines parallel to each other helps in the characterization of the upstream velocity. The fiber diameter ( $D_f$ ), particle diameter ( $D_{\text{Particle}}$ ), fluid viscosity, fluid velocity, and density determine the point of diversion near the fiber surface. The downstream velocity field streamlines further converge beyond this point in the parallel direction [125].

The elimination of scattered particles by fiber from the velocity field can take place by five various mechanisms: a) Interception, b) Inertial impaction, c) Diffusion, d) Deposition (Gravitational), and e) Electrostatic attraction. The characterization of the filtration system concerning fluid media factors (temperature, viscosity, velocity, density), fiber characteristics (Alignment, thickness, electrostatic charge), and particle characteristics (charge, size, shape) helps in the relative analysis of magnitudes involved with particle entrapment mechanism [124,125].

**Interception:** The sub-micrometer particles flying in the direction of air streamlines are captured after coming in a particle radius of fiber by the process of interception [Figure. 2.26 (c)]. The capture intensity in the interception process is given by the dimensionless quantity ( $N_{\text{Rf}} = D_{\text{particle}}/D_{\text{fiber}}$ ) [125]. The particle size is an important factor that regulates the capture intensity in the interception process at a specific fiber diameter value.

**Inertial impaction:** The micrometer-sized particles with flight track in the direction of flow streamlines to the point of fluid media diversion or acceleration past the fiber surroundings leads to the particle drifting from the stream because of its inertial force. These particles are captured after coming in contact with a particle radius distance of fiber surface [Figure. 2.26 (d)]. The intensity of capture in this process is given by;  $N_{\text{If}} = [(\rho_p - \rho_m) D_{\text{particle}}^2 V_o] / 18\mu D_{\text{fiber}}$  [126]. The intensity is the direct relationship between the diameter of fiber and distance traveled by particle before impaction. Therefore, the increase in the two quantities, the diameter of particle and fluid velocity, will increase the intensity of capture by inertial impaction [126].

**Diffusion:** The nanometer range particles that exhibit Brownian motion after coming in contact with fluid media molecules drift from streamline flow. The particles deviating in such a random fashion are captured when escorted close to a particle radius around fiber

[Figure. 2.26 (e)]. The capture intensity of randomly moving particles is given by;  $N_{Mf} = D / (V_o D_f)$  [Diffusion coefficient ( $D$ ) =  $KT / 3\pi\mu D_{particle}$ ] [125]. The surface contact and particle entrapment increase with the decrease in two factors; fluid velocity (provides more time for particles to travel around the fiber surface) and fluid viscosity (the random movement of particles increases relatively with the fluid) [125].

Deposition (Gravitational): The scattered particles in this mechanism gravitate to the particle radius distance of fiber because of density difference with fluid [Figure. 2.26 (f)]. The capture intensity in gravitational deposition mechanism is given by;  $N_{Gf} = v_g / V_o$  [Particle settling velocity ( $v_g$ ) =  $\{D_{particle}^2 g (\rho_p - \rho_m)\} / 18\mu$ ] [123]. The capture intensity is the direct relationship between the fluid velocity (upstream) and particle settling velocity.

Electrostatic attraction: The capture mechanism of electrostatic attraction depends on the charge present on fiber and particle [Figure. 2.26 (g)]. The particles are captured due to the opposite charges carried by them, and the intensity is given by;  $N_{Ef} = 4Qq / (3\pi\mu D_{particle} D_{fiber} V_o)$ . The intensity of capture in the electrostatic mechanism increases with the increase in the number of electrical charges on fiber/particle [125].

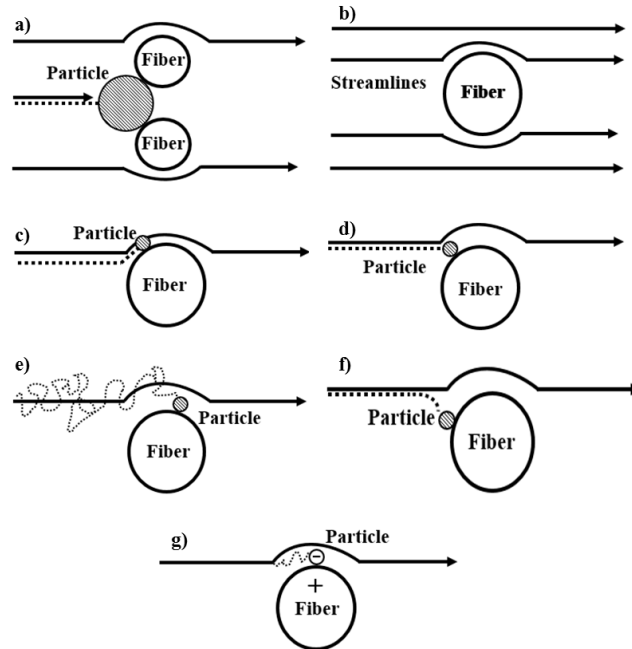


Figure 2.26: Schematic illustration of various filtration mechanisms through a single unique fiber; (a) Sieving, (b) Fluid flow description near fiber surface, (c) Interception, (d) Inertial impaction, (e) Diffusion, (f) Deposition (Gravitational), and (g) Electrostatic attraction.

### 2.5.1.2 Particle Capture Mechanism by Single Pore

The capture mechanism of particles by a unique single pore has also been studied graphically by field lines illustration in the flow direction around pore with circular cross-section area, aligned in the direction normal to fluid flow [Figure. 2.27 (a)]. The capture mechanism of particles through the pore surface by sieving is shown in Figure. 2.27 (b). The capture mechanism of particles in the interception mechanism is  $N_{Rp} = D_p / D_c$  [Figure. 2.27 (c)]. It means that the intensity of interception capture will increase with particle size and decrease in pore size. The inertial impaction of the particle around the pore surface is shown in Figure. 2.27 (d) and its capture intensity is given by;  $N_{Ip} = [(\rho_p - \rho_m) D_p^2 V_o] / 18\mu D_c$ . The intensity of capture by inertial impaction increases with particle size, the density of particle, velocity, and lower pore diameter values. When drifted away from the flow stream, the particles in the diffusion mechanism are captured inside the pore by hitting the pore walls/boundaries [Figure. 2.27 (e)]. The capture intensity of the pore in this mechanism is given by;  $N_{Mp} = (2DL) / D_c^2 V_c$ , which means the capture intensity can be improved significantly by the reduction in the pore diameter size. The higher pore length in the membrane can significantly reduce the particle velocity, which yields a higher value of diffusion coefficient. The capture intensity of particles in a gravity-assisted deposition is given by;  $N_{Gp} = 3v_g L / 4D_c V_c$ . The capture intensity in this deposition mechanism can be improved by smaller pore size and reduced fluid velocity [Figure. 2.27 (f)] [125].

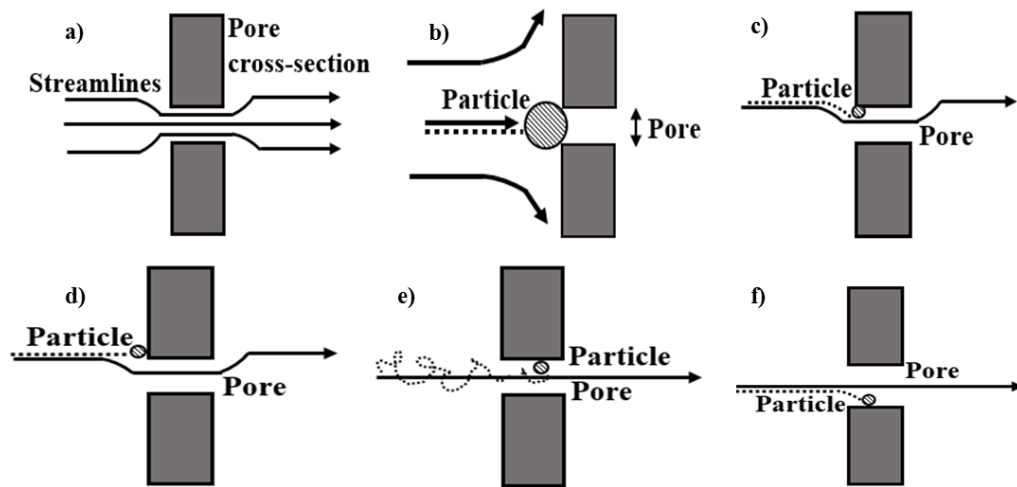


Figure 2.27: Schematic illustration of various filtration mechanisms through a single unique pore; (a) Description of fluid flow lines through pores, (b) Sieving, (c) Interception, (d) Inertial Impaction, (e) Diffusion, and (f) Deposition (Gravitational).



## 2.5.2 Filtration Performance Tests

The filtration performance of the filter medium manufactured from a wide variety of materials can be determined by performing two of the significant characterization tests, i.e., filtration efficiency test ( $\eta$ ) and the pressure drop (breathability) test over the medium surfaces. The evaluation of these performance standards can be carried out with different experimental set-up designed and operated in reference to international standards. This study mainly focuses on the pressure drop and particle filtration efficiency measurements of the nanofiber-based filter medium produced from electrospinning. In this section, the fundamentals of the filtration performance test with a specific experimental setup have been discussed.

### 2.5.2.1 Filtration Efficiency

The filtration efficiency or fractional efficiency of the filter medium fabricated from different materials or layers can be determined by Equation 2.32 [127];

$$\eta = \left[ 1 - \frac{C_{Downstream}}{C_{Upstream}} \right] \times 100\% \quad (2.32)$$

Wherein,

$\eta$  = Capture efficiency or collection efficiency of the filter medium.

$C_{Downstream}$  = Concentration of aerosol after passing through the filter medium.

$C_{Upstream}$  = Concentration of aerosol before passing through the filter medium.

The computation of filtration efficiency of an entire filter medium is a complicated method but the filtration analysis utilizing this approach is a better way to address the problem. The calculation of efficiency for a single fiber for an individual particle is the precise methodology to characterize the filter material. As discussed earlier, the capture mechanism for a single fiber is affected by several parameters; a) the diameter of particle ( $d_p$ ), b) fiber length, c) the diameter of fibers ( $D_f$ ), d) the thickness of fiber media ( $t$ ), e) face velocity ( $U$ ), f) volume fraction of solid medium ( $\alpha$ ), and g) orientation of fibers. The variation in the measurement of fiber diameter ( $d_F$ ) significantly affects the filtration efficiency of the medium [128]. It was observed in the case of a filter medium with constant

material thickness and volume fraction of solid; when the size of the fiber is reduced, the minimum efficiency increases [129].

The total filtration efficiency of the medium can be calculated by considering the effects of several parameters through Equation 2.33 [128,130–133];

$$\eta_t = 1 - (1 - N_{Mf})(1 - N_{If})(1 - N_{Rf})(1 - N_{Gf}) \quad (2.33)$$

$$\eta = 1 - \exp \left[ -\frac{4\alpha N_{If}t}{\pi(1-\alpha)D_f} \right] \quad (2.34)$$

Wherein,  $\eta_t$  is defined as the total efficiency of the single fiber,  $N_{Mf}$  is the capture intensity in the diffusion process,  $N_{If}$  is the capture intensity in the inertial impaction process,  $N_{Rf}$  is the capture intensity in the interception process, and  $N_{Gf}$  is the capture intensity in the deposition process.

The calculation of overall filtration efficiency includes the effect of fibers surrounding the single fiber in the modern theory of efficiency computation. The overall efficiency ( $\eta$ ) can be obtained with the integration of these capture mechanisms. Conclusively, the filtration efficiency, in consideration of all the capture mechanisms, significantly depends on the fiber diameter measurements, particle size, and velocity of gas or air, which can be modified or tuned by applying the electrospinning technique [134,135].

### 2.5.2.2 Pressure Drop Measurement

The resistance offered by filter material or medium (in air filtration) plays a significant role in filter performance mapping as it characterizes the breathability of the filters. The air resistance value ( $R_f$ ) of these filters can be measured by Equation 2.35 (utilizing filtration theory) [136];

$$R_f = \frac{\Delta P}{v} \quad (2.35)$$

The filter medium pressure drop is given by  $\Delta P$ , and the velocity of air traveling through the filter medium is given by  $v$ .

When the air travels through a fibrous material filter medium, every fiber resists the air passing through it; this air resistance possessed by fibers causes a pressure drop across

the filter medium or membrane. The quantity of pressure drop generated by the airflow through the membranes is defined as material pressure drop ( $\Delta P$ ) [128]. The air filtration materials can be fabricated from various porous material types: fibrous or granular. The membranes made from these materials follows Darcy's law of laminar flow and is constituted by Equation 2.36 [137];

$$\frac{\Delta P}{U} = \frac{\mu \alpha t}{k} \quad (2.36)$$

Where, the face velocity is given by the airflow rate over the front area, i.e.,  $Q/A$  is given by  $U$ , the volume fraction of solid fiber medium or membrane is denoted as  $\alpha$ ,  $(1 - \alpha)$  is the porosity of the medium, the thickness of the filter media is denoted as  $t$ , the dynamic viscosity of air is represented as  $\mu$ , and the permeability of the surrounding air is  $k$ . According to Darcy's law, with the reduction in air permeability ( $k$ ), the pressure drops across the medium increase (keeping face velocity constant). Pressure drop is the most repeated parameter that is generally calculated or determined to demonstrate the filtration performance of the filter material or membrane [137].

The combination of two significant factors; pressure drop and filtration efficiency, gives a single factor, defined as Quality Factor (QF) and is given by Equation 2.37 [137];

$$QF = -\frac{\ln(1-\eta)}{\Delta P} \quad (2.37)$$

The filtration efficiency is denoted by  $\eta$  with the pressure drop of  $\Delta P$  across the filter medium. The quality factor is a type of profit-to-cost ratio wherein the filtration efficiency (normalized) acts profit and the pressure drop acts as cost. The manufacturing of filters with higher filter efficiency and lower pressure drop demonstrates a very high-quality factor that possesses an excellent quality, but filtration efficiency improvement keeps pressure drops to lower values is a challenge in the air filtration industry [135,137]. The filtration performance characterization of fiber membranes carried out in this study mainly focuses on the pressure drop and particle filtration efficiency measurements and analysis of fiber properties like fiber diameter, air gaps, and structure.

### **2.5.3 Effect of Nanofiber Properties on Filtration Performance**

The fiber morphology and structure play a significant role in the air filtration medium design. These fundamental fiber attributes or associated physical characteristics have a significant effect on the membrane's filtration performance. These morphological or structural parameters include the following; a) Fiber diameter, b) Fiber diameter distribution, c) Surface area of fibers, d) Air gaps or pore distribution, e) Weight of the fiber membrane or thickness, and f) Packing density of fibers in a membrane [135,138–141]. The average diameter has a significant effect on the membrane's filtration performance. The correlation between the diametric value and quality factor has been made in several studies through the morphological characterization of fibers. The nanofibers manufactured from the process of electrospinning result in smooth and uniform fibers of a specific diameter. The filtration efficiency of the PAN nanofiber-based filter was observed to decrease with higher fiber diameters, whereas it significantly improved with a decrease in diameter [138,139]. Other studies observed that with smaller diameter values, the surface cover of fiber increased, resulting in lower pressure drop [131]. In order to improve the filtration performance of the nanofiber-based media, an optimum fiber diameter value has to be achieved to maintain a balance between efficiency and pressure drop. The nanofiber membranes of Poly (lactic acid) have been manufactured in the past with the bead on fiber structure pattern for air filtration applications. The study observed that with higher fiber surface areas of nanofibers and a large surface cover of beads, excellent filtration performance could be achieved [141].

Mathematical modeling between pore size of PVA nanofibers loaded with surface micro-pores and the associated filtration efficiency has been performed. The study observed that the fabricated PVA membrane with micro-sized pores offers better filtration efficiency [142]. It was generally observed that filter medium composed of thinner fibers or pores clogs up more frequently due to the tiny size and higher particle accumulation [143]. Higher fiber membrane weights favor higher filtration efficiencies but limit themselves, resulting in lower QF's due to associated higher pressure drops. The multi-layering concept of stacking single electro-spun nanofiber membranes is another productive approach to improving the QF [144]. Similarly, the thickness analysis of the

filter membrane of PAN nanofibers demonstrates the requirement of optimum thickness to enhance filtration performance because, with higher thickness, pressure drop increases significantly [145]. The dependence of filtration efficiency and fiber packing density of PEO fiber-based membranes shows that higher fiber density will lead to the higher weight, which further shows the reduction in QF of the associated nanofiber membranes [140].

#### **2.5.4 Viruses and Pollutants**

Severe Acute Respiratory Syndrome Coronavirus-2 (SARS-CoV-2/COVID-19), which emerged in Wuhan – Hubei, China, has been recently articulated as a global pandemic in March-2020 by World Health Organization (WHO). This airborne career virus is a threat to humanity, especially frontline workers, as it is a matter of concern regarding protection gadgets (medical grade facemasks, face sheets, oxygen respirators, and ventilators) required against it. The novel SARS-CoV-2/COVID-19 virus has reported average size of 100nm with a mean aerosol size  $\leq$  of 100nm. When fused with a virus, particulates from contaminated human body discharge (nasal droplets/saliva) make it airborne. The crown-shaped nano-sized spikes on the exterior virus surface have an estimated height  $< 12\text{nm}$  (approximate) [146]. The SARS-CoV-2/COVID-19 virus affiliates itself from the coronavirus family background, of which other viruses like MERS (Middle East Respiratory Syndrome) and SARS (Severe acute respiratory syndrome) originated. The size of the SARS and MERS virus was approximately about the size of 81nm (SARS-Capsid wrapped virus-15spikes) and 118-136nm (MERS-16-21nm spike size structures) [17,147,148]. The spikes present on the exterior surface of the virus are predominantly proteins that attach themselves to the carrier cells in the human body and multiply inside to host them [146]. These viruses can amalgamate with the surrounding aerosols that can be anchored on fluid particles leaving the infected person's body. When the virus reaches the airborne stage, it transfers easily from the surrounding aerosol carriers. With the smaller aerosol size, the virus stays longer in the air environment with a higher possibility of higher distance transmission. The transmission concept in terms of particulate size and surrounding aerosol applies to air pollution. The particulates can stay floating in the air for a longer time and are seriously dangerous for human health [17].

The minimum reported size of SARS-CoV-2/COVID-19 is approximately 60nm. When the virus is anchored with smaller size aerosol, the resultant size is 60nm. In contrast, if the virus is attached to a bigger size aerosol, the size becomes approximately 100-300nm [Figure 2.28 (a-b)] [146]. The test standards for size less than 300nm have not been developed at present, and the traditional microfiber loaded filter materials offer very low filtration performance [146].

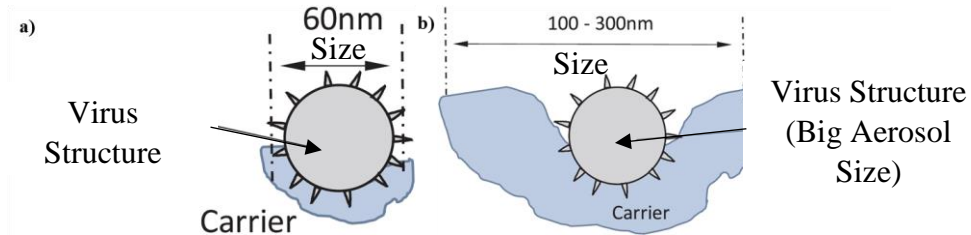


Figure 2.28: Schematic description of; a) Coronavirus attachment with aerosol size structure of 60nm, and b) Coronavirus attachment with higher size aerosol of 100-300nm. Rep. with permission [17].

Air filtration is also predominantly required for pollutants present in the air with harmful or hazardous aerosols. The surrounding aerosols generated from the engine exhaust of the gasoline or diesel-powered engines have a typical size of 100nm to some micrometers. The particulates of these pollutants mix well with ambient air to form bigger aerosols [149]. Finely sized particles suspended in the air include a wide variety of matter, including; carbon particulates (from industries), mineral fine powders, coal particulates, vehicle exhaust emissions, pollen, bacteria, and other micro-organisms. These harmful particulate matters in the ambient air can have detrimental effects on human respiratory organs. They could lead to various health issues like asthma, lung disorders, cardiovascular problems, and heart failure. The impact of particulate matter sized less than  $2.5\mu\text{m}$  (PM<sub>2.5</sub>) on the cardiovascular system has been studied and observed significantly in the past. The nano-size particles present in the air possess an immediate and prolonged effect on human health [135,150,151]. The respiratory nasal canal can prevent the entry of some microscale particles or thoracic particulates, but the hazard of these matters depends on the size of suspended aerosols. The size of various particulates is defined as following; thoracic particles were reported to be less than  $10\mu\text{m}$  (PM<sub>10</sub>), fine particulate matter was reported to be less than  $2.5\mu\text{m}$ , and nanoparticles suspended possess a reported size of  $0.1\mu\text{m}$ . These micro-scale-sized particles can probe through the circulatory system and can cause severe

respiratory or cardiovascular health problems [150,152,153]. Therefore, the development of nanofibers that can filter these small particulates has become a requisite as the ultrafine particles provide challenges in air filtration with traditional micro-fibers.

### 2.5.5 Electro-spun Nanofibers as Filter Media

The nanofibers manufactured from the multifaceted electrospinning technique have been used as the filter mediums for air filtration application since 1980. The nanofiber loaded filter medium possesses better surface characteristics such as; better porosity, extremely high surface area, lightweight and thin, nano-scale smooth and uniform fibers, and better surface to surface adhesion. The electro-spun nanofiber membranes are currently used in the air filtration media frequently. These electro-spun membranes made from different polymeric materials have been used in the air filtration field for over 35 years. These electro-spun nanofiber membranes are used in various filtration industrial areas like respirators, face masks, room air filtration, car air filters, gas cleaning filters in multiple industries, air purification units in community areas, etc. [135].

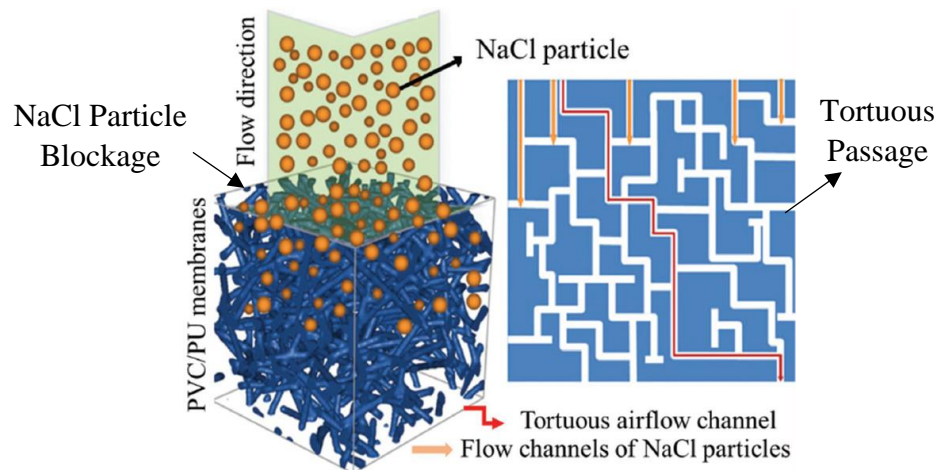


Figure 2.29: PVC-PU nanofiber membrane structure with many flow channels loaded in the network. Rep. with permission [135,154].

Wang et al. [154] successfully fabricated the nanofiber membrane-based composite of two polymer blends such as PVC and PU with different weight ratios. Electro-spun membranes made from an optimal blend of these two polymers offered better filtration performance and high tensile strength of 9.9MPa. The fiber structure fabricated from the combination of PVC-PU blend possesses higher air permeability (154.1mm/s) with the

high amount of flow channels present on the surface of produced filter media [Figure 2.29]. The filter medium structure was observed with a higher filtration efficiency of 99.5% and with a lower pressure drop of 144Pa. The schematic description of the fibrous membrane structure shows the tortuous path provided by the PVC-PU membrane, which prevented or blocked the NaCl particles efficiently with higher breathability comfort.

Wan et al. [155] investigated the effect of TiO<sub>2</sub> nanoparticle inclusion on the filtration performance of Polysulfone (PSF) fiber structures [Figure 2.30 (a-d)]. The study reported the fabrication of a superhydrophobic filter membrane with a WAC of 152°. The electro-spun membranes of PSF-based polymers were loaded with TiO<sub>2</sub> nanoparticles in varying concentrations. These composite fibers were further layered with the traditional non-woven structure for better air filtration. Higher filtration efficiency of 99.9997% was achieved with these structures with a pressure drop of 45.3Pa.

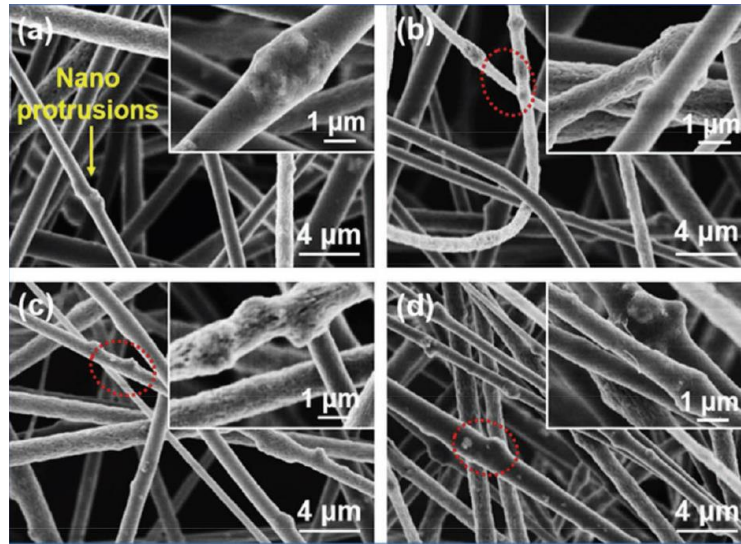


Figure 2.30: SEM micro-graphs of Polysulfone (PSF) based membrane structure modified with TiO<sub>2</sub> nanoparticles in varying concentrations of: (a) 2.5wt.%, (b) 5wt.%, (c) 7.5 wt.%, and (d) 10wt.% . Rep. with permission [135,155].

Yang et al. [156] investigated the effect of multi-layering of nanofiber membranes manufactured from different polymer base materials on the air filtration performance of these structures. In his studies, he designed a multi-layered structure of sandwiched electro-spun fibers in the following order: Polyamide-6 (PA-6), PAN, and PA-6 for improving the filtration performance. The structure was comprised of larger air cavities made by stacking of 20nm (approx.) thick nanofibers with more fiber webs of bead on fiber structure



membranes [Figure 2.31]. Two-dimensional nano-scale fiber nets made from PA-6 and bead-loaded PAN membranes possessed very high porosity and packing, which further improved the filtration efficiency to 99.9998% with a very low-pressure drop of 117.5Pa. Zhang et al. [157] also investigated the effect of the multilayered structure of PAN-based nanofiber membrane on the filtration efficiency and pressure drop measurements. The study analyzed the effect of several thicknesses on the efficiency and QF of the prepared structure. It was generally observed that the membranes with lower thickness offered better QF than the thicker filter membranes. It was attributed in the study that layering of thin nanofiber membranes provides more QF with lower pressure drop and good efficiency than thicker layer of single nanofiber membrane.

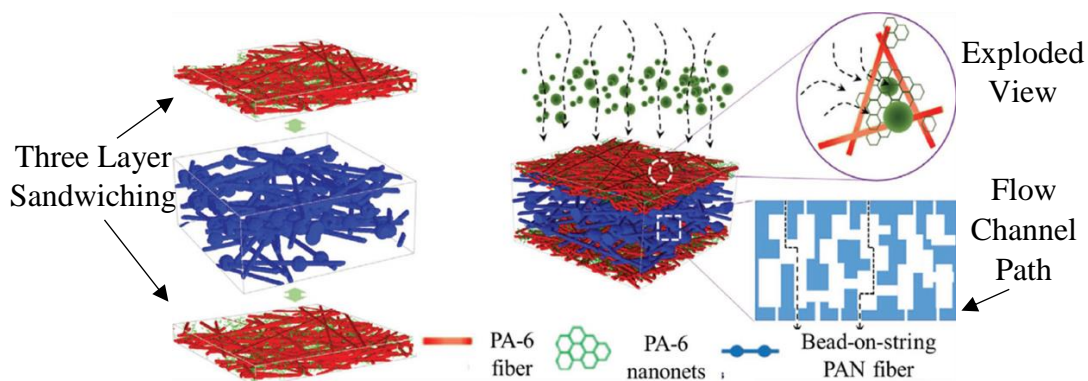


Figure 2.31: Sand witching of PA-6 and PAN nanofiber membrane explaining the filtration technique through the structures. Rep. with permission [135,156].

Particles suspended in the air carry viruses, bacteria, pollens, and various allergens, and these suspended particulates can transmit different diseases and could even lead to a virus outbreak. Several additives have been used in the past to fabricate anti-bacterial filter materials made from fillers like silver nanoparticles, copper nanoparticles, carbon nanotubes, titanium dioxide, etc. [135]. Selvam et al. [158] demonstrated an investigative study of silver nanoparticle inclusion (with varying concentration) on nanofiber structures of the PAN polymer base. These silver nanoparticles loaded anti-bacterial membranes were successfully tested against *S. Aureus* and *E. Coli* for 6 hours. The Ag Np concentration of 10-12.5 wt.% resulted in higher bacterial efficiency of 99%, and the action of the Np's against the bacteria is demonstrated in Figure 2.32 (a). When interacting with positively charged nanoparticles loaded fiber membranes, negligent charged cell walls of bacteria or viruses resulted in the breaking up of bacterial cell walls, which further ended in the

microorganism death or expiration [159]. Zhang et al. [160] demonstrated the interaction of Ag Np's on the structure of PAN fiber membranes towards the bacteria. The anti-microbial properties of the membrane improved significantly with the action of  $\text{NH}_2\text{OH}$  solution and  $\text{Ag}^+$  ions. The fiber membrane's filtration efficiency and morphological attributes remain unaltered, with this action improving anti-microbial properties. Zhang et al.[161] in his further studies with Wang C., investigated the silk fiber-based lightweight filter media possessing anti-bacterial properties [Figure 2.32 (b)]. The silk-based fibers were added with nano-scale Ag clusters by the action of  $\text{AgNO}_3$  with the formic acid. The attachment of Ag clusters on the fiber structure of silk membranes is demonstrated in Figure 2.32 (c). The silk-based filter membranes were bio-compatible and eco-friendly, offering higher filtration efficiencies, higher breathability, lower weight, and anti-bacterial properties. The manufacturing of nanofiber membranes with the inclusion of anti-bacterial nanoparticles improves the filter performance without compromising with the breathability of the user. The electro-spun membranes with these exceptional properties offer a better solution in the filtration industry towards any type of virus, bacteria, or pollutants.

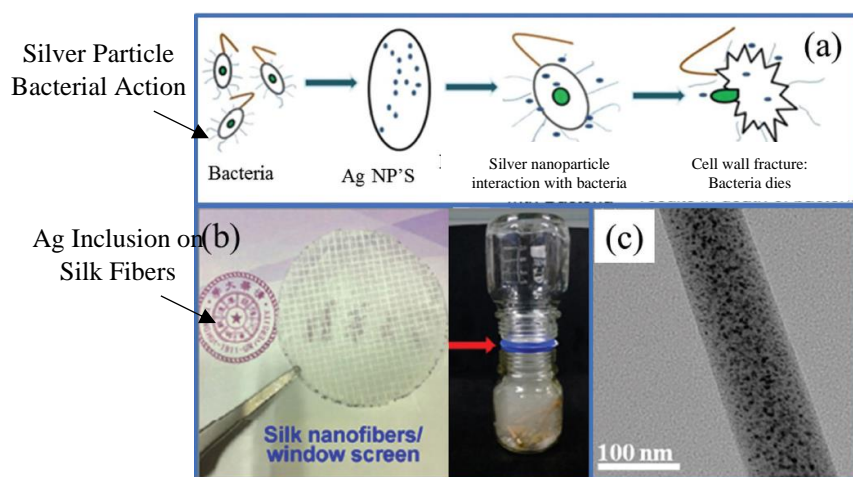


Figure 2.32: (a) Silver nanoparticles (Ag Nps) action on the bacteria [135,158], (b) Silk fibers loaded with Ag to prevent the diffusion of smoke, and c) TEM image of silver nanoparticles doped on the silk nanofiber structure. Rep. with permission [135,161].

## 2.6 Literature Review Summary and Knowledge Gap

The comprehensive study of extensive literature and theoretical background shows that the polymeric nanofibers manufactured by electrospinning offer several exceptional properties, making them a suitable contestant for various industrial applications.

There are different techniques of noise mitigation that involves noise control at the source, in the transmission path, and at receiver's end. Active and passive noise control are the two techniques found in the literature wherein the application of sensitive external energy components like electronic sensors, actuators, vibro-meters, etc. limits the user due to calibration imbalance sensitivity leading to system failure. Passive noise control techniques are comparatively more reliable and feasible alternate solution that involves application of absorptive medium which can easily be tuned specific to frequency dependant geometric dimensions. Conventional sound-absorbing material offers better acoustic performance in the higher frequency range but limits the higher absorption of low-frequency noise. Traditional microfibers possess higher thickness and higher weight which provides a constraint for various industrial applications where space and weight are of prime concern, such as transportation, aerospace, airplanes, and buildings. Electro-spun nanofiber membranes provide a better solution to low-frequency sound absorption with the associated extreme low weight and thickness. Higher sound energy interaction and conversion to heat as losses of the electro-spun fibers depend on the morphology and structure of the fiber membranes produced. Multi-layering or stacking of polymeric nanofiber layers improves the acoustic performance of the material in the low and medium frequency range. This experimental study includes manufacturing thin and light nanofiber membranes that possess higher sound absorption in low or medium frequency zones. The acoustic nanofibers used in the study were first designed, optimized, and modeled based on fiber diameter, thickness, and weight concerning the five electrospinning parameters. The study is complemented with the addition of filler to the fiber structure to analyze the electro-spun membrane's respective thermal, mechanical, morphological, and acoustic properties. Very few studies have focused on applying nanofibers for noise attenuation. The concept of fiber modeling concerning electrospinning parameters for acoustic applications has not been concentrated in the previous studies in the open literature. The concept of multi-layering with composites of pristine polymer fiber layers and with filler-loaded membrane layers to provide a more tortuous path for sound wave energy dissipation has been investigated in the study at different back cavities.

The electro-spun fiber membranes are often categorized as smart fiber-based materials with the responsive ability towards different external stimuli with associated micro/nano

level variation in structural arrangement or properties. The exposure of these membranes towards plane acoustic sound waves and polluted air stimulus triggers its response ability to absorb sound and to filter out micro/nano particles in the medium. Electro-spun nanofiber membranes offer better filtration performance than the traditional microfiber-loaded filter mediums. Several studies performed on nanofiber membranes for air filtration show that traditional micro-scale fiber-based filters are not effective for preventing humans from nano-sized particulates like pollutants, viruses or bacteria, and others micro-organisms. In this study, polymeric electro-spun nanofiber membranes were manufactured with optimized fiber diameter, weight and thickness where the nano-scale fiber structure possessed better filtration performance against these particles. These thin and lightweight membranes have fibers in nano-scale with very tiny air gaps in between the fiber webs. The study involves the fabrication of nanofiber loaded filter media at varying concentrations of pure polymer, electrospinning time, and complemented with filler inclusion. Anti-bacterial/anti-viral fillers like MWCNT's, GN,  $\text{TiO}_2$ , and Copper nanoparticles with high electrostatic attraction were studied in this work. The layering of extremely thin nanofiber membranes to the conventional surgical mask for improving the filtration performance to the level of N-95 masks was performed in the study.

## Chapter 3. Experimental Methodology

### 3.1 Experimental Materials

The manufacturing of nanofibers for various industrial applications was carried out utilizing two different polymeric materials; Polyvinylpyrrolidone (PVP) and Polyvinylidene Fluoride (PVDF). The fine powder of PVP with an average molecular weight of 1300000g/mol (100% purity) was obtained from Sigma Aldrich – USA. Solid pellets of PVDF with an average molecular of 280000g/mol were obtained Kynar-740 from Arkema Group-Canada. Polymeric nanofibers fabricated from PVP and PVDF material were used for sound absorption application, whereas PVDF was used for filtration application.

In the experimental study, two different types of solvents were used to make polymeric solutions of different concentrations. PVP powders were dissolved in the solvent base of ethanol with a molecular weight of 46.07g/mol obtained from ACP Chemicals – Canada with 95% purity. On the other hand, PVDF pellets were dissolved in N, N-Dimethylformamide (DMF) with a molecular weight of 73.09g/mol was obtained from ACP Chemicals – Canada with 99.8% purity. Polymeric solutions with varying concentrations were prepared by mixing polymeric material in a liquid solvent. The mixing of the polymer in the solvent was carried out by magnetic stirring, and the filler added solution requires a step of mixing with an ultrasonic mixer.

Several types of filler materials (micro/nano-sized) were used in the study for different applications. For sound absorption application, the nanofiber membranes were produced from PVP and PVDF material wherein the filler based nano-composites were fabricated from the following materials, namely; Multi-Walled Carbon Nano-Tubes (MWCNTs) with length 10-20 $\mu$ m and outer diameter 30-50nm, Graphene particles (GN) with size 5 $\mu$ m and surface area 120-150m<sup>2</sup>/g (both MWCNT's and GN) was provided by Dr. Simon Park – the University of Calgary, Fumed Silica (FS) with a molecular weight of 60.08g/mol was obtained from Sigma Aldrich – USA, Micro-Fiber Glass (FG) with fiber diameter 16microns, and Mica powder (MC) - 21microns was obtained from Fibertec – USA. For filtration applications, the nanofibers were produced from PVDF material wherein the following filler materials were added; MWCNT's, GN, Titanium (IV) Oxide (TiO<sub>2</sub>) nano-

powders with 21nm particle size and average molecular weight 79.87g/mol was obtained from Sigma Aldrich – USA, and Copper nano-powder with 25nm particle size and average molecular weight 63.55g/mol was also obtained from Sigma Aldrich – USA.

In this experimental study, the selection of polymeric or filler material was made based on each material's inherent properties. PVP is a synthetic polymer that is water-soluble, biocompatible, high electro-spin ability, non-toxic, and offers better solubility with a wide variety of nano/microparticles [162]. It is a polymer lactam with high polarity due to the amide group attachment to the side rings which gives it better solubility in various polar solvents. It provides the ease in producing thin membranes by electrospinning the ethanol based polymeric solutions with inherent advantage of environmental friendliness when compared with other non-soluble polymers. PVDF is a semi-crystalline polymer with different crystalline phase's:  $\alpha$ ,  $\beta$ ,  $\gamma$ , and  $\delta$ . Among these phases,  $\beta$  phase PVDF offers the higher piezoelectric effect because of its non-centrosymmetric conformation of molecular orientation & distribution [163]. It has a higher number of strong dipoles orientated in a polymer chain, making it a better piezoelectric polymeric material that can generate electric energy when the material is applied with any mechanical force or stress. Transducers used in an audio system are also piezoelectric that transforms mechanical input into an electric signal. Hence, these materials can also attenuate noise or sound vibrations in the acoustics field. The materials also offer better thermal, mechanical, and electric strength, making them a better candidate for filtration applications [17,164]. The nanofiber mats were modified by adding fillers in a polymer matrix where FS contains microparticles of amorphous silica, which offer a larger surface area (50-400 m<sup>2</sup>/g), higher particle interaction with polymers, and has better reinforcing properties [165]. The micro-glass particles (FG) reinforced plastics are used for various engineering applications, including sound absorption because of their lower weight, high mechanical and thermal properties, cost, and easy availability [166,167]. The MWCNTs and GN are allotropes of carbon arranged in the form of cylindrical nanotubes and hexagonal structures. The MWCNTs and GN nanoparticles have a high aspect ratio and exhibit better thermal, mechanical and electrical properties [121,168]. Reinforcing fillers like MC have been widely used because of their higher physical and mechanical strength when reinforced with polymer materials [169]. Bacteria or viruses have exterior structures consisting of spikes of protein

arrangement. When it interacts with low pH exposure, the external layer breaks apart the protein structure and kills the micro-organisms or bacteria. The positive charge loaded metal ions like copper, silver, or zinc attaches to the negative charge loaded group present on an exterior surface of virus or bacteria to inactivate them. Copper nanoparticles (Cu NP's) and Titanium oxide (TiO<sub>2</sub>) are the types of biocides used in the study which attaches to the fiber structure without effecting the electrostatic charge bearing capacity of fibers or without changing the fiber structure that regulates the filtration performance [135,170]. MWCNT's and GN can also de-activates the bacteria or virus when it comes in direct surface contact with their exterior walls, according to several studies performed in the air filtration field [171]. The tabular representation of different polymeric materials and fillers used for different applications in provided in Table 3.1.

Table 3.1: Description of different polymeric, filler materials, and solvents used for various applications.

Acoustic Nanofibers					Filtration Nanofibers				
Polymer Base									
Polymer 1		Polymer 2			Polymer 1				
PVP (Ethanol)		PVDF (DMF)			PVDF (DMF)				
Fillers used for acoustic nanofibers					Fillers used for filtration nanofibers				
Filler 1	Filler 2	Filler 3	Filler 4	Filler 5	Filler 1	Filler 2	Filler 3	Filler 4	
CNT	GN	FS	FG	MC	CNT	GN	TiO2	Cu NP's	
Conventional Material									
1			2		1	2	3	4	5
Rockwool Comfort Batt			Rockwool SafenSound		Surgical Mask	N-95 (8200)	N-95 (8110S)	N-95 (1860)	N-95 (9500)

### 3.2 Electrospinning Experimental Set-up

Pristine or filler-modified polymeric nanofibers were manufactured using an electrospinning experimental set-up. The laboratory-scale set-up has the following components; a) A high voltage power supply source purchased from Gamma High Voltage Research Inc. (ES50P-5W) – USA with voltage control from 0-50KV, b) Polymer solution flow control syringe pump (NE-1600) purchased from New Era Pump Systems Inc. – USA, c) Stainless steel rotating drum cylinder with RPM control regulator, d) Needle clamping hub fixed on screw connected to Arduino controlled stepper motor for to-and-fro motion control of the needle, and e) Cubical acrylic based high voltage safety casing. Polymer

powder or pellets were dissolved in the solvent, and the prepared solution was loaded in the syringe-needle unit, which was further mounted on the syringe pump. The pump was set to a specific flow rate and powered for the solution to be pushed out from the needle tip. Needle extended from the pipe through a syringe is properly mounted on the hub with the positive end of the high side connected to it through alligator clips. The needle motion was started by powering up the Arduino-controlled stepper motor, and then the grounded collector was powered with set RPM. Finally, the limit switch enabled acrylic safety door was closed for safety, and then the high voltage supply was turned ON with set voltage for the nanofiber fabrication process. The polymer solution was forced to pull out from the needle tip in the form of droplets, and the droplet stretches out in an electric field environment to form a Taylor cone. Polymer jet stream experiences bending instabilities, and the jet further stretches out because of mutual charge repulsion. The forces acting on polymer jet due to electric field environment elongates in form fibers which were further accumulated on the surface of collector screen. Moving needle tip powered from Arduino controls the translational motion for homogenous deposition of fibers on the collector. Accumulated fibers were finally extracted from the collector surface in thin and lightweight nanofiber membranes, which were further dried for 24 hours for end applications. The three-dimensional model of the electrospinning laboratory-scale experimental setup is provided in Figure 3.1(a-b).

### **3.3 Material or Specimen Preparation**

#### **3.3.1 Polymeric Solution Preparation**

Two different types of polymer materials, PVP and PVDF, were used in this study for various applications. The polymeric solution of PVP was prepared by mixing PVP powders in ethanol solution varying from 08wt.% to 12wt.% in concentration. The prepared mixture was continuously stirred at 60°C for 24hours using the magnetic stirrer for homogenous mixing of the solution. PVDF solid pellets were mixed in DMF solution in varying concentrations of 20wt.% to 25wt.% at 75°C for 24 hours. A description of the pristine polymeric solution concentration range used in the study is provided in Table 3.2.



Table 3.2: Tabular description of polymer solution concentration range (wt.%).

Polymeric Material	Solvent	Polymer Solution Concentration (wt.%)
PVP	Ethanol	08 to 12
PVDF	DMF	20 to 25

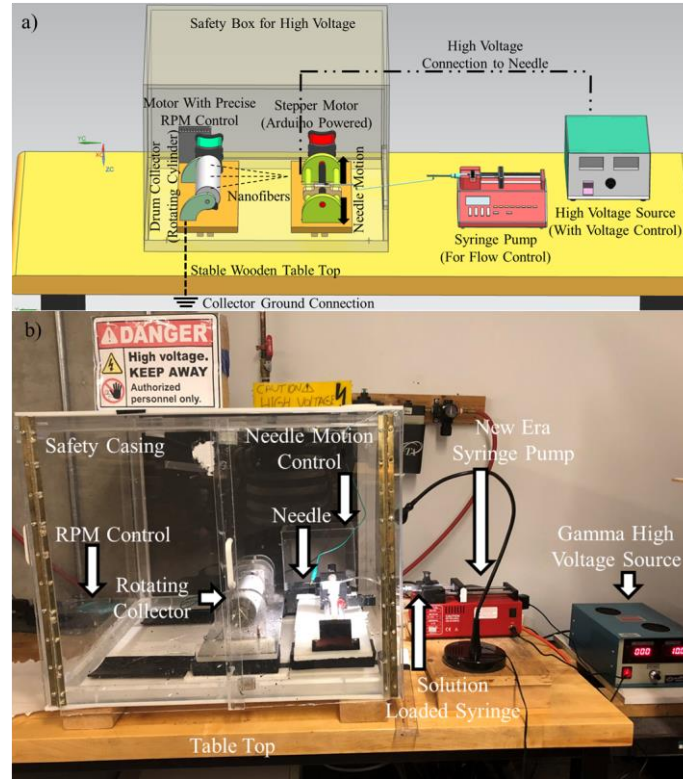


Figure 3.1: (a) Schematic description of the electrospinning set-up and (b) Laboratory-scale unit.

### 3.3.2 Polymeric-Filler Solution Preparation

Different type of application-based fillers was used in the study with different polymeric materials. Nanofiber composites composed of these fillers were manufactured in varying concentrations of 0.25wt.% to 1wt.% for acoustic applications and 0.25wt.% for filtration applications [as described in Table 3.3]. The step-wise description of nanofiber membrane fabrication process includes; Step 1: Filler in different wt.% was added to the appropriate solvent. The mixture was sonicated for the duration of 30minutes in an adequately sealed conical beaker. Step 2: Polymeric powders or pellets were then added to the prepared solution for continuous mixing on a magnetic stirrer for 24 hours at an

appropriate temperature range. Step3: The filler added polymeric solution was filled in needle-syringe unit to mount on syringe pump. Step 4: The electrospinning of the prepared solution was carried using an experimental set-up. Step 5: For the sound absorption analysis in the impedance tube test set up, the nanofiber sample was cut in a circular shape with a 10cm diameter. The sample was mounted on a circular aluminum ring using double-sided adhesive tape. The nanofiber membranes without any surface wrinkles were then mounted in the piston-cylinder unit for acoustic testing. Step 6: For pressure drop measurements, the untouched and undisturbed electro-spun samples with no wrinkles were placed on the adhesive masking tape from the sides. The tape ensures the proper handling of extremely thin and delicate nanofiber membranes for pressure drop measurements and the layering process. The step-by-step methodology from polymer mixing to nanofiber accumulation in the form of membranes is provided in Figure 3.2.

Table 3.3: Tabular description of polymer-filler concentration range (wt.%).

Filler Material (Wt.%)	Acoustics	Filler Material (Wt.%)	Filtration
	PVP/PVDF		PVDF
MWCNT's	0.25 to 1.0	MWCNT's	0.25
GN	0.25 to 1.0	GN	0.25
FS	0.25 to 1.0	TiO <sub>2</sub>	0.25
FG	0.25 to 1.0	CuNP's	0.25
MC	0.25 to 1.0		

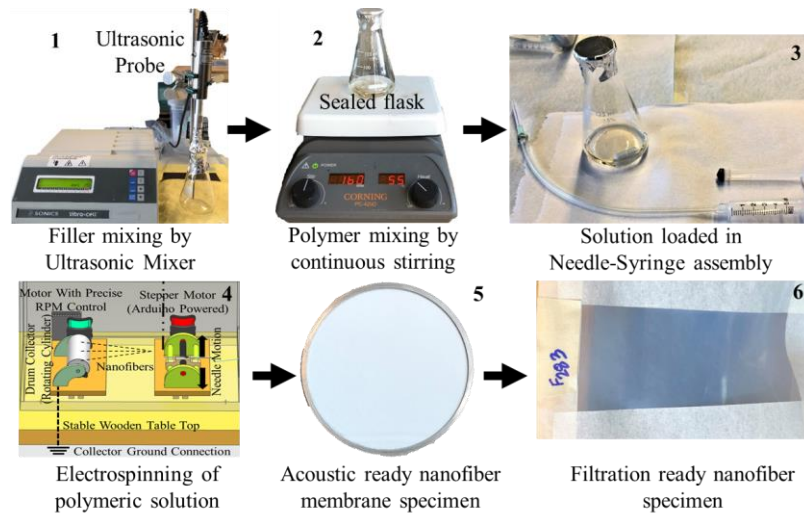


Figure 3.2: Step-by-Step description electro-spun nanofiber membrane fabrication process.

### 3.4 Thermal, Mechanical, and Morphological Characterization

#### 3.4.1 Thermo-gravimetric Analysis (TGA)

The thermo-gravimetric analyzer used in the study for thermal analysis was Q50 by TA instruments – USA [Figure 3.3]. Variation in the polymeric sample mass concerning time or temperature is studied through the TGA analysis. The analysis is typically used to compute the decomposition temperature of the polymeric material where the onset of degradation or mass change shows the decomposition point. Measurements of time or temperature at which the maximum loss of sample mass has occurred are derived from the derivative of the first curve known as the TG curve. The peak of the derivative curve, known as the DTG curve, provides the maximum degradation temperature. TGA was carried out in the nitrogen environment for all the pure polymer and nanofiber samples to prevent oxidation in the chamber. All these tests were performed on a sample weight less than 10mg for pure polymer and less than 20mg for nanofibers at a calibrated heating rate of 10°C/min for the temperature range at the ramp of 600°C (for PVP and its composites) and 800°C (for PVDF and its composites). The resultant TGA graphs were further used to compute the onset of degradation (°C), maximum decomposition temperature or peak of derivative (°C), and percentage residue [Appendix (A1-A4)].



Figure 3.3: Thermo-gravimetric Analyzer - TGA (Q series – Q50).

#### 3.4.2 Differential Scanning Calorimetry (DSC)

Differential Scanning Calorimeter (DSC) used in the study for thermal analysis was Q20 obtained from TA Instruments – USA [Figure 3.4]. The instrument measures the polymeric sample heat flux concerning time or temperature where the ambient atmosphere maintained inside the chamber is mainly nitrogen. Pure polymeric and nanofibers samples

were placed in a sample pan inside the chamber wherein the reference pan (empty) also undergoes the same temperature variation. The instrument tries to sustain a temperature difference of zero between the samples, and the corresponding heat flux that maintains this difference provides DSC plots. For all the DSC tests, the sample weight of 3mg to 6mg was maintained at a calibrated heating rate of 10°C/min for the temperature Heat-Cool-Heat range of 300°C-60°C-300°C (for PVP/PVDF and its composites). The corresponding DSC curves provide various temperature points like melting temperature (°C), crystallization temperature (°C), and glass transition temperature (°C) [Appendix (B1-B4)].



Figure 3.4: Differential Scanning Calorimeter - DSC (Q series – Q20).

### 3.4.3 Dynamic Mechanical Analysis (DMA)

Dynamic Mechanical Analyzer (DMA) used in the study for mechanical analysis was Q800 obtained from TA Instruments – USA [Figure 3.5]. The tensile strength of the fabricated polymeric nanofiber samples was determined using DMA at a set temperature of 30°C with a displacement rate of 1000µm/min. The electro-spun nanofiber-based membrane specimens were trimmed in a rectangular shape to meet the test mount requirement of the film tension clamp. The test specimens were trimmed utilizing the DMA sharp film cutters that maintain uniform width of 5.3mm for all samples, and the length of the specimens was in the range of 15mm to 20mm. Specimens were tested using the DMA strain mode with the preload force of 0.05N at an initial displacement of 20µm, and the displacement rate was set to 1000µm/min. The test was performed on three to five samples of the same specimen, and an average value was reported in the study. The mechanical characterization of the specimen carried out using DMA reports include; a) Tensile strength (MPa), b) Elongation at break (%), and c) Young's Modulus (MPa) [Appendix (C1-C4)].

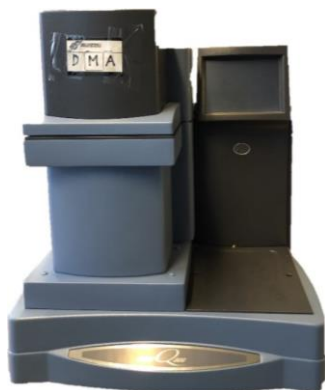


Figure 3.5: Dynamic Mechanical Analyzer - DMA (Q series – Q800).

#### 3.4.4 Scanning Electron Microscopy (SEM)

The Scanning Electron Microscope used in the study for the morphological characterization was FlexSEM 1000 by Hitachi [Figure 3.6]. The non-conductive nanofiber membrane samples manufactured from the electrospinning technique were analyzed in this microscope to study fiber diameter measurements, distribution, and fiber structure. The fiber samples were first placed on adhesive conductive tapes such as carbon or copper tapes. They were further sputter coated with gold to a thickness of approximately 20nm to improve specimen conductivity. Finally, the coated electro-spun nanofiber samples were mounted inside the SEM chamber, and the resultant electron images (backscattered) were captured at different magnifications for morphological studies. Fiber diameter computations were carried out by employing the SEM images in the ImageJ software; a Java encoded processing tool for image analysis. The average diameter of at least 20-50 fibers scattered at different spots in a membrane was used for calculations.

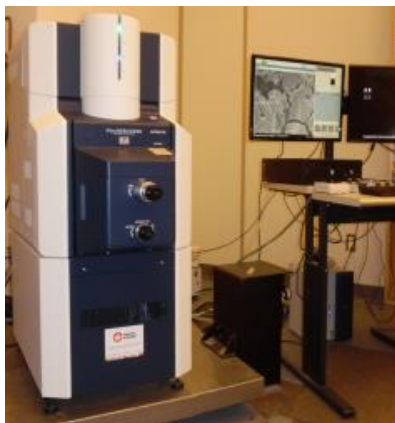


Figure 3.6: Scanning Electron Microscope – SEM (FlexSEM 1000).

### 3.4.5 Digital Microscope (DM)

Digital Microscope (DM) used in the study for morphological characterization was VHX-1000 obtained from Keyence – Canada [Figure 3.7]. Pure polymeric and filler-modified nanofiber samples were characterized under this microscope for thickness analysis. The fiber thickness of the specimens was measured utilizing the Keyence measurement tool built in the microscope system. Measurements of the specimen's average thickness were carried out at 20-30 different spots of untouched and undisturbed electro-spun nanofiber membranes.



Figure 3.7: Digital Microscope – DM (VHX – 1000).

## 3.5 Acoustic Characterization of Nanofiber Membranes and Composites

### 3.5.1 Introduction

In the field of acoustics engineering, the sound absorption coefficient value refers to as the predominant factor for characterizing the acoustic performance or behavior of any sound absorptive material or membrane. Sound absorption coefficient ( $\alpha$ ) value provides the precise measure of material's absorptivity or reflectivity for better selection of high-performance acoustic material [172]. The acoustic behavior of any material can be determined by calculating the sound absorption coefficient value through the following standard methodologies;

- a) Transfer function method – ISO 10534-2 [173].
- b) Standing wave ratio method – ISO 10534-1 [174].
- c) Reverberation chamber method – ISO 10534 [175].

Transfer function method and standing wave ratio measure the normal incident sound absorption coefficient values wherein the impedance tube experimental set-up (ISO 10534-

1 and ISO 10534-2) can be employed with the transfer function method for reducing the measurement time. On the contrary, the reverberation chamber method measures the random incident sound absorption coefficient values. It requires an extra room space with a higher volume of  $300\text{m}^3$  with a larger sample size of  $12\text{m}^2$  surface cover [176].

### **3.5.2 Impedance Tube Experimental Set-up**

The acoustic performance of the electro-spun nanofiber membranes was determined utilizing the laboratory scale impedance tube set up, which was built following ASTM1050 and ISO10534-2 for normal incidence acoustical measurements [Figure 3.8 (a-b)] [176,177]. The test set up comprises of several components, which includes the following: a) A long cylindrical PVC based tube of length (L) 117cm (tube length was maintained greater than three times the diameter of the tube) & diameter (D) 10cm was used for propagation of plane sound waves; b) A loudspeaker insulated in a box was mounted on one side of the tube and is connected to the signal generator and amplifier to produce the white noise; c) Three  $\frac{1}{4}$ " microphones were mounted on tube set-up on sample side at a certain distance to cover plane wave decomposition in the frequency range from 99Hz-2000Hz (as shown in Table 3.4); d) A sample holder unit of the piston (aluminum) – cylinder (stainless steel) arrangement that holds the nanofiber membranes and is placed on the other end of the tube. The back cavity behind the sample can be adjusted for different runs by moving the piston at specific distances in a cylindrical component. Electro-spun membranes placed on the aluminum ring with adhesive tape guarantees the wrinkle-less and undisturbed mounting of the specimens in holder. After the installation of membrane specimens, the holder unit was coupled with a tube with a clay seal covered with masking tape to ensure the proper acoustic seal.

The transfer function method was used for the acoustic characterization of the composites mounted in impedance tube set-up. The approach is straightforward and requires less space, wherein it can be implemented easily for impedance tube testing, which requires a small sample size. The absorption coefficient value can be determined at all frequencies in less time than the standing wave ratio method, where coefficient value is determined at each frequency separately [178].



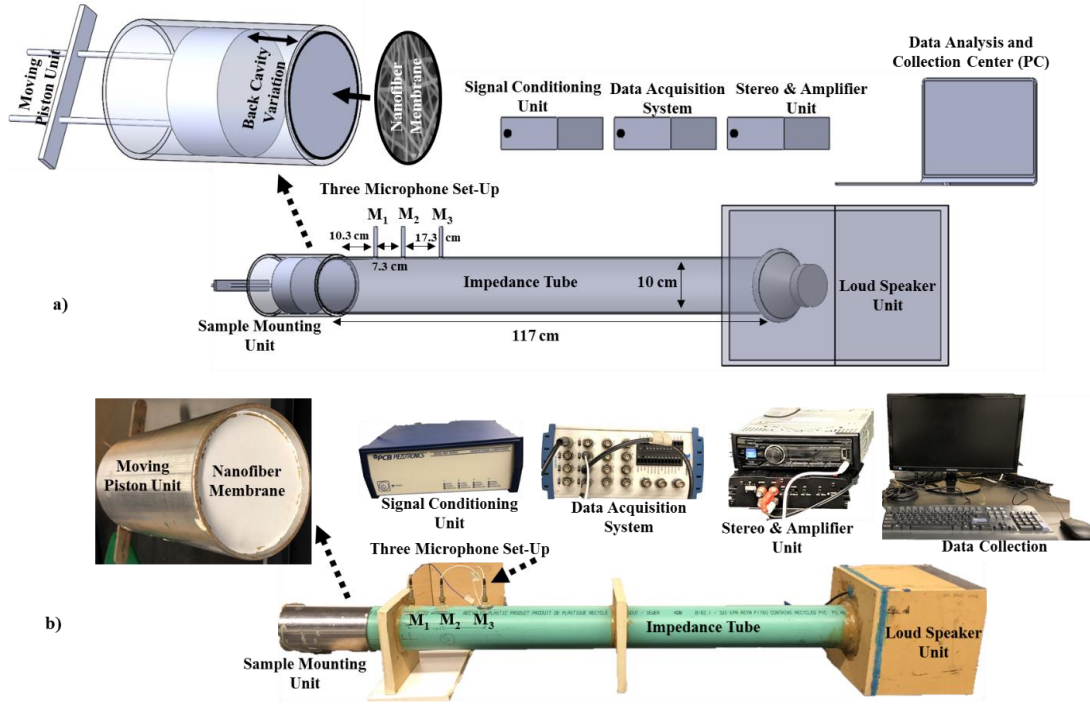


Figure 3.8: (a) Impedance tube experimental set-up schematics and (b) Pictorial demonstration of laboratory-scale set-up.

A loudspeaker is connected at one end of the tube with a signal generator through an amplifier & stereo system for volume and power control. The sample is placed on the other end of the tube with proper acoustic sealing. When the plane waves generated by the speaker incidents on the sample, the microphones mounted at three positions measures the sound pressures at those locations. The signals from the microphones transfer to the signal conditioner, which smoothens the rough signals and sends them to the Data Acquisition (DAQ) system, which digitizes the analog signal and transfers the data to the PC. The transfer function was determined for the two sets of the microphones chosen for different frequency range, and the corresponding reflection coefficient value is determined using Equation 3.1 [176];

$$R = \frac{H_{12} - H_I}{H_R - H_{12}} e^{2jkx} \quad (3.1)$$

The absorption coefficient can be determined using Equation 3.2;

$$\alpha = 1 - |R|^2 \quad (3.2)$$



Where,

$H_{12}$  = Transfer function between mic 1 to mic 2

$H_I = (e^{-jks})$  = Transfer function of the incident wave

$H_R = (e^{jks})$  = Transfer function of reflected wave

$x$  = Distance between sample & adjacent microphone,  $j = \sqrt{-1}$

$k = \frac{2\pi f}{c}$  = wave number;  $f$  is the frequency in Hz and  $c$  is the speed of sound

$s$  = spacing between the microphones.

The maximum frequency measures by the impedance tube set-up with corresponding tube diameter is given by [178];

$$F = \frac{1.84C}{\pi d} \quad (3.3)$$

Where  $d$  is tube diameter in meters.

Three microphones were mounted in the drilled holes on the tube to determine coefficient values from two mic configurations limited to specific frequency zones [Table 3.4]. The frequency ranges for different configuration of mic position selected depends on the spacing between them, and the upper & lower range is given by [178];

$$f_1 = \frac{0.05C}{s} \quad (3.4)$$

$$f_u = \frac{0.45C}{s} \quad (3.5)$$

Table 3.4: Description of coefficient measurement frequency range.

Distance between microphones (cm)		Frequency measurement range	
		Low-frequency range (Hz)	High-frequency range (Hz)
M1-M2	7.3	234	2000
M2-M3	10	171	1543
M1-M3	17.3	99	892

Lab-view and MATLAB software was used to function the impedance tube and white noise [Figure 3.9(a-b)]. The software codes were developed in the same regard to

computing the acoustic performance factors such as sound reflection coefficient and sound absorption coefficient of manufactured membranes specimens. Before starting the acoustic test for samples, the microphone calibration was carried out by performing the correction of phase mismatch. The speaker unit was powered ON for 10 minutes before the acoustic testing of the samples for temperature stability inside the impedance tube [179]. The corresponding pressure signal was used as input in developed MATLAB code to calculate absorption or reflection coefficient value. The graphical representation of the absorption coefficient value with respect to the frequency was plotted using the Microsoft Excel software.

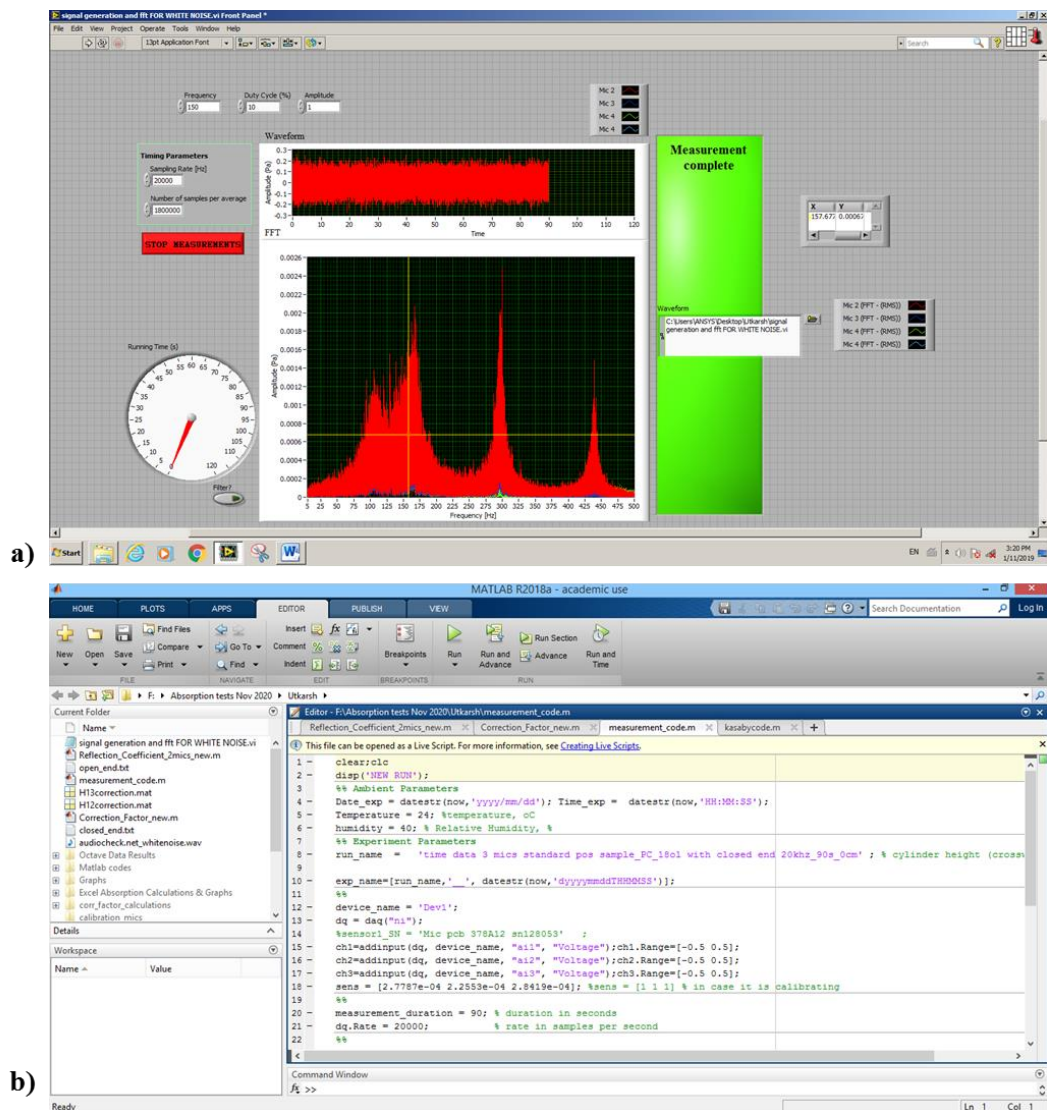


Figure 3.9: a) Lab-view software for pressure signal measurement and b) MATLAB software for pressure signal and absorption coefficient measurement.

### 3.5.3 Impedance Tube Validation Study

The validation of the tube set-up design was carried out by determining the reflection coefficient measurements of the tube with an open end, and the coefficient values were compared with the theoretical value of the open end tube (non-flanged) given by Equation 3.6 [180];

$$R_{th} = \exp\{-(ka)^2\} \left[ 1 + \frac{1}{6}(ka)^4 \left\{ \log \frac{1}{\gamma ka} + \frac{19}{12} \right\} \right] \quad (3.6)$$

Where (a) is the radius of the pipe,  $k = 2\pi/\lambda$  and  $\gamma = 3.77746$ . As shown in Figure 3.10, the absorption coefficient measurements are in good agreement with the theoretical measurements with respect to the calculated frequency range.

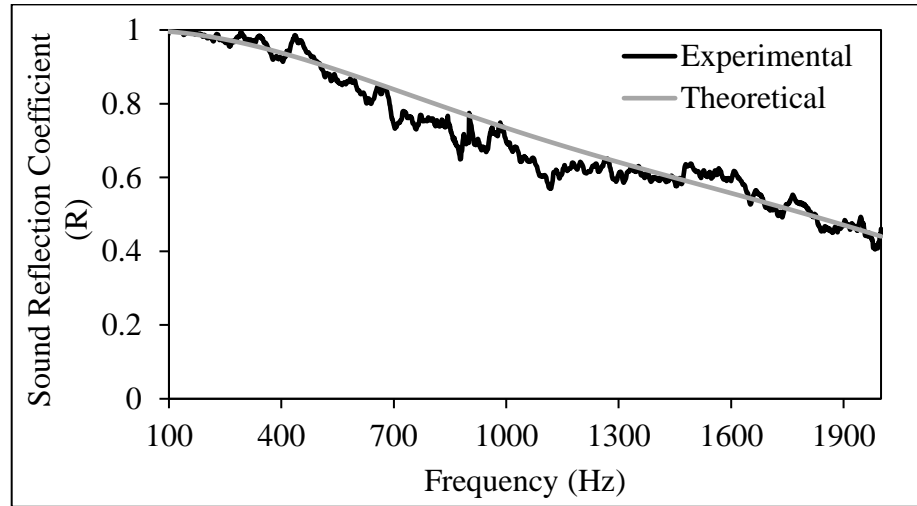


Figure 3.10: Comparison of the reflection coefficient experimental value with the theoretical value for open-end test for validation.

## 3.6 Filtration Characterization

### 3.6.1 Introduction

The filtration performance of the mask significantly depends on the breathability or the air permeability of the filter medium, which can be determined by measuring the pressure drop across the surface of the mask material at specific ambient conditions of temperature, humidity, and airflow rate [137]. The differential pressure measurement set-up was developed following EN 14683:2019+AC:2019 (E) [Medical face masks – Requirements and test methods] to determine the pressure drop across various filter

samples. The standard is required for the medical masks that shield the human nose, mouth, and chin with the material and blocks the infective agents from transmission from one person to another. The standard test method and requirements mentioned in this standard or equivalent standard ASTM F2100-11 should be complied with by the medical face mask provided in the 93/42 directive or UE/2017/745 regulations [181].

### **3.6.2 Differential Pressure Measurement Experimental Set-Up**

Differential pressure ( $\Delta P$ ) measurement was carried out in the laboratory scale pressure drop experimental set-up [Figure 3.11 (a-b)]. The instrument comprises of following components: a) An electric vacuum pump (RS-1.5 - Norman Vacuum Pump) of force air displacement 4CFM with an ultimate vacuum capacity of 30Pa that draws out air from the metal block opening of defined surface area with constant air flowing through the channel, b) Digital differential manometer (Perfect Prime – AR1890) that determines the differential pressure across the surface of a face mask material, c) Mass flow meters (RMB-52D-SSV flow meter, 5-50 SCFH/2-23 LPM AIR by Dwyer) to measure the airflow rate through the channel and sample holders, d) Sample holding unit designed following respective standards was made of aluminum with in-built extruded metal ring for proper sealing, e) Clamping mechanism consists of screw tightened top holders on a moving station for which a lever can manually control the movement, and the bottom holder was screwed to the stationary clamping base. During the test, the sample can be placed between these holders, and the clamping will ensure zero air leakage from the holding set-up.

Before starting the test, the top and bottom holders are clamped together with no specimen in between, and the vacuum pump was started with an 8LPM flow rate maintained to zero the differential pressure gauge. Figure 3.11 (b) demonstrates the lab-scale experimental set-up for the breathability test. The breathability testing starts by powering the vacuum pump. The flowmeter regulates the air suction flow of 8LPM from the sample holder molds, wherein the air suction takes place from the top holder through the bottom. The mask material was placed in between the top and bottom mold of the sample holder unit. The differential pressure gauge measures the pressure difference across the sample when connected to either end of the pipe linings [Figure 3.11 (b)]. The internal diameter of the top and bottom holder in the contact area of the filter material was designed

with a  $25 \pm 1$  mm cylindrical hole. A 3mm thick metallic ring is engraved on the top holder to ensure the proper seal and leak-proof set-up. The push-to-connect tube fitting was used to provide leak-proof pipe lining connections [Figure 3.11 (b)].

The test sample of mask materials was placed flat between the holders, and the pressure drop measurements were carried out on three different spots with a single specimen's respective surface test area cover. The average pressure drop of three to five samples was reported in the study at room temperature and humidity. The differential pressure per unit area was calculated using Equation 3.7;

$$\Delta P = \frac{P_1 - P_2}{4.9} \quad (3.7)$$

Wherein,  $(P_1 - P_2)$  is the pressure difference measured by digital manometer from the difference of low-pressure side to the high-pressure side (near the vacuum pump side) of connection ports, 4.9 is the surface area in  $\text{cm}^2$  of the specimen under test, and  $\Delta P$  is defined as the differential pressure measured per unit surface area in Pa.

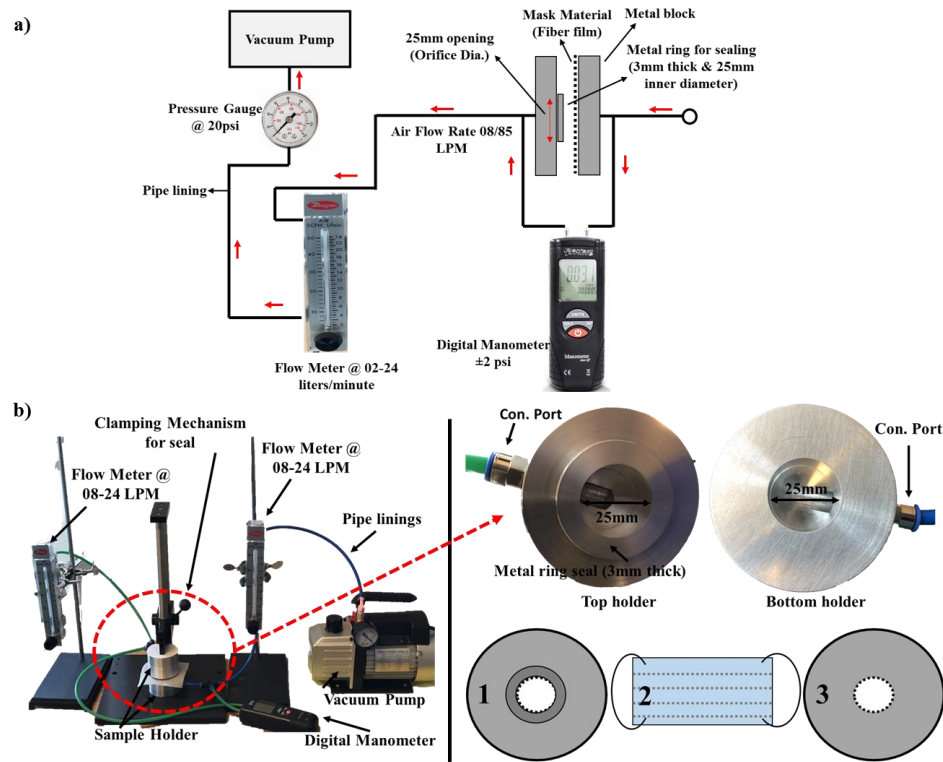


Figure 3.11: Experimental set-up for differential pressure ( $\Delta P$ ) measurement; (a) Schematic description and (b) Laboratory-scale set-up with exploded view of sample holder and mask placement between the mold.

### **3.7 Modelling and Optimization of Electrospinning Parameters for Manufacturing of PVP Fibers**

#### **3.7.1 Introduction**

In this study, the polymeric nanofibers of PVP were manufactured using the electrospinning technique. The electrospinning process parameters such as voltage, concentration, the rotational speed of collecting drum, collecting distance, and flow rate were studied utilizing the experimental design technique of Taguchi's. The effects of these parameters on the fiber diameter, membrane thickness, and weight as output responses were investigated by ANOVA and Taguchi's array design. Furthermore, a mathematical model was generated using RSM and GP to model the electrospinning process.

The parametric assessment of the selected governing electrospinning parameters was performed using the ANOVA to evaluate the statistical significance of process variables. The resultant output responses such as fiber diameter, thickness, and weight tabulated using Taguchi's design was used for ANOVA study wherein the significant electrospinning factors were determined at different confidence and risk levels. The analysis involves statistical computations of data variance, sum of squares, and F-test values for the individual factors at different levels to determine the optimum conditions and significance on designed output responses.

RSM is statistical regression-based tool used in this study to empirically analyze and manifest the relationship between the corresponding input variables and output response. It is a practical modelling-based technique that involves polynomial regressions instead of approximations associated with output response and input variables. The objective of implementing RSM was to improve the output response model that was regulated by five different independent electrospinning variables. This statistical tool provides the benefit of reducing the repeated experimental trials at different factor levels to save time and cost.

GP is artificial intelligence-based technique which is considered as the most powerful for modelling in different engineering applications. GP consists of several programming units, making it a tree structure with functions and terminals as basic building blocks of each program, known as genotype. Terminals of the programs are leaves and program functions are programming and mathematical functions with arithmetic operations. The

empirical models of the process were generated based on these input variables and functions where each model is classified as single chromosome which is evaluated by the fitness function. The possible error between the input variables or training data and output is estimated by this function for each model. The two significant factors such as mutation and crossover are known as the genetic operators which are responsible for generating new chromosomes. In this study, Eureka software was used to create empirical models for three output responses such as, fiber diameter, thickness, and weight.

### 3.7.2 Experimental Methodology

The polymeric solution was prepared via mixing PVP powders in ethanol at different concentrations of; 8, 10, and 12 wt.% by magnetic stirring for 24 hours at ambient temperature. PVP fiber membranes were prepared using the electrospinning experimental set-up. The measurements of PVP fiber diameter and its distribution in a test sample were carried out using the SEM images in ImageJ software. The fiber diameter measurements were carried out at least 50 fibers scattered at different spots in a test specimen. The deposited nanofiber membrane thickness was evaluated by calculating the average of 30 measurements taken at different locations of the test specimen using DM.

The selected values of the five electrospinning parameters are given in Table 3.5. Each parameter was assigned with a three-level variation. Taguchi's method, being robust and straightforward, was used in this study to design experiments and optimization. The design consists of 27 rows and 13 columns (max) with three-level variation [182]. The mean output performance and variation were studied with the applied Taguchi's quality loss function design. Table 3.7 shows the design of experiments where the columns indicated the process parameters and the rows indicates the designated values.

Table 3.5: Electrospinning control factors and levels

Control Factors	Symbol	Level 1	Level 2	Level 3
High Voltage (KV)	A	10	13	15
Concentration (Wt. %)	B	8	10	12
Rotational Speed (RPM)	C	500	1000	1500
Collecting Distance (cm)	D	10	13	15
Flow Rate (ml/h)	E	0.6	0.8	1

### **3.7.3 Results and Discussion**

#### **3.7.3.1 Morphological Characterization of Electro-Spun PVP Fibers**

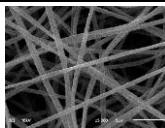
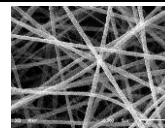
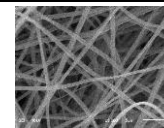
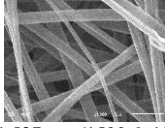
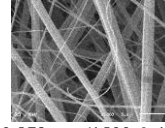
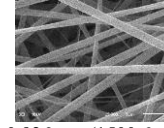
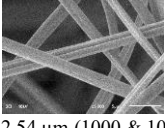
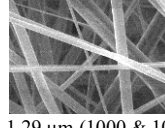
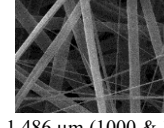
The nanofiber characteristics, fiber shape, diameter, and distribution are affected significantly by the change in electrospinning parameters [183]. This phenomenon is explained in the SEM micrographs of PVP nanofibers which suggests visually that high voltage (10-15KV) and concentration (8-12wt.%) has a significant effect on the fiber diameter [Table 3.6]. The minimum fiber diameter value of  $0.536\mu\text{m}$  was observed at the lowest concentration (8wt.%) and highest voltage (15KV). The maximum fiber diameter value of  $2.54\mu\text{m}$  was obtained at the highest concentration (12wt.%) and lowest voltage (10KV). The analysis shows that the average fiber diameter value decreases with a decrease in the polymer concentration and an increase in the supplied voltage. This may be attributed because if the polymer solution concentration is very low, the viscoelastic forces would not be sufficient to escape columbic repulsion force that breaks up the jet to form fibers, and hence it results in beads. It was noticed that to achieve uniform bead-less fibers, the viscoelastic force should be sufficient to break the polymer jet with higher columbic stress that influences the jet elongation. Hence, with the further increase in concentration, the fiber diameter of the resultant fiber reduces [162]. If the solution concentration is high, the fiber diameter will increase substantially. If the concentration is too high, it will restrict the continuous flow and block the needle [53].

The fiber diameter value decreases with an increase in high voltage because the amount of charge flowing in a jet increases, increasing the repulsion force. The increased repulsion force increases the stretching force acting on the polymer jet leading to the development of thinner fibers [184]. At 8wt% concentration, a substantial number of thin uniform fibers of average diameter less than  $0.7\mu\text{m}$  were observed with a narrow range of diameters. On the other hand, at higher concentrations of 10-12wt.%, an adequate amount of mixed fibers, thin and thick, were observed with an increase in applied voltage. A similar phenomenon is also reported in few works that studied electrospinning of PVP [185,186]. The broader distribution may be attributed because of increased electric field intensity that influences thin fiber generation. At higher concentrations, fibers were stretched out in different shapes, and some were twisted to each other in various patterns [53,162,184]. The



difference in stretching force on polymer jet and electrostatic force of attraction between fibers exposed to higher electric field is the main reason behind this phenomenon [70,187]. Moreover, the higher surface tension of the polymer solution prevents the decrease in the size of jet extruding out from the needle, and fibers subside on each other when the solvent dries up [162].

Table 3.6: SEM images to study fiber morphology at different parametric levels.

PVP Concentration (Wt%)	Applied voltage Supply (KV)			Solution Flow rate (ml/h)
	10	13	15	
8	 0.662 $\mu\text{m}$ -(500 & 10)	 0.605 $\mu\text{m}$ -(500 & 10)	 0.536 $\mu\text{m}$ -(500 & 10)	0.6
10	 1.527 $\mu\text{m}$ -(1500 & 10)	 0.879 $\mu\text{m}$ -(1500 & 10)	 0.926 $\mu\text{m}$ -(1500 & 10)	0.8
12	 2.54 $\mu\text{m}$ -(1000 & 10)	 1.29 $\mu\text{m}$ -(1000 & 10)	 1.486 $\mu\text{m}$ -(1000 & 10)	1.0
*Fiber diameter ( $\mu\text{m}$ )-(RPM & Needle to collector distance - cm)				

### 3.7.3.2 Design of Experiments (DOE) Using Orthogonal Array

The average value and the standard deviation of the obtained fiber diameters, thickness, and weight for each trial are given in the far-right column in Table 3.7. The reported fiber diameter is the average of at least twenty fiber diameter measurements at different locations on the nanofiber mat [Figure 3.12(a-b)]. The average thickness measurements of fabricated nanofiber membrane were reported by precisely calculating the size at 30 different spots or locations of a membrane.

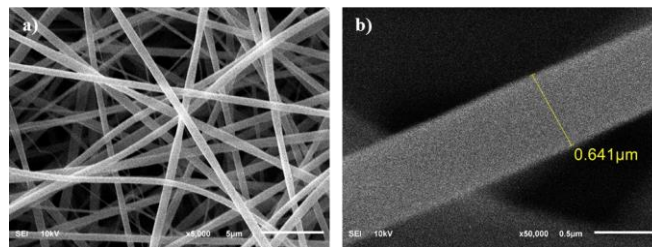


Figure 3.12: SEM image of the PVP nanofibers at (a) 5000X (Scale: 5 $\mu\text{m}$ ) and (b) 50000X (Scale: 0.5 $\mu\text{m}$ ).

The results of the fiber diameter measurements suggest that the least fiber diameter values were achieved with the experimental run numbers 12, 19, and 20, namely, at the lower concentrations and higher voltage values. The least fiber diameter value was observed at the experimental run 19 that resulted in a diameter value of 536nm at a polymer concentration of 8wt %, an applied voltage of 15KV, a 500 collector RPM, a 10cm collecting distance, and a low flow rate of 0.6ml/hr. The corresponding fiber diameter values range from 536nm to 598nm and the highest diameter observed was 2.54 $\mu$ m, as mentioned in Table 3.7.

Table 3.7: Experimental plan for parametric analysis of PVP nanofibers using L27 Orthogonal array.

Run#	A	B	C	D	E	Avg. Fiber Diameter ( $\mu$ m)	Avg. Thickness ( $\mu$ m)	Weight (g)
1	10	8	500	10	0.6	0.662 $\pm$ 0.14	122.47 $\pm$ 7.72	0.2287
2	10	8	1000	13	0.8	0.933 $\pm$ 0.15	145.97 $\pm$ 8.45	0.054
3	10	8	1500	15	1	0.744 $\pm$ 0.13	152.28 $\pm$ 10.71	0.3544
4	10	10	500	13	1	1.253 $\pm$ 0.19	165.58 $\pm$ 15.99	0.3604
5	10	10	1000	15	0.6	1.243 $\pm$ 0.23	94.93 $\pm$ 10.32	0.3119
6	10	10	1500	10	0.8	1.527 $\pm$ 0.34	106.43 $\pm$ 9.85	0.4258
7	10	12	500	15	0.8	1.865 $\pm$ 0.33	170.62 $\pm$ 17.42	0.413
8	10	12	1000	10	1	2.54 $\pm$ 0.348	143.80 $\pm$ 15.44	0.4496
9	10	12	1500	13	0.6	1.507 $\pm$ 0.58	137.05 $\pm$ 15.76	0.3714
10	13	8	500	10	0.6	0.605 $\pm$ 0.10	112.26 $\pm$ 9.66	0.2764
11	13	8	1000	13	0.8	0.819 $\pm$ 0.12	151.05 $\pm$ 7.32	0.2558
12	13	8	1500	15	1	0.570 $\pm$ 0.39	154.04 $\pm$ 7.36	0.3053
13	13	10	500	13	1	1.091 $\pm$ 0.61	224.77 $\pm$ 16.70	0.4341
14	13	10	1000	15	0.6	1.048 $\pm$ 0.39	94.12 $\pm$ 7.82	0.3677
15	13	10	1500	10	0.8	0.879 $\pm$ 0.61	140.72 $\pm$ 16.30	0.432
16	13	12	500	15	0.8	2.075 $\pm$ 0.38	228.44 $\pm$ 26.82	0.4039
17	13	12	1000	10	1	1.29 $\pm$ 0.75	208.40 $\pm$ 24.31	0.4709
18	13	12	1500	13	0.6	1.12 $\pm$ 0.67	237.22 $\pm$ 17.68	0.4053
19	15	8	500	10	0.6	0.536 $\pm$ 0.15	92.86 $\pm$ 5.79	0.291
20	15	8	1000	13	0.8	0.598 $\pm$ 0.11	97.54 $\pm$ 6.01	0.3164
21	15	8	1500	15	1	0.921 $\pm$ 0.21	144.26 $\pm$ 8.92	0.343
22	15	10	500	13	1	0.668 $\pm$ 0.43	188.78 $\pm$ 14.99	0.4231
23	15	10	1000	15	0.6	1.074 $\pm$ 0.16	152.62 $\pm$ 5.43	0.4028
24	15	10	1500	10	0.8	0.926 $\pm$ 0.34	209.57 $\pm$ 12.51	0.4033
25	15	12	500	15	0.8	1.465 $\pm$ 0.47	305.26 $\pm$ 24.99	0.422
26	15	12	1000	10	1	1.486 $\pm$ 0.66	276.61 $\pm$ 11.34	0.3174
27	15	12	1500	13	0.6	1.56 $\pm$ 0.54	287.95 $\pm$ 25.42	0.4223

### 3.7.3.3 Evaluation of Electrospinning Parameters: ANOVA Study

The evaluation of the control factors and their significance was carried out using ANOVA software. The mean output response for individual trial at each level was investigated and shown in Table 3.8. It was observed that the high voltage (A) and polymer concentration (B) introduced significant effects on the fiber diameter. The corresponding F-test values confirm the significance of high voltage at 95% confidence level and concentration at 99% confidence level (i.e. looking at Table 3.8,  $F_A > F_{2,16@90\%}$  and  $F_{2,16@95\%}$ , and similarly  $F_B > F_{2,16@90\%}$ ,  $F_{2,16@95\%}$  and  $F_{2,16@99\%}$ ). On the other hand, the parameters such as collector RPM, needle-collector distance, and flow rate had the least effects. They were considered to be insignificant because of their minimum statistical summation of diameter values, i.e., 0.63, 0.82 & 1.2.

Table 3.8: Fiber diameter ANOVA results

ANOVA: Fiber Diameter ( $\mu\text{m}$ )											
A <sub>1</sub>	12.274	B <sub>1</sub>	6.388	C <sub>1</sub>	10.22	D <sub>1</sub>	10.451	E <sub>1</sub>	9.355	SS <sub>T</sub>	6.2912
A <sub>2</sub>	9.497	B <sub>2</sub>	9.709	C <sub>2</sub>	11.031	D <sub>2</sub>	9.549	E <sub>2</sub>	11.087		
A <sub>3</sub>	9.234	B <sub>3</sub>	14.908	C <sub>3</sub>	9.754	D <sub>3</sub>	11.005	E <sub>3</sub>	10.563		
SS <sub>A</sub>	0.6305	SS <sub>B</sub>	4.0981	SS <sub>C</sub>	0.0928	SS <sub>D</sub>	0.12	SS <sub>E</sub>	0.1753	SS <sub>Error</sub>	1.1745
V <sub>A</sub>	0.3152	V <sub>B</sub>	2.0491	V <sub>C</sub>	0.0464	V <sub>D</sub>	0.06	V <sub>E</sub>	0.0877	V <sub>Error</sub>	0.0734
F)A	4.2943	F)B	27.914	F)C	0.6321	F)D	0.8175	F)E	1.1942		
p <sub>A</sub>	0.0321	p <sub>B</sub>	0.0001	p <sub>C</sub>	0.5442	p <sub>D</sub>	0.4592	p <sub>E</sub>	0.1758		
F)2,16 @ 90% confidence level										2.66	
F)2,16 @ 95% confidence level										3.63	
F)2,16 @ 99% confidence level										6.22	

The ANOVA illustration in Table 3.9. shows that high voltage supply - A and polymeric concentration – B are the two factors that influenced the nanofiber membrane thickness at different confidence levels. F-test analysis of high voltage factor was observed with high significance at a confidence level of 90% [ $F_A > F_{2,16 - 90\%}$  (2.66)] with an associated higher risk factor of [ $p_A < 0.05$ ]. Contrastingly, the polymer concentration was observed to be highly significant when compared with voltage, at 99% confidence level [ $F_B > F_{2,16 @ 99\%}$ ] with significantly lower risk levels of 0.0006 [ $p_D > 0.05$ ], which stipulates the highest significance of the polymer concentration on thickness. Other

parameters like RPM, needle to collector distance, and feed rate were observed to have a minimal effect on thickness.

Table 3.9: Thickness ANOVA results

ANOVA: Thickness ( $\mu\text{m}$ )											
A1	1239.1	B1	1172.7	C1	1611	D1	1413.1	E1	1331.5	SST	95174
A2	1551	B2	1377.5	C2	1365	D2	1635.9	E2	1555.6		
A3	1755.5	B3	1995.4	C3	1569.5	D3	1496.6	E3	1658.5		
SSA	15024	SSB	40754	SSC	3853.8	SSD	2815.4	SSE	6214	SSError	26513
VA	7512.1	VB	20377	VC	1926.9	VD	1407.7	VE	3107	VError	1657.1
F)A	4.5334	F)B	12.297	F)C	1.1628	F)D	0.8495	F)E	1.875		
p)A	0.0276	p)B	0.0006	p)C	0.3377	p)D	0.446	p)E	0.1855		
F)2,16 @ 90% confidence level										2.66	
F)2,16 @ 95% confidence level										3.63	
F)2,16 @ 99% confidence level										6.22	

ANOVA study investigated in Table 3.10. shows PVP concentration - B to be the most significant parameter with a strong influence on the weight of the PVP fiber membrane samples manufactured at different experimental runs. Statistical summation study-based F-test confirms the highest significance at 99% confidence level and lowest risk levels of  $p < 0.001$ . The respective F-test value for concentration was observed to be;  $F)_{\text{B}}$  (15.8) was reported to be considerably greater than  $F)_{2,16}$  @ 99% confidence level. Remaining factors like high voltage (A), collector speed (C), collector-needle distance (D), and solution feed rate (E) demonstrates the least effect on nanofiber weight with measurements of  $F)_{\text{A}}$ ,  $F)_{\text{C}}$ ,  $F)_{\text{D}}$ , and  $F)_{\text{E}}$  considerably lower than  $F)_{2,16}$  @ 90%.

Table 3.10: Weight ANOVA results

ANOVA: Weight (g)											
A1	2.9692	B1	2.425	C1	3.2526	D1	3.2951	E1	3.0775	SST	0.2004
A2	3.3514	B2	3.5611	C2	2.9465	D2	3.0428	E2	3.1262		
A3	3.3413	B3	3.6758	C3	3.4628	D3	3.324	E3	3.4582		
SSA	0.0105	SSB	0.1062	SSC	0.015	SSD	0.0053	SSE	0.0095	SSError	0.0538
VA	0.0053	VB	0.0531	VC	0.0075	VD	0.0027	VE	0.0048	VError	0.0034
F)A	1.5673	F)B	15.794	F)C	2.227	F)D	0.7905	F)E	1.418		
p)A	0.239	p)B	0.0002	p)C	0.1402	p)D	0.4705	p)E	0.271		
F)2,16 @ 90% confidence level										2.66	
F)2,16 @ 95% confidence level										3.63	
F)2,16 @ 99% confidence level										6.22	

#### **3.7.3.4 Effect of Electrospinning Designed Parameters on Fiber Diameter, Weight and Thickness**

The graphical representation of the summation values of fiber diameter is plotted with the corresponding control variable/factor in Figure 3.13. A substantial variation in diameter values was observed for the different levels of concentration and high voltage, which indicates the high significance of these factors compared to others. There are many controversial results on the effect of high voltage on fiber diameter as there are reports that say it increases with an increase in voltage for PVA polymer solution [187]. On the other hand, few reports on electrospinning on PVP investigated that the fiber diameter decreases with an incentive increase in voltage that enhances the repulsion force. Further increase in electric field intensity increases the diameter, which may be because of high electrostatic force [162] [188–190]. The effect of forces like; Repulsion and electrostatic might be the reason for conflict in the variation of diameter with voltage. The high voltage compared with the other factors like flow rate, needle-collector distance, and collector rpm had a significant effect on diameter. This phenomenon is in close agreement with the work where PVP fiber diameter decreases with voltage increase to 15KV except for the increase in diameter with further voltage increment [162]. Hence, voltage affects diameter, but its significance depends on the variation level, polymer, and concentration [191]. With the increase in the high voltage supply from A1 to A3 and the decrease in the concentration from B3 to B1, the fiber diameter values decreased to a minimum value. This may be because a higher voltage increases the repulsive forces, increasing the polymer solution stretching, resulting in a smaller fiber diameter [66,67]. A higher fiber diameter variation was observed with an increase in concentration because of an increase in the amount of polymer content in the extruded jet from the Taylor cone. At this point thicker jet is excited towards the collector end that leads to the thicker fibers and sometimes beads [192]. Further, the differences between the maximum and minimum summation values for the factors, applied voltage and concentration, were observed to be 3.04 & 8.52, respectively, which were the highest compared with those of the other factors, i.e., 1.28, 1.456 & 1.732. The analysis confirms that the polymer concentration is the most prominent factor with the highest variability effect whereas the other factors, namely RPM, flow rate, and distance do not seem to have any significant effect on the diameter values.

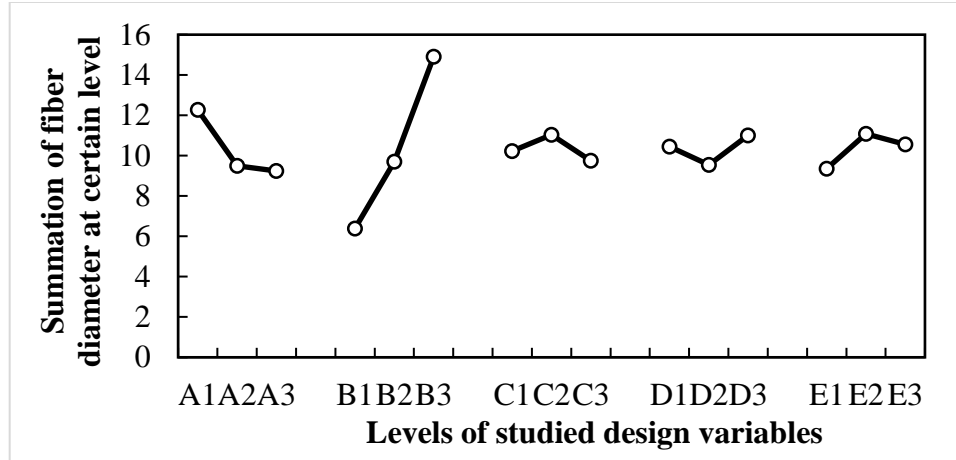


Figure 3.13: Graphical representation of main effects of electrospinning control factors on fiber diameter.

As shown in Figure 3.14., the highest variability of the polymer concentration from B1 to B3 was evident through the summation point of thickness values. The highest significance of the respective parameter was stipulated through these thickness measurements compared with other parameters with low variability. The summation spots clarify that the PVP fiber-based membrane thickness increases with increased concentration values from B1 to B3. A higher difference between the extreme level summation point of polymer concentration (B: 822.6) confirms the substantial effect on thickness value. On the contrary, other parameters like high voltage (A), rotation speed (C), needle-collector distance (D), and feed rate (E) demonstrates lower variability with the minor effect of these parameters on output response.

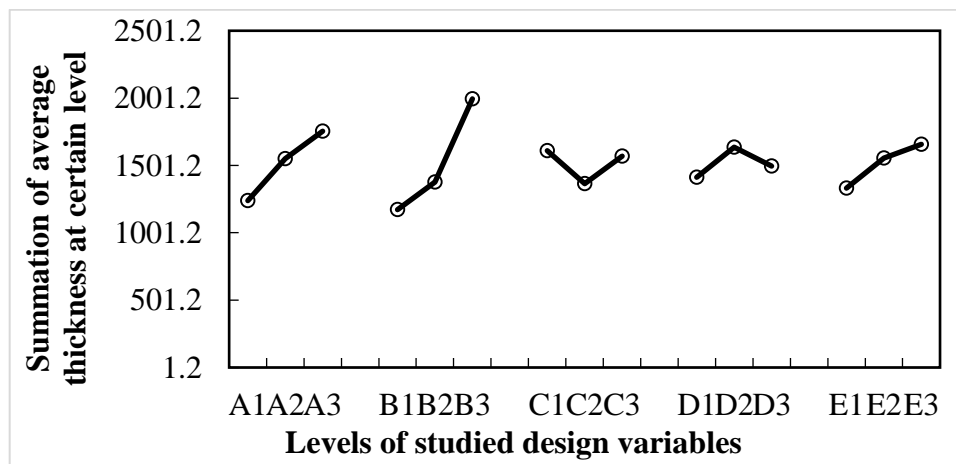


Figure 3.14: Graphical representation of main effects of electrospinning control factors on membrane thickness.

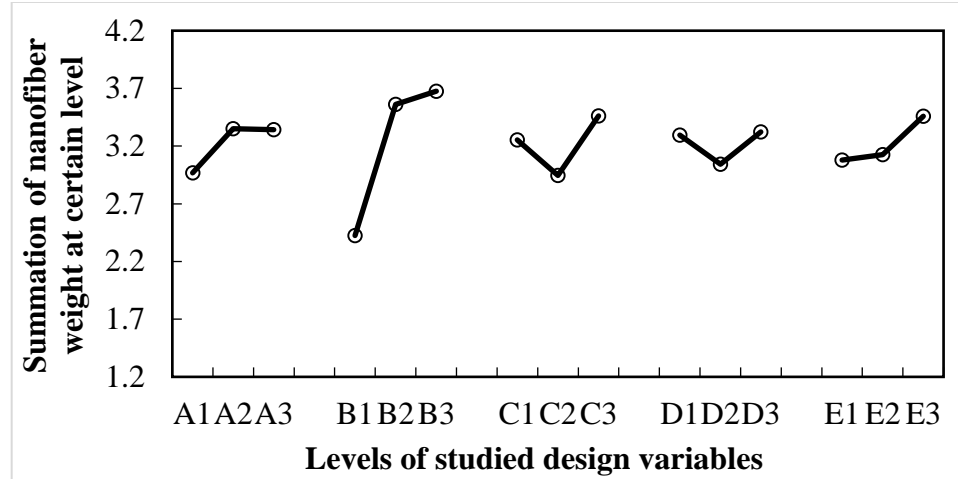


Figure 3.15: Graphical representation of main effects of electrospinning control factors on nanofiber weight.

In figure 3.15., a higher influence of a single factor: PVP polymer concentration (B), was reported with higher variability of the summation points at different levels of control factor. The summation study observed that the PVP nanofiber membrane weight increases with an increase in concentration level from B1 to B3. Furthermore, the highest difference at extreme summation points of level variation confirms the higher significance of the respective factor (B: 1.25), whereas the other parameters remain to have a lower effect on weight with lower variability when compared with concentration.

### 3.7.3.5 Electrospinning Process Modelling Using RSM

The significance of individual factors influencing the output response was investigated using multiple regression techniques. The mathematical model was developed for the fiber diameter, thickness, and weight response using RSM to predict the accuracy of the electrospinning model. The study investigates the effect of five parameters with three levels, leading to  $3^5 = 243$  trials for the complete analysis, but orthogonal array design reduces it to 27 trials. The mathematical model developed for the single effect of the process variables on output response (fiber diameter, thickness, and weight) is represented by the following three Equations (3.8 – 3.10);

$$\begin{aligned} \text{Fiber Diameter} = & 5.6522 - 0.5087A - 0.2850B + 0.0008C - 0.5591D + 5.3488E + 0.0176A^2 \\ & + 0.0260B^2 - 4.6e^{-7}C^2 + 0.0228D^2 - 3.1333E^2 \end{aligned} \quad (3.8)$$

$$\text{Thickness} = -250.5700 + 12.4507A - 91.8828B - 0.2048C + 81.8174D + 360.1778E - 0.0388A^2 + 5.7367B^2 + 0.0001C^2 - 3.1985D^2 - 168.3333E^2 \quad (3.9)$$

$$\text{Weight} = -0.8859 + 0.0818A + 0.3184B - 0.0003C - 0.1242D - 0.5238E - 0.0029A^2 - 0.0142B^2 + 1.8e-7C^2 + 0.0049D^2 + 0.3934E^2 \quad (3.10)$$

The average model accuracy of the model can be calculated as follows:

$$\text{Accuracy (A)} = [1 - \text{ABS} \frac{(Y_{\text{exp.}} - Y)}{Y_{\text{exp.}}}] * 100 \quad (3.11)$$

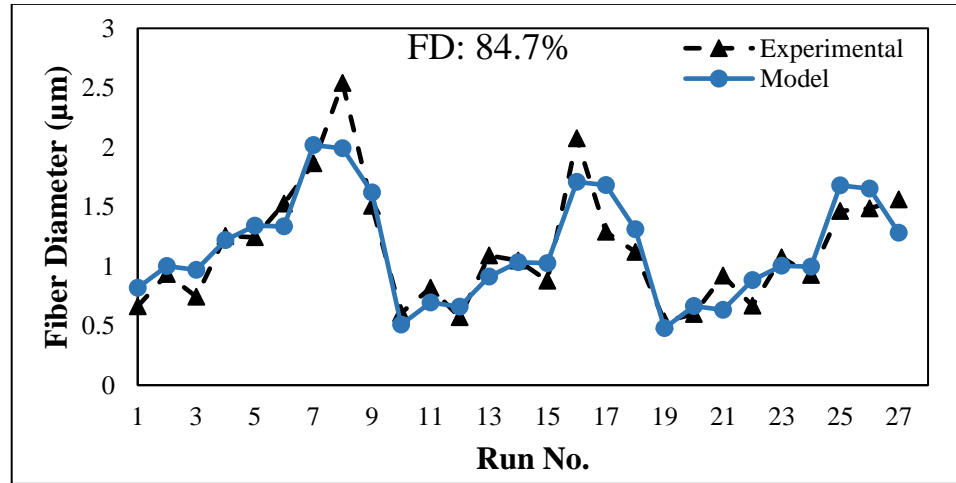


Figure 3.16: Mathematical model validation with experimental results for fiber diameter measurements.

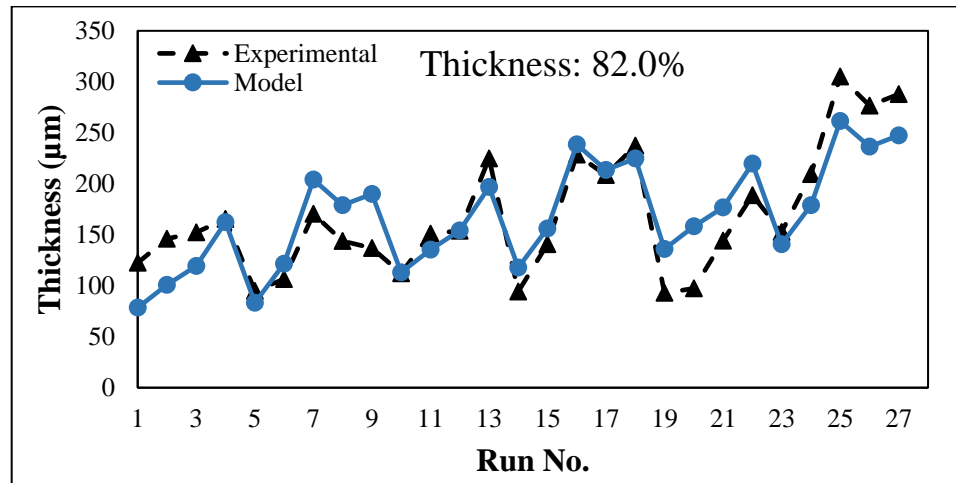


Figure 3.17: Mathematical model validation with experimental results for thickness measurements.



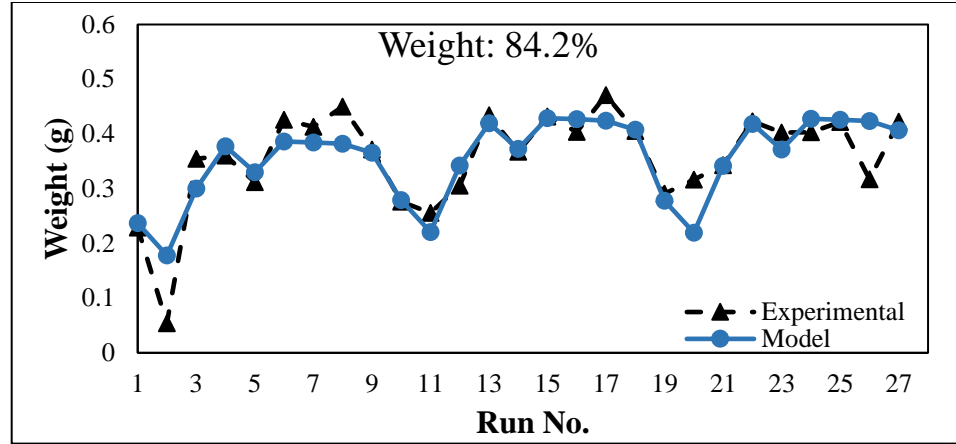


Figure 3.18: Mathematical model validation with experimental results for membrane weight measurements.

The graphical representation shown in Figures 3.16, 3.17, and 3.18 compares the mathematical model with the experimental results to analyze the model accuracy of three outputs. The average model accuracy of 84.7%, 82.0%, and 84.2% were obtained for the entire experimental trials, whereas a model accuracy of (90-98) % was observed for the few individual runs. The calculated average accuracy is considered as the acceptable range for model verification. The three-dimensional surface and contour plots were developed using these RSM models [Appendix (D1)].

### 3.7.3.6 Electrospinning Process Modelling Using GP

Genetic Programming (GP) was used to empirically model the fiber diameter, thickness, and nanofiber weight of the PVP membrane. Equation 3.12 shows the developed model for the PVP fiber diameter. It can be noticed that a good agreement was found between the experimental and predicted results. The fiber diameter output response was observed with average model accuracy of 88.5% [Figure 3.19]. The fiber membrane thickness was modeled using Equation 3.13, wherein an average model accuracy of 91.6% was noticed [Figure 3.20]. Regarding the nanofiber weight measurements, an acceptable agreement has been noticed with an average model accuracy of almost 80.1% [Figure 3.21]. The developed model for the nanofiber weight is provided in Equation 3.14.

$$\text{Fiber Diameter} = 0.0517 * E * B^2 + 0.0006 * D * E * A^2 - 0.1846 - 0.03150 * A - 5.7462e^{-6} * D * B^4 - 0.0318 * A * B * E^2 \quad (3.12)$$

$$\text{Thickness} = 1136.3181 + 668.0433 * E + -7185.6879 * E/D + 0.4108 * A * B^2 - 31.3939 * A - 34.4828 * D - 73.4696 * B \quad (3.13)$$

$$\text{Weight} = 0.3853 * E + 0.2830 * B + 0.0405 * A + 0.0002 * C * E - 1.7256 - 7.3247 e^{-6} * A * C - 0.0322 * A * E - 0.0123 * B^2 \quad (3.14)$$

The three-dimensional surface and contour plots were developed using these GP models [Appendix (D2)]. The optimization criteria and S/N ratio conversion is provided in Appendix E.

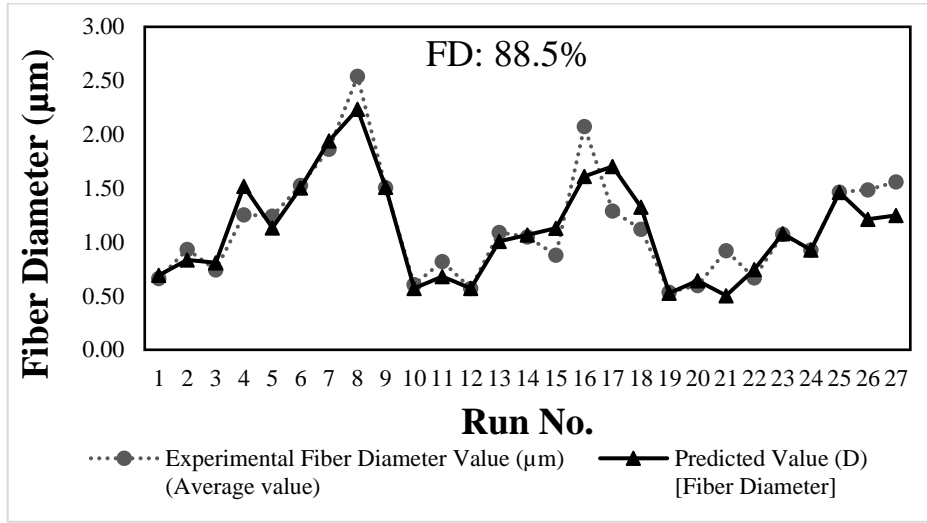


Figure 3.19: Experimental values of fiber diameter versus modeled value using GP at 27 experimental runs.

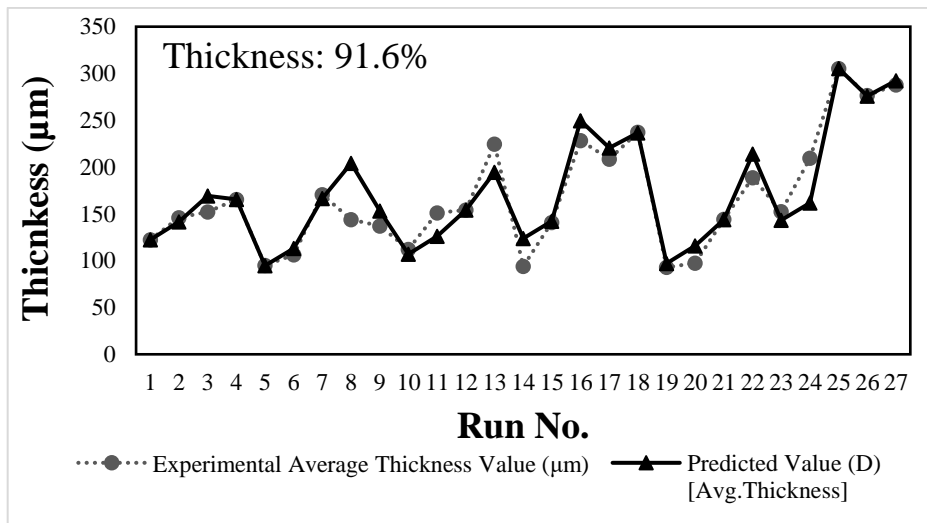


Figure 3.20: Experimental values of PVP fiber membrane thickness versus modeled value using GP at 27 experimental runs.

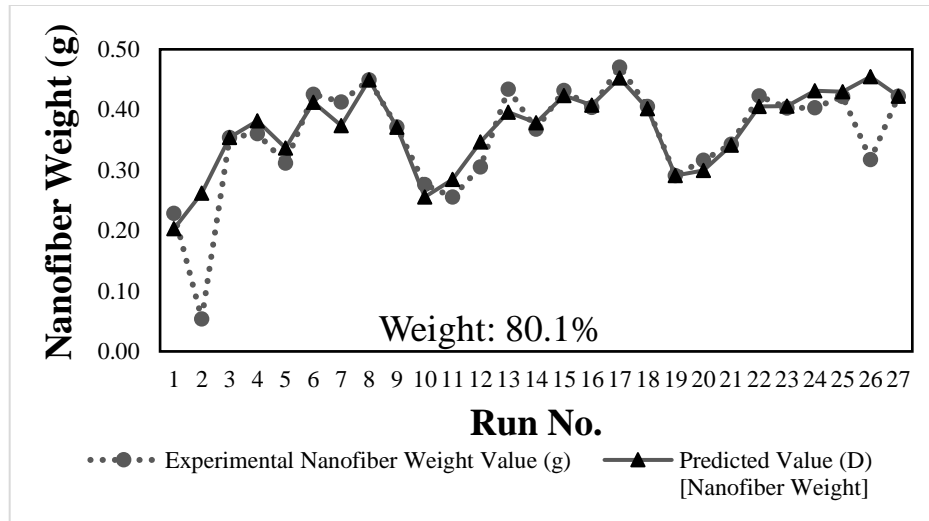


Figure 3.21: Experimental values of PVP membrane weight versus modeled value using GP at 27 experimental runs

### 3.7.4 Conclusions

In this work, an attempt has been made to investigate the electrospinning process of fabricating PVP nanofibers, and the parametric study of the process was investigated. The effects of five major parameters were studied using Taguchi L27OA with three levels at each parameter. The parametric evaluation was carried out to study the effect of electrospinning variables on three output responses; fiber diameter, thickness, and weight. For the 27 experimental trails, the electro-spun PVP average fiber diameter was observed to be 536nm to 2.54 $\mu$ m, the thickness was observed to be in the range of 94.12 $\mu$ m to 237.22 $\mu$ m, and weight was noticed in the range of 0.054g to 0.4709g. ANOVA study confirms the higher significance of high voltage and polymer concentration at 95% and 99% confidence levels. On the other hand, thickness and weight measurements were observed to be controlled by polymer concentration at higher significance levels of 99% and low-risk levels. The mathematical model developed using RSM predicted the average model accuracy of 84.7%, 82.0%, and 84.2% for diameter, thickness, and weight measurements for the range of chosen control parameters. Furthermore, empirical models were generated using GP for the same designed output responses, i.e., diameter, thickness, and weight measurements. High average model accuracies of 92.8% (fiber diameter), 86.7% (thickness), and 80% (weight) were observed when compared with RSM, which indicates the acceptable range for model verification.

### **3.8 Modelling and Optimization of Electrospinning Parameters for Manufacturing of PVDF Fibers**

#### **3.8.1 Introduction**

Polymeric nanofibers of PVDF-based solution were manufactured utilizing the electrospinning process. The control parameters of the electrospinning process, including high voltage, the concentration of a polymeric solution, collector rotational speed, the distance between needle and collector surface, and the flow rate of polymer solution, were investigated in this study utilizing Taguchi's experimental design methodology. The parametric study was carried out to examine the effect of electrospinning parameters on fiber diameter, membrane thickness, and membrane weight as three output responses. The experimental investigation based on Taguchi's experimental design involves parametric assessment and modeling using statistical tools like ANOVA and GP.

#### **3.8.2 Experimental Methodology**

The PVDF-based liquid polymeric solution was produced by mixing polymer pellets into DMF at different concentrations of; 20wt.%, 22wt.%, and 25wt.% by non-stop magnetic stirring at 70°C for straight 24 hours. The production of PVDF nanofibers was executed utilizing the electrospinning experimental set-up.

The morphological attributes of the electro-spun PVDF fibers were analyzed utilizing the SEM micro-graphs. The fiber diameter study was carried out by precisely measuring the fiber size of a single fiber scattered at different spots using ImageJ software. The average diametric calculation of 50 fibers was reported in the study, and an exploded view of fiber diameter calculation is presented in Figure 3.22 (a-b). A thin fibrous sheet of nanofiber membrane was safely placed in a microscope glass slide for thickness measurements [Figure 3.23 (a)]. The average thickness measurements of fabricated nanofiber membrane were reported by precisely calculating the size at 30 different spots or locations of a membrane [Figure 3.23 (b-c)].

The five governing control parameters of the electrospinning process selected for this experimental study were V, C, S, D, and F in Table 3.11. These control factors were varied at three different levels of  $X_1$ ,  $X_2$ , and  $X_3$ .

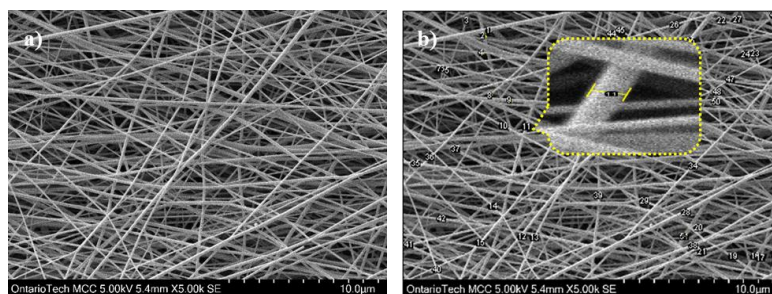


Figure 3.22: SEM micro-graphs (Scale 10 $\mu$ m at 5000X) of: (a) PVDF based electro-spun nanofibers and (b) Fiber diameter measurements.

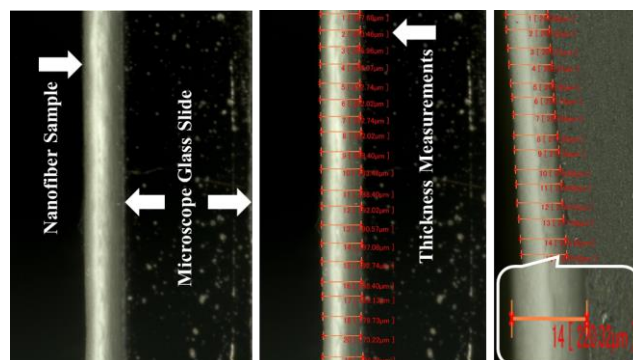


Figure 3.23: Microscopic images of; (a) Membrane sample, (b) Thickness calculation at different spots, and (c) Exploded view of measurements.

Table 3.11: Electrospinning process parameters at different control levels.

Symbol	Parameters	Units	Level 1: X <sub>1</sub>	Level 2: X <sub>2</sub>	Level 3: X <sub>3</sub>
V	Voltage	KV	14	18	22
C	Polymer Concentration	Wt.%	20	22	25
S	Rotational Speed of Drum	RPM	500	1000	1500
D	Needle Tip-Collector Distance	cm.	10	13	15
F	Solution Flow Rate	ml./h.	0.6	0.8	1

### 3.8.3 Results and Discussion

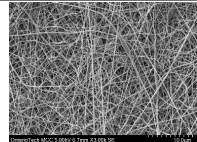
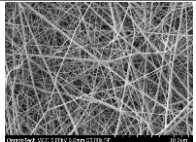
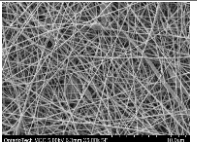
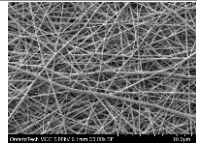
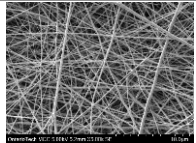
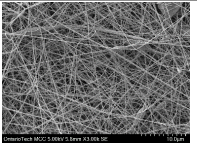
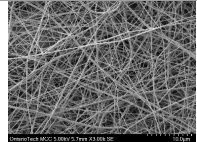
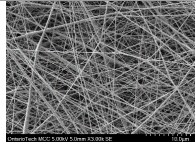
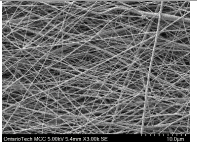
#### 3.8.3.1 Morphological Characterization of Electro-Spun PVDF Fibers

The electro-spun PVDF nanofibers fabricated at different levels of electrospinning variables possess distinctive morphological features. The characterization of fiber morphology and features were examined using SEM micro-graphs taken at different experimental trials. Table 3.12 demonstrates the morphological attributes of nine different samples produced at varying levels of electrospinning factors. PVDF nanofibers fabricated

at reported variables possess a random arrangement of smooth and long nanofibers with the very least appearance of conventional bead deformity. The corresponding description also illustrates the average fiber diameter, thickness, and weight measurement values. The visual representation of the fibers shows that the average fiber diameter value increases with the increase in PVDF concentration at all levels of voltage and feed rate. The highest diameter value of  $0.192\mu\text{m}$  was observed at the highest weight percentage concentration of 25. Thus, the polymer concentration predominantly affects the diameter shape and size of the produced fibers. On the contrary, the high voltage variation results in diameter fluctuations in a random fashion, making it a non-significant parameter in diameter regulation. Lower concentration of 20wt.% with a voltage varying from 14KV to 22KV results in thin and smooth fibers. The presence of sturdy and thin fibers was reported at higher concentrations (C3: 25wt.%), resulting in broader fiber distribution comparatively with variation from 14 to 22 KV's.

The morphological attributes of the fibers were significantly affected by polymer concentration because the associated viscoelastic force of the solution varies with concentration. The solution has to overcome this force to split up in the forms of fibers under the influence of columbic repulsion forces generated due to the electrostatic charge present in the jet. Generation of the deformities like beads or lumps is evident with very low concentration wherein the viscous force is not adequate for droplet elongation or stretching. Conversely, at very high concentrations, the polymer solution flow reduces significantly due to higher viscosities resulting in needle blockage at the tip [193,194]. The optimum polymer concentration with optimally increased viscoelastic force is required to generate smooth fibers where polymer jet stretching/elongation is dominant. The droplet gets away from the initial split-up (that results in beads of spraying) and repulsive force between the charges present in the polymer stream. The fiber diameter measurements increase with higher concentration variations, and the distribution broadens itself with voltage variation because of stretching force fluctuations on electro-statistically charged polymer stream [195,196]. The existence of a similar experimental phenomenon has been pointed out in few research works of literature studying the morphological effect of electrospinning parameters on polymeric fibers [193,194,197].

Table 3.12: SEM micro-graphs of PVDF nanofibers fabricated at different levels.

Polymer Concentration (PVDF)- Wt. %	High Voltage Supply - KV			PVDF Solution Feed Rate - ml/h
	V1: 14	V2: 18	V3: 22	
C1: 20	 0.135μm   356.84μm   0.1827g	 0.132μm   344.28μm   0.5111g	 0.142μm   353.67μm   0.3941g	F1: 0.6
RPM: 500 & Needle to collector Distance: 10cm				
C2: 22	 0.139μm   245.14μm   0.2956g	 0.173μm   405.76μm   0.6252g	 0.128μm   640.50μm   0.6367g	F2: 0.8
RPM: 1500 & Needle to collector Distance: 10cm				
C3: 25	 0.178μm   310.18μm   0.3813g	 0.192μm   340.37μm   0.6879g	 0.182μm   269.43μm   0.6441g	F3: 1.0
RPM: 1000 & Needle to collector Distance: 10cm				
*Average Fiber diameter - μm   Average Thickness - μm   Nanofiber Weight - g				

### 3.8.3.2 Design of Experiments (DOE) Using Orthogonal Array

The evaluation of five selective electrospinning parameters was carried out utilizing the ANOVA technique, and the corresponding data for such statistical analysis was obtained from Taguchi's design of experiment L27 configuration. The average measurements of fiber diameter, thickness, and nanofiber weight and respective standard deviations were reported in extreme right columns of Table 3.13. The average fiber diameter values computed in 27 experimental trials show that the minimum diameter of 0.112μm and 0.128μm was reported at 3rd, 11th, and 24th experimental trials with lower concentration level variation of X1 and X2. The least experimental value of 0.112μm with a standard deviation of 0.031 was reported at a PVDF concentration of 20wt.%, 14KV supply voltage, 1500 collector-drum RPM, 1ml/hr. solution feed rate and 15cm needle to drum collection distance. The average fiber diameter measurements were observed in the range of 0.112μm to 0.240μm. The nanofiber samples fabricated at these trials reached the highest thickness of 654.04μm with 13.59 standard deviation at the 22<sup>nd</sup> experimental trial. The maximum thickness was reported with the highest voltage level of 22KV, and a low concentration of 22wt.% (X2) with the respective rpm value of 500, 13cm distance, and 1ml/hr of feed rate. The experimental thickness values vary in the range of 40.39μm to

654.04 $\mu$ m. Maximum average thickness measurements were noticed broadly at a higher voltage of 22KV. Higher nanofiber weight values of 0.6879g, 0.6618g, and 0.6441g were observed in 17<sup>th</sup>, 27<sup>th</sup>, and 26<sup>th</sup> trials at higher levels of voltage and concentration variation X2 and X3. A maximum weight of 0.6879g was observed at 18KV's, 25wt.% PVDF concentration, 1000RPM, 13cm distance, and 1ml/hr. feed rate. It was generally observed that higher nanofiber weight measurements were observed at a higher voltage level.

Table 3.13: Experimental scheme for parametric analysis following Taguchi's orthogonal array (L-27) configuration.

Exp. Trial s	V	C	S	D	F	Fiber Diameter ( $\mu$ m)	Thickness ( $\mu$ m)	Nanofiber Weight (g)
1	14	20	500	10	0.6	0.135 $\pm$ 0.069	356.84 $\pm$ 04.85	0.1827
2	14	20	1000	13	0.8	0.138 $\pm$ 0.048	073.22 $\pm$ 02.83	0.1268
3	14	20	1500	15	1	0.112 $\pm$ 0.031	040.39 $\pm$ 04.28	0.0704
4	14	22	500	13	1	0.202 $\pm$ 0.131	141.20 $\pm$ 02.78	0.1389
5	14	22	1000	15	0.6	0.139 $\pm$ 0.059	94.77 $\pm$ 05.07	0.1351
6	14	22	1500	10	0.8	0.139 $\pm$ 0.056	245.14 $\pm$ 08.86	0.2956
7	14	25	500	15	0.8	0.160 $\pm$ 0.048	125.50 $\pm$ 03.89	0.1672
8	14	25	1000	10	1	0.178 $\pm$ 0.075	310.18 $\pm$ 06.69	0.3813
9	14	25	1500	13	0.6	0.157 $\pm$ 0.061	200.58 $\pm$ 13.53	0.2064
10	18	20	500	10	0.6	0.132 $\pm$ 0.072	344.28 $\pm$ 18.02	0.5111
11	18	20	1000	13	0.8	0.128 $\pm$ 0.048	213.80 $\pm$ 06.81	0.2850
12	18	20	1500	15	1	0.137 $\pm$ 0.048	310.49 $\pm$ 08.27	0.1992
13	18	22	500	13	1	0.144 $\pm$ 0.061	289.56 $\pm$ 05.44	0.3183
14	18	22	1000	15	0.6	0.198 $\pm$ 0.059	296.43 $\pm$ 07.83	0.2980
15	18	22	1500	10	0.8	0.173 $\pm$ 0.118	405.76 $\pm$ 02.83	0.6252
16	18	25	500	15	0.8	0.211 $\pm$ 0.115	333.65 $\pm$ 03.88	0.4672
17	18	25	1000	10	1	0.192 $\pm$ 0.107	340.37 $\pm$ 04.08	0.6879
18	18	25	1500	13	0.6	0.193 $\pm$ 0.102	329.68 $\pm$ 08.19	0.5021
19	22	20	500	10	0.6	0.142 $\pm$ 0.067	353.67 $\pm$ 11.37	0.3941
20	22	20	1000	13	0.8	0.176 $\pm$ 0.159	353.93 $\pm$ 04.05	0.3960
21	22	20	1500	15	1	0.169 $\pm$ 0.106	257.72 $\pm$ 08.94	0.4229
22	22	22	500	13	1	0.204 $\pm$ 0.126	654.04 $\pm$ 13.59	0.6236
23	22	22	1000	15	0.6	0.149 $\pm$ 0.053	452.45 $\pm$ 08.15	0.5301
24	22	22	1500	10	0.8	0.128 $\pm$ 0.042	640.50 $\pm$ 15.10	0.6367
25	22	25	500	15	0.8	0.240 $\pm$ 0.180	209.65 $\pm$ 04.10	0.5699
26	22	25	1000	10	1	0.182 $\pm$ 0.087	269.43 $\pm$ 19.89	0.6441
27	22	25	1500	13	0.6	0.194 $\pm$ 0.128	327.58 $\pm$ 04.73	0.6618



### 3.8.3.3 Evaluation of Electrospinning Parameters: ANOVA Study

The assessment of the selective electrospinning parameters and their importance on the output variables was investigated by employing the ANOVA technique on results obtained in preceding trials. This statistical analysis involves the evaluation of the mean output response received at discrete trails for single-level variation at a time. The ANOVA study described in Table 3.14 shows the parametric impact on the diameter size of PVDF nanofibers. The PVDF concentration was observed to be a significant factor that regulates the fiber diameter measurements. The respective F-test analysis confirms its significance at a higher confidence level of 99% with lower risk levels of 0.0027. The confidence and risk level of concentration factor was decided from the F and p values reported as  $F_C$  and  $p_C$  in the table where  $F_C > F_{2,16}$  (6.22) signifies 99% confidence and  $p_C < 0.01$  means higher significance at lower risk level. Contrastingly, other parameters like voltage, drum speed, distance, and feed rate were observed as non-significant parameters with minimal effect on the diameter values. The F-test values of these parameters were reported to be  $F_V$ : 2.36,  $F_S$ : 1.28,  $F_D$ : 0.96, and  $F_F$ : 0.31, which is lesser than the reported  $F_{2,16}$  – 90% confidence level value (2.66) [Table 3.14].

Table 3.14: ANOVA study for fiber diameter measurements.

ANOVA Study: Fiber Diameter ( $\mu\text{m}$ )											
V1	1.36	C1	1.269	S1	1.57	D1	1.401	F1	1.439	SS <sub>T</sub>	0.026449
V2	1.508	C2	1.476	S2	1.48	D2	1.536	F2	1.493		
V3	1.584	C3	1.707	S3	1.402	D3	1.515	F3	1.52		
SS <sub>V</sub>	0.002884	SS <sub>C</sub>	0.010669	SS <sub>S</sub>	0.001571	SS <sub>D</sub>	0.001173	SS <sub>F</sub>	0.000378	SS <sub>Error</sub>	0.009775
V <sub>V</sub>	0.001442	V <sub>C</sub>	0.005334	V <sub>S</sub>	0.000785	V <sub>D</sub>	0.000586	V <sub>F</sub>	0.000189	V <sub>Error</sub>	0.000611
$F_V$	2.359916	$F_C$	8.73129	$F_S$	1.285441	$F_D$	0.959716	$F_F$	0.309357		
$p_V$	0.1264	$p_C$	0.0027	$p_S$	0.3036	$p_D$	0.4040	$p_F$	0.7382		
F <sub>2,16</sub> @ 90% confidence level										2.66	
F <sub>2,16</sub> @ 95% confidence level										3.63	
F <sub>2,16</sub> @ 99% confidence level										6.22	

In Table 3.15, High voltage supply and collection distance were noticed to have a major effect on the thickness measurements but at different confidence levels. The F-test analysis validates the higher significance of the applied voltage at 99% confidence level [ $F_V > F_{2,16} - 99\%$  (6.22)] and lower risk factor [ $p_V < 0.01$ ]. On the other hand, the needle to collector surface distance was observed to be less significant than voltage comparatively, with a 90% confidence level [ $F_D > F_{2,16} @ 90\%$ ] with higher risk levels of 0.0676 [ $p_D > 0.05$ ] which indicates the non-significance of the respective parameter. The remaining three parameters, such as; concentration, RPM, and feed rate, were observed to have the minimal effect of thickness and were appeared to be insignificant with  $F_C$ ,  $F_S$ , and  $F_F$  values lower than 90% confidence level values.

Table 3.15: ANOVA study for average thickness measurements.

ANOVA Study: Thickness ( $\mu\text{m}$ )											
V1	1587.82	C1	2304.34	S1	2808.39	D1	3266.17	F1	2756.28	SS <sub>T</sub>	538635.3
V2	2864.02	C2	3219.85	S2	2404.58	D2	2583.59	F2	2601.15		
V3	3518.97	C3	2446.62	S3	2757.84	D3	2121.05	F3	2613.38		
SS <sub>V</sub>	214332.8	SS <sub>C</sub>	53936.55	SS <sub>S</sub>	10755.94	SS <sub>D</sub>	73746.61	SS <sub>F</sub>	1653.159	SS <sub>Error</sub>	184210.2
V <sub>V</sub>	107166.4	V <sub>C</sub>	26968.27	V <sub>S</sub>	5377.971	V <sub>D</sub>	36873.31	V <sub>F</sub>	826.5796	V <sub>Error</sub>	11513.14
F <sub>V</sub>	9.308187	F <sub>C</sub>	2.342392	F <sub>S</sub>	0.467116	F <sub>D</sub>	3.202716	F <sub>F</sub>	0.071794		
p <sub>V</sub>	0.0021	p <sub>C</sub>	0.1282	p <sub>S</sub>	0.6351	p <sub>D</sub>	0.0676	p <sub>F</sub>	0.9310		
F <sub>2,16</sub> @ 90% confidence level										2.66	
F <sub>2,16</sub> @ 95% confidence level										3.63	
F <sub>2,16</sub> @ 99% confidence level										6.22	

As shown in Table 3.16, three control variables, high voltage, PVDF concentration, and distance, were observed to be the most significant factors that significantly affect the weight of the PVDF nanofiber membrane produced at reported experimental trials. The F-test study based on statistical summation confirms the highest significance of these three variables at 99% confidence level and lowest risk levels of  $p < 0.001$ . The corresponding F-test values;  $F_V$  (51.00 approx.),  $F_C$  (14.11), and  $F_D$  (11.63) were reported to be considerably greater than  $F_{2,16} @ 99\%$  confidence level. The associated lowest risk

levels;  $p_v$ ,  $p_c$ , and  $p_D$  signifies higher statistical significance. The other factors like collector speed and solution feed rate demonstrate the least effect on nanofiber weight with measurements of  $F_s$  and  $F_F$  considerably lower than  $F_{2,16}$  @ 90%.

Table 3.16: ANOVA study for membrane weight (g) measurements.

ANOVA Study: Weight (g)											
V1	1.7044	C1	2.5882	S1	3.373	D1	4.3587	F1	3.4214	SS <sub>T</sub>	0.97994
V2	3.894	C2	3.6015	S2	3.4843	D2	3.2589	F2	3.5696		
V3	4.8792	C3	4.2879	S3	3.6203	D3	2.86	F3	3.4866		
SS <sub>V</sub>	0.586827	SS <sub>C</sub>	0.162478	SS <sub>S</sub>	0.003409	SS <sub>D</sub>	0.133881	SS <sub>F</sub>	0.001226	SS <sub>Error</sub>	0.092119
V <sub>V</sub>	0.293413	V <sub>C</sub>	0.081239	V <sub>S</sub>	0.001704	V <sub>D</sub>	0.06694	V <sub>F</sub>	0.000613	V <sub>Error</sub>	0.005757
F <sub>V</sub>	50.96237	F <sub>C</sub>	14.11022	F <sub>S</sub>	0.296045	F <sub>D</sub>	11.62675	F <sub>F</sub>	0.106475		
p <sub>V</sub>	0.0001	p <sub>C</sub>	0.0003	p <sub>S</sub>	0.7477	p <sub>D</sub>	0.0008	p <sub>F</sub>	0.8996		
F <sub>2,16</sub> @ 90% confidence level										2.66	
F <sub>2,16</sub> @ 95% confidence level										3.63	
F <sub>2,16</sub> @ 99% confidence level										6.22	

#### 3.8.4.4 Effect of Electrospinning Designed Parameter on Fiber Diameter, Weight and Thickness of Electro-Spun Membrane

The graphical plot of the average fiber diameter summation measurements with respect to electrospinning variables at each level variation is demonstrated in Figure 3.24. The summation points displayed in the graph represent every single fiber diameter measurement at that respective level of the parameter in consideration. The diameter output response was observed to have the highest variation with the change in PVDF concentration levels from C1 to C3, indicating the higher significance of the concentration factor over the other variables comparatively. The summation points also suggest that the lower fiber diameter measurements can be achieved at a lower concentration level (C1) as diameter increases with an increase in PVDF concentration. Additionally, the difference between the maximum and minimum control level summation points further validates the variable significance and its effect on output response. A higher difference of 0.44 for

polymer concentration variation was noted when compared with other parameters at the difference of 0.224 (V), 0.168 (S), 0.114 (D), and 0.081 (F).

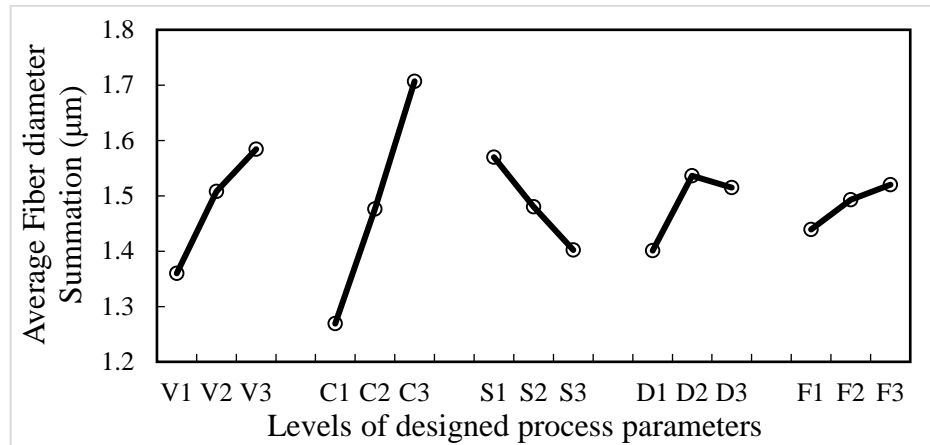


Figure 3.24: Significant effect of electrospinning process variables on average fiber diameter

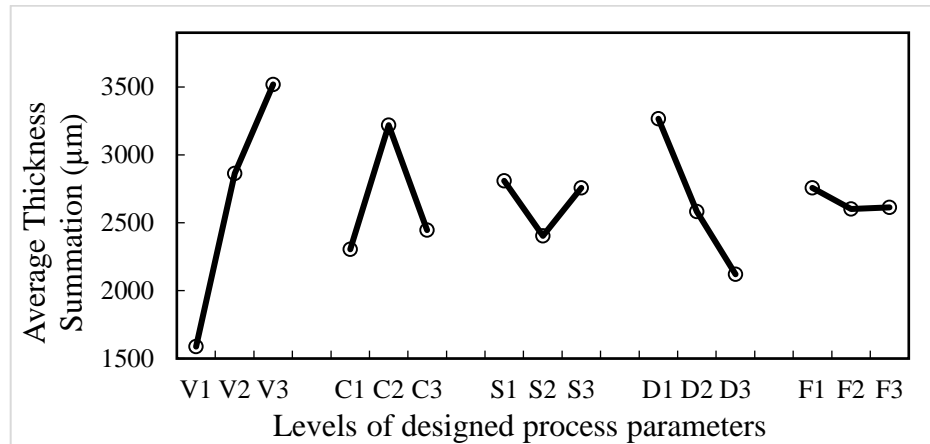


Figure 3.25: Significant effect of electrospinning process variables on the average thickness

As shown in Figure 3.25, The thickness summation spots reveal the highest variability for the two factors, high voltage (V) and distance (D). It indicates the higher significance of these two parameters on thickness measurements over the other factors with lower variability. The summation points clarify that the thickness values increase with an increase in voltage supply. On the contrary, an opposite trend was observed with collection distance. The thickness was increasing with a decrease in the distance, which means a closer needle position to the collector surface at higher voltages will provide more fiber accumulation leading to a high thickness of nanofiber membranes. A higher difference between the

extreme level summation point of voltage (V: 1931.15) and collection distance (D: 1145.12) confirms the substantial effect on thickness value. On the contrary, the difference of 142.28, 50.55, and 142.90 was observed for concentration, rotation speed, and feed rate, demonstrating the least effect of these parameters on output response.

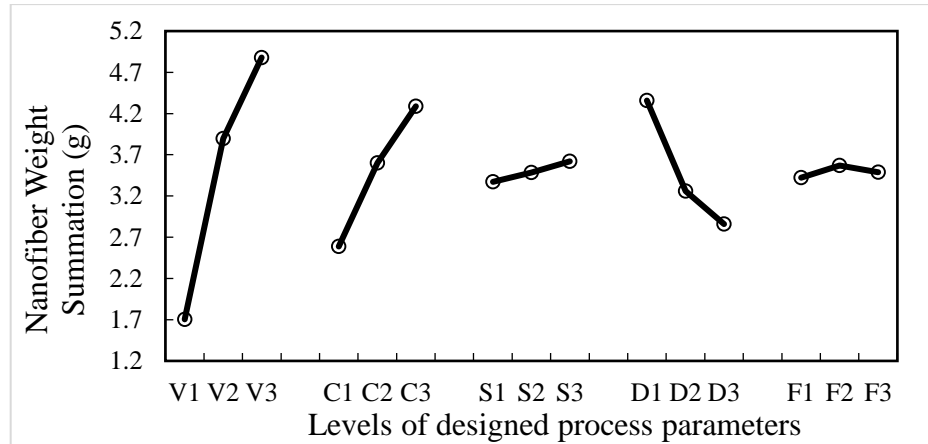


Figure 3.26: Significant effect of electrospinning process variables on PVDF nanofiber membrane

Stronger influence of three factors: voltage (V), concentration (C), and distance (D), was clearly reported with higher variability of the summation points at different levels of control factor in Figure 3.26. The nanofiber weight of the PVDF-based membrane was reported to increase with an increase in voltage and concentration level. In contrast, the decrease in needle point to collector surface distance resulted in higher weight measurements. Furthermore, the higher difference at extreme points of level variation confirms the higher significance of these factors (V: 3.17, C: 1.69, and D: 1.49), whereas the other parameters remain to have a lower weight effect with the lower difference of 0.25 (S) and 0.06 (F).

### 3.8.3.5 Electrospinning Process Modelling Using RSM

Multiple regression techniques were used in investigating the significance of individual factors influencing the output response of PVDF nanofiber diameter, thickness, and weight. The mathematical model was developed for the three individual responses using RSM to predict the accuracy of the electrospinning model. The study investigates the effect of five parameters with three levels, leading to  $3^5 = 243$  trials for the complete analysis, but orthogonal array design reduces it to 27 trials. The mathematical model

developed for the single effect of the process variables on output response (fiber diameter, thickness, and weight) is represented by the following three Equations [3.15 – 3.17];

$$\text{Fiber Diameter} = -0.72211 + 0.01211V + 0.03623C - 0.00002S + 0.03336D + 0.0825F - 0.00025V^2 - 0.00058C^2 - 0.00123D^2 - 0.0375F^2 \quad (3.15)$$

$$\text{Thickness} = -8286.0415 + 104.4778V + 718.6601C - 0.3421S - 23.3675D - 411.6055F - 2.1571V^2 - 15.8999C^2 + 0.0001S^2 - 0.0831D^2 + 232.4444F^2 \quad (3.16)$$

$$\text{Weight} = -4.9069 + 0.1946V + 0.3156C + 0.00002S - 0.1261D + 0.5318F - 0.0041V^2 - 0.0062C^2 + 1e^{-8}S^2 + 0.00372D^2 - 0.32111F^2 \quad (3.17)$$

The average model accuracy of the model can be calculated as follows:

$$\text{Accuracy (A)} = [1 - \text{ABS} \frac{(Y_{\text{exp.}} - Y)}{Y_{\text{exp.}}}] * 100 \quad (3.18)$$

The graphical representation shown in Figures 3.27, 3.28, and 3.29 compares the mathematical model with the experimental results to analyze the model accuracy of three outputs. The average model accuracy of 90.8%, 71.0%, and 84.0% were obtained for the entire experimental trials, whereas a model accuracy of (90-98) % was observed for the few individual runs. The calculated average accuracy is considered as the acceptable range for model verification. The three-dimensional surface and contour plots were developed using these RSM models [Appendix (D3)].

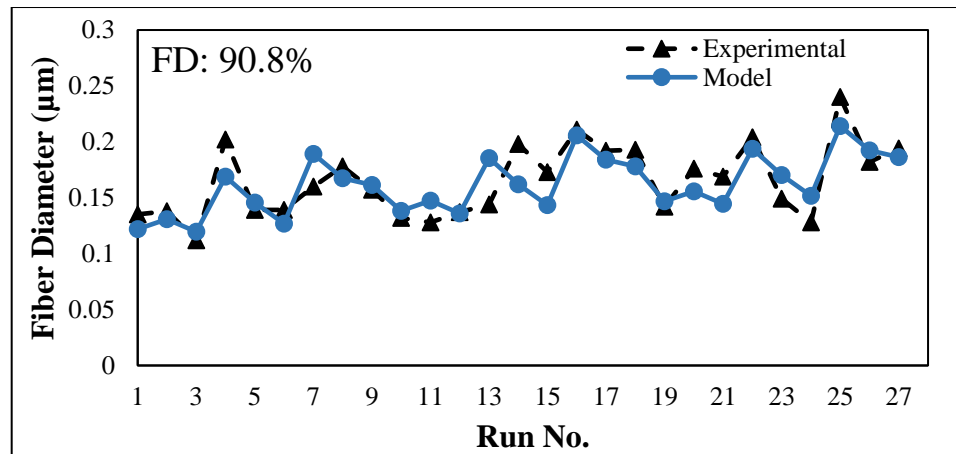


Figure 3.27: Mathematical model validation with experimental results for PVDF nanofiber diameter measurements.

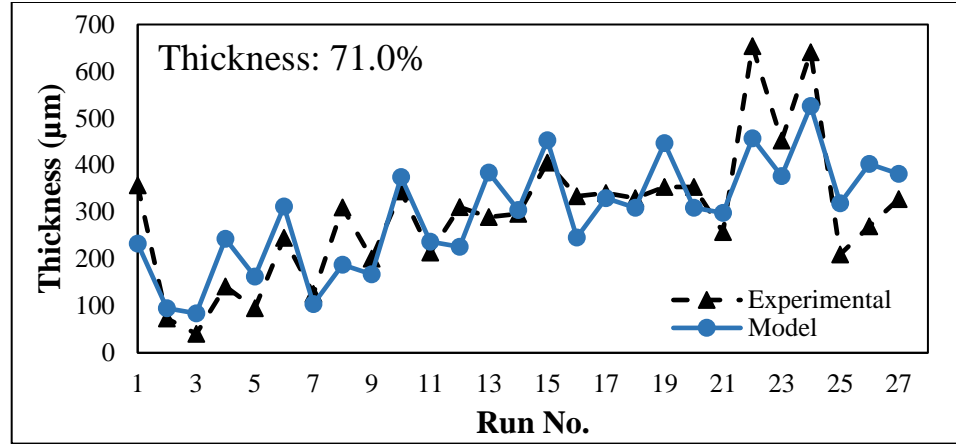


Figure 3.28: Mathematical model validation with experimental results for PVDF membrane thickness measurements.

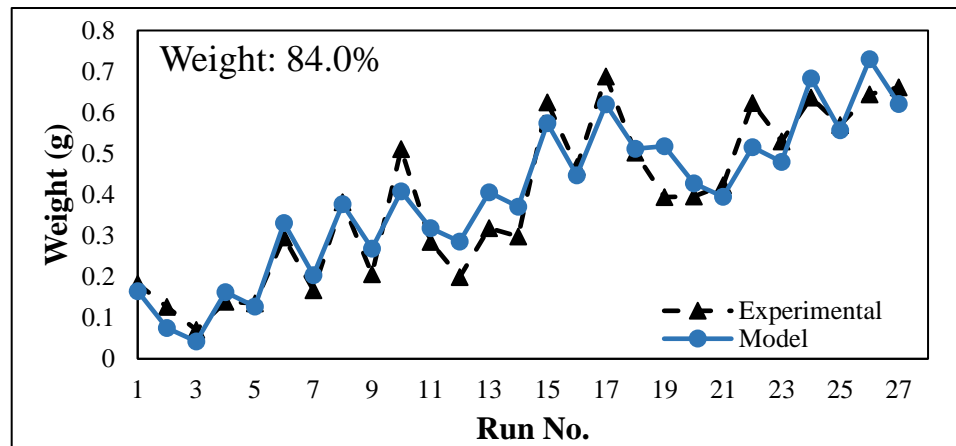


Figure 3.29: Mathematical model validation with experimental results for PVDF membrane weight measurements.

### 3.8.3.6 Electrospinning Process Modelling Using GP

GP was used to empirically model the fiber diameter, thickness, and nanofiber weight. Equation 3.19 shows the developed model for the fiber diameter. It can be noticed that a good agreement was found between the experimental and predicted results. The average model accuracy for the fiber diameter model was about 92.8% [Figure 3.30]. Equation 3.20 shows the developed model in terms of membrane thickness, where an average accuracy of 86.7% was noticed [Figure 3.31]. Regarding the nanofiber weight, an acceptable agreement has been noticed with an average model accuracy of almost 80% [Figure 3.32]. The developed model for the nanofiber weight is provided in Equation 3.21.

$$\text{Fiber Diameter} = 0.2135 + 0.0411 * E + 0.0013 * A * D + -0.0499 * E / C + 1.6135 e^{-7} * C * B^2 - 0.0101 * D - 0.0127 * A - 8.3543 e^{-6} * C * D \quad (3.19)$$

$$\text{Thickness} = 25297.7783 + 2591.1964 * A + 1.1508 * B^3 + -37584.5145 * A / B - 34.6556 * D - 1710.4827 * B - 1.7251 * A * B^2 \quad (3.20)$$

$$\text{Weight} = 0.1045 * A + 10.5551 / D + 0.0022 * A * D + 0.0021 * A * B + 8.9782 e^{-6} * A * C - 2.3849 - 0.0002 * C - 0.0039 * A^2 \quad (3.21)$$

The three-dimensional surface and contour plots were developed using these GP models [Appendix (D4)]. The optimization criteria and S/N ratio conversion is provided in Appendix E.

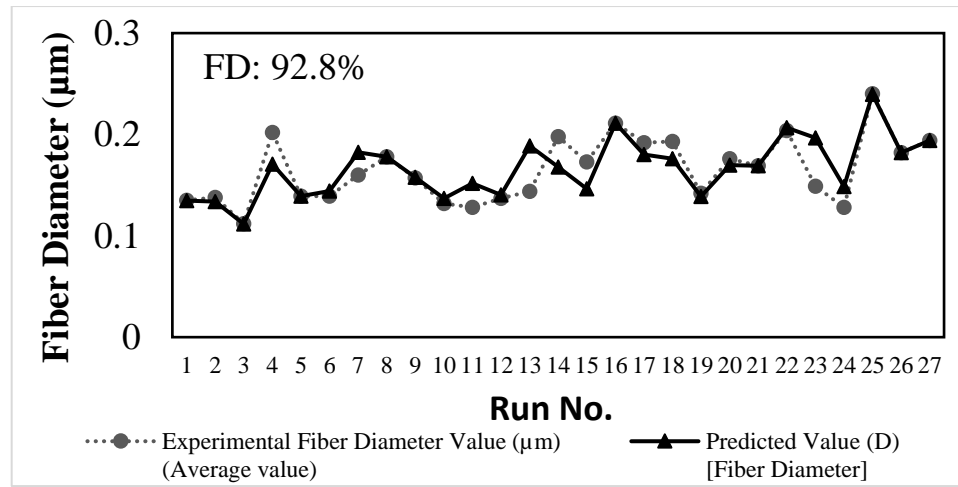


Figure 3.30: Experimental fiber diameter value versus modeled value at 27 trials.

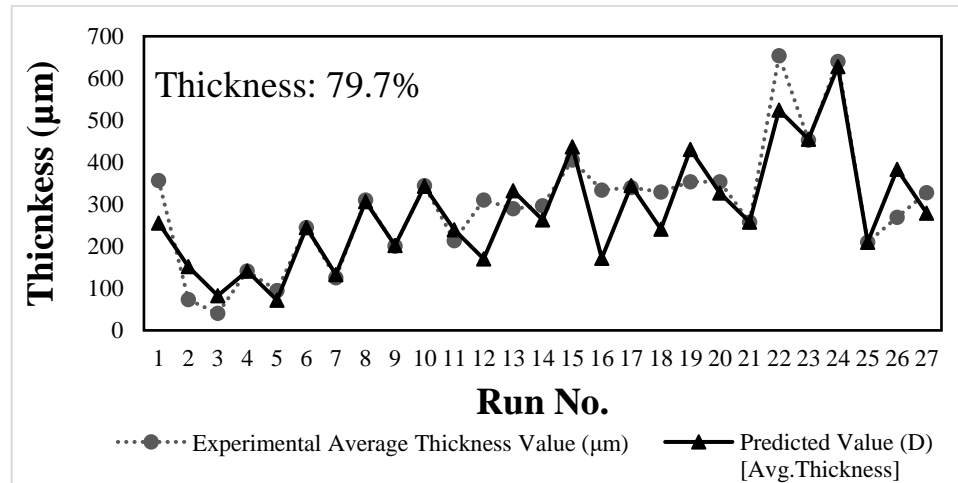


Figure 3.31: Experimental thickness value versus modeled value at 27 trials.



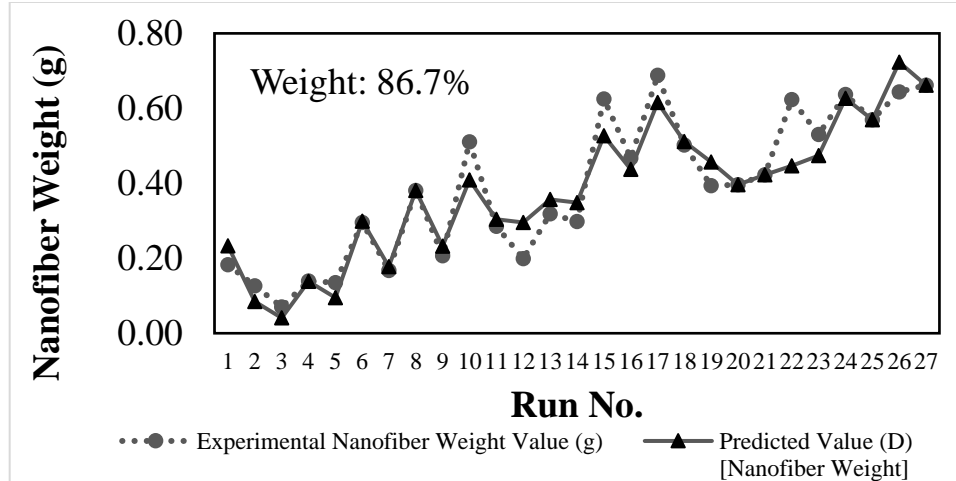


Figure 3.32: Experimental weight value versus modeled value at 27 trials.

### 3.8.4 Conclusions

In this experimental study, PVDF nanofibers was manufactured by employing an electrospinning technique wherein the parametric assessment of the control parameters was carried out utilizing Taguchi's orthogonal array design. The experimental investigation of five selected parameters was executed at three different variation levels with an L27 design. Parametric assessment utilizing statistical methodologies was performed to study the effect of electrospinning variables on fiber diameter, thickness, and weight as output response. PVDF nanofibers obtained trials had the diameter in the range of  $0.112\mu\text{m} - 0.240\mu\text{m}$ , thickness in the range of  $40.39\mu\text{m} - 654.04\mu\text{m}$ , and weight in the range of  $0.0704\text{g} - 0.6879\text{g}$ . According to the ANOVA study, PVDF concentration was observed to be the significant factor regulating the fiber diameter at a 99% confidence level (Risk level: 0.0027). On the contrary, the average thickness of membranes was controlled by the input high voltage at a 99% confidence level (Risk level: 0.0021). Nanofiber weight measurements of the respective membranes were observed to be controlled by three significant factors; concentration, voltage, and distance at a 99% confidence level with respective risk levels of 0.0001, 0.0003, and 0.0008. Mathematical models generated using RSM resulted in average model accuracy of 90.8%, 70.1%, and 84.0%. The empirical model developed using GP for three designed output responses was observed with higher average model accuracies of 92.8% (fiber diameter), 86.7% (thickness), and 80% (weight) when compared with RSM, which indicates the acceptable range for model verification.

## Chapter 4. Sound Absorption Performance of Nanofiber Composites

### 4.1 Introduction

The sound absorption performance of pure and filler infused fiber membranes was investigated at different back cavities and layering patterns. Fiber membranes were manufactured from two different polymeric bases: PVP and PVDF. When the plane sound waves interact with these fibers-based membranes or layers, the air molecules surrounding the fibers vibrate. The vibration causes the movement between the pores and fiber, resulting in sound energy loss to heat. The energy dissipation leads to absorption of sound and is measured in terms of sound absorption coefficient ( $\alpha$ ). The coefficient measurements of several combinations of PVP and PVDF-based membranes were studied in this section.

Different filler like CNT, GN, FS, FG, and MC were used to manufacture membranes composites. These small particles stick to the fiber structure and modify the surface cover for acoustic wave interaction. The effect of different types of fillers added to the polymeric base fibers was investigated in this section. Filler-loaded fiber membranes manufactured at different concentrations possess unique tortuous structures. These membranes were further layered in various patterns to improve sound absorption in lower frequency range.

### 4.2 Sound Absorption Characteristics of PVP Fibers and Its Composites

#### 4.2.1 Acoustic Sample Formulation

The acoustic ready samples of electro-spun PVP fiber membranes were prepared in the following layering order, a) Single membrane, b) Two membranes, c) Four membranes, d) Eight membranes, e) Sixteen membranes, and f) Twenty membranes. The composites were tested at different Back Cavities (BC's) of 0cm, 3cm, and 5cm [Figure 4.1 (a-b)].

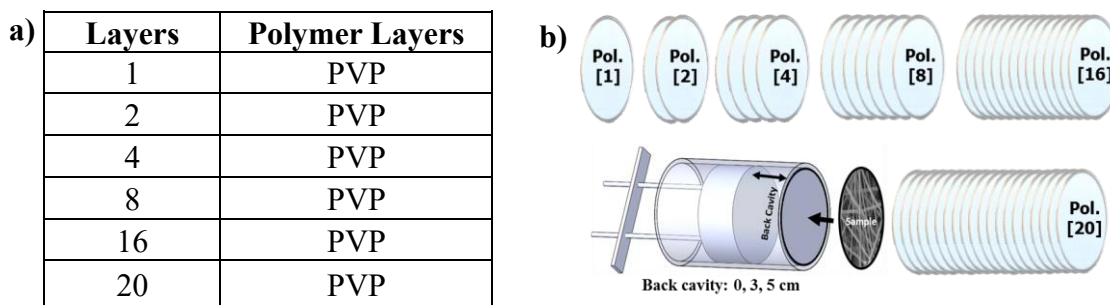


Figure 4.1: a) PVP membrane layering order and b) Schematics of layering pattern.

#### 4.2.2 Sound Absorption Performance (SAP) of Single PVP Fiber Membrane

The SAP of a single PVP membrane tested in the frequency range of 99Hz to 2000Hz at different back cavities is shown in Figure 4.2 (a). Schematic description of layering arrangement and cavity variation is displayed in Figure 4.2 (b). Lower coefficient values less than 0.3 were observed with the single thin membrane of 356.64 $\mu$ m thick in the entire frequency range when the specimen was touching the piston surface inside the tube unit, i.e., with 0cm BC. Sharp absorption peaks were observed with the increase in BC to 3cm, wherein the sample is not touching any surface from both sides. The maximum absorption peak was observed with an  $\alpha$  value of 0.8 at 1159Hz of frequency and other small peaks at different frequencies. Furthermore, the peak appearances increased with an increase in BC to 5cm in the low-frequency range. Higher coefficient values of 0.7, 0.6, and 0.7 were noticed at multiple frequencies of 748, 1036, and 1698Hz.

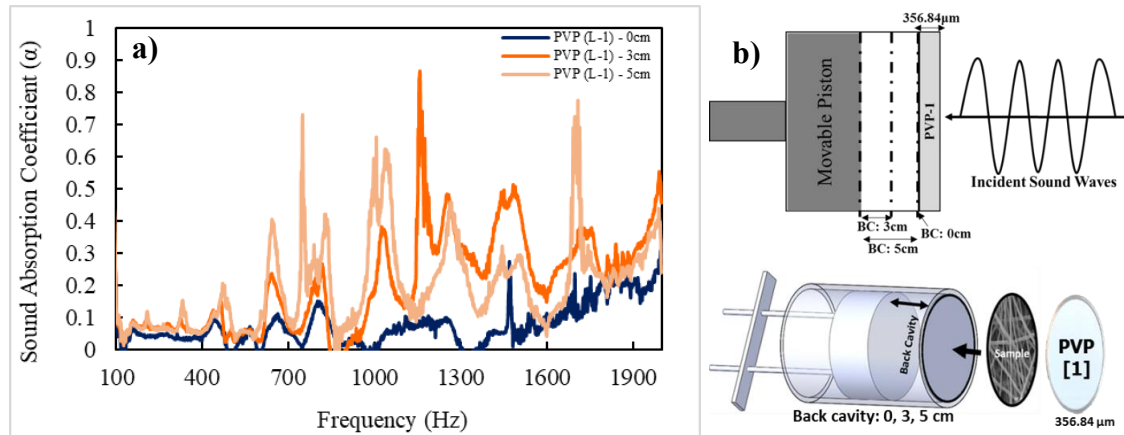


Figure 4.2: a) Sound absorption coefficient of single PVP fiber membrane at three discrete BC's and b) Schematics of layering configuration.

Sharp absorption peak occurrence with a high coefficient due to increased BC can be attributed to the fiber membrane's relative thickness. This traditional methodology of integrating air cavity is an economical approach for improving low-frequency absorption [198]. The vibration of air molecules and fiber surface with the sound wave propagation dissipates energy resulting in sound absorption. The wave interaction with fiber cover doesn't occur efficiently when the specimen is placed in surface contact with the piston wall, i.e., 0cm BC. The BC provides room for the membrane to vibrate and dissipate energy, resulting in better SAP. Multiple sharp peaks with thin specimens can be due to the

resonant frequency of the membranes [199]. These peaks are the classic response of thin, flexible fiber membranes, and the absorption value depends on the discrete frequency.

### 4.2.3 SAP of Multiple Layers of PVP Membrane at 3 Discrete BC

#### 4.2.3.1 SAP of Two Layers

The sound absorption coefficient of two combined layers of PVP membranes was determined at different BC's in Figure 4.3 (a-b). The twin layered composite was observed with the lower coefficient less than 0.3 with 0cm BC for the entire frequency range. The coefficient reached to the maximum of 0.55, enveloping the broader frequency range from 1000–1200Hz at 3cm BC. Absorption coefficient ranging from 0.45 – 0.50 was observed to be shifted towards a lower frequency range of 700-1000Hz with further increase in BC to 5cm. The combined thickness of the material was 538 $\mu$ m which was higher than the single membrane. Layering combinations of twin layers resulted in the disappearance of multiple sharp peaks that occurred due to the resonance effect with a single membrane. The effect decreases with a higher value of thickness and specific mass [200]. Low-frequency absorption depends significantly on the material thickness, wherein the coefficient increases with thickness, but the effect is minor for high-frequency absorption [201]. The absorption peak shift towards the lower frequency range was observed with a higher BC due to increased thickness and higher energy interaction of low-frequency waves [118].

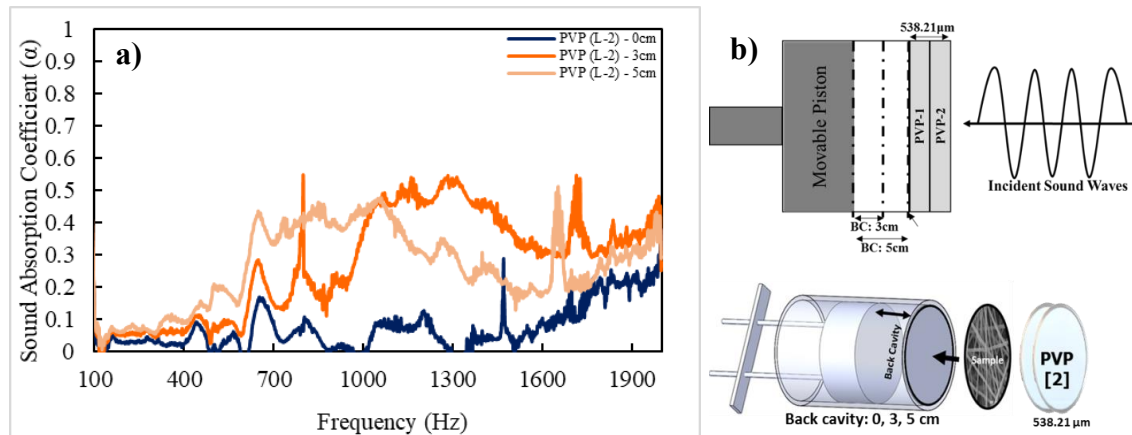


Figure 4.3: a) Sound absorption coefficient of two layers of PVP fiber membranes at three discrete BC's and b) Schematics of layering configuration.

#### 4.2.3.2 SAP of Four Layers

The acoustic response of the four layers of PVP membrane composite stacked in surface contact with each other is shown in Figure 4.4 (a-b) for discrete BC's. The composite of thickness 914 $\mu$ m was observed with a very low coefficient less than 0.3 for the entire frequency range with 0cm BC. On the other hand, bell-shaped absorption peaks were marked with a maximum coefficient value of 0.88 at 1053Hz frequency with increased BC to 3cm. A higher absorption peak was shifted towards a lower frequency of 733Hz with a maximum coefficient of 0.72 as the BC increased to 5cm. The SAP of the four-layered composite was observed to be improved compared with the previous composites. The improvement could be attributed to the higher thickness of membrane comprising nanofibers that increases low-frequency wave energy interaction. The increased tortuosity of the designed composite favors higher interaction with fibers and respective pores, which increases energy dissipation due to frictional losses [202].

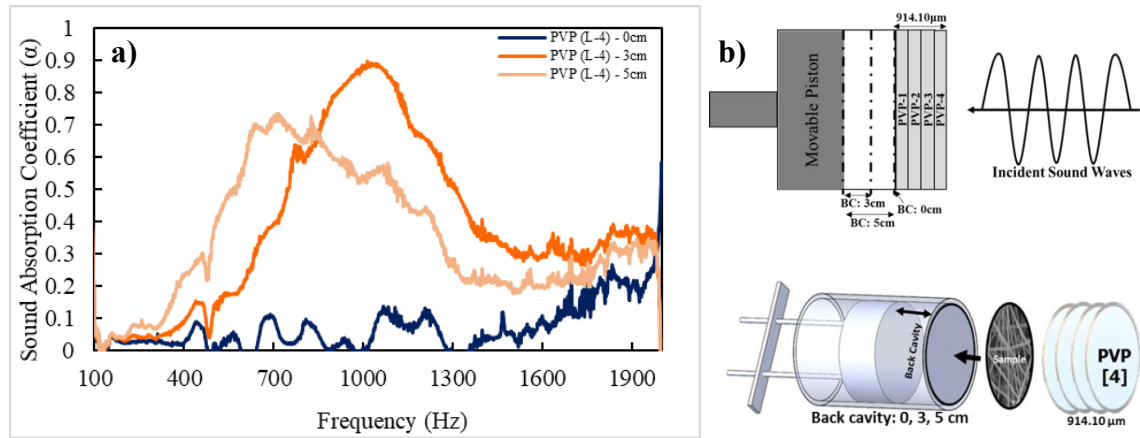


Figure 4.4: a) Sound absorption coefficient of four layers of PVP fiber membranes at three discrete BC's and b) Schematics of layering configuration.

#### 4.2.3.3 SAP of Eight Layers

The progressive layering of the PVP fiber membrane was carried out to improve the SAP in the low-frequency range. The SAP of eight layered composite of 2028.51 $\mu$ m thickness was investigated at different BC's in Figure 4.5 (a-b). The sound absorption coefficient for 0cm BC resulted in a similar absorption phenomenon as preceding samples ( $\alpha < 0.3$ ). A maximum coefficient of 0.87 was observed at lower frequencies of 700-750Hz with an increase in BC to 3cm. The BC supplement of 5cm resulted in a higher coefficient

value of 0.83 at a reduced frequency of 550Hz. The phenomenon of maximum absorption peaks shifting towards the lower frequency side, with the same coefficient value, was evident with higher back cavities and layer thicknesses. The fiber activation and air-induced vibrations between the layers increase with higher layers, leading to the entrapment of sound waves that further increases the visco-thermal losses [202].

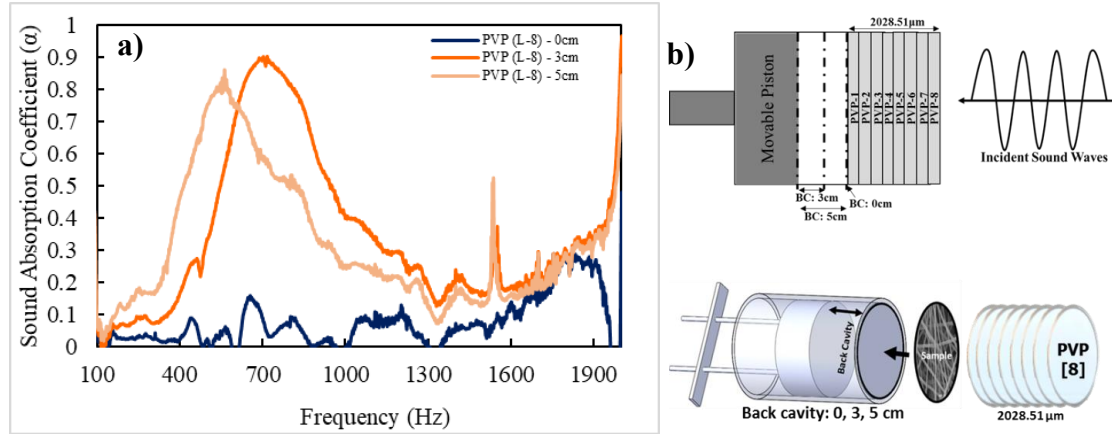


Figure 4.5: a) Sound absorption coefficient of eight layers of PVP fiber membranes at three discrete BC's and b) Schematics of layering configuration.

#### 4.2.3.4 SAP of Sixteen Layers

The SAP of sixteen layered stacked composite was investigated at the designed BC's in Figure 4.6 (a-b). A higher coefficient value of 0.93 at a frequency of 1695Hz was observed at 0cm BC. The acoustic performance of the current sixteen layered composite was remarkably high compared with the preceding two, four, and eight-layered composites. The substantial increase in coefficient value of the composite is mainly due to increased thickness of 3688  $\mu$ m and weight 3.5g of the specimen. A higher absorption coefficient of 0.98 was achieved at a lower frequency of 537Hz that appeared with a bell-shaped absorption peak at 3cm BC. With the BC extension to 5cm, the highest absorption coefficient value of 0.985 was observed at a lower frequency of 400Hz. The sixteen layered specimen resulted in the highest acoustic performance at a lower frequency range. The absorption curve shifted from 537Hz to 400Hz with the highest coefficient value of 0.985. With the increase in the electro-spun layers, the sound wave propagation passage through these high surface cover nanofibers increases, which in turn increases the energy loss by contact friction [203].

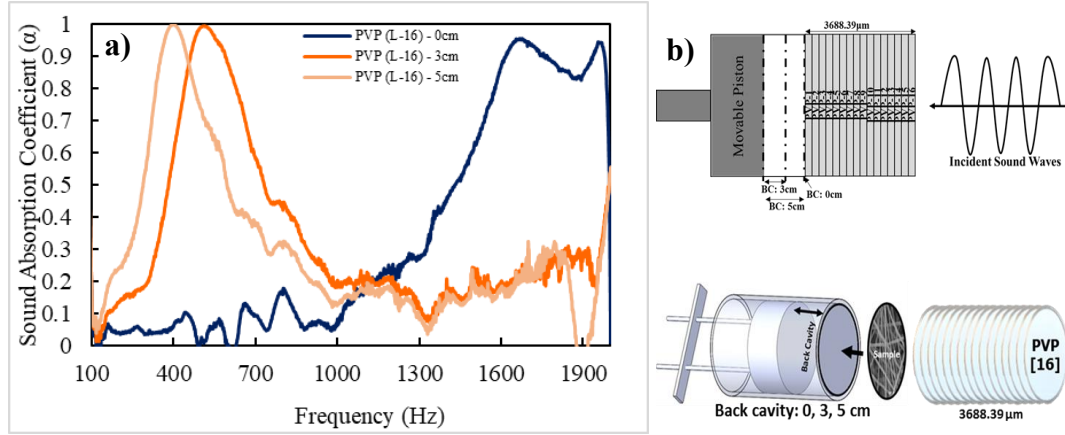


Figure 4.6: a) Sound absorption coefficient of sixteen layers of PVP fiber membranes at three discrete BC's and b) Schematics of layering configuration.

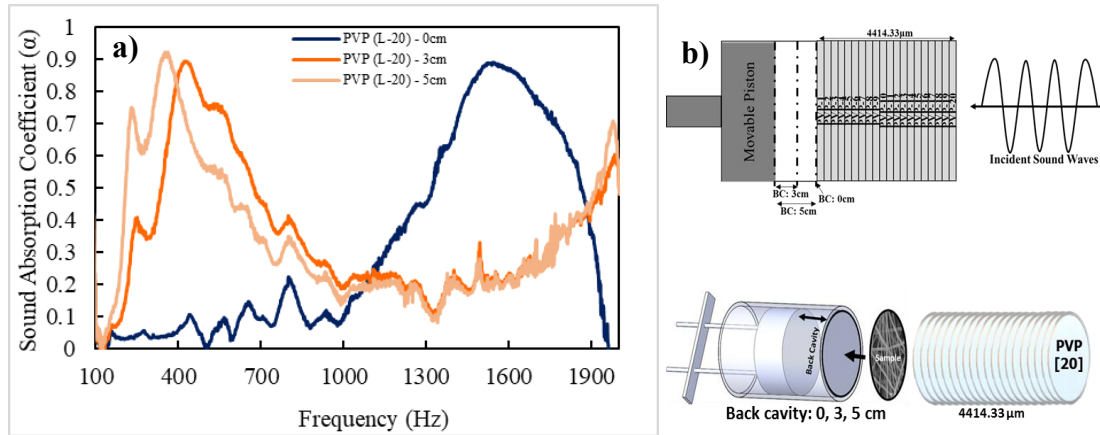


Figure 4.7: a) Sound absorption coefficient of twenty layers of PVP fiber membranes at three discrete BC's and b) Schematics of layering configuration.

#### 4.2.3.5 SAP of Twenty Layers

The SAP of the twenty-membrane layered composite was investigated at different BC's in Figure 4.7 (a-b). A maximum coefficient value of 0.88 was observed at 1560Hz at 0cm BC. The absorption coefficient value reduced from 0.9 to 0.88 compared with a sixteen layered composite, whereas the peak shifted from 1695Hz to 1560Hz. With the BC extension to 3cm, a maximum coefficient of 0.87 was observed at a significantly lower frequency of 390Hz. The acoustic behavior of these thin (4414 $\mu\text{m}$ ) and light weighted (4.4g) membrane composite was observed to be exceptionally better than preceding composites in the lower frequency range. The maximum absorption coefficient of 0.9 was



achieved at a frequency of 368Hz with a BC of 5cm. The curve was also observed with a secondary peak and a coefficient of 0.73 at even a lower frequency of 236Hz.

#### 4.2.3.6 Sound Absorption Coefficient Variation with Change in Thickness at Different Frequency Bands (1/3 Octave Plots)

The graphical plot of sound absorption coefficient percentage increase with the variation in thickness of layered membrane from 356.34 $\mu$ m to 4414.33 $\mu$ m was investigated at the discrete frequency band of 1/3 octave plots [Figure 4.8]. The coefficient variation and absorption peak shift regarding the thickness variation was studied using this analysis at different BC's [Table 4.1].

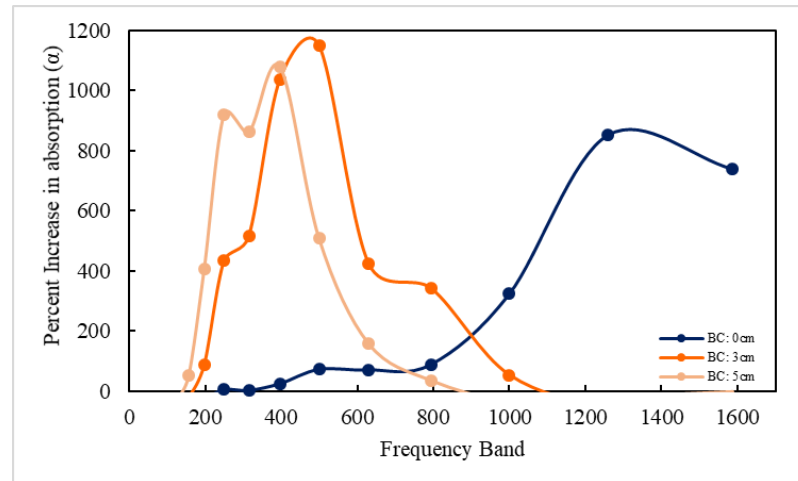


Figure 4.8: Sound absorption coefficient percent increase with thickness variation at discrete BC's for PVP layers.

Table 4.1: Percentage increase data for different frequency bands (1/3 - Octave plot).

BC	Percent increase in $\alpha$ at discrete octave frequency (Hz)											
	125	157	198	250	315	397	500	630	794	1000	1260	1587
0cm	-99	-34	-27	5	2	25	72	70	89	324	854	739
3cm	-70	-21	88	434	515	1038	1148	424	342	54	-46	-27
5cm	-32	51	408	921	862	1080	508	159	36	-32	-19	-1

The experimental investigation on SAP shows that the absorption peaks shifted towards the lower frequency region, maintaining the higher coefficient values, increasing the BC and thickness. In the case of 0cm BC, an increase of 853% was observed at a frequency of 1587Hz. The highest percentage improvement of 1148% was noticed for 3cm BC at a lower frequency band of 500Hz. In the case of 5cm BC, 50.81%, 408.39%,



921.41%, and 1079.57%, improvement was observed at lower frequencies of 157Hz, 198Hz, 250Hz, and 397Hz. The absorption peaks of the bell-shaped structure can be regulated persistently by tuning the composite material thickness and adjusting the BC. The peak shift in the low-frequency zone was reported following the same phenomenon reported in other works [202]. At 0cm BC, the absorption peaks drifted from 2000Hz to 1560Hz at higher thicknesses with a 0.9  $\alpha$ -value. A substantial peak shift from 1155Hz to 390Hz with 0.88  $\alpha$ -value was observed at 3cm BC. Additional BC extension of 5cm resulted in a noteworthy peak shift with 0.9  $\alpha$ -value to the lowest frequency of 366 Hz.

### 4.3 Sound Absorption Characteristics of PVDF Fibers and Its Composites

#### 4.3.1 Acoustic Sample Formulation

The acoustic ready specimens of PVDF-based composites were fabricated in the following order; a) Single membrane, b) Double layer composite, c) Four-layer composite, d) Eight-layer composite, e) Sixteen-layer composite, and d) Twenty-layer composite [Figure 4.9 (a-b)].

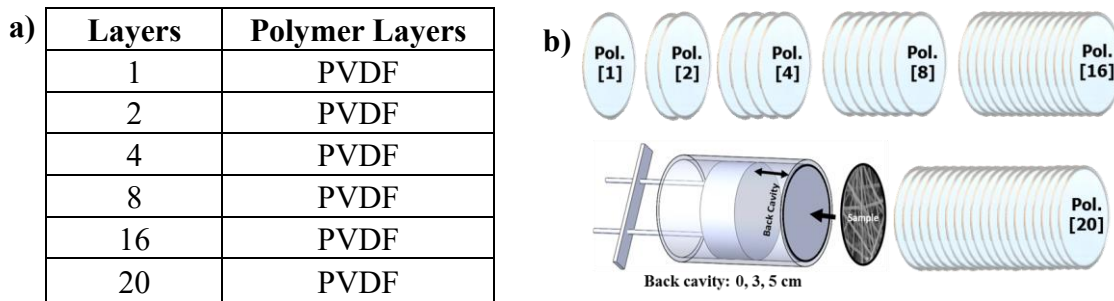


Figure 4.9: a) PVDF membrane layering order and b) Schematics of layering pattern.

#### 4.3.2 SAP of Single PVDF Fiber Membrane at Three Discrete BC

The SAP of a single PVDF membrane loaded with nanofibers of diameter ranging 200nm to 400nm was tested at different BC's in Figure 4.10 (a-b). In the case of 0cm BC, the coefficient values were observed to be less than 0.3 in the complete frequency range. On the contrary, multiple absorption peaks with  $\alpha$ -value of 0.5 and 0.6 were observed at different higher frequencies of 991, 1207, and 1481Hz with an increased BC to 3cm. The SAP was observed with multiple peaks attributed to the resonance of the membrane that further depends on the material's flexibility. An additional increase in BC to 5cm resulted

in higher absorption peaks with coefficient values of 0.83 and 0.84 at frequencies of 758 and 1004Hz, which was moved from higher frequency range of 1200-1400Hz.

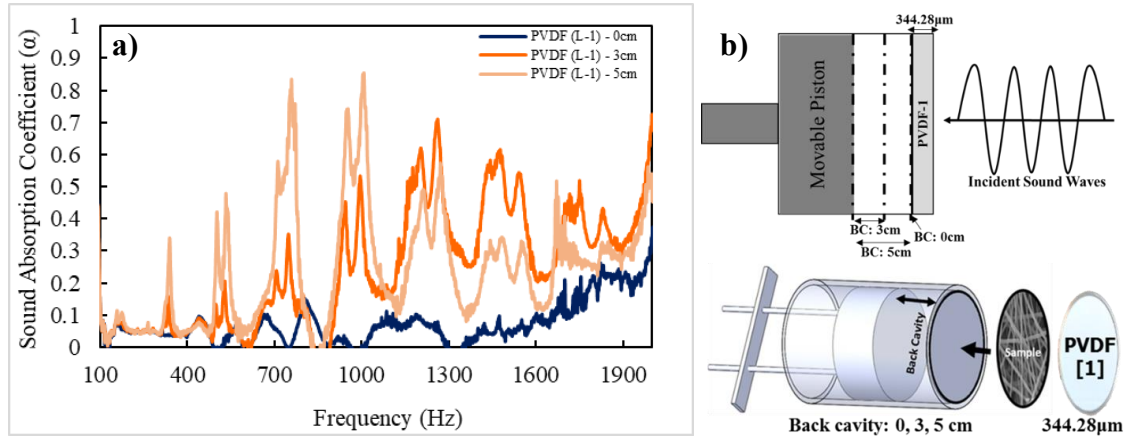


Figure 4.10: a) Sound absorption coefficient of single PVDF fiber membrane at three discrete BC's and b) Schematics of layering configuration.

### 4.3.3 SAP of Multiple Layers of PVDF Membrane at Three Discrete BC

#### 4.3.3.1 SAP of Two Layers

The acoustic behavior of two PVDF membrane layered composite was investigated in Figure 4.11 (a-b) at different BC's. With zero air gap, the membrane resulted in similar acoustic behavior observed in preceding specimens with lower absorption for the designed frequency zone. The coefficient values of 0.64 and 0.67 was reported at frequencies of 767Hz and 1081Hz with dual absorption peaks at 3cm BC. These nanofiber composites 998 $\mu$ m thick exhibits better absorption in lower frequencies when compared with double PVP membrane configuration. Further addition of BC to 5cm resulted in sharp peaks of  $\alpha$ -value 0.78 and 0.67 at lower frequencies of 642Hz and 866Hz.

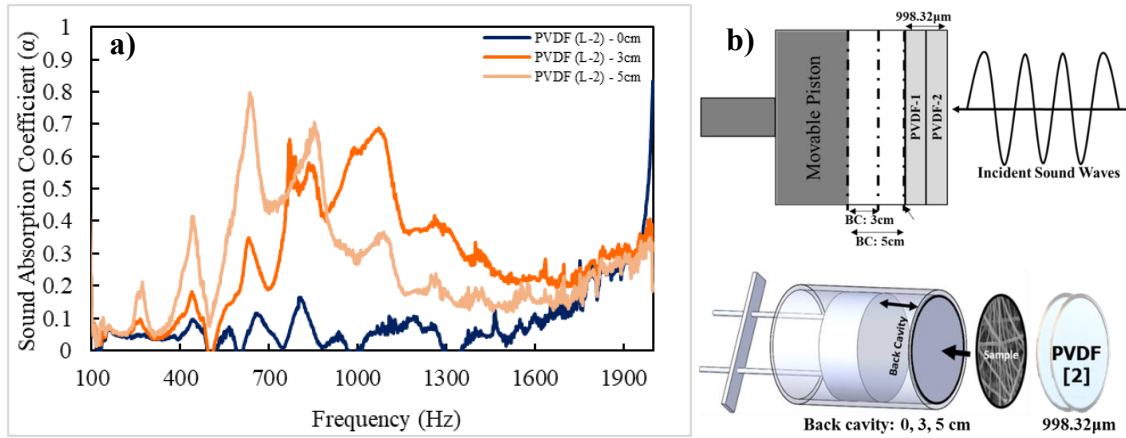


Figure 4.11: a) Sound absorption coefficient of two layers of PVDF fiber membranes at three discrete BC's and b) Schematics of layering configuration.

#### 4.3.3.2 SAP of Four Layers

The sound absorption performance of four layered composite was presented at different cavities at reported thickness of 2091.27  $\mu\text{m}$  in Figure 4.12. The thickness of the composites was higher than the PVP four layered composite and even the fiber diameter range was smaller relatively. Higher absorption peak of 0.78 coefficient value at higher frequency of 1950-2000Hz was observed with PVDF composite which was absent in the preceding specimens with layers less than sixteen. It could be due to the relatively higher thickness of the membrane loaded with smaller fibers comparatively. Substantial increase in coefficient value to 0.85 was reported at lower frequency of 754 Hz with 3cm air cavity. Such a significant increase with 3cm BC was reported in eight layers of PVP at approximately similar thickness of 2000-2500  $\mu\text{m}$  but PVDF composites it has moved to even lower frequencies. Furthermore, with an addition in back cavity to 5cm, the four layered composite had the ability to achieve coefficient of 0.84 and 0.92 at lower frequencies of 384 and 584Hz which was the lowest when compared with similar layered composite of PVP membranes. These thin and light weighted membrane can be used as a better sound absorbing material in low frequency range which will save significant amount of time and space for construction.

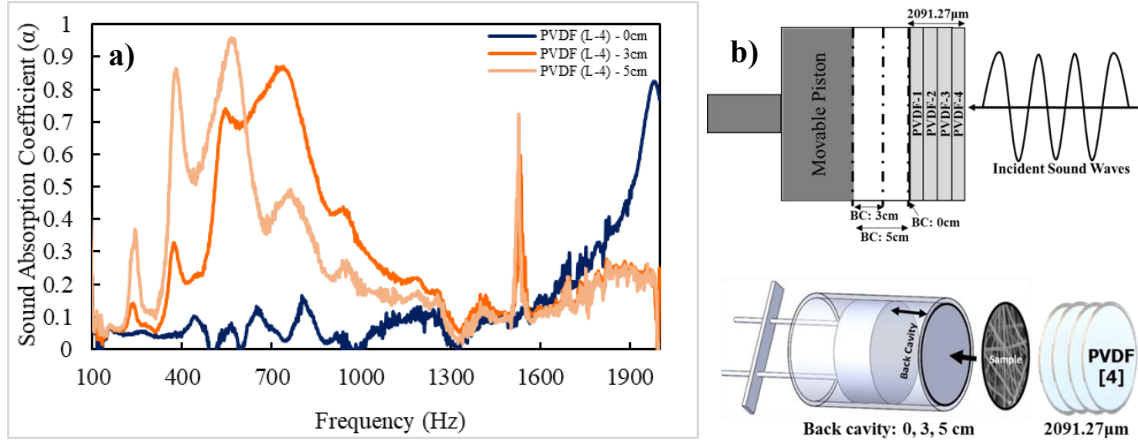


Figure 4.12: a) Sound absorption coefficient of four layers of PVDF fiber membranes at three discrete BC's and b) Schematic of layering configuration.

#### 4.3.3.3 SAP of Eight Layers

The acoustic behavior of eight layered composite with a micro-scaled thickness of 3545  $\mu$ m was investigated in Figure 4.13 (a-b) at different BC's. With a 0 cm air cavity, the highest coefficient value of 0.98 was achieved at a frequency of 1635 Hz. With the BC extension of 3 cm, multiple peaks of higher coefficient values, 0.88, 0.87, and 0.91, were reported at different frequencies of 359, 479, and 572 Hz, which covers the relatively broad range 350-600 Hz. The BC extension of 5 cm resulted in a significant rise in coefficient value from 0.80 to 0.96 covering even lower frequencies of 230-430 Hz than 3 cm BC. The composite achieved a higher absorption with a relatively smaller number of layers when compared with PVP membrane composites.

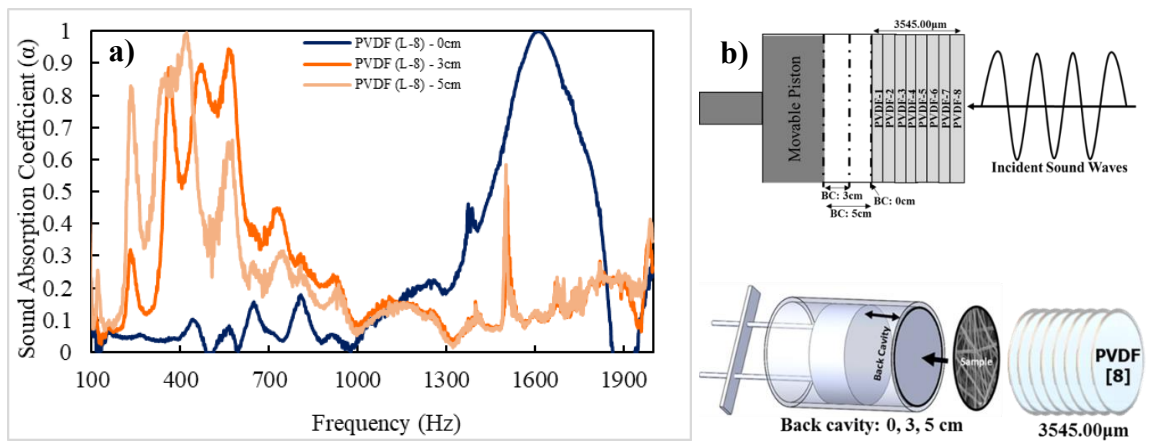


Figure 4.13: a) Sound absorption coefficient of eight layers of PVDF fiber membranes at three discrete BC's and b) Schematics of layering configuration.

#### 4.3.3.4 SAP of Sixteen Layers

The SAP of sixteen layered membrane composite was investigated at different BC combinations in Figure 4.14 (a-b). The composite resulted in a maximum coefficient of 0.95 at 1032Hz frequency, a significant frequency sweep from 2000Hz observed with a four layered composite at 0cm BC. The composite with a thickness of 6000 $\mu$ m resulted in a maximum coefficient value of 0.99 at 367Hz with increased BC to 3cm. Multiple absorption peaks were observed in the lower frequency range of 270-370Hz with an  $\alpha$ -value higher than 0.8. With the BC addition of 5cm, the absorption curve shifted significantly towards the lower frequency range of 240-330Hz, maintaining the highest coefficient values of 0.98.

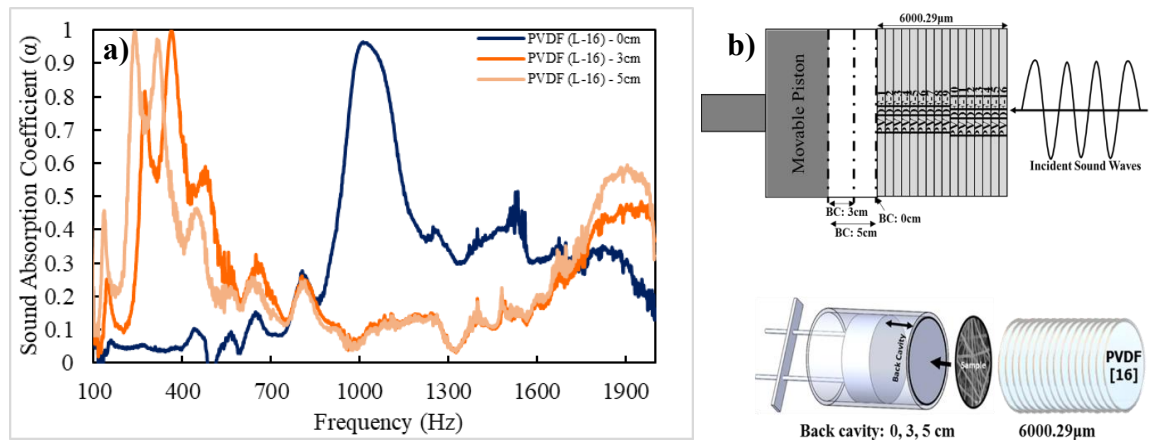


Figure 4.14: a) Sound absorption coefficient of sixteen layers of PVDF fiber membranes at three discrete BC's and b) Schematics of layering configuration.

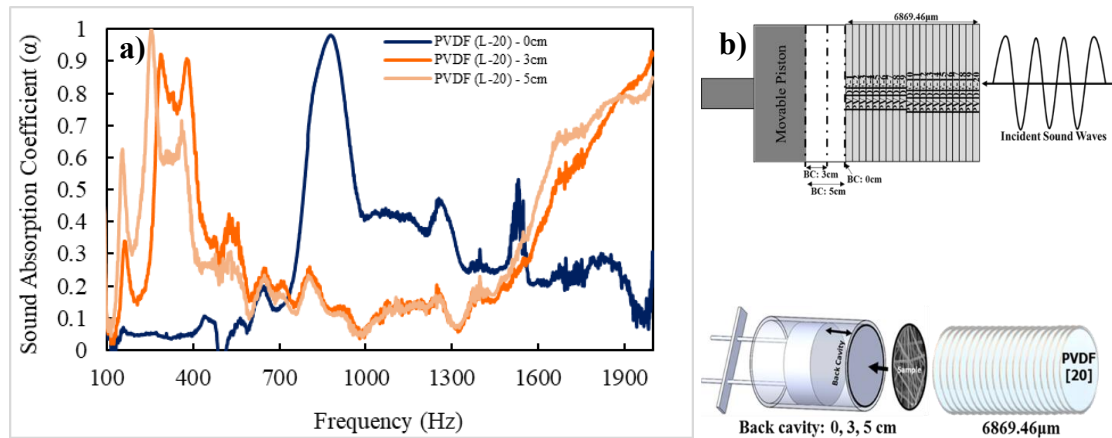


Figure 4.15: a) Sound absorption coefficient of twenty layers of PVDF fiber membranes at three discrete BC's and b) Schematics of layering configuration.

#### **4.3.3.5 SAP of Twenty Layers**

The acoustic performance of twenty membranes was investigated in Figure 4.15 (a-b) at different BC's. The maximum coefficient of 0.96 was observed at a frequency of 894Hz. The peak moved from 1000Hz observed in sixteen layered composites maintaining the same coefficient value with an increased thickness of 6869 $\mu$ m. With the increase in BC to 3cm, two absorption peaks were observed in two different frequency ranges. The composite was observed with an  $\alpha$ -value of 0.88-0.90 at 250-350Hz and a coefficient value of 0.9 at 1900Hz. The dual-frequency absorption behavior of PVDF membrane composites was observed only with a twenty-layer composite. The BC extension of 5cm resulted in a very sharp peak of 0.999  $\alpha$ -value at 256Hz and 0.85 at 1900Hz range. These thin and lightweight composites possess exceptionally better sound absorption behavior in both high and low-frequency ranges. Such absorption peaks in the high-frequency range are generally noticed with thick traditional materials.

#### **4.3.3.6 Sound Absorption Coefficient ( $\alpha$ ) Variation with Change in Thickness at Different Frequency Bands (1/3 Octave Plots)**

Graphical representation of the sound absorption coefficient percentage increase with change in composite thickness from 344.28 $\mu$ m to 6869.96 $\mu$ m was investigated in Figure 4.16 for discrete BC's at frequency bands of 1/3 octave plot. The study of coefficient variation and absorption peak curve movement with thickness was examined using this analysis in Table 4.2. The experimental investigation on SAP shows the presence of absorption peaks at two extremes of the frequency range. These peaks were observed with higher coefficient values for twenty layered composites. With 0cm BC, the highest percentage increase of 1502% was marked at 1000Hz, and a rise of 500% was noticed at 794Hz. On the contrary, a percentage increase of 1177% was reported with 3cm BC at a lower frequency of 315Hz. With further expansion in BC, the percentage improvement ranging from 500-1500% was noticed at even lower frequency bands of 157-397Hz. It was evident from the experimental coefficient measurements that the higher coefficient values of 0.8-0.9 can be achieved with an increase in layer thickness and back cavity. In the case 0cm BC, the absorption peak was noticed in the frequency range of 1900-2000Hz, but the peaks drifted to 894Hz, maintaining the  $\alpha$ -value of 0.9 with the increase in material

thickness. With BC extension to 3cm, the composites resulted in an  $\alpha$ -value of 0.9 with a substantial peak shift from 754Hz to 268Hz. With further addition in BC to 5cm, composites resulted in a noteworthy shift in absorption peak ( $\alpha$  value – 0.99) to the lowest frequency of 261Hz.

Table 4.2: Percentage increase data for different frequency bands (1/3 - Octave plot).

BC	Percent increase in $\alpha$ at discrete octave frequency (Hz)											
	125	157	198	250	315	397	500	630	794	1000	1260	1587
0cm	-20	-11	-1	-6	2	13	41	184	920	1502	754	200
3cm	42	251	219	650	1178	1104	327	173	90	-56	-69	-8
5cm	263	508	520	1506	454	688	43	39	-42	-76	-51	78

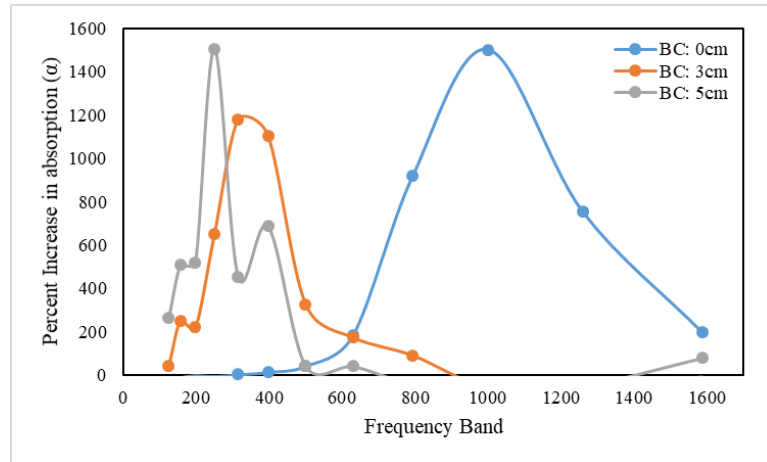


Figure 4.16: Sound absorption coefficient percent increase with thickness variation at discrete BC's for PVDF layers.

#### 4.4 Sound Absorption Characteristics of Combined PVP and PVDF Composites

PVP based membranes have fiber diameter ranging from 0.536 $\mu$ m to 2.54 $\mu$ m, whereas the fiber diameter of the PVDF membrane varies in the range of 0.112 $\mu$ m to 0.240 $\mu$ m. The resultant composite consists of alternate layers of both membranes, and the SAP of respective components was tested in this section.

##### 4.4.1 Acoustic Sample Formulation

The acoustic ready samples of two polymeric based membranes were stacked together in the following manner; a) Single membrane of PVP and PVDF, b) Alternate layers of two PVP and PVDF membrane, c) Alternate layers of four PVP and PVDF membranes, d)



Alternate layers of eight PVP and PVDF membranes, and e) Alternate layers of ten PVP and PVDF membrane [Figure 5.17 (a-b)]. The resultant composites have a total of the following layers for each combination; 2, 4, 8, 16, and 20.

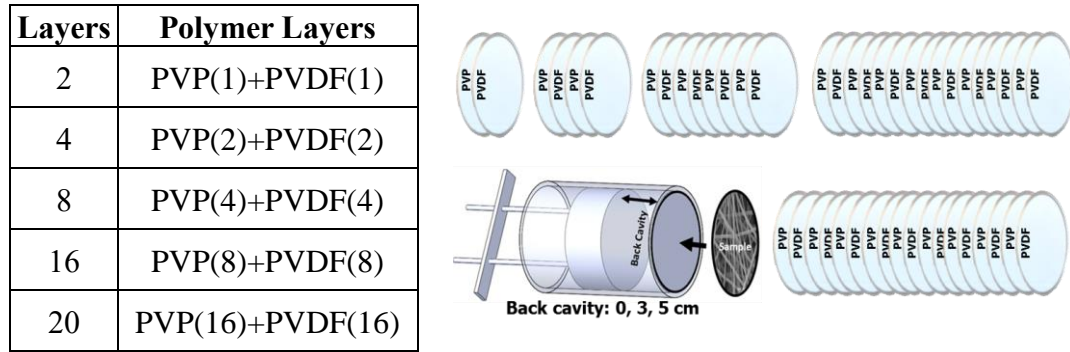


Figure 4.17: a) PVP and PVDF membrane layering order and b) Schematics of layering pattern.

#### 4.4.2 SAP of Alternate Layers of PVP and PVDF Membrane at Three Discrete BC

##### 4.4.2.1 SAP of Two Layers

The SAP of combined alternate layers of single PVP and PVDF membrane has been investigated in Figure 4.18 (a-b). With 0cm BC, absorption peaks were observed with lower coefficient values less than 0.3 for the entire frequency range. Conversely, with 3cm BC, numerous absorption peaks were observed with a maximum  $\alpha$ -value of 0.78 at 1081Hz. With an additional increase in BC to 5cm, multiple peaks increased more towards the lower frequency region with the maximum  $\alpha$ -value of 0.75 at 830Hz.

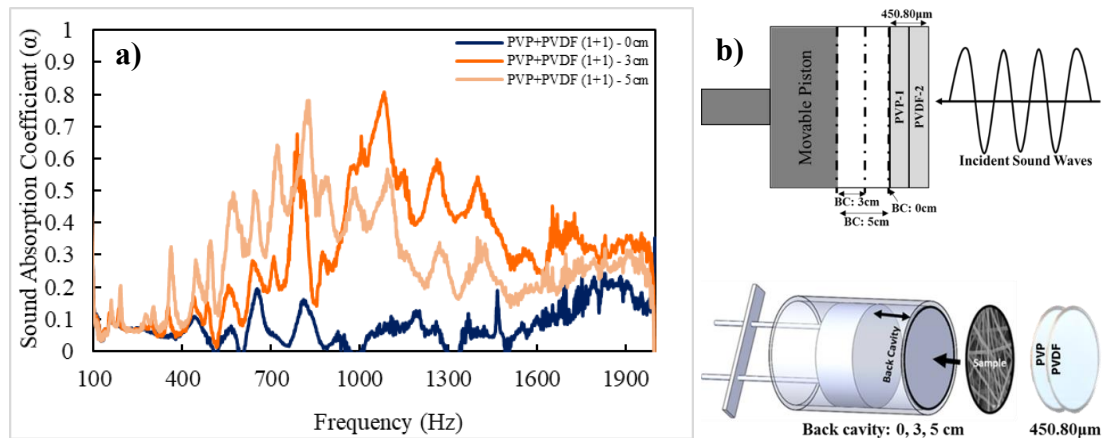


Figure 4.18: a) Sound absorption coefficient of two alternate layers of PVP and PVDF fiber membranes at three discrete BC's and b) Schematics of layering configuration.



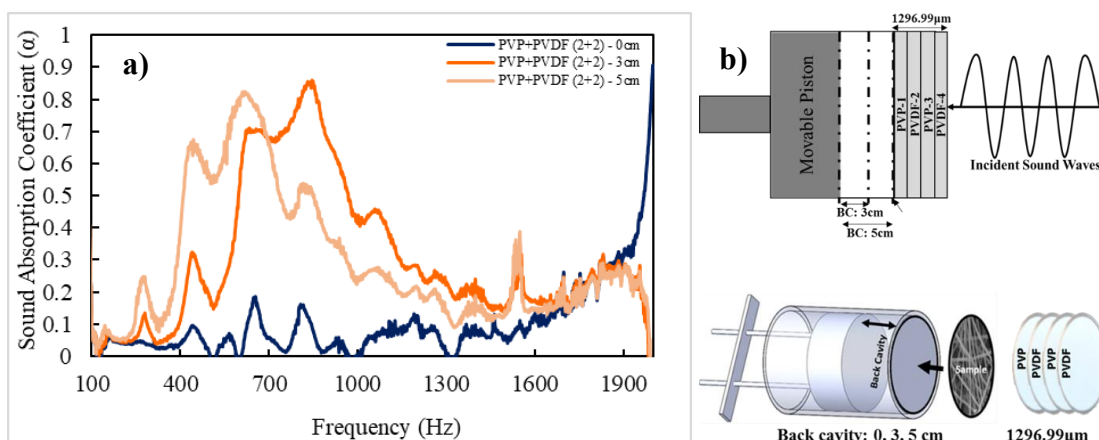


Figure 4.19: a) Sound absorption coefficient of four alternate layers of PVP and PVDF fiber membranes at three discrete BC's and b) Schematics of layering configuration.

#### 4.4.2.2 SAP of Four Layers

The four-layered alternate PVP and PVDF membrane composite was tested at different BC's in Figure 4.19 (a-b). At 0cm BC, the absorption peak was observed in the frequency range of 2000Hz with a maximum  $\alpha$ -value of 0.9. On the other hand, the coefficient value of 0.82 was marked at a lower frequency of 857Hz. Further expansion in BC to 5cm resulted in absorption peak shift towards the lower frequency side, maintaining an  $\alpha$ -value of 0.8 at 648Hz.

#### 4.4.2.3 SAP of Eight Layers

The combined alternate layers of four PVP and PVDF membranes were investigated at different BC's in Figure 4.20 (a-b). The composite of thickness 2794.61  $\mu\text{m}$  resulted in a higher coefficient of 0.96 at 1948Hz, which initially appeared at 1600Hz for pure PVDF eight-layered composite. Sharp absorption peaks were observed with an  $\alpha$ -value 0.95 at 566Hz with an increase in BC to 3cm. The results show that the coefficient of 0.95 can be achieved in the low-frequency range with a lower thickness of material made from two different fibers. With the 5cm BC extension, the peak with a coefficient value of 0.94 drifted more towards a lower frequency of 427Hz. Higher absorption close to 0.9 can be achieved with alternately layered composite in the frequency range of 400-600 Hz, but to reach the same absorption at a frequency less than 350Hz pure PVDF membrane composites are required.

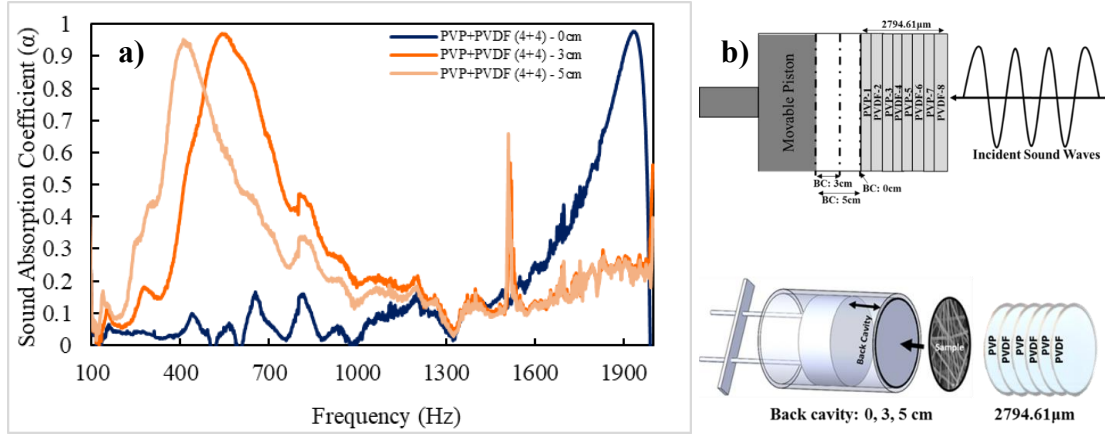


Figure 4.20: a) Sound absorption coefficient of eight alternate layers of PVP and PVDF fiber membranes at three discrete BC's and b) Schematics of layering configuration.

#### 4.4.2.4 SAP of Sixteen Layers

The SAP of sixteen layered composite prepared from alternate stacking of eight PVP and PVDF layers was investigated at three discrete BC's in Figure 4.21 (a-b). The combined membrane with a thickness of 5472.13  $\mu\text{m}$  was reported with a coefficient value of 0.93 at 1261 Hz, wherein this peak was not evident in the preceding combinations at 0 cm BC. With a 3 cm BC extension, the absorption peak moved towards the lower frequency of 415 Hz with the highest  $\alpha$ -value of 0.98. Furthermore, the BC variation of 5 cm resulted in higher absorption of 0.96 at a lower frequency of 333 Hz which was moved from 415 Hz reported at 3 cm BC.

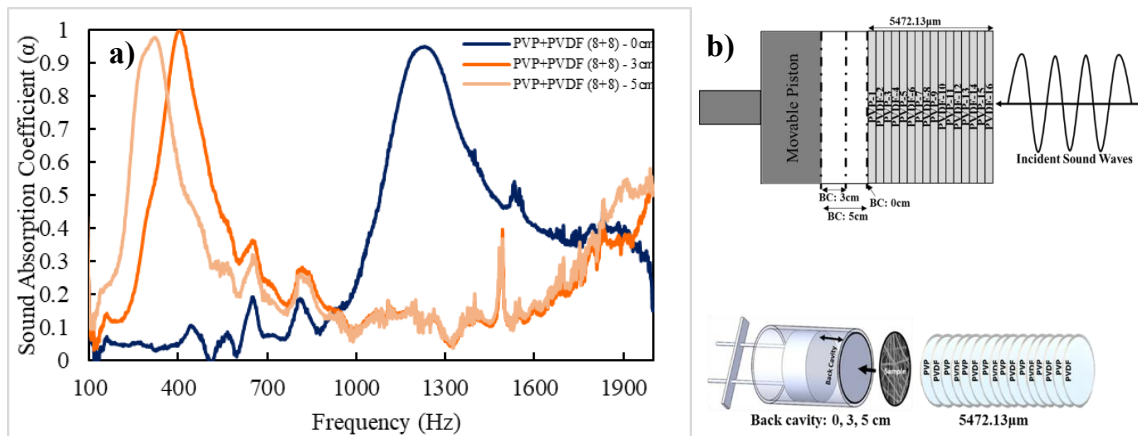


Figure 4.21: a) Sound absorption coefficient of sixteen alternate layers of PVP and PVDF fiber membranes at three discrete BC's and b) Schematics of layering configuration.

#### 4.4.2.5 SAP of Twenty Layers

The SAP of twenty combined membranes with ten layers of PVP and PVDF was investigated at three discrete BC's in Figure 4.22 (a-b). The sound absorption coefficient value reached its peak of 0.94 at 1078Hz with zero BC. The absorption peak shifted to 1078Hz from 1952Hz observed at eight-layered composite. With a 3cm BC, the coefficient value of 0.83 was observed at 399Hz, and an  $\alpha$ -value of 0.68 was also observed beyond 1900Hz. Further extension of 5cm in BC resulted in absorption peak shift with an  $\alpha$ -value of 0.92 at 263Hz frequency, and the second peak was noticed with a 0.75 coefficient value beyond 1800Hz.

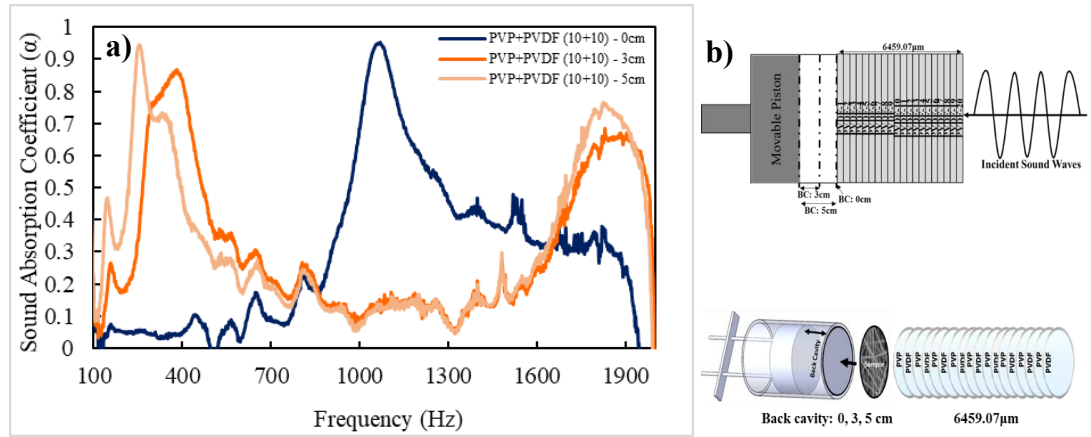


Figure 4.22: a) Sound absorption coefficient of twenty alternate layers of PVP and PVDF fiber membranes at three discrete BC's and b) Schematics of layering configuration.

#### 4.4.2.6 Sound Absorption Coefficient ( $\alpha$ ) Variation with Change in Thickness at Different Frequency Bands (1/3 Octave Plots)

The sound absorption coefficient percent increase with change in composite thickness from 450.80 $\mu$ m to 6459.07 $\mu$ m was described in Figure 4.23 for discrete BC's at frequency bands of 1/3 octave plot. The experimental analysis on  $\alpha$ -variation with peak drifting towards lower frequency was studied using this analysis in Table 4.3. With the twenty layered composite, absorption peaks were reported to appear at frequency extremes, but the coefficient values at the peak were slightly lower than twenty layered pure PVP and PVDF composites. In the case of 0cm BC, the maximum increase of 1844% and 904% was observed at 1000Hz and 1260Hz. In contrast, the percentage increase of 968% and 819% was observed with 3cm BC at lower frequency bands of 315Hz and 397Hz. With the further

5cm BC extension, absorption increase ranging from 283-1010% was noticed at even lower frequency bands of 125-397Hz. The experimental  $\alpha$ -value of these composites indicates that the value of 0.8-0.9 can be achieved with a higher layer thickness and tuning BC. With 0cm BC, the absorption peak was noticed at 1900-2000Hz frequency, but the peaks moved to 1078Hz, maintaining the  $\alpha$ -value of 0.9 with the increase in material thickness. In the case of 3cm BC extension, resultant composites were noticed with significant peak shifts from 840Hz to 383Hz with a 0.9  $\alpha$ -value. With further addition in BC to 5cm, composites resulted in a noteworthy shift of absorption peak to 262Hz with an  $\alpha$ -value of 0.91.

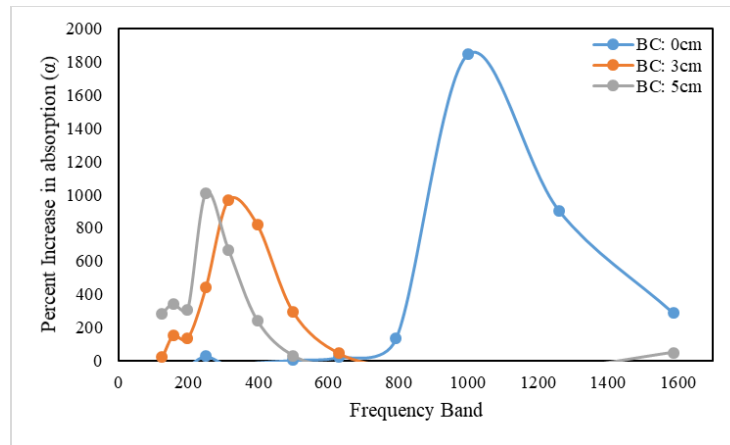


Figure 4.23: Sound absorption coefficient percent increase with thickness variation at discrete BC's for PVP and PVDF combined layers.

Table 4.3: Percentage increase data for different frequency bands (1/3 - Octave plot).

BC	Percent increase in $\alpha$ at discrete octave frequency (Hz)											
	125	157	198	250	315	397	500	630	794	1000	1260	1587
0cm	-50	-31	-30	26	-28	-11	3	20	132	1844	905	288
3cm	21	152	134	442	968	819	292	46	-40	-78	-74	-13
5cm	283	343	307	1011	665	240	27	-43	-69	-75	-53	49

## 4.5 Sound Absorption Characteristics of Filler Infused PVP Fibers and Its Composites

### 4.5.1 Acoustic Sample Formulation

The acoustic test-ready samples were tested in two stages; the first stage involves combining different concentration layers of each filler-infused membrane that were added for up to a total of four layers. The second stage involves acoustic testing of multiple layers

of filler infused membranes wherein four layers of each filler composites prepared in the first stage was stacked to form seven, ten, thirteen, and sixteen layered filler composites.

Filler Infused Membrane Layering Pattern							
Layers	2	3	4	7	10	13	16
CNT (C)	P+C1						
	P+C1+C2						
	P+C1+C2+C3						
GN (G)	P+G1						
	P+G1+G2						
	P+G1+G2+G3						
FS (S)	P+S1						
	P+S1+S2						
	P+S1+S2+S3						
FG (F)	P+F1						
	P+F1+F2						
	P+F1+F2+F3						
MC (M)	P+M1						
	P+M1+M2						
	P+M1+M2+M3						
C+G	P+(C1+C2+C3)+(G1+G2+G3)						
C+G+S	P+(C1+C2+C3)+(G1+G2+G3)+(S1+S2+S3)						
C+G+S+F	P+(C1+C2+C3)+(G1+G2+G3)+(S1+S2+S3)+(F1+F2+F3)						
C+G+S+F+M	P+(C1+C2+C3)+(G1+G2+G3)+(S1+S2+S3)+(F1+F2+F3)+(M1+M2+M3)						

Figure 4.24: Filler infused PVP membranes layering blocks.

## 4.5.2 SAP of Multiple Layers of Filler Infused PVP Membranes at 3 Discrete BC

### 4.5.2.1 SAP of CNT Based Layers

The SAP of two, three, and four-layered CNT infused composite was investigated at different BC's in Figure 4.25 (a-c). With 3cm BC, multiples peaks were observed in the frequency range of 700-1300Hz with an  $\alpha$ -value of 0.70-0.75 at 767-797Hz [Figure 4.25 (a)]. The material thickness varies from 646-1163 $\mu$ m with this configuration. With the further extension of 5cm in BC, similar absorption peaks appeared at 640-900Hz, which means peaks moved to the lower frequency side with higher BC and reached the  $\alpha$ -value of 0.7 at 854Hz [Figure 4.25 (b)]. The absorption peaks were observed to appear in the lower frequency range of 700-800Hz, whereas with four-layered pure PVP composite, it appeared in a slightly higher range of 800-1000Hz.

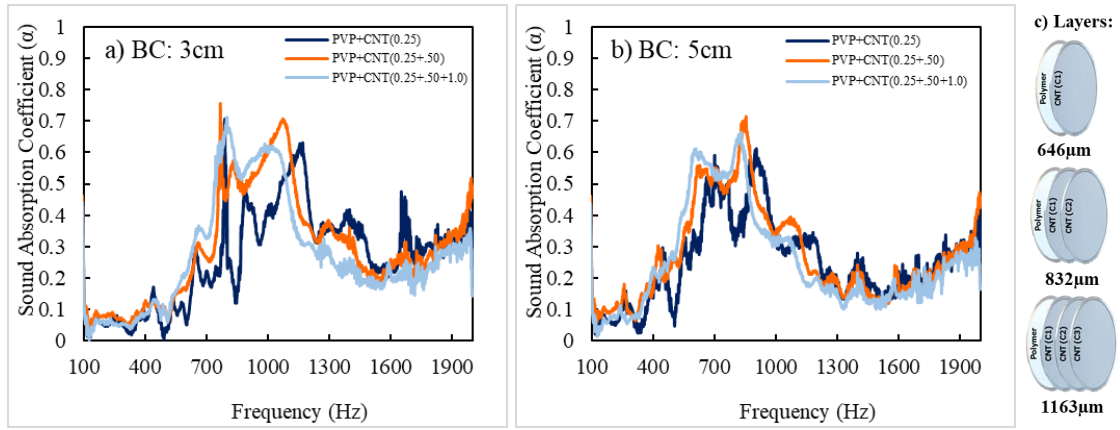


Figure 4.25: Sound absorption coefficient of CNT infused PVP membrane layers at different BC's: a) 3cm and b) 5cm; and c) Schematics of layering configuration.

#### 4.5.2.2 SAP of GN Based Layers

The SAP of GN infused PVP membrane layered composites were studied at different BC's in Figure 4.26 (a-c). The BC extension of 3cm resulted in a similar occurrence of peaks as CNT-based composites. In this case, the absorption peaks were observed in a broader frequency range of 700-1300Hz compared to the previous composite. A coefficient value of 0.7 was observed at 830Hz with both three, and four-layered composites, whereas the CNT-based peaks appeared in lower frequency relatively [Figure 4.26 (a)]. Further increase in 5cm BC resulted in similar peaks for all three composites in the frequency range of 600-830Hz with an  $\alpha$ -value of 0.66 [Figure 4.26 (b)].

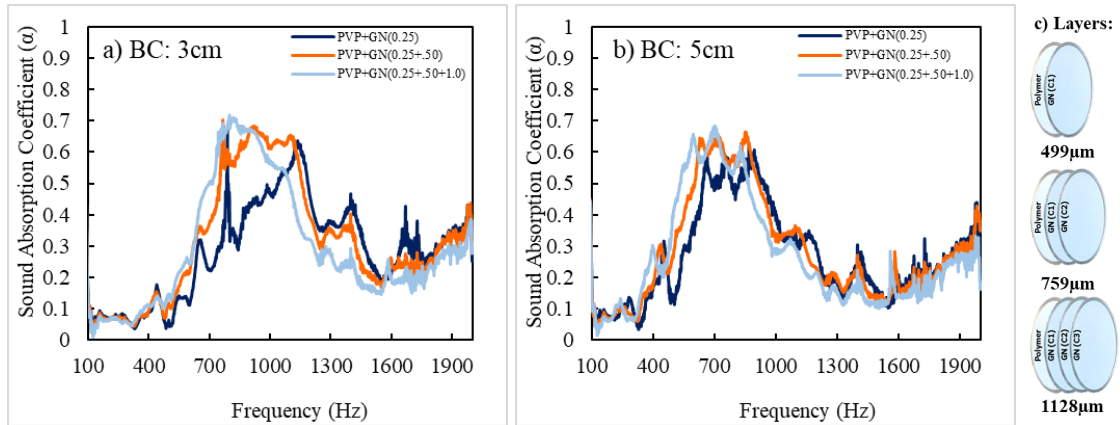


Figure 4.26: Sound absorption coefficient of GN infused PVP membrane layers at different BC's: a) 3cm and b) 5cm; and c) Schematics of layering configuration.

#### 4.5.2.3 SAP of FS Based Layers

The acoustic response of FS-infused membrane layers was investigated in Figure 4.27 (a-c). The respective layered membranes were marked with thickness ranging from 538-932 $\mu$ m. At 3cm BC, sharp absorption peaks were noticed in the range of 700-1300Hz. The coefficient value reached the maximum of 0.75 at 900Hz for both three and four-layered configurations [Figure 4.27 (a)]. With the increase in BC to 5cm, similar absorption peaks with coefficient values of 0.7 were observed in a slightly lower frequency range of 600-900Hz [Figure 4.27 (b)]. A maximum coefficient value of 0.72 was observed at 725Hz for FS-based four-layered composite.

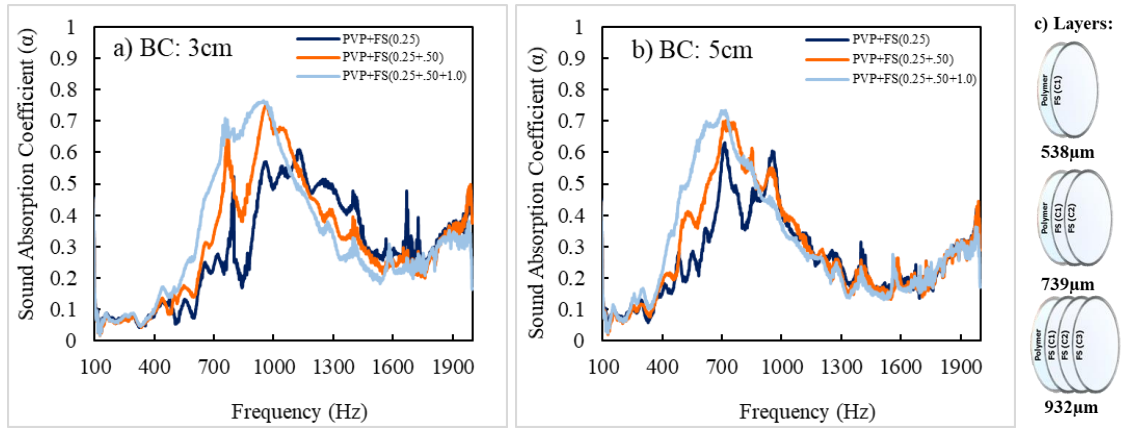


Figure 4.27: Sound absorption coefficient of FS infused PVP membrane layers at different BC's: a) 3cm and b) 5cm; and c) Schematics of layering configuration.

#### 4.5.2.4 SAP of FG Based Layers

The acoustic behavior of FG-infused layered composites was investigated in Figure 4.28 (a-c) at different BC's. At 3cm BC, multiple peaks were observed in the frequency range of 750-1200Hz, which was slightly higher than all preceding samples. A coefficient value of 0.64 was observed with four layers at 872Hz [Figure 4.28 (a)]. Further expansion in BC to 5cm resulted in a similar curve but with sharp peaks of  $\alpha$ -value 0.6 at a lower frequency range of 640-840Hz [Figure 4.28 (b)].



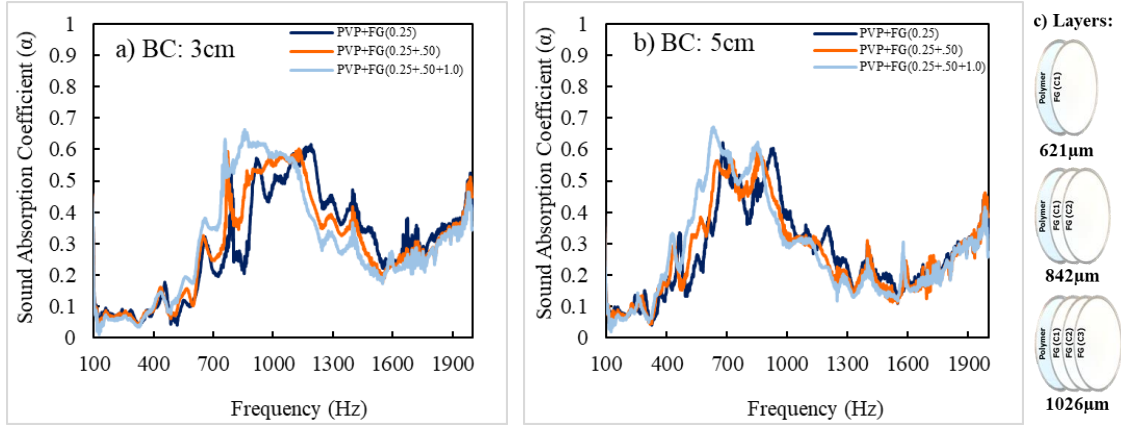


Figure 4.28: Sound absorption coefficient of FG infused PVP membrane layers at different BC's: a) 3cm and b) 5cm; and c) Schematics of layering configuration.

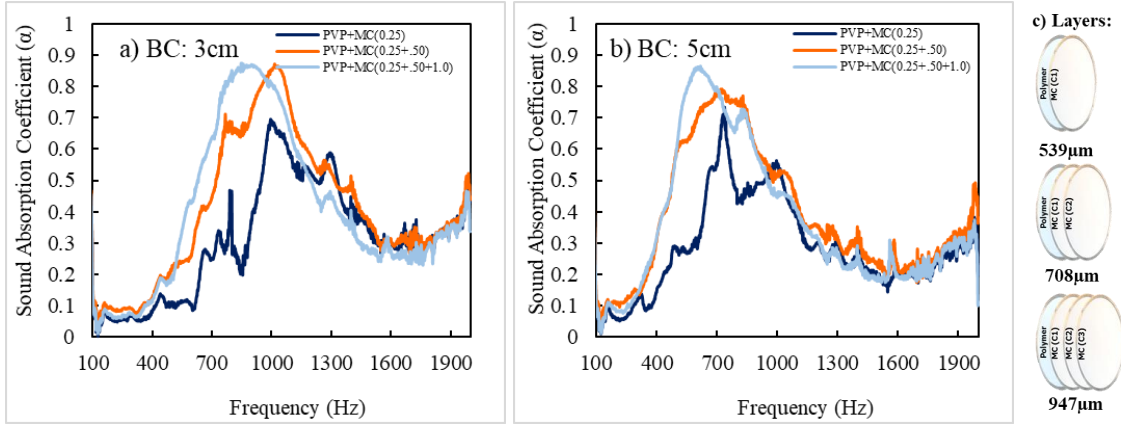


Figure 4.29: Sound absorption coefficient of MC infused PVP membrane layers at different BC's: a) 3cm and b) 5cm; and c) Schematics of layering configuration.

#### 4.5.2.5 SAP of MC Based Layers

The SAP of MC-based membrane layers was investigated in Figure 4.29 (a-c). Absorption peaks with the highest coefficient value of 0.86, was observed with three and four-layered composites at 906Hz and 923 Hz. The MC-based composite was observed with the highest absorption peaks in the frequency range of 700-1300Hz compared with all preceding specimens at 3cm BC [Figure 4.29 (a)]. With 5cm BC, the absorption peaks shifted towards a lower frequency range of 500-900Hz with the maximum  $\alpha$ -value of 0.83 at 635Hz for four-layer and 0.77 at 774Hz for three-layer [Figure 4.29 (b)].



#### 4.5.2.6 Sound Absorption Coefficient ( $\alpha$ ) Variation with Change in Thickness at Different Frequency Bands (1/3 Octave Plots)

The graphical plots of percentage increase in the sound absorption coefficient of the filler-infused membrane composites with thickness variation were plotted in Figure 4.30 (a-b) at different BC's for designed frequency bands of 1/3 octave plots. The experimental analysis on coefficient variation and absorption peak shift was studied using Table 6.4 for 3cm BC. At 3cm BC, a significant increase of 112%, 181%, and 178% in  $\alpha$ -value was observed in the frequency range of 500, 630, and 794Hz with MC-based composites. Followed by MC composites, FS composites offer an increase of 118% and 148% at 630Hz and 794Hz. These composites follow the descending coefficient peaks in the following order; MC, FS, CNT, FG, and GN in the respective frequency range [Figure 4.30 (a)]. An addition of BC to 5cm resulted in an increase of 131% at 500Hz for MC-based composite, which moved from 794Hz observed with 3cm BC [Figure 4.30 (b)]. The coefficient increase follows the descending trend in order of; MC>FS>GN>CNT>FG. It was evident from the investigation that the MC composites offered a better coefficient value of 0.85 in the lower frequency range of 600Hz with a four-layer membrane.

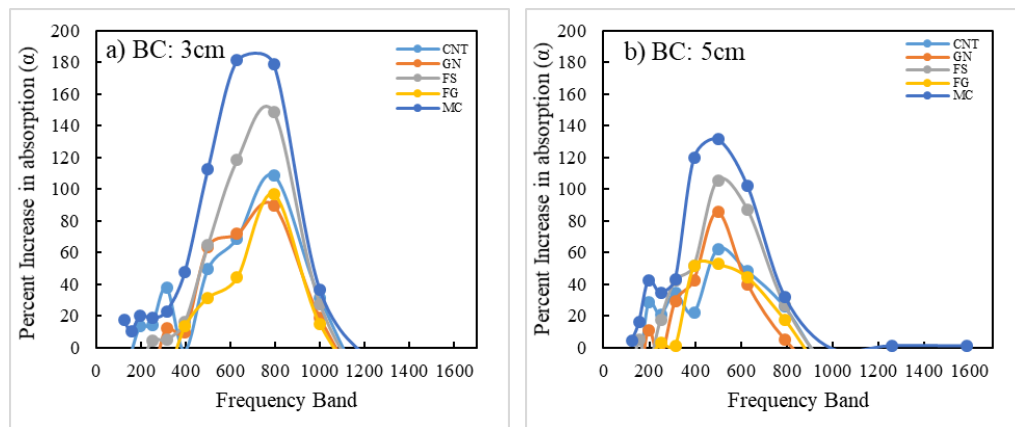


Figure 4.30: Sound absorption coefficient percent increase with thickness variation at discrete BC's for filler-infused PVP membrane layers.

Table 4.4: Percent increase data for different frequency bands (1/3-Octave plot) 3cm BC.

Fillers	Percent increase in $\alpha$ at discrete octave frequency (Hz) for BC: 3cm											
	125	157	198	250	315	397	500	630	794	1000	1260	1587
CNT	-17	-3	13	14	38	-2	49	69	109	31	-33	-30
GN	-33	-20	-7	-17	12	9	64	72	90	19	-34	-31
FS	-15	-5	-12	4	5	16	64	118	149	28	-27	-22
FG	-39	-27	-21	-20	-19	13	32	44	97	15	-27	-21
MC	17	11	20	19	23	48	113	181	179	36	-10	-14

#### 4.5.3 SAP of Combined Layers of Filler Infused PVP at Varying BC

The progressive layering of the filler-based membranes was performed in the following order; a) Seven-layers composite with PVP, three CNT, and GN infused layers, b) Ten-layers with three FS-infused layers on stack prepared in (a), c) Thirteen-layers with three FG layers on stack (b), and d) Sixteen-layers with three MC layers assembled on (c).

##### 4.5.3.1 SAP of progressive layering of filler infused PVP membrane at discrete BC's

The SAP of combined multiple layers of filler-infused PVP membranes was investigated at different BC's in Figure 4.31 (a-d). In the case of 0cm BC, peaks were observed near the frequency range of 1900-2000Hz, wherein, with an increase in layers to sixteen, the peaks shifted to a low-frequency range of 1600-1800Hz. The absorption coefficient of 0.85 and 0.94 was observed at 2000Hz for seven-layer and ten-layer composite, respectively. The thirteen and sixteen layered composites reached the maximum coefficient value of 0.82 at 1950Hz and 0.95 at 1650Hz [Figure 4.31 (a)]. With a BC extension of 3cm, multiple peaks with  $\alpha$ -value ranging from 0.8-0.96 were observed in the lower frequency range of 400-800Hz. The  $\alpha$ -value of 0.85 and 0.93 were observed at 753Hz and 619Hz for seven and ten layered composites. The maximum coefficient value of 0.96 was marked at 570Hz with the FG layer added to the stack. The  $\alpha$ -value of 0.96 was shifted to 503Hz for sixteen layers [Figure 4.31 (b)]. With 5cm BC, the absorption peaks moved to a lower frequency range of 300-600Hz, maintaining high  $\alpha$ -values. The coefficient of 0.77 was observed with a seven-layer composite at 576Hz. Ten-layer composite resulted in  $\alpha$ -value of 0.93 at 495Hz, and with further addition, the  $\alpha$ -value of 0.98 was achieved at 478Hz. With the sixteen layers, the highest coefficient value of 0.99 was achieved at 387Hz, which is considered an exceptionally significant absorption in the low-frequency

range [Figure 4.31 (c)]. These filler-based composites have an overall thickness lesser than all preceding layered composites.

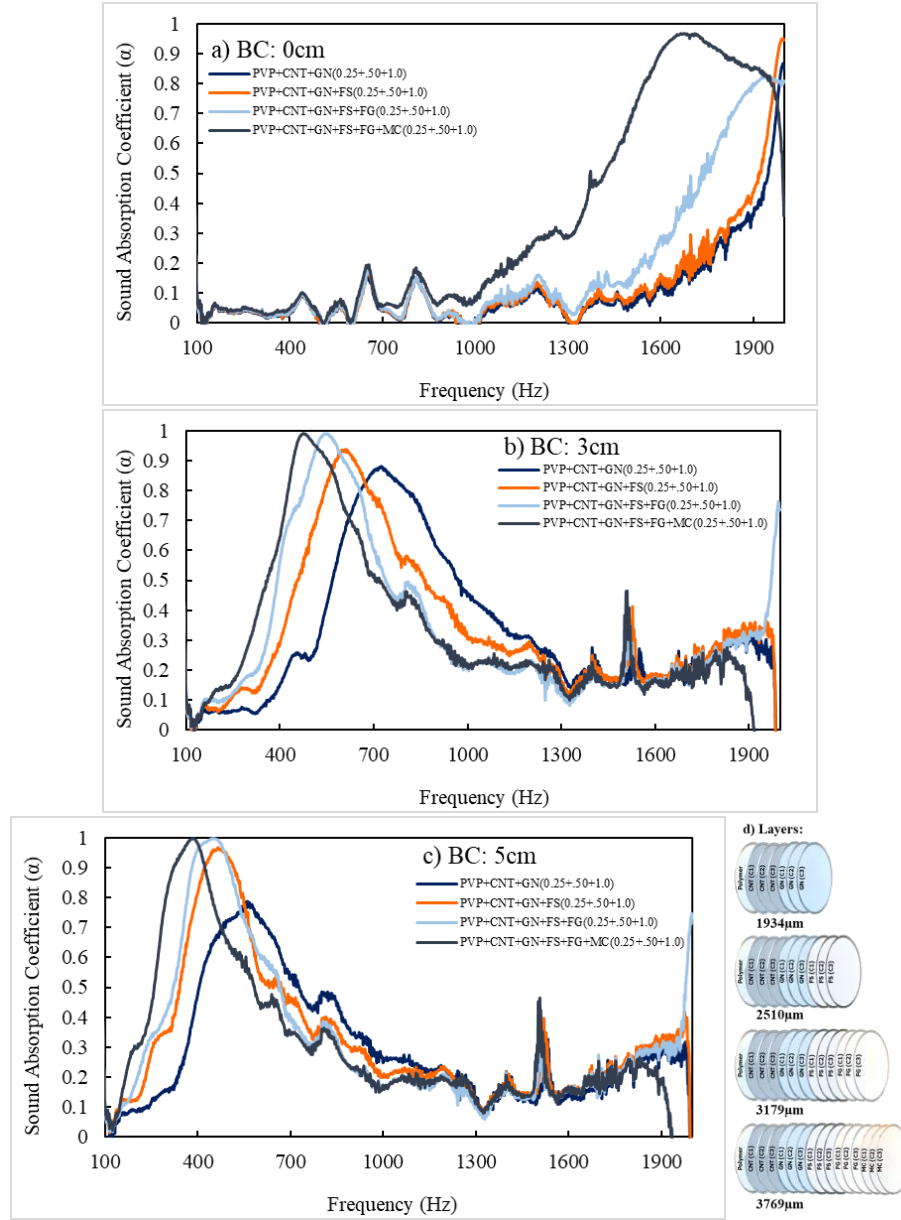


Figure 4.31: Sound absorption coefficient of filler-infused PVP membranes multiple layers at BC's: a) 0cm, b) 3cm, and c) 5cm; and d) Schematics of layering configuration.

#### 4.5.3.2 Sound Absorption Coefficient ( $\alpha$ ) Variation with Change in Thickness at Different Frequency Bands (1/3 Octave Plots)

The sound absorption coefficient variation as a function of composite thickness from seven to sixteen layers at three discrete BC's is shown in Figure 4.32. This peak shift and coefficient variation with thickness and BC was studied utilizing this analysis [Table 4.5].

With 0cm BC, an  $\alpha$ -value increment of 320%, 388%, and 561% was reported at frequency bands of 1000, 1260, and 1587Hz. At 3cm BC, the coefficient values improved significantly on the low-frequency side, which was a significant drift observed with BC variation. An  $\alpha$ -value increase of 116% to 320% was observed at 198-500Hz frequency band. With the expansion of 5cm BC, the maximum increase in absorption value of 100% to 370% was noticed at even lower frequency bands of 157-397Hz.

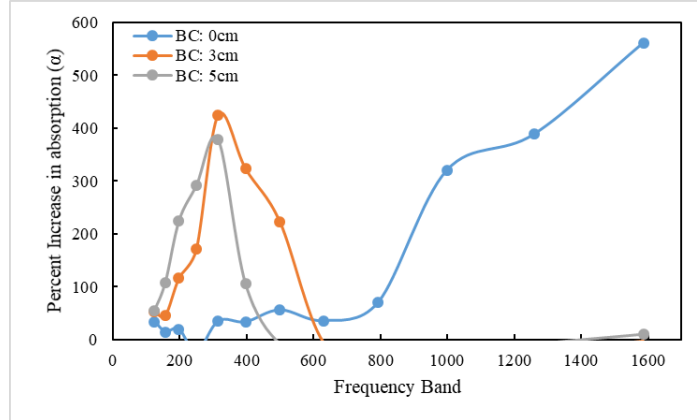


Figure 4.32: Sound absorption coefficient percent increase with thickness variation at discrete BC's for filler-infused PVP membrane multiple layers.

Table 4.5: Percent increase data for different frequency bands (1/3-Octave plot) 3cm BC.

BC	Percent increase in $\alpha$ at discrete octave frequency (Hz)											
	125	157	198	250	315	397	500	630	794	1000	1260	1587
0cm	34	15	19	-24	35	33	56	35	70	321	389	562
3cm	52	46	117	171	424	323	222	-4	-47	-48	-24	-2
5cm	55	108	225	292	378	105	-8	-35	-32	-32	-9	10

## 4.6 Sound Absorption Characteristics of Filler-Infused PVDF Fibers and Its Composites

### 4.6.1 Acoustic Sample Formulation

The PVDF specimens were prepared following section 4.5.1 [Figure 4.33].

### 4.6.2 SAP of Multiple Layers of Filler Infused PVDF Membranes at 3 Discrete BC

SAP of multiple layers of each filler infused PVDF membrane with two, three, and four layers were investigated in this section.

Filler Infused Membrane Layering Pattern							
Layers	2	3	4	7	10	13	16
CNT (C)	P+C1						
	P+C1+C2						
	P+C1+C2+C3						
GN (G)	P+G1						
	P+G1+G2						
	P+G1+G2+G3						
FS (S)	P+S1						
	P+S1+S2						
	P+S1+S2+S3						
FG (F)	P+F1						
	P+F1+F2						
	P+F1+F2+F3						
MC (M)	P+M1						
	P+M1+M2						
	P+M1+M2+M3						
C+G	P+(C1+C2+C3)+(G1+G2+G3)						
C+G+S	P+(C1+C2+C3)+(G1+G2+G3)+(S1+S2+S3)						
C+G+S+F	P+(C1+C2+C3)+(G1+G2+G3)+(S1+S2+S3)+(F1+F2+F3)						
C+G+S+F+M	P+(C1+C2+C3)+(G1+G2+G3)+(S1+S2+S3)+(F1+F2+F3)+(M1+M2+M3)						

Figure 4.33: Filler infused PVDF membranes layering blocks.

#### 4.6.2.1 SAP of CNT Based Layers

The acoustic response of the CNT filler-based layers was investigated at different BC's in Figure 4.34 (a-c). The four-layered composite was observed with a coefficient value of 0.92 at 2000Hz for zero air cavity. At 3cm BC, sharp peaks drifted to the lower frequency range of 600-1200Hz. The coefficient values of 0.68, 0.78, and 0.75 were observed for two, three, and four-layered composite at 925Hz, 860Hz, and 761Hz, which was higher than the CNT-infused PVP composites [Figure 4.34 (a)]. With 5cm BC, absorption peaks were observed in the lower frequency range of 500-700Hz. The  $\alpha$ -value of 0.7 was marked with four layers at a frequency of 724Hz [Figure 4.34 (b)].

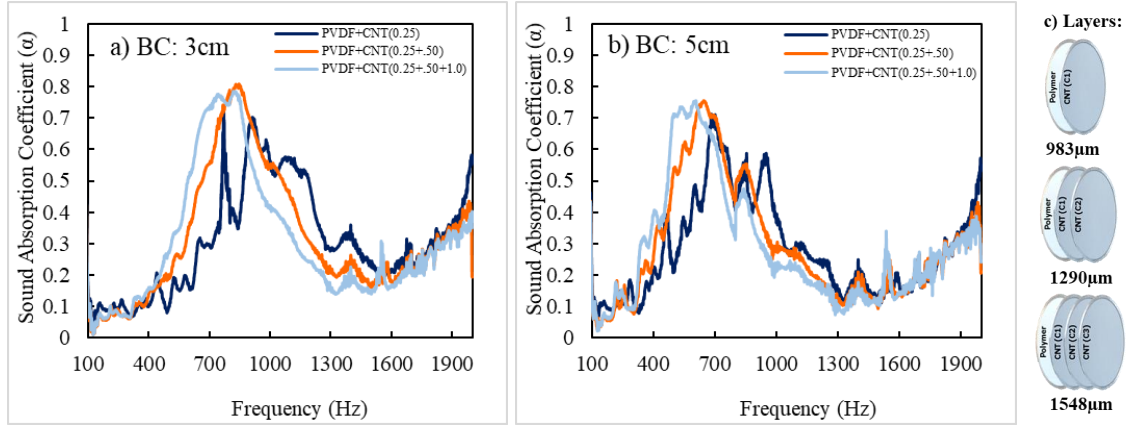


Figure 4.34: Sound absorption coefficient of CNT infused PVDF membrane layers at different BC's: a) 3cm and b) 5cm; and c) Schematics of layering configuration.

#### 4.6.2.2 SAP of GN Based Layers

The SAP of GN-based layered composites was investigated at different BC's in Figure 4.35 (a-c). The four-layered composite was observed with a coefficient value of 0.94 at 2000Hz for zero air cavity. At 3cm BC, sharp absorption peaks were observed at a lower frequency of 700-1200Hz, which was similar in range with CNT composites. The coefficient value of 0.62, 0.73, and 0.78 was observed with two, three, and four-layered composite at 958Hz, 854Hz, and 768Hz [Figure 4.35 (a)]. With 5cm BC, peaks with coefficient values of 0.6, 0.7, and 0.8 were noticed at 768Hz, 622Hz, and 558 Hz for three designed layered configurations [Figure 4.35 (b)].

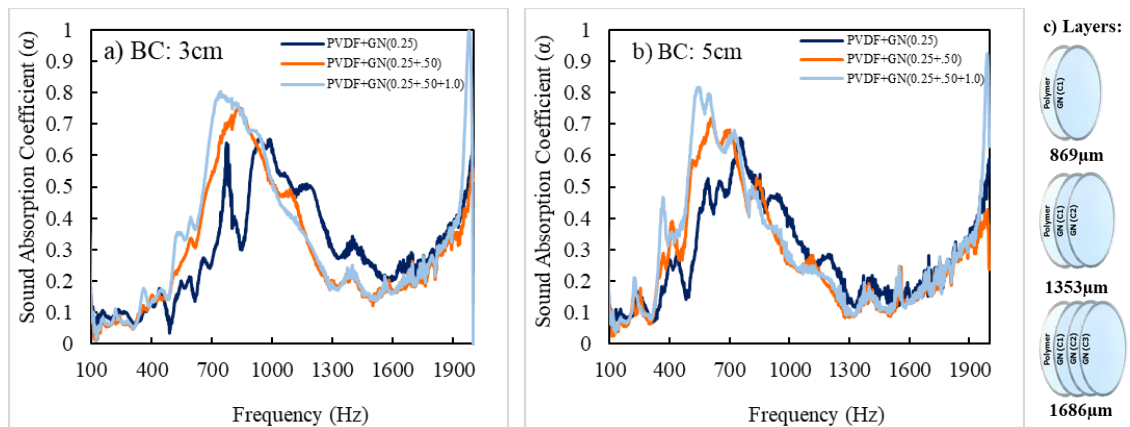


Figure 4.35: Sound absorption coefficient of GN infused PVDF membrane layers at different BC's: a) 3cm and b) 5cm; and c) Schematics of layering configuration.

#### 4.6.2.3 SAP of FS Based Layers

The SAP of FS infused PVDF layered composites were investigated at discrete BC's in Figure 4.36 (a-c). The four-layered composite was observed with a similar  $\alpha$ -value of 0.94 at 2000Hz for zero air cavity. The absorption peaks with an  $\alpha$ -value of 0.9 were not observed in PVP filler-based layered composites and not reported until eight layered PVP or PVDF composites. At 3cm BC, sharp absorption peaks were observed in the frequency range of 700-1200Hz. The maximum coefficient value of 0.74 was marked with a four-layered composite at 741Hz [Figure 4.36 (a)]. With 5cm BC, these absorption peaks moved to the frequency range of 500-700Hz with an  $\alpha$ -value of 0.7 at 692Hz and 534Hz for two and four-layered composites [Figure 4.36 (b)].

#### 4.6.2.4 SAP of FG Based Layers

The acoustic behavior of FG infused PVDF composite was tested at different BC's in Figure 4.37 (a-c). According to an existing trend, absorption peaks moved to a similar frequency range of 700-1200Hz with increased BC to 3cm. The maximum coefficient value of 0.8 was observed for four layers at 772Hz [Figure 4.37 (a)]. The maximum  $\alpha$ -value of 0.7 was observed at 558Hz for four-layered composite at 5cm BC [Figure 4.37 (b)].

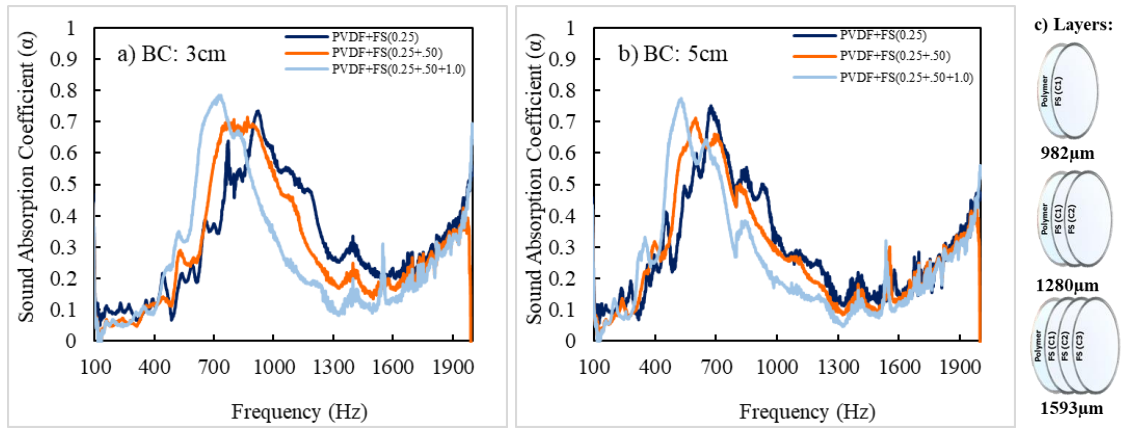


Figure 4.36: Sound absorption coefficient of FS infused PVDF membrane layers at different BC's: a) 3cm and b) 5cm; and c) Schematics of layering configuration.

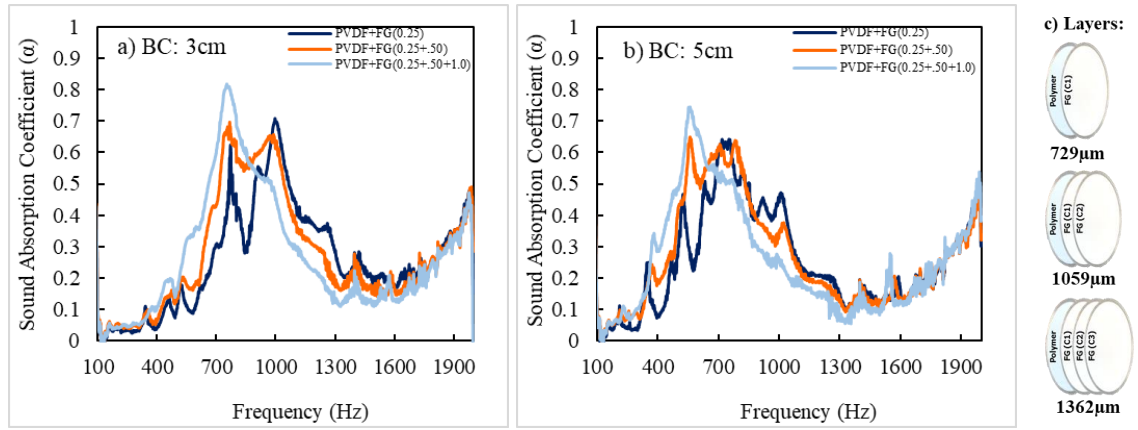


Figure 4.37: Sound absorption coefficient of FG infused PVDF membrane layers at different BC's: a) 3cm and b) 5cm; and c) Schematics of layering configuration.

#### 4.6.2.5 SAP of MC Based Layers

The SAP of MC filler-based PVDF layered composite was investigated at three BC's in Figure 4.38 (a-c). At 3cm BC, sharp peaks were noticed in the frequency range of 600-1000Hz, with a maximum  $\alpha$ -value of 0.87 at 733Hz for four-layered composite [Figure 4.38 (a)]. The MC-based four-layered composite showed better absorption than all previous samples in the specified frequency range. The addition of BC to 5cm resulted in higher absorption peaks with a shifted frequency range of 500-700Hz. The maximum coefficient of 0.78 was observed at 545Hz for four-layered composite [Figure 4.38 (b)].

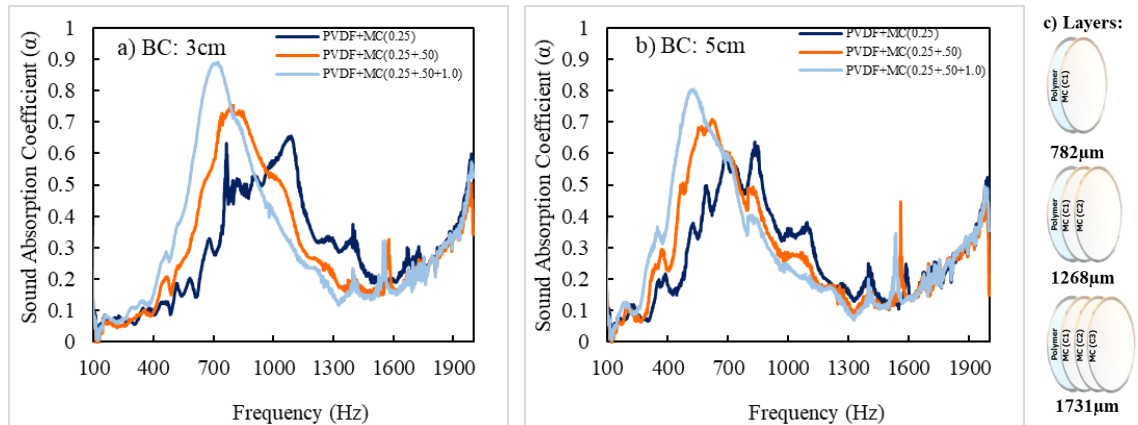


Figure 4.38: Sound absorption coefficient of MC infused PVDF membrane layers at different BC's: a) 3cm and b) 5cm; and c) Schematics of layering configuration.



#### 4.6.2.6 Sound Absorption Coefficient ( $\alpha$ ) Variation with Change in Thickness at Different Frequency Bands (1/3 Octave Plots)

The percentage increase in absorption measurements of all consecutive filler-based layered composites with thickness variation was represented in Figure 4.39 (a-b) at different BC's. The coefficient variation and absorption peak shift as a function of thickness was studied utilizing this analysis in Table 4.6. The highest increase in absorption of 136% and 203% was observed with MC-based composites at frequency bands of 500Hz and 630Hz. The variation in coefficient percent increase at frequency bands ranging from 500-800Hz follows descending order as follows; MC>CNT>FG>GN>FS [Figure 4.39 (a)]. With 5cm BC, the highest SAP was reported with MC-based composites with a maximum increase of 160% at 315Hz and 500Hz [Figure 4.39 (b)]. It was evident that the MC-based composites had a higher absorption increase with change in thickness and BC compared with preceding specimens. In general, it was noticed that PVDF based filler composites offered better absorption in low frequency than filler infused PVP composites.

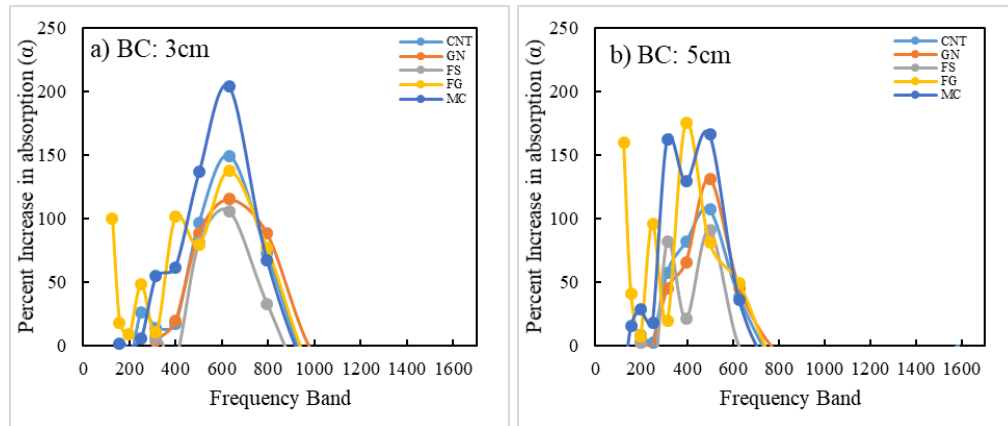


Figure 4.39: Sound absorption coefficient percent increase with thickness variation at discrete BC's for filler-infused PVDF membrane layers.

Table 4.6: Percent increase data for different frequency bands (1/3-Octave plot) 3cm BC.

Fillers	Percent increase in $\alpha$ at discrete octave frequency (Hz) for BC: 3cm											
	125	157	198	250	315	397	500	630	794	1000	1260	1587
CNT	-45	-35	-18	26	14	17	97	149	72	-28	-46	-21
GN	-32	-25	-11	-21	4	19	88	115	88	-8	-34	-23
FS	-76	-49	-36	-49	6	-12	81	106	33	-44	-58	-33
FG	100	18	9	48	11	101	79	138	77	-23	-41	-26
MC	-22	1	-2	6	55	61	136	204	67	-29	-44	-18

#### **4.6.3 SAP of Combined Layers of Filler Infused PVDF at Varying BC**

The progressive layering of the filler-based membranes was performed in the following order; a) Seven-layers composite with PVDF, three CNT, and GN infused layers, b) Ten-layers with three FS-infused layers on stack prepared in (a), c) Thirteen-layers with three FG layers on stack (b), and d) Sixteen-layers with three MC layers assembled on (c).

##### **4.6.3.1 SAP of progressive layering of filler infused PVDF membrane at discrete BC**

The SAP of combined multiple layers of filler-infused PVDF membranes was investigated at different BC's in Figure 4.40 (a-d). At 0cm BC, multiple sharp peaks were observed near the higher frequency range of 1170-1950Hz. The absorption coefficient values of 0.98, 0.98, 0.96, and 0.93 were observed for seven, ten, thirteen, and sixteen layered composites at 1950Hz, 1685Hz, 1413Hz, and 1200Hz [Figure 4.40 (a)]. The SAP of PVDF filler composites was better in the low-frequency range than PVP filler composites. With 3cm BC, sharp peaks were noticed with high coefficient values of more than 0.9 in the drifted frequency range of 400-527Hz. The absorption coefficients of 0.93, 0.98, 0.99, and 0.93 were observed for each progressive layer at 581Hz, 496Hz, 447Hz, and 406Hz, respectively [Figure 4.40 (b)]. Sixteen layered filler-based PVP composite reached the  $\alpha$ -value of 0.98 at 488 Hz with a lesser thickness of 3760 $\mu$ m, whereas sixteen-layer filler PVDF composite reached 0.99 at 447Hz with a thickness of 6496 $\mu$ m. It means that a higher thickness of composite has been compromised to maintain similar coefficient values for a little shift in respective frequencies. With 5cm BC, absorption peaks corresponding to all progressive layers moved towards a lower frequency range of 300-400Hz. The maximum absorption coefficients of 0.98 and 0.96 were observed at 347Hz and 309Hz for thirteen and sixteen layered composites [Figure 4.40 (c)].

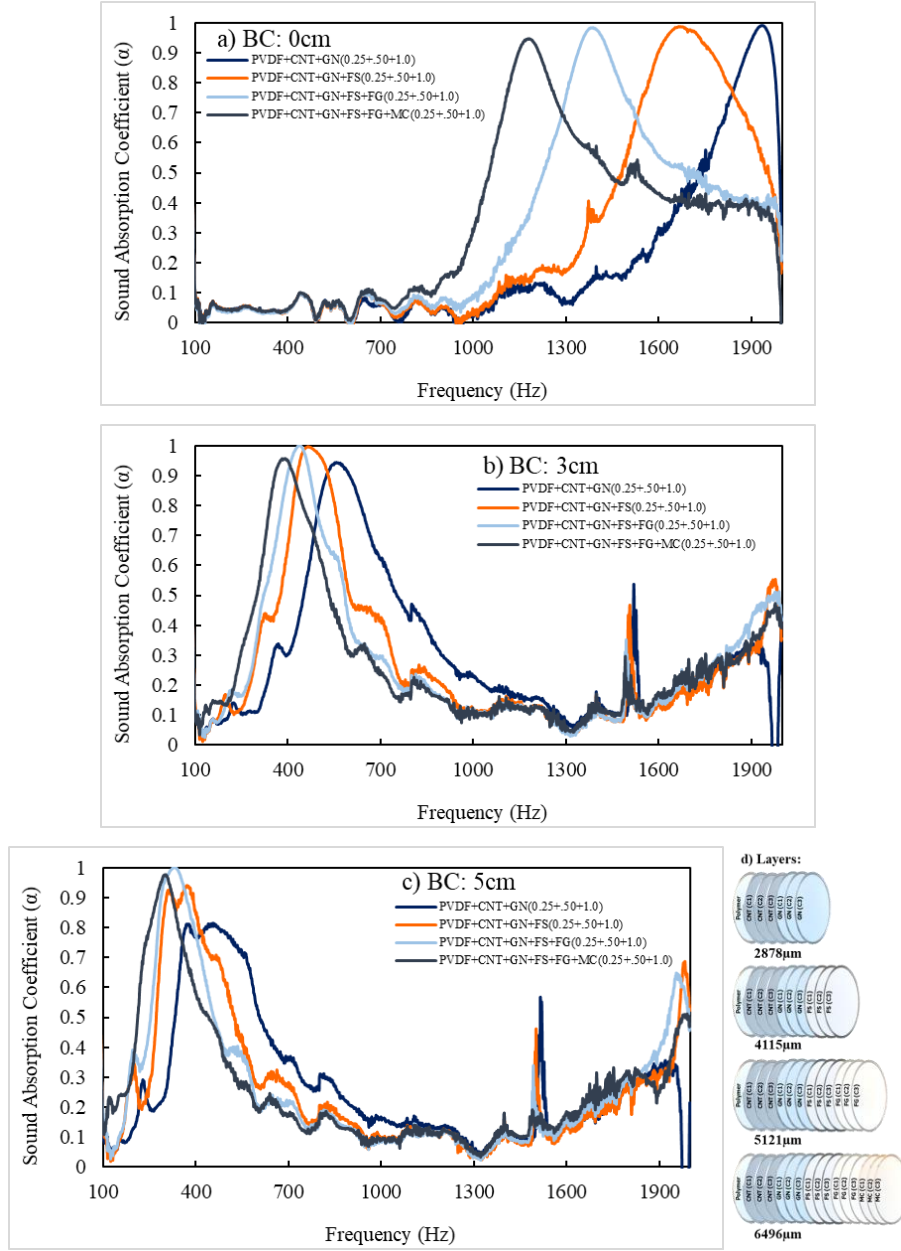


Figure 4.40: Sound absorption coefficient of filler-infused PVDF membranes multiple layers at BC's: a) 0cm, b) 3cm, and c) 5cm; and d) Schematics of layering configuration.

#### 4.6.3.2 Sound Absorption Coefficient ( $\alpha$ ) Variation with Change in Thickness at Different Frequency Bands (1/3 Octave Plots)

The SAP of these progressively layered composites was studied in terms of percentage increase in coefficient as a function of composite thickness at different BC's in Figure 4.41. The acoustic characterization carried out on composites indicates the movement of absorption peaks to low-frequency regions with a change in BC and layer thickness. The

improvement in  $\alpha$ -value with thickness variation at three discrete BC was studied in Table 4.7. With 0cm BC, an increase of 109%, 694%, and 576% in the  $\alpha$ -value was reported at frequency bands of 794, 1000, and 1260Hz. At 3cm BC, an increase of 163%, 270%, and 166% was noticed in lower frequency bands of 250Hz, 315Hz, and 397Hz. Higher percentage increments moved from 1260Hz to 315Hz with a change in BC to 3cm from 0cm, signifying the high importance of BC variation for low-frequency sound absorption. With 5cm BC variation, an increase of 218%, 193%, 176%, 257%, and 134% was observed in relatively lower frequency bands ranging from 125Hz to 315Hz.

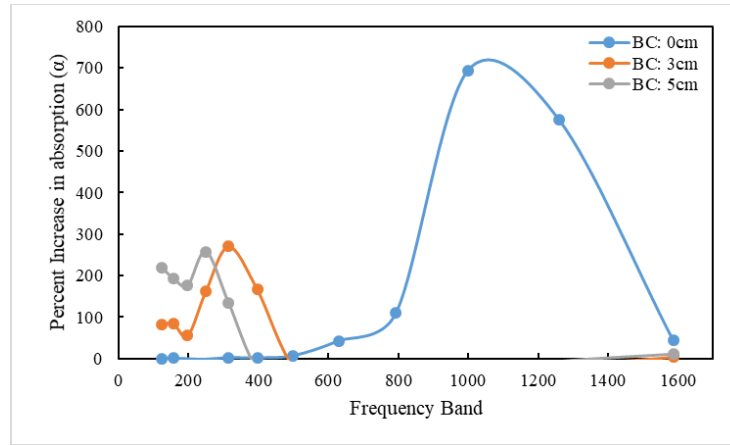


Figure 4.41: Sound absorption coefficient percent increase with thickness variation at discrete BC's for filler-infused PVDF membrane multiple layers.

Table 4.7: Percent increase data for different frequency bands (1/3-Octave plot) 3cm BC.

BC	Percent increase in $\alpha$ at discrete octave frequency (Hz)											
	125	157	198	250	315	397	500	630	794	1000	1260	1587
0cm	0.4	1	0	-1	2	2	7	43	110	695	576	44
3cm	82	85	55	163	270	167	-18	-61	-60	-47	-20	4
5cm	218	193	177	257	134	-23	-53	-55	-48	-36	-6	11

#### 4.7 Summary and Conclusions

The experimental investigations suggest that the maximum coefficient values of 0.95, 0.98, and 0.99 were observed at 1663, 526, 406Hz with a pure PVP-based sixteen-layer composite at different BC's of 0, 3, and 5cm. On the other hand, twenty layers resulted in a maximum coefficient value of 0.92 at the lowest frequency of 363Hz at 5cm BC [Table 4.8]. The acoustic response of PVDF fiber membranes was generally observed to be better

than PVP membranes due to variation in thickness. Maximum  $\alpha$ -values of 0.96, 0.99, 0.99 were observed at lower frequencies of 1028, 363, and 238Hz, which was very close to PVP composites, but the frequency range was observed on the lower frequency side. Similarly, for twenty layers, the highest coefficient value of 0.98 was observed at an even lower frequency of 259Hz at 5cm BC [Table 4.9]. The PVP and PVDF layers' combination resulted in a maximum coefficient of 0.94, 0.99, and 0.98 at 1249, 406, and 322 Hz. These peaks were observed in the mid-frequency range of the PVP and PVDF sixteen layers pattern [Table 4.10].

Table 4.8: Maximum  $\alpha$ -values at respective frequencies for PVP nanocomposites.

PVP Layers	BC: 0cm		BC: 3cm		BC: 5cm	
	Max. Absorption Peak		Max. Absorption Peak		Max. Absorption Peak	
	f (Hz)	$\alpha$	f (Hz)	$\alpha$	f (Hz)	$\alpha$
L-1	2000	0.32	1157	0.86	1709	0.77
L-2	2000	0.37	1300/1727	0.53	1066	0.46
L-4	2000	0.52	1027	0.89	721	0.73
L-8	2000	0.48	724	0.89	563	0.86
L-16	1663	0.95	526	0.98	406	0.99
L-20	1536	0.88	435	0.88	229/363	0.74/0.92

Table 4.9: Maximum  $\alpha$ -values at respective frequencies for PVDF nanocomposites.

PVDF Layers	BC: 0cm		BC: 3cm		BC: 5cm	
	Max. Absorption Peak		Max. Absorption Peak		Max. Absorption Peak	
	f (Hz)	$\alpha$	f (Hz)	$\alpha$	f (Hz)	$\alpha$
L-1	2000	0.37	1260	0.71	758/1004	0.83/0.84
L-2	2000	0.83	1075	0.68	642	0.78
L-4	1985	0.82	743	0.86	383/578	0.85/0.94
L-8	1624	0.99	364/565	0.87/0.93	236/423	0.82/0.99
L-16	1028	0.96	273/363	0.82/0.99	238/321	0.99/0.96
L-20	892	0.96	291/2000	0.92	259/2000	0.98/0.85

Table 4.10: Maximum  $\alpha$ -values for combined PVP and PVDF nanocomposites.

BC: 0cm			BC: 3cm		BC: 5cm	
PVP/PVDF	Max. Absorption Peak		Max. Absorption Peak		Max. Absorption Peak	
Layers	f (Hz)	$\alpha$	f (Hz)	$\alpha$	f (Hz)	$\alpha$
L-2	2000	0.35	1085	0.79	829	0.78
L-4	2000	0.91	849	0.85	628	0.82
L-8	1937	0.98	556	0.96	417	0.95
L-16	1249	0.94	406	0.99	322	0.98
L-20	1075	0.94	384	0.86	257	0.94

The experimental investigation shows that the PVP filler-based composites resulted in a maximum coefficient of 0.86 with MC-based four-layered composite 947 $\mu$ m thick at 907Hz (3cm BC) and 636Hz (5cm BC). The MC-based four-layered composites resulted in a slightly higher coefficient value at the reduced frequency when compared with pure PVP four-layered membrane of a similar thickness at different BC's. Similarly, for the PVDF filler-based layered composites, the maximum coefficient values of 0.88 and 0.80 were observed with four-layered MC-based composites 1731 $\mu$ m thick at 710Hz (3cm BC) and 530Hz (5cm BC). PVDF MC-based four-layered composites resulted in a slight frequency shift from 743 to 710Hz -3cm BC and from 578 to 530Hz -5cm BC with an  $\alpha$ -value of 0.87 compared with pure PVDF four-layered composite 2091 $\mu$ m thick.

Experimental investigations for the PVP filler-based progressive layering composites resulted in higher coefficient values of 0.96 (0cm BC), 0.99 (3cm BC), and 0.99 (5cm BC) at lower frequencies of 1689, 483, and 392Hz, respectively for sixteen layered composite - 3769 $\mu$ m thick. With filler-based sixteen layers,  $\alpha$ -values greater than 0.96 were observed at lower frequencies than pure PVP-based sixteen layered composite where  $\alpha > 0.96$  was reported at 526Hz and 406Hz for 3cm and 5cm BC's. The PVP-based filler composites achieved the maximum sound absorption coefficient value of 0.99 at different BC's for the frequency range of 390-500Hz [Table 4.11]. The acoustic response of the PVDF filler-based progressive layering composites resulted in  $\alpha$ -values of 0.94, 0.95, and 0.97 at even lower frequencies of 1189 (0cm BC), 399 (3cm BC), and 305Hz (5cm BC) for sixteen layers - 6496 $\mu$ m thick when compared with PVP filler-based composites. Higher  $\alpha$ -values of 0.98 and 0.99 were achieved with thirteen layers, but the peaks were present in a slightly higher frequency range of 560Hz and 460Hz. The PVDF filler-based layered composites

achieved coefficient values greater than 0.96 in the lower frequency range of 300-450Hz at different BC's [Table 4.12].

Table 4.11: Maximum  $\alpha$ -values for PVP-Filler-based composites.

<b>PVP+Filler Layers</b>	<b>BC: 0cm</b>		<b>BC: 3cm</b>		<b>BC: 5cm</b>	
	<b>Max. Absorption Peak</b>		<b>Max. Absorption Peak</b>		<b>Max. Absorption Peak</b>	
	<b>f (Hz)</b>	<b><math>\alpha</math></b>	<b>f (Hz)</b>	<b><math>\alpha</math></b>	<b>f (Hz)</b>	<b><math>\alpha</math></b>
L-7	2000	0.85	729	0.87	566	0.78
L-10	2000	0.94	623	0.92	474	0.96
L-13	1948	0.82	560	0.98	460	0.99
L-16	1689	0.96	483	0.99	392	0.99

Table 4.12: Maximum  $\alpha$ -values for PVDF-Filler-based composites.

<b>PVDF+Filler Layers</b>	<b>BC: 0cm</b>		<b>BC: 3cm</b>		<b>BC: 5cm</b>	
	<b>Max. Absorption Peak</b>		<b>Max. Absorption Peak</b>		<b>Max. Absorption Peak</b>	
	<b>f (Hz)</b>	<b><math>\alpha</math></b>	<b>f (Hz)</b>	<b><math>\alpha</math></b>	<b>f (Hz)</b>	<b><math>\alpha</math></b>
L-7	1937	0.99	565	0.94	469	0.8
L-10	1686	0.98	478	0.99	382	0.94
L-13	1398	0.98	449	0.99	342	0.98
L-16	1189	0.94	399	0.95	305	0.97

## **Chapter 5. Filtration Characteristics of Electro-Spun Nanofiber Composites**

### **5.1 Introduction**

The filtration characteristics of the electro-spun PVDF nanofiber membranes, its filler composites, conventional masks, and nanofiber loaded surgical masks were investigated in this section. The breathability of these membranes and their composites was tested in a laboratory-scale pressure drop measurement experimental set-up. The morphological attributes of the nanofiber membranes were carried out using the SEM micrographs. These membranes were fabricated to prevent or filter the micro or nano-scale bacteria, viruses, pollutants, or aerosols. The fillers chosen for this study includes CNT, GN, TiO<sub>2</sub>, and Cu NP's. These fillers exhibit anti-bacterial or anti-viral behavior wherein the positively charged ions of these substance attacks the exterior layer of bacteria or virus and deactivates them by breaking their protein structure. Nanofiber membranes were designed to achieve the pressure drop rating of these N-95 medical-grade masks wherein readily available surgical masks with microfibers were modified with nanofiber layers to filter our particles nano-scale, maintaining the N-95 level pressure drop.

### **5.2 Experimental Methodology**

#### **5.2.1 Filtration-Ready Specimen Formulation**

The filtration characterization of designed filter media was carried out in five stages: 1) Stage 1 includes testing of different conventional masks including Surgical Masks (SM) and different grade N-95 masks used by front liners, manufacturing industry, and COVID healthcare professionals, 2) Stage 2 involves testing of PVDF nanofiber samples manufactured from varying concentrations of; 0.25wt.%, 0.5wt.%, and 1.0wt.% at different electrospinning time of 6, 8, and 10 minutes, 3) Stage 3 includes testing of filler infused nanofiber samples manufactured from four different fillers (0.25wt.%) at designed electrospinning times, 4) Stage 4 involves the testing of nanofiber membranes manufactured at different times to reach the N-95  $\Delta P$  equivalency, and 5) Stage 5 includes testing of resultant nanofiber membranes layered on microfiber loaded SM to reach N-95 pressure drop barrier level rating and to filter out particles at nano-scale level [Table 5.1].



Table 5.1: Description of various filtration-ready specimens.

Filtration-Ready Specimen Formulation					
Stage 1	Conventional masks				
	1	2	3	4	5
	Surgical Mask	N-95 (8200)	N-95 (8110S)	N-95 (1860)	N-95 (9500)
Stage 2	PVDF nanofibers at varying concentrations				
	C1		C2	C3	
	20wt.%		22wt.%	25wt.%	
Stage 3	PVDF + Varying fillers nanofibers				
	Filler 1	Filler 2	Filler 3	Filler 4	
	CNT	GN	TiO2	Cu NP's	
Stage 4	Nanofibers at varied electro-spin times (343Pa)				
	PVDF (C1 C2 C3)		PVDF + Fillers		
Stage 5	Nanofiber layering with surgical masks				
	PVDF (C1 C2 C3)		PVDF + Fillers		

### 5.2.2 Fabrication of Filter-Ready Electro-Spun Samples

Polymeric solution of PVDF was prepared at three different concentrations of 20, 22, and 25wt.% in DMF solution at 75°C for 24 hours utilizing the magnetic stirrer. Similarly, the filler-based solutions were prepared by mixing filler micro/nano particles in polymeric solution using the ultrasonic mixer for 30min. The prepared solution was transformed into nanofibers utilizing a lab-scale electrospinning set-up [Figure 5.1]. All the filtration-ready membranes manufactured at different electrospinning times of 6, 8, and 10min were extracted in rectangular mask sheet form using masking tapes. The extraction process ensures the membrane structural integrity while testing and provides the wrinkle-free surface for further analysis.

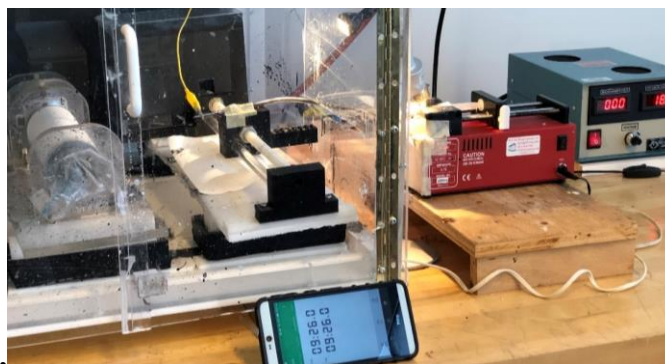


Figure 5.1: Demonstration of the time-controlled electrospinning process for manufacturing of filtration-ready nanofiber membranes.

### 5.2.3 Characterization and Testing of Filter Media

Nanofiber membrane-based filter materials were produced with precise time-controlled electrospinning to regulate the specific weight of the sheets. In order to ensure the homogenous nanofiber layering pattern, the precise needle movement was regulated by the Arduino-powered stepper motor. The homogenous layering pattern ensures the pressure drop data repeatability at different spots on a mask material. Figure 5.2 (a) shows the nanofiber membrane samples produced for pressure drop testing. The red dotted circles show the testing locations on the membrane surface. Figure 5.2 (b-d) shows the real-time pictures of the testing. The pressure drop measurements were carried out at three locations of a filter material sheet, and the average pressure drop data of three sheets were reported in further sections. Morphological attributes of these nanofiber filter membranes were studied using the SEM micrographs. The average of at least fifty fibers was taken at different locations of a sample in SEM images.

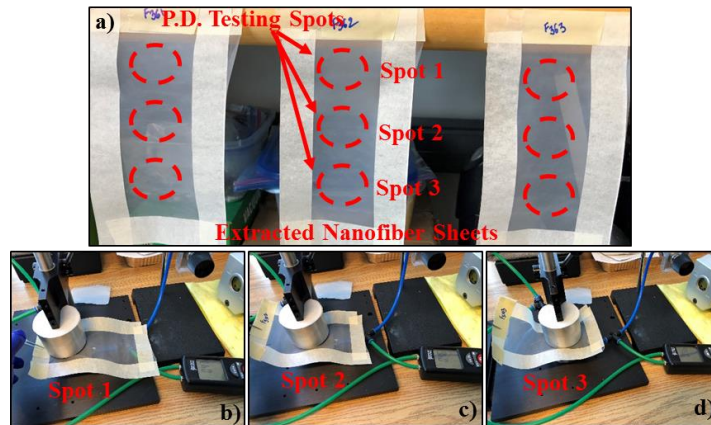


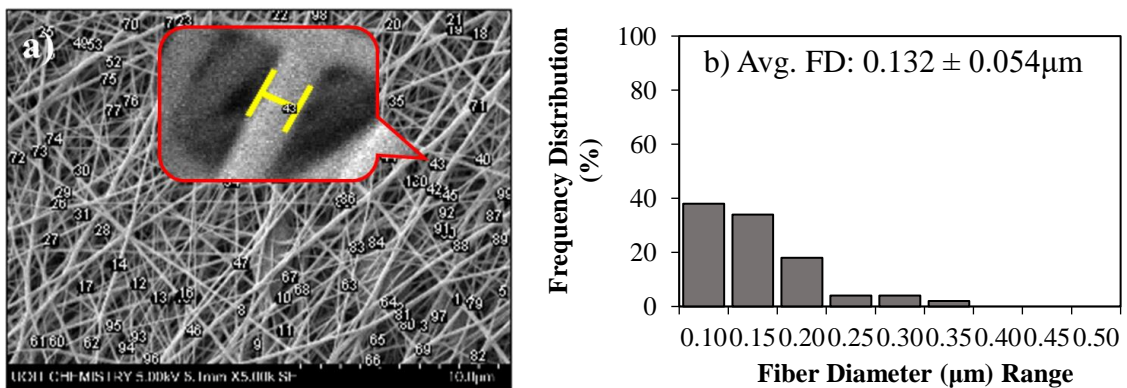
Figure 5.2: (a) Filter-ready nanofiber membrane samples with dotted red circles representing testing locations, and Pressure drop testing of single specimen at spot 1 (b), spot 2 (c), and spot 3 (d).

## 5.3 Results and Discussion

### 5.3.1 Morphological Characterization of Electro-Spun Filter Samples

The fiber-based filter media's filtration characteristics depend on the fiber morphology of the samples wherein fiber diameter and distribution play a significant role in regulating the filtration properties [204]. The nanofiber samples manufactured from the process of electrospinning consist of very thin fiber with a high ratio of surface area to volume and

pores, which can intercept the micro/nano particles [205]. Figure 5.3 (a-f) demonstrates the fiber diameter measurements and distribution of PVDF nanofibers manufactured at a different polymeric concentration of 20, 22, and 25wt.%. Figure 5.3 (a) shows the SEM micrograph of the PVDF 20wt.% nanofiber membrane. Figure 5.3 (b) shows the diametric distribution of the fibers, and it shows that the average fiber diameter was approximately  $0.132\mu\text{m}$  with a standard deviation of 0.054. Fibers at PVDF20 appear to be thin and smooth, with very small gaps in between when compared to other concentration configurations. High density of smaller fibers with a narrow fiber diameter distribution range of  $0.100\mu\text{m}$  to  $0.200\mu\text{m}$  was observed for PVDF20. Figure 5.3 (c) describes the fiber structure of PVDF 22wt.%, and Figure 5.3 (d) shows the respective distribution. It was observed the fibers were relatively bigger than the previous configuration with an average diameter of  $0.167 \pm 0.069\mu\text{m}$ . The distribution shows that membranes comprise fibers lying in the range of  $0.150\mu\text{m}$  and SEM image visual appearance indicates higher air gaps. Figure 5.3 (e) shows the SEM representation of PVDF 25wt.% with diameter distribution determined in Figure 5.3 (f). The diametric measurements indicate the higher diameter value of  $0.301 \pm 0.138\mu\text{m}$  when compared with other configurations. The mixed combination of thick and thin fibers scattered in broader distribution was observed with the current configuration. The visual appearance of fibers indicates a higher air gap between the fiber structures. Fiber structure with the least diameter and low air gap results in higher pressure drop due to less space for the air to travel. Larger fibers with comparatively high air gaps reduce the pressure drop by providing more passage for the air and particulates to travel. Higher filtration efficiencies can be achieved with the least fiber diameter and small air gaps, but the breathability is compromised with higher pressure drop [137,205].



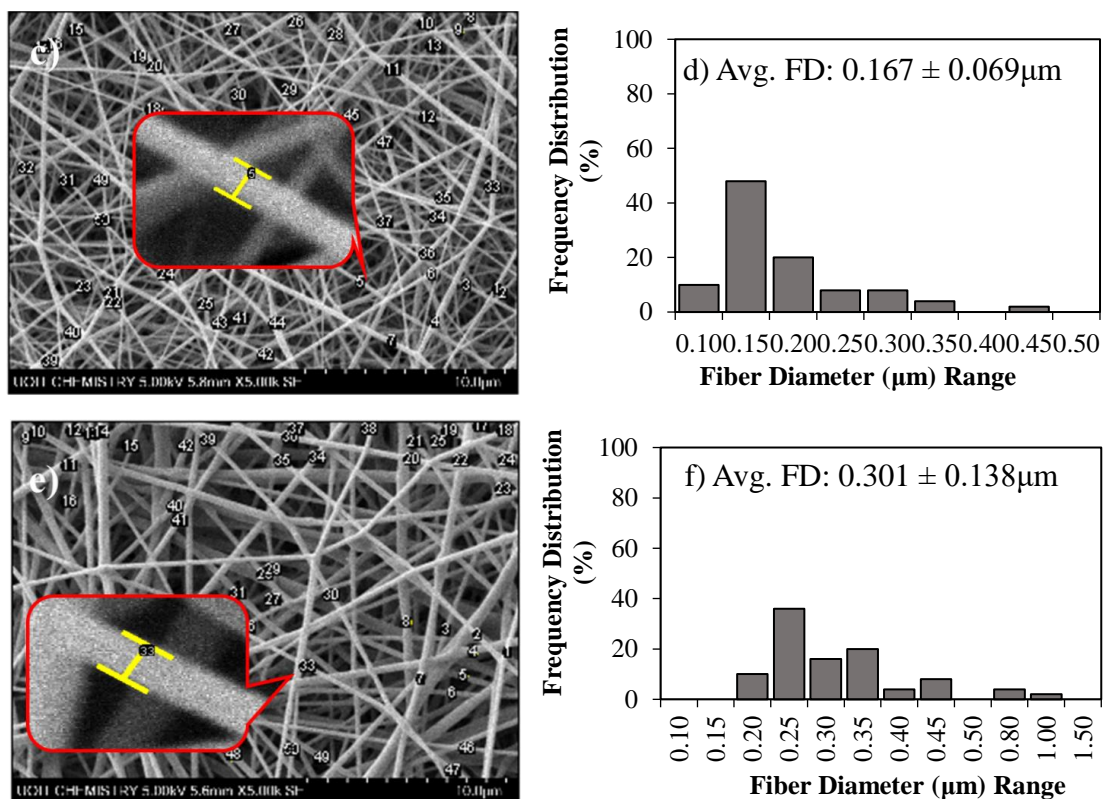


Figure 5.3: SEM micrographs with fiber diameter and distribution for samples; PVDF 20wt.% (a-b), PVDF 22wt.% (c-d), and PVDF 25wt.% (e-f).

Filtration characteristics of filler infused PVDF membranes were investigated in this section [Figure 5.4 (a-h)]. The inclusion of various metal and non-metal-based fillers was carried out to de-activate the virus/bacterial attack on the structure. These micro/nano particles adhere to the fiber structure without affecting the charge bearing capacity of electro-spun fibers (classic behavior) and without any change in the structural integrity of the fibers [206]. Addition of various filler particles like Carbon Nanotubes (CNT) [171], Graphene (GN) [207], Titanium Oxide ( $\text{TiO}_2$ ) [155,204,206], and Copper Nano-Particles (CuNP's) [206] have been reported in several studies investigating filtration characteristics of filler infused nanofiber membranes. Figure 5.4 (a) shows the diametric measurements of CNT (0.25wt.%) infused PVDF nanofibers, and Figure 5.4 (b) shows the respective fiber diameter distribution. It was observed that with the addition of CNT particles in PVDF 20wt% solution, the average fiber diameter increased to  $0.251 \mu\text{m}$  with a standard deviation of 0.108. Fibers were scattered in a narrow range of  $0.200\text{--}0.300 \mu\text{m}$  with this configuration. CNT infused fibers were observed to be smooth and long, with very few beads present on

the structure. The electrospinning of the CNT added PVDF solution was complicated compared with other filler-based solutions due to the solution viscosity and corresponding electric field action. Figure 5.4 (c) demonstrates the fiber diameter and structure of the GN (0.25wt.%) infused fibers with the corresponding fiber distribution chart described in Figure 5.4 (d). Average fiber diameter measurements of  $0.220 \pm 0.055\mu\text{m}$  were observed with current configuration with a narrow distribution of fibers, lying in the range of 0.200-0.250 $\mu\text{m}$ . GN infused fibers were observed to carry the fibers thinner than the CNT infused fibers with lesser air gap comparatively, which can be attributed to the high surface area, smaller size, and better electro-spin ability graphene infused polymers [208]. The fibers were observed with very few beads and smooth and long structures with comparatively thinner fibers on the surface. Figure 5.4 (e) shows the diametric measurements of  $\text{TiO}_2$  (0.25wt.%) infused PVDF fiber. Figure 5.4 (f) shows the fiber diameter distribution. The fibers diameters were observed to be very close in measurement with GN nanofibers with an average diameter value of  $0.219 \pm 0.106\mu\text{m}$ , wherein the fibers were observed in the range of 0.200-0.250 $\mu\text{m}$ . Smooth fibers with very few beads on structure were observed with a broader distribution range of diameters than preceding samples. Reduced diameter measurements (compared with CNT-based fibers) of  $\text{TiO}_2$  infused fibers could be attributed to the high surface area and smaller  $\text{TiO}_2$  particles [209]. Figure 5.4 (g) shows the SEM micrograph of the copper nanoparticles (0.25wt.%) infused PVDF nanofibers. The diametric measurements and their distribution were explained in Figure 5.4 (h). The average fiber diameter was observed to be  $0.229 \pm 0.110\mu\text{m}$ , which was slightly higher than GN, and  $\text{TiO}_2$  infused nanofibers. CuNP infused nanofibers were observed to be loaded with few beads (comparatively higher than all preceding samples) with broader distribution of fiber measurements. The visual appearance of the Cu-infused nanofiber membranes was brown, which was different from all other samples, and the particles had no significant effect on the diameter measurements [210].



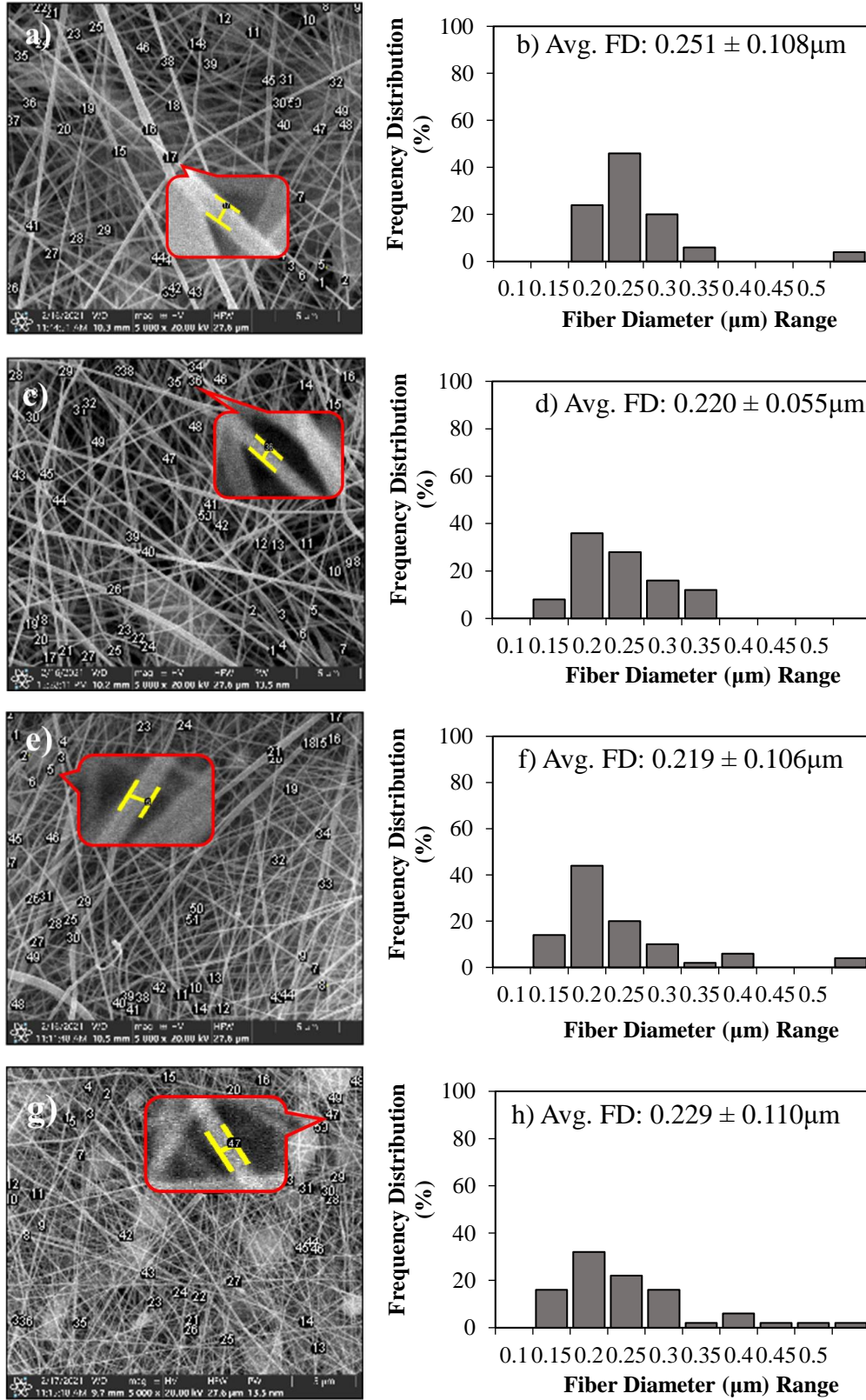


Figure 5.4: SEM micrographs with fiber diameter and distribution for samples; CNT 0.25wt.% (a-b), GN 0.25wt.% (c-d), TiO<sub>2</sub> 0.25wt.% (e-f), and CuNP's 0.25wt.% (g-h).

### 5.3.2 Pressure Drop ( $\Delta P$ ) Measurements of Conventional Masks

Pressure drop measurements of various conventional mask specimens were tested in this section, and the pressure drop data for each sample was compared with technical data available for the respective masks. Different types of masks currently used by frontline workers and the ordinary public were tested. The test results were very close to the available technical data issued by the company. Figure 5.5 shows the samples of conventional used for the test, and Table 5.2 below provides the detailed description of the mask.

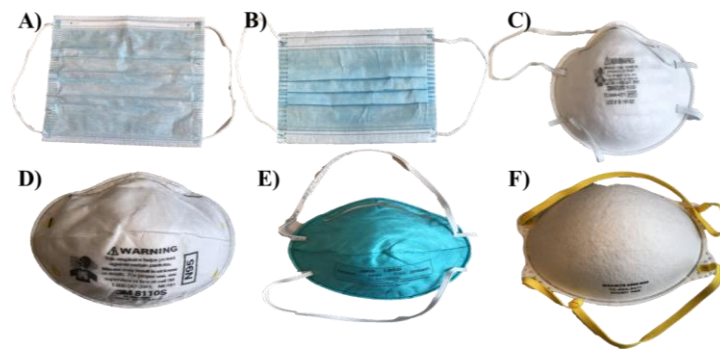


Figure 5.5: Description of the various conventional mask samples.

Table 5.2: Detailed description of masks represented by symbols (A-F).

Sample Name	Sample
A	Surgical Face Mask-1 Blue-3Ply-Universal-With ear loops
B	Surgical Face Mask-2 Blue-3Ply-Universal-With ear loops
C	N-95 Particulate Respirator – 8200
D	N-95 Particulate Respirator - 8110S
E	N-95 Healthcare Particulate Respirator & Surgical Mask - 1860
F	N-95 Particulate Respirator - 9500

The conventional Surgical Masks (SM) were observed to have a low-pressure drop of approximately 194Pa (Sample A). The least pressure drop of 106Pa was observed with sample B. SM's are generally used by most public and are comparatively comfortable for long duration wear ability. These masks offer comfort, but the layered microfibers are not sufficient to prevent us from nano-scale viral/bacterial infections. Different grade of N-95 masks was tested, and measurements show that the mask currently in use by the COVID ward frontline workers (Sample E) has the highest pressure drop of 344Pa. This is very

close to the pressure drop data issued by the company (343Pa approx.). On the other hand, the surgical face mask has the lowest pressure drop compared to different N-95 masks. This can be attributed because the N-95 mask has more layers densely packed together with higher thickness. These N-95 masks are currently NIOSH approved for medical use, but it provides discomfort to the users because of tight enclosure and elastic straps. The average pressure drop data for these masks calculated in this section also validates measurement accuracy compared with the available technical data [Figure 5.6].

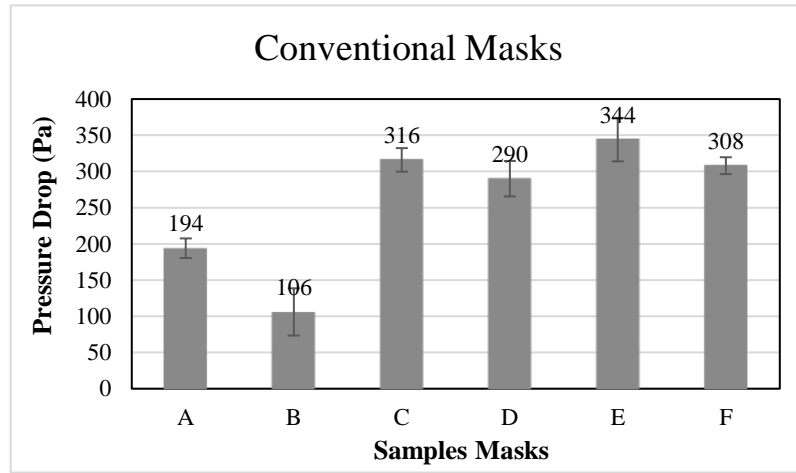


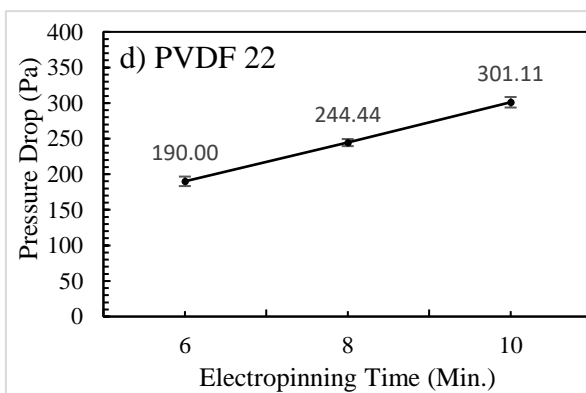
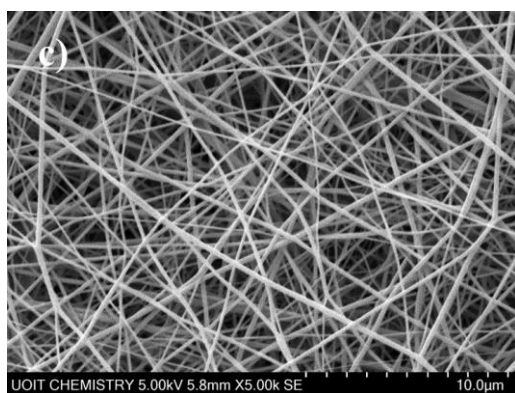
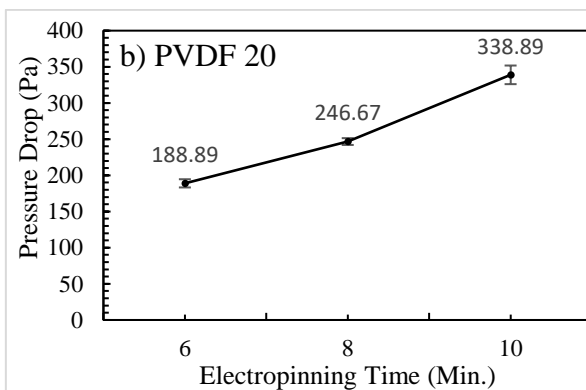
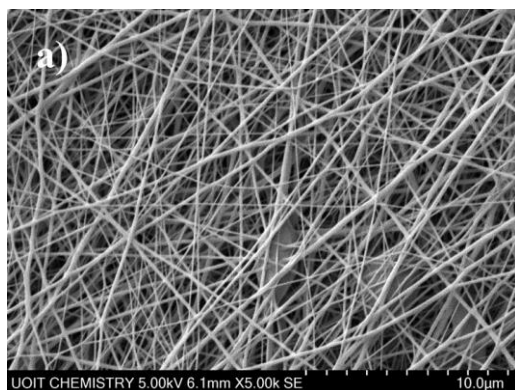
Figure 5.6: Average pressure drop measurements of various conventional masks.

### 5.3.3 Effect of Polymer Concentration on $\Delta P$ Measurements of Nanofiber Samples

The pressure drop measurements of the polymeric nanofiber membranes manufactured at different electrospinning times were investigated in Figure 5.7 (b), (d), and (f) along with their respective SEM micrographs [Figure 5.7 (a), (c), and (e)]. Pressure drop measurements for PVDF 20wt.% were observed to be the highest among all configurations. The pressure drop values were reported to be 188, 246, and 338Pa for 6, 8, and 10min time [Figure 5.7 (b)]. The pressure drop values increased with an increase in electro-spin time as it changes the weight and deposition amount of fibers on the surface. More fibers were present on the membrane surface with higher time, which prevents the air flow and the pressure drop reduces. Low fiber diameter measurements of  $0.132\mu\text{m}$  were observed for PVDF 20, with a more significant number of smaller fibers present on the surface [Figure 5.7 (a)]. Polymer concentration plays an essential role in regulating the fiber diameter and structures wherein higher concentration results in higher fiber diameter



[182,211]. With the further increase in polymer concentration to 22wt.%, the pressure drop remains almost similar for 6min spun membrane (190Pa). In contrast, it decreases slightly to a lower value of 244Pa (8min) and 301Pa (10min) [Figure 5.7 (d)]. The visual attributes of this configuration shows larger fibers with more air gaps in between compared with PVDF20. The average fiber diameter value was  $0.167\mu\text{m}$ , which was higher than PVDF20. With bigger fibers and larger pore sizes, it's relatively easier for the air to pass through the channels, further reducing the pressure drop through the material thickness [204,205]. Higher concentration of 25wt.% results in minimum pressure drop with lowest values of 128, 162, and 192 Pa which was a significant drop in pressure across the surface compared to other configurations [Figure 5.7 (f)]. The corresponding membrane has an average diameter of  $300\mu\text{m}$  with broader distribution of fibers [Figure 5.7 (e)]. It was evident from the experimental investigations that with increased concentration, the fiber diameter was increasing with broader distribution of fiber sizes and pore gaps, resulting in a significant drop in pressure measurements.



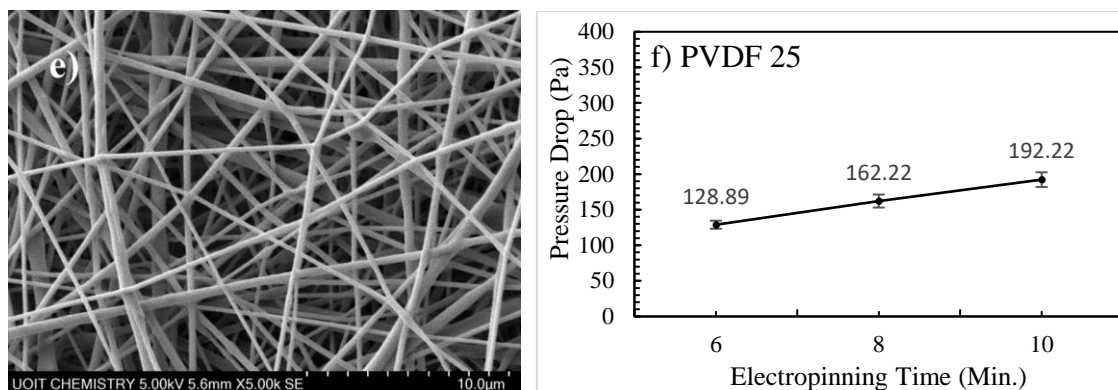


Figure 5.7: SEM micrographs and  $\Delta P$  measurements at different electrospinning times for configurations; PVDF 20wt.% (a-b), PVDF 22wt.% (c-d), and PVDF 25wt.% (e-f).

The electrospinning time regulates the number of fibers accumulated on the collector screen, and the extracted membrane weight changes with variation in time. Figure 5.8 shows the variation in nanofiber membrane specific weight with time. It was evident that with an increase in electrospinning time, the basis weight was increasing, which is due to the increased amount of fiber deposition in a specific area. It was observed that with concentration change from 20wt.% to 25wt.%, the basis weight increased significantly, which can be due to the change in single fiber weight as the fiber diameter increased from 0.132 μm to 0.301 μm. The higher fiber diameter carried more material per unit length affecting the pressure drop across these membranes.

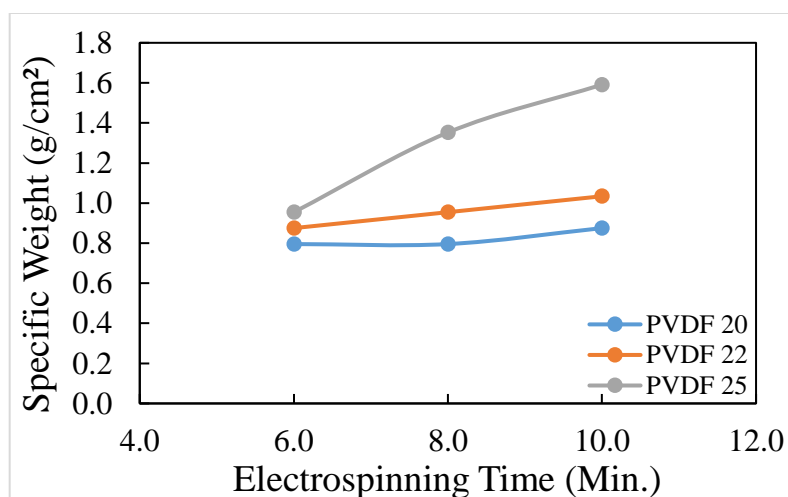


Figure 5.8: Variation in the specific weight of PVDF nanofiber membrane at different electrospinning times for varying polymeric concentrations.

The effect of fiber diameter variation on pressure drop with change in time and concentration was investigated in Figure 5.9. The minimum and maximum pressure drop of 128.89Pa and 338.89Pa were observed for 6min PVDF 25 and 10min PVDF20 samples. With the smallest fiber diameter of 0.132 $\mu\text{m}$ , higher pressure drop values were noticed, and with a high fiber diameter of 0.300 $\mu\text{m}$ , the lowest pressure drop values were observed. Higher pressure drop measurements corresponding to the lowest diameter confirm the high density of small nano-scale fibers present in a volume that can prevent particulates of that size or even smaller to infiltrate past the membrane.

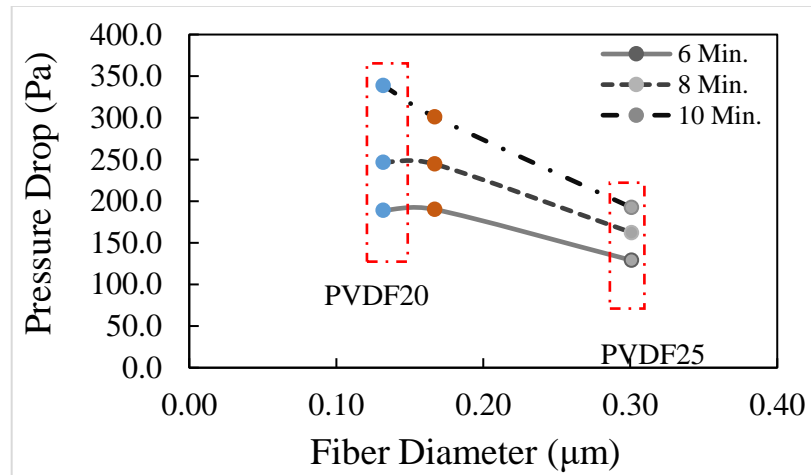
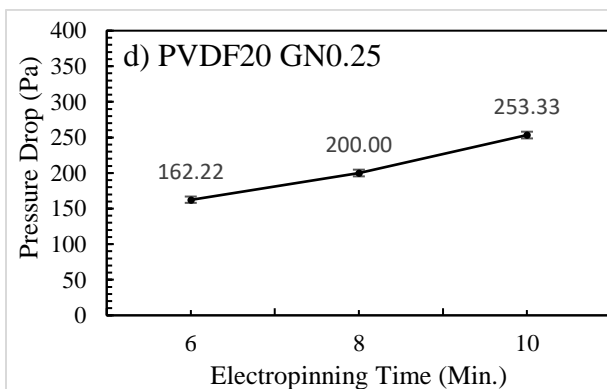
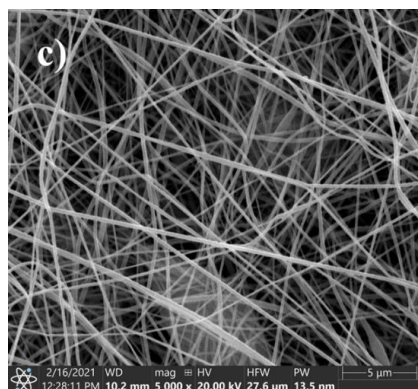
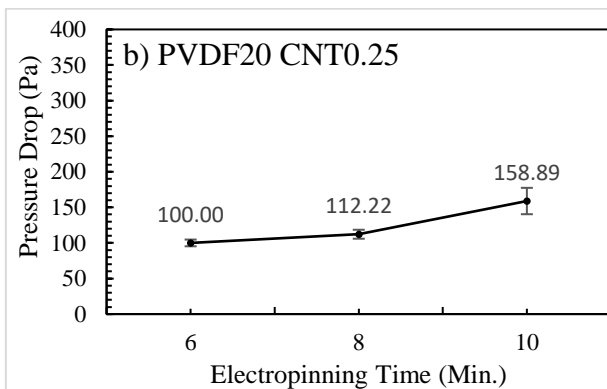
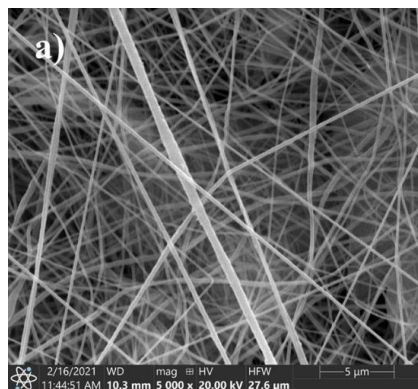


Figure 5.9: Fiber diameter versus pressure drop of nanofiber membranes produced at different electrospinning times and concentrations.

#### 5.3.4 Effect of Filler Infusion on $\Delta P$ Measurements of Nanofiber Samples

The pressure drop measurements of the filler-infused nanofiber membranes manufactured at different electrospinning times were investigated in Figure 5.10 (b, d, f, and h). The fiber morphology of the respective samples was analyzed using SEM images in Figure 5.10 (a, c, e, and g). Figure 5.10 (b) shows the pressure drop measurements of CNT infused PVDF20 membrane, and it shows the least pressure drop among all samples tested in this chapter. The lowest pressure drops of 100, 112, and 158Pa were reported at 6, 8, and 10min electrospinning time. Nanofibers were observed with an average diameter of 0.251 $\mu\text{m}$ . The lowest pressure drop could be attributed due to the complexity in electrospinning of CNT added viscous solution. Membranes infused with CNT were thinner with comparatively larger air gaps than other samples leading to the significant pressure drop [Figure 5.10 (a)]. On the contrary, GN infused membranes resulted in higher

pressure drop of 162, 200, 253Pa at respective electrospinning time, which was higher than the CNT-based membranes [Figure 5.10 (d)]. Graphene has a higher surface area and solubility with polymeric solution, resulting in smooth electrospinning of nanofibers with smaller diameters [212]. GN infused membranes show smooth and thinner fibers oriented in random order. The fiber diameter of 0.220 $\mu$ m was observed, with the majority of the fibers lying in the range of 0.220-0.250 $\mu$ m [Figure 5.10 (c)]. TiO<sub>2</sub> infused membranes exhibit similar pressure drop behavior as the GN infused membranes with approximate values of 160, 197, and 251Pa at respective electro-spun times [Figure 5.10 (e)]. The corresponding fiber diameter measurements had a similar diametric average of 219 $\mu$ m compared with GN-based membranes. The fibers also appeared smooth, long, and with very few beads on the fiber structure [Figure 5.10 (c)]. On the contrary, CuNP infused membranes result in a slightly lower pressure drop of 151, 190, and 240Pa than GN and TiO<sub>2</sub> membranes [Figure 5.10 (h)]. A marginally higher diameter value of 0.229 $\mu$ m with broader fiber distribution was observed with CuNP's infused membranes [Figure 5.10 (g)]. It was generally observed that with the increase in diameter values, the pressure drop values were decreasing because of associated air gaps.



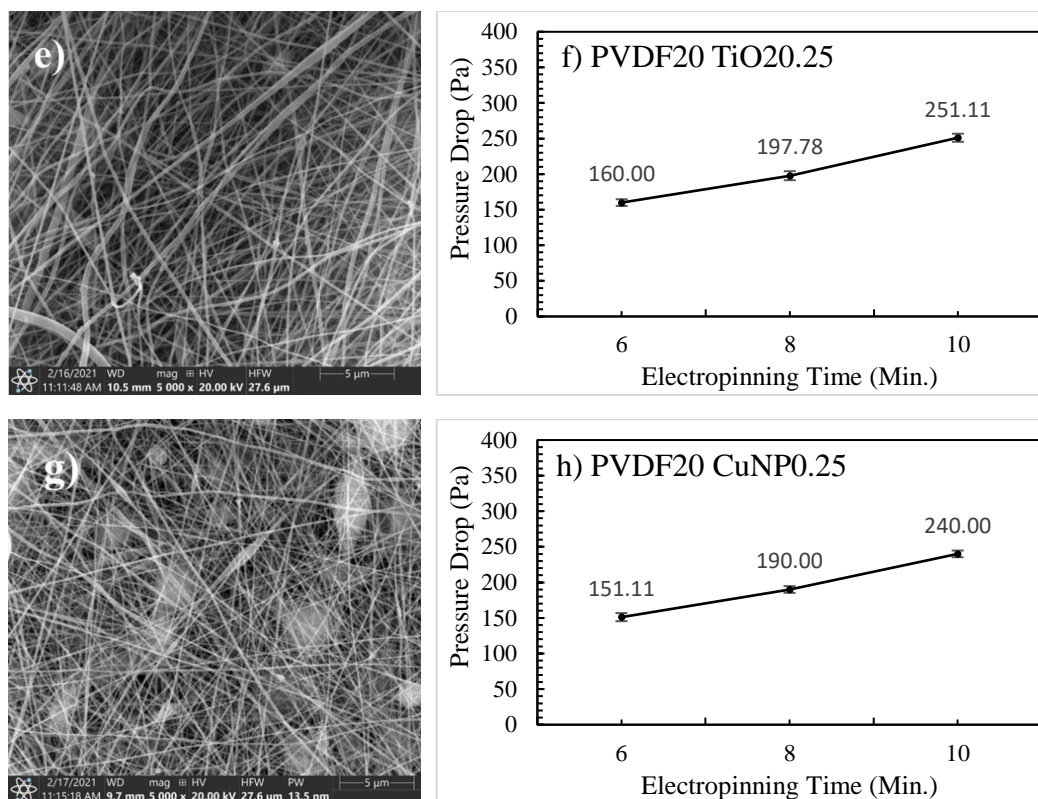


Figure 5.10: SEM micrographs and  $\Delta P$  measurements at different electrospinning time for configuration; CNT 0.25wt.% (a-b), GN 0.25wt.% (c-d), TiO<sub>2</sub> 0.25wt.% (e-f), and CuNP's 0.25wt.% (g-h).

The basis weight measurements of the filler infused membranes were investigated in Figure 5.11. Lower basis weight was observed with CNT-infused membrane when compared with other filler membranes. CNT-based membranes were loaded with the higher fiber diameter values of 0.251 μm. GN and TiO<sub>2</sub> based membranes were observed with similar basis weight values. Both GN and TiO<sub>2</sub> exhibit a large specific surface area and better polymer interaction when mixed with a solution making it easy to electro-spin. The filler particles attach to the fiber surface without significantly affecting the structure [208,209,213]. On the other hand, copper nano-particles infused membranes had the highest basis weight compared with other fillers and had higher fiber diameter measurements of 0.229 μm than GN and TiO<sub>2</sub> nanofibers.

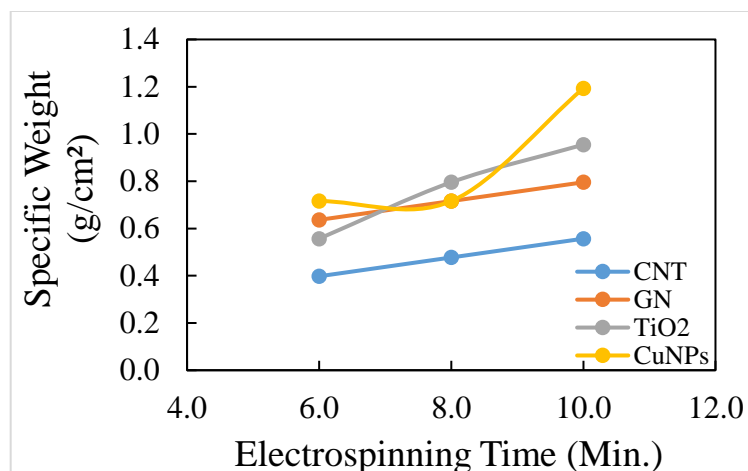


Figure 5.11: Specific weight of filler infused membranes produced at different electrospinning times.

The relationship between the fiber diameter measurements and respective  $\Delta P$  values was established in Figure 5.12. The lowest pressure drop values were observed with CNT-based membranes at all electro-spin times. This can be attributed to the highest diameter measurements ( $0.251\mu\text{m}$ ) and the lowest basis weight compared with other specimens. GN and  $\text{TiO}_2$  based membranes were observed with similar diameter measurements of  $0.220\mu\text{m}$  and  $0.219\mu\text{m}$ . The corresponding pressure drop values were approximately close to each other. On the other hand, CuNP infused nanofiber membranes were observed with a higher fiber diameter value of  $0.229\mu\text{m}$ , resulting in lower pressure drop values than GN and  $\text{TiO}_2$  membranes.

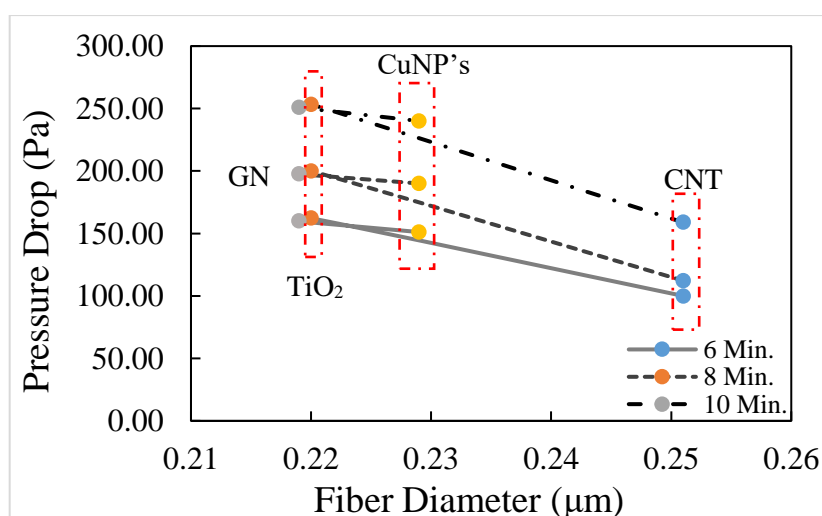


Figure 5.12: Fiber diameter versus pressure drop of filler infused nanofiber membranes produced at different electrospinning times.

### 5.3.5 Effect of Electrospinning Time on $\Delta P$ Measurements of Nanofiber Samples to Reach N-95 Equivalency

The pressure drop measurements of the conventional high-grade N-95 medical-grade mask have a pressure rating of approximately 344Pa with thick layers of melt-blown PP fibers. Single nanofiber membrane-based filters with significantly lower thickness than traditional N-95 mask layers were observed with similar pressure drop ratings when manufactured at higher electrospinning time. Figure 5.13 demonstrates the electrospinning time required for PVDF-based filter membranes to reach the pressure drop equivalency of the N-95 medical-grade mask. The pressure drop measurement shows that; it requires lesser time for low diameter configurations to reach the pressure drop value of 340Pa. It was observed that the electrospinning time increases with an increase in diameter and its distribution, with an exception for CNT-infused membrane configuration. The highest electro-spin time of 19 minutes was observed for the CNT-infused membrane to reach the N-95 grade equivalency, whereas the lowest time of 10 minutes was recorded for the PVDF20 membrane.

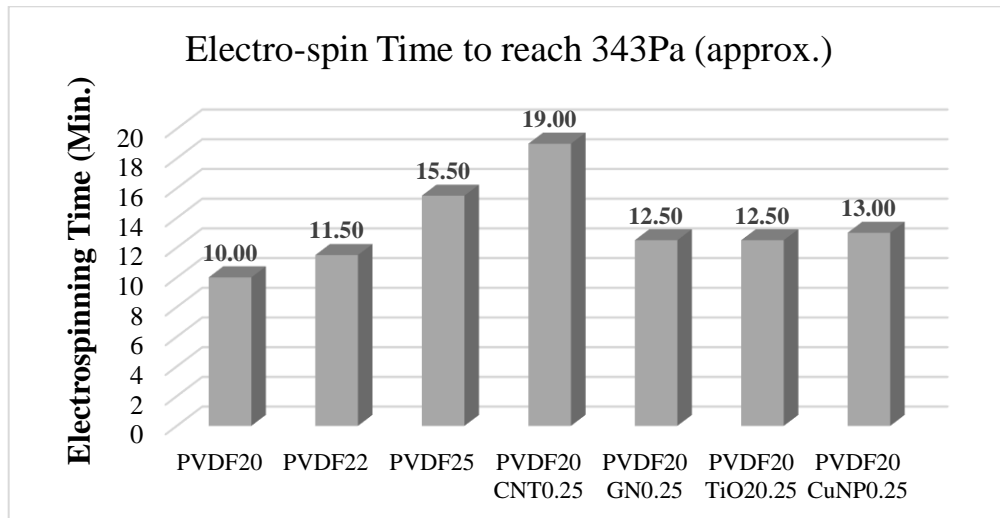


Figure 5.13: Electrospinning time required to reach the N-95  $\Delta P$  equivalency.

### 5.3.6 Effect of Electro-Spun Membrane Layering on $\Delta P$ Measurements of Surgical Masks (SM)

Surgical Masks (SM) are thin, light-weighted, and less bulky in structure compared with N-95 masks. They are readily available and provide better wear-ability comfort for a longer time duration. Microfiber-loaded SM consists of more significant pore gaps and can



only filter out larger particles. Owing to their smaller thickness and fiber size, they were observed with very low-pressure drops. In this section, the conventional SM's were layered with PVDF-based nanofiber membranes to prevent nano-scale particle bypassing and reach the N-95 medical-grade pressure drop equivalency. Figure 5.14 shows the step-wise methodology of nanofiber membrane layering on SM's in the following order; a) First step involves dismantling of surgical mask in various parts splitting three main layers containing microfibers and other fixtures like ear loops and face fittings, b) Second step involves carefully handling the thin nanofiber membranes ensuring no surface wrinkles on placement with SM's, c) Third step involves careful sandwiching of the membrane between the top and middle layer ensuring zero damage on layers, d) Careful placement of the fabricated layers between the top and bottom holder of pressure drop measurement set-up for final testing [Figure 5.14 (a-d)].

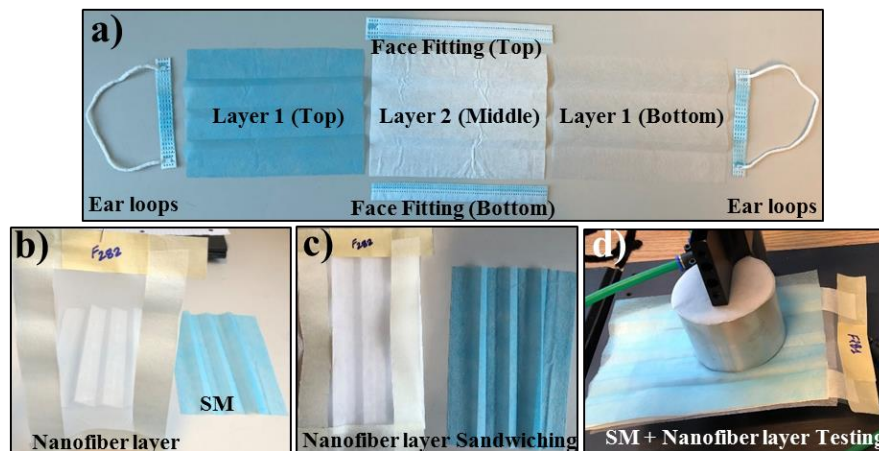


Figure 5.14: Step-wise nanofiber layering methodology on SM; a) Layer-wise dismantling of SM, b) Membrane handling, c) Nanofiber membrane sandwiching; and d) Placement of sandwiched layer for final testing.

The pressure drop measurements of SM and its nanofiber layered configuration were investigated in Figure 5.15. Table 5.4 shows the different electro-spun timed membrane layering with respective pressure drop data. SM's were observed to have the least pressure drop of 100Pa approximately, but the pressure drop rating increased from 100Pa to 340Pa roughly with a thin nanofiber layer addition. The nanofiber layer sandwiched between the SM layers can filter out nano-scale range particles maintaining the pressure drop requirements. These nanofiber filters also exhibit anti-bacterial and anti-viral properties. For the composites fabricated with PVDF20 and PVDF22 based nanofiber layer



sandwiching, only 6min electro-spun layers were sufficient to reach the  $\Delta P$  of 336Pa and 340Pa, respectively. SM composites loaded with 6min spun membranes had lower fiber diameters compared to other filter samples. PVDF20 and CNT infused nanofiber sample required 10min electro-spun layer to reach the N-95 pressure drop equivalency. These two samples were observed with higher fiber diameters, and the CNT-based layer was comparatively thinner, due to which higher spinning time was required. The SM's were modified with the anti-bacterial/viral filler-infused nanofiber layers. The samples with GN, TiO<sub>2</sub>, and CuNP sandwiched nanofiber-SM layer required 8min spun samples to reach the N-95 pressure drop equivalency. These samples comprised approximately similar fiber diameters with a respective pressure drop value of 337Pa roughly. The  $\Delta P$  value of SM increased from 100Pa to 340Pa roughly with the addition of the nanofiber layers to SM. The layering of membranes will provide several benefits over traditional SM's; a) Nano-scale fiber-based sheets provide more hindrance to contaminants of smaller size, b) Tiny air gaps and pores prevents contaminant by-passing, c) Electrostatically charged sheets can trap more contaminants by electrostatic attraction, improving viral/bacterial filtration efficacy, and d) Anti-bacterial and biocide fillers can be loaded on nanofibers without affecting the morphology of fibers which in turn will boost the efficiency of SM equivalent to N-95 mask.

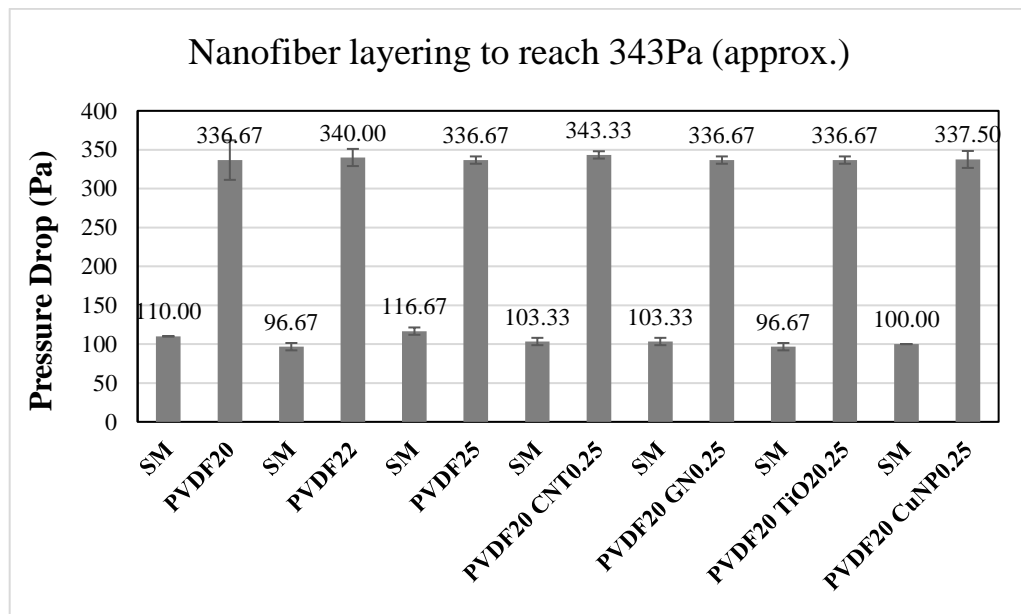


Figure 5.15:  $\Delta P$  measurements of SM's and respective nanofiber layered configurations.

Table 5.3:  $\Delta P$  measurements with the electro-spun time of nanofiber layered SM's.

Sample	Electrospinning Time (Min.)	Pressure Drop (Pa)
PVDF20	SM   SM+6min.	110   $336.67 \pm 25.44$
PVDF22	SM   SM+6min.	96.67   $340.00 \pm 11.05$
PVDF25	SM   SM+10min.	116.67   $336.67 \pm 4.71$
PVDF20 CNT0.25	SM   SM+10min.	103.33   $343.33 \pm 4.72$
PVDF20 GN0.25	SM   SM+8min.	103.33   $336.67 \pm 4.71$
PVDF20 TiO20.25	SM   SM+8min.	96.67   $336.67 \pm 4.71$
PVDF20 CuNP0.25	SM   SM+8min.	100   $337.50 \pm 10.88$

### 5.3.7 Particle Filtration Efficiency (PFE) of Electro-Spun Membrane Layered SM's

In this section, the experimental Particle Filtration Efficiency (PFE) test of SM and its nanofiber layered configuration was carried out on the NW261 PFE tester located in Melt95, Bolton, ON. The PFE was determined at different particulate sizes of NaCl aerosol, such as 0.3, 0.5, 1.0, 2.5, 5.0, 10.0 $\mu\text{m}$  at a flow rate of 32LPM for 10 seconds [Figure 5.16]. Table 5.4 shows the different electro-spun timed membrane SM layering with respective PFE data. The experimental PFE results shown in Figure 5.16 reveal that SM's filtration efficiency was the lowest compared to all electro-spun layered SM composites with PFE of 34.8%, being the least at 0.3 $\mu\text{m}$  and 85.16% at 10.0 $\mu\text{m}$ . The electro-spun membrane layering with SM improved the PFE by 60-64%, approximately in the particle range of 0.3 $\mu\text{m}$ , incorporating nano-scale fibers in the diameter range from 132nm to 250nm. Figure 5.17 shows the PFE centered at a fine particulate size of 0.3 $\mu\text{m}$  for all layered configurations. The measurements reveal that with the decrease in fiber diameter value, the PFE increases. For PVDF20 composite, a high PFE of 97.8% was observed with fibers of 132nm diametric scale, which further got reduced to 87.23% with increased concentration to PVDF25 composite fabricated at a higher diameter of 300nm. The inclusion of fillers to the pure composite resulted in even better PFE's of 96%, 98%, 99%, and 92% compared with other composites in CNT, GN, TiO<sub>2</sub>, and CuNP based layers, respectively. For all the filler-infused layered composite, the PFE reached the maximum of approximately 100% for a particulate size higher than equal to 1.0 $\mu\text{m}$ .

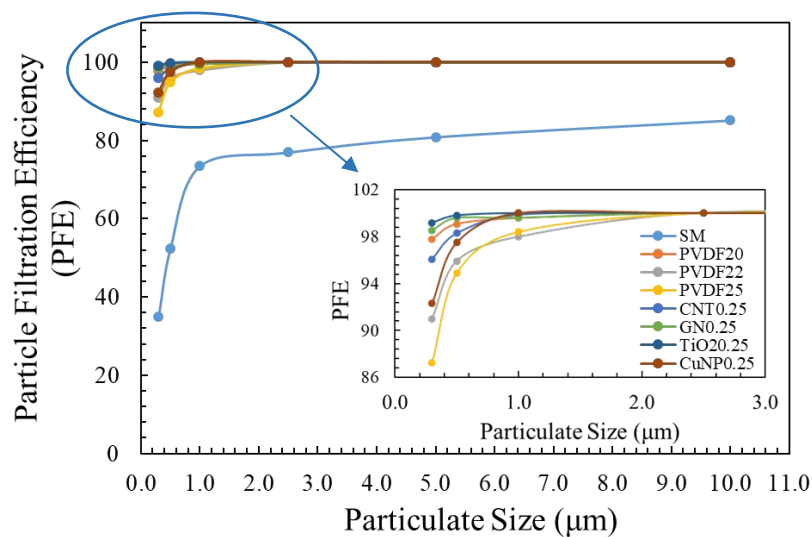


Figure 5.16: PFE measurements of SM's and respective nanofiber layered configurations at the particulate size of 0.3, 0.5, 1.0, 2.5, 5.0, and 10μm.

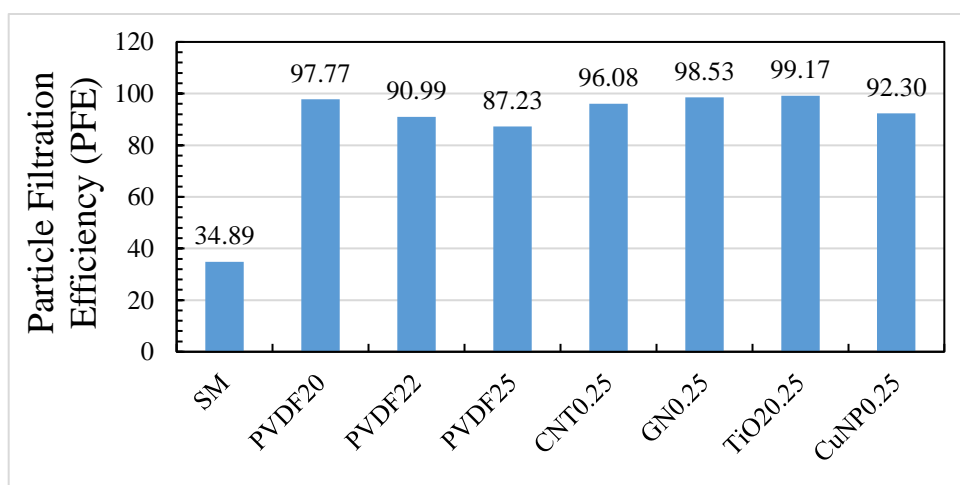


Figure 5.17: PFE measurements of SM's and respective nanofiber layered configurations at the particulate size of 0.3μm.

Table 5.4: PFE measurements of nanofiber layered SM's.

Particle Size (μm)	PFE							
	SM	PVDF 20	PVDF 22	PVDF 25	CNT 0.25	GN 0.25	TiO2 0.25	CuNP 0.25
0.3	34.89	97.77	90.99	87.23	96.08	98.53	99.17	92.30
0.5	52.36	99.06	95.92	94.90	98.28	99.58	99.80	97.49
1.0	73.42	99.57	97.97	98.41	99.86	99.59	100.00	100.00
2.5	76.95	100.00	100.00	100.00	100.00	100.00	100.00	100.00
5.0	80.87	100.00	100.00	100.00	100.00	100.00	100.00	100.00
10.0	85.16	100.00	100.00	100.00	100.00	100.00	100.00	100.00

## 5.4 Summary and Conclusions

In this chapter, electro-spun nanofiber membranes were produced from a PVDF base for filtration application. Pressure drop measurement lab-scale experimental set-up was developed following the standards. Traditional surgical and N-95 medical/industrial grade masks were tested based on pressure drop measurements. Pure polymeric and filler-infused nanofiber membranes were manufactured at three different electrospinning times and concentrations. The morphological attributes of these membranes were analyzed using the SEM micrographs. Relation between the basis weight with respect to electro-spin time and pressure drop versus fiber diameter was established. Electro-spun time of configurations producing a single nanofiber membrane was reported in terms of N-95  $\Delta P$  equivalency. Finally, the layering of nanofiber membranes with SM was carried out to reach the pressure drop equivalency of N-95 masks.

Pressure drop measurement validation was carried for the existing experimental set-up with reported values of medical-grade N-95 face masks and surgical masks. The measurements were in good agreement with the rated N-95 values. SM's were observed with lower pressure drop barrier levels of 194Pa and 106Pa. The morphological attributes show that polymer concentration plays an essential role in regulating the fiber diameter of nanofibers. Pure PVDF nanofibers were observed with a diameter range from 0.132 $\mu\text{m}$  (PVDF 20wt.%) to 0.301 $\mu\text{m}$  (PVDF 25wt.%). SEM micrograph indicates more air gaps and thicker fibers with a higher PVDF concentration. Anti-viral/bacterial fillers, CNT, GN, TiO<sub>2</sub>, and CuNP, infused with PVDF fiber structure, show no significant effect on the morphology of nanofiber structures. Fiber diameter measurements of 0.251 $\mu\text{m}$ , 0.220 $\mu\text{m}$ , 0.219 $\mu\text{m}$ , and 0.229 $\mu\text{m}$  with respective distribution were reported in the study. The highest pressure drop of 338.89Pa was observed with the lowest fiber diameter configuration of PVDF20 – 132nm at 10min electro-spin time. The basis weight and electro-spin time relation indicate that the membranes' specific weight increases with an increase in time due to high fiber accumulation in a specific volume. Pressure drop versus fiber diameter measurements confirms the rise in pressure values regarding low diameter fibers. The highest pressure drops were reported with GN and TiO<sub>2</sub> based filler membranes. The diameter measurements for both fillers were smaller and similar to each other than CNT

and CuNP based nanofibers. Single nanofiber membrane electro-spun at 10 min. for PVDF20 configuration was observed to reach the N-95  $\Delta P$  equivalency with 338Pa. SM loaded with PVDF 20 membrane (6min) resulted in a higher pressure drop of 336.67Pa. The SM was modified with a nanofiber layer to prevent particles of 132nm or less from infiltrating. The anti-viral or anti-bacterial filler-loaded nanofiber membranes with SM achieved a higher N-95 pressure drop barrier level with 8min spun layers (GN, TiO<sub>2</sub>, and CuNP) and can prevent the infiltration of particles in size range of 220nm – 250nm or less. High PFE's of 90-99% was observed at the particulate size of 0.3 $\mu$ m all configuration, and a further increase in particulate size to 1.0 $\mu$ m or more resulted in approximately 100%PFE. The layering was performed to improve the filtration efficacy of SM in terms of particulate size and achieve the N-95 pressure drop barrier level with anti-viral/bacterial fillers.

## **Chapter 6. Conclusions, Contributions, and Future Recommendations**

### **6.1 Summary**

Electro-spun nanofibers offer exceptional properties providing an efficient alternative solution to low-frequency noise mitigation and filtration problems. The greater surface area of electro-spun nanofibers in a confined volume results in higher exposure of sound waves with fibers and pores, leading to higher sound absorption. These nanofiber-based structures favor the sound absorption of low and medium-frequency sound waves. Several studies performed in the past focused on developing the sound absorptive fibers but these materials offered better acoustic properties in a high-frequency range greater than 1500Hz at the cost of the material thickness. Nano-scale fiber diameters and pores also prevent the infiltration of pollutants, bacteria, or viruses, making nanofiber membranes a better candidate for filter media applications. The nanofiber membranes were manufactured to improve filtration efficiency and pressure drop in several studies, but these membranes were not used to modify existing conventional SM's. In this context, the present work was directed at manufacturing electro-spun nanofiber membranes with low fiber diameter and thickness for better low-frequency acoustic applications and improving filtration properties of conventional SM's. These membranes were also reinforced with micro/nano-sized fillers to enhance acoustic and filtration characteristics.

### **6.2 Thesis Contributions**

The main thesis contributions of the experimental study can be outlined as follows:

- **Development of statistical models for evaluating effects of five electrospinning process parameters on production of PVP and PVDF nanofiber membranes utilizing ANOVA, RSM, and GP.**

Polymeric nanofiber membranes of PVP and PVDF were manufactured using the electrospinning process. Five electrospinning control parameters were studied utilizing Taguchi's L27 Orthogonal Array Design at three-level variation for each parameter. Parametric analysis was carried out to investigate the effect on three output responses: fiber diameter, membrane thickness, and membrane weight. The

experimental investigation involves parametric assessment and modeling using statistical tools like ANOVA, RSM, and GP. For the PVP nanofibers, the high voltage and polymer concentration were the most significant parameters with a 95% and 99% confidence level in regulating the fiber diameter measurements at lower risk levels. The thickness and weight measurements, on the other hand, were observed to be affected by polymer concentration at a high significance level of 99%. The mathematical models generated for the respective three outputs using RSM predicted the average model accuracy of 84.7%, 82.0%, and 84.2%, which is considered the acceptable range for the model verification. The empirical model generated using GP improved the model accuracy to 88.5% - fiber diameter, 91.6% - thickness, and 80.1% - weight.

For the PVDF nanofibers, polymer concentration was the most significant parameter in controlling the fiber diameter. For thickness measurements, high voltage was observed to significantly affect the thickness with a 99% confidence level at a low-risk factor. The membrane weight was observed to be regulated by the three parameters like high voltage, concentration, and needle-collector distance at high confidence levels of 99% with low associated risk factors. Mathematical modeling of the corresponding responses using RSM predicted the average model accuracy of 90.8%, 70.1%, and 84%. The empirical model generated using GP resulted in improved model accuracy of 92.8%, 79.7%, and 86.7%.

- **Development of multi-layered pure polymeric nanofiber-based composites in various combinations/patterns to enhance low-frequency sound absorption with the incorporation of three discrete BC's.**

Polymeric nanofiber membranes of PVP and PVDF were prepared and stacked in different layering combinations. For PVP-based multi-layer composite, the maximum coefficient values of 0.95, 0.98, and 0.99 were observed with 16 layered composites 3688 $\mu$ m thick for frequencies of 1663, 526, and 406Hz at different BC's 0, 3, and 5cm, respectively. The peaks shifted to the lower frequency of 1536, 435, and 363Hz with coefficient values of 0.88, 0.88, and 0.92 for twenty-layered composite 4414 $\mu$ m thick. Higher coefficient values of 0.96, 0.99, and 0.99 were

observed with sixteen-layered PVDF composite 6000 $\mu$ m thick at even lower frequencies of 1028, 273, and 238Hz at three BC's, respectively. The combined sixteen-layered combination of PVP and PVDF - 5472 $\mu$ m thick resulted in coefficient values 0.94, 0.99, and 0.98 at frequency range of 1249Hz (0cm), 406Hz (3cm), and 322Hz (5cm). These pure polymeric membrane nano-composites resulted in a higher coefficient value of 0.9 in the lower frequency range of 200-300Hz.

- **Development of multi-layered filler-based polymeric nanofiber-based composites in various combinations/patterns to enhance low-frequency sound absorption with the incorporation of three discrete BC's.**

Filler modified polymeric nanofiber membranes were prepared from two polymeric base materials, PVP and PVDF, wherein five fillers like CNT, GN, FS, FG, and MC were infused at different concentrations. For PVP filler-based composites, maximum absorption coefficient values of 0.96 (0cm BC), 0.99 (3cm BC), 0.99 (5cm BC) were achieved with sixteen layered composite - 3769 $\mu$ m thick at a frequency range of 1689, 483, and 392Hz, respectively. For PVDF filler-based composites, the maximum coefficient values of 0.94, 0.95, and 0.97 were achieved at different BC's of 0, 3, and 5cm for sixteen layered composite - 6496 $\mu$ m thick at even lower frequency range of 1189, 399, and 305Hz compared with PVP filler-based membranes. These fillers-based composites achieved higher coefficient values greater than 0.9 at different BC's for a lower frequency range of 300-500Hz.

- **Development of thin and lightweight nanofiber-based filtration membranes in several configurations to achieve pressure drop barrier level of medical grade N-95 masks and to improve filtration characteristics in terms of fiber size.**

Fiber diameter measurements of 132nm, 167nm, and 301nm were achieved at 20, 22, and 22wt.% concentration of pure PVDF membrane with a pressure drop level of 338.89Pa, 301.11Pa, and 192.22Pa respectively, for a 10min membrane layer. Fiber diameter measurements of 251nm, 220nm, 219nm, and 229nm were observed



with CNT, GN, TiO<sub>2</sub>, and CuNp's based filler membranes with pressure drops of 158.89Pa, 253.33Pa, 251.11Pa, 240.00Pa for 10min membrane layer respectively. Relation between the basis weight of the membranes and electro-spin times was established wherein the weight was observed to increase with the increase in time due to higher fiber accumulation. Relation between the fiber diameter and the pressure drop was established for all configurations. Lower fiber diameter measurements and higher electro-spun timed membranes were observed with higher pressure drops. The thin membranes were observed in the basis weight range of 0.4g/m<sup>2</sup> to 2.2g/m<sup>2</sup>. The nanofiber membranes of each configuration were layered with SM's to reach the pressure drop barrier level equivalency of medical-grade N-95 masks. The smallest fiber diameter (132nm) loaded membrane of PVDF20-6min reached the pressure drop level of 336.67Pa when layered with SM's. Anti-viral/bacterial filler-loaded membrane with the least diameter value of 219nm reached the pressure drop level of 336.67Pa with 8min spun membrane layering. These thin and lightweight electro-spun membranes achieved the high PFE's of 90-99% in the fine particulate size of 300nm for all the layered configurations.

### **6.3 Future Recommendations**

Future research can be directed with the following recommendations;

- The acoustic response evaluation of nanofiber membranes from different polymeric and filler materials that possess more porous fiber structures and thinner diameters.
- The evaluation of sound absorption coefficient of nanofiber membranes by developing statistical models concerning fiber diameter, thickness, and weight of membranes or composites.
- Development of electrospinning experimental set-up with precise control on nanofiber alignment for sound absorption, and filtration applications.
- Development of filtration efficiency measurement experimental set-up to characterize the nanofiber-based filter media with the inclusion of various other anti-bacterial/viral fillers.

## References

- [1] D. Paul, L.M. Robeson, Polymer nanotechnology: nanocomposites, *Polymer*. 49 (2008) 3187–3204.
- [2] A.K. Alves, C.P. Bergmann, F.A. Berutti, “Novel synthesis and characterization of nanostructured materials” ch. 1, pp. 1-9, Springer, 2013.
- [3] C.T. Lim, Nanofiber technology: current status and emerging developments, *Prog. Polym. Sci.* 70 (2017) 1–17.
- [4] Z.-M. Huang, Y.-Z. Zhang, M. Kotaki, S. Ramakrishna, A review on polymer nanofibers by electrospinning and their applications in nanocomposites, *Compos. Sci. Technol.* 63 (2003) 2223–2253.
- [5] D. Ficaí, A.M. Grumezescu, “Nanostructures for novel therapy: synthesis, characterization and applications” ch. 11, pp. 289-290, Elsevier, 2017.
- [6] J. Doshi, D.H. Reneker, Electrospinning process and applications of electrospun fibers, *J. Electrostat.* 35 (1995) 151–160.
- [7] W. Lu, J. Sun, X. Jiang, Recent advances in electrospinning technology and biomedical applications of electrospun fibers, *J. Mater. Chem. B*. 2 (2014) 2369–2380.
- [8] W.E. Teo, S. Ramakrishna, A review on electrospinning design and nanofibre assemblies, *Nanotechnology*. 17 (2006) R89.
- [9] F.E. Ahmed, B.S. Lalia, R. Hashaiekh, A review on electrospinning for membrane fabrication: challenges and applications, *Desalination*. 356 (2015) 15–30.
- [10] A.L. Andradý, “Science and technology of polymer nanofibers” ch. 1-4, pp. 27-109., John Wiley & Sons, 2008.
- [11] D. Reneker, A. Yarin, E. Zussman, H. Xu, Electrospinning of nanofibers from polymer solutions and melts, *Adv. Appl. Mech.* 41 (2007) 43–346.
- [12] W. Yang, Y. Li, Sound absorption performance of natural fibers and their composites, *Sci. China Technol. Sci.* 55 (2012) 2278–2283.
- [13] B. Berglund, T. Lindvall, D.H. Schwela, World Health Organization, Guidelines for community noise, (1999).
- [14] D. Stránská, L. Mares, O. Jirsák, K. Kalinová, Production method of layered sound absorptive non-woven fabric, (2010).
- [15] S. Subramonian, L. Remy, D. Schroer, Acoustics and forming of novel polyolefin blend foams, *Cell. Polym.* 23 (2004) 349–367.
- [16] N. Zhu, D. Zhang, W. Wang, X. Li, B. Yang, J. Song, X. Zhao, B. Huang, W. Shi, R. Lu, A novel coronavirus from patients with pneumonia in China, 2019, *N. Engl. J. Med.* (2020).
- [17] W.W.-F. Leung, Q. Sun, Charged PVDF multilayer nanofiber filter in filtering simulated airborne novel coronavirus (COVID-19) using ambient nano-aerosols, *Sep. Purif. Technol.* 245 (2020) 116887.
- [18] W.W.-F. Leung, Y.T. Chau, Experiments on filtering nano-aerosols from vehicular and atmospheric pollutants under dominant diffusion using nanofiber filter, *Sep. Purif. Technol.* 213 (2019) 186–198.
- [19] R.W. Whatmore, Nanotechnology—what is it? Should we be worried?, *Occup. Med.* 56 (2006) 295–299.

- [20] A.K. Hussein, Applications of nanotechnology in renewable energies—A comprehensive overview and understanding, *Renew. Sustain. Energy Rev.* 42 (2015) 460–476.
- [21] J.N. Tiwari, R.N. Tiwari, K.S. Kim, Zero-dimensional, one-dimensional, two-dimensional and three-dimensional nanostructured materials for advanced electrochemical energy devices, *Prog. Mater. Sci.* 57 (2012) 724–803.
- [22] K. Jayaraman, M. Kotaki, Y. Zhang, X. Mo, S. Ramakrishna, Recent advances in polymer nanofibers, *J. Nanosci. Nanotechnol.* 4 (2004) 52–65.
- [23] S. Thenmozhi, N. Dharmaraj, K. Kadirvelu, H.Y. Kim, Electrospun nanofibers: New generation materials for advanced applications, *Mater. Sci. Eng. B.* 217 (2017) 36–48.
- [24] J. Wu, N. Wang, Y. Zhao, L. Jiang, Electrospinning of multilevel structured functional micro-/nanofibers and their applications, *J. Mater. Chem. A.* 1 (2013) 7290–7305.
- [25] T. Ondarcuhu, C. Joachim, Drawing a single nanofibre over hundreds of microns, *EPL Europhys. Lett.* 42 (1998) 215.
- [26] R. Seeram, L. Teik-cheng, F. Kazutoshi, “An introduction to electrospinning and nanofibers” ch.1-3, pp. 10-154., World scientific, 2005.
- [27] G. Yan, J. Yu, Y. Qiu, X. Yi, J. Lu, X. Zhou, X. Bai, Self-assembly of electrospun polymer nanofibers: A general phenomenon generating honeycomb-patterned nanofibrous structures, *Langmuir.* 27 (2011) 4285–4289.
- [28] J.D. Hartgerink, E. Beniash, S.I. Stupp, Self-assembly and mineralization of peptide-amphiphile nanofibers, *Science.* 294 (2001) 1684–1688.
- [29] G.M. Whitesides, B. Grzybowski, Self-assembly at all scales, *Science.* 295 (2002) 2418–2421.
- [30] L. Feng, S. Li, H. Li, J. Zhai, Y. Song, L. Jiang, D. Zhu, Super-hydrophobic surface of aligned polyacrylonitrile nanofibers, *Angew. Chem. Int. Ed.* 41 (2002) 1221–1223.
- [31] C. Martin, R. Parthasarathy, V. Menon, Template synthesis of electronically conductive polymers—preparation of thin films, *Electrochimica Acta.* 39 (1994) 1309–1313.
- [32] Y.S. Nam, T.G. Park, Porous biodegradable polymeric scaffolds prepared by thermally induced phase separation, *J. Biomed. Mater. Res. Off. J. Soc. Biomater. Jpn. Soc. Biomater. Aust. Soc. Biomater. Korean Soc. Biomater.* 47 (1999) 8–17.
- [33] P.X. Ma, R. Zhang, Synthetic nano-scale fibrous extracellular matrix, *J. Biomed. Mater. Res. Off. J. Soc. Biomater. Jpn. Soc. Biomater. Aust. Soc. Biomater.* 46 (1999) 60–72.
- [34] N. Tucker, J.J. Stanger, M.P. Staiger, H. Razzaq, K. Hofman, The history of the science and technology of electrospinning from 1600 to 1995, *J. Eng. Fibers Fabr.* 7 (2012) 155892501200702S10.
- [35] D.B. Khadka, D.T. Haynie, Protein-and peptide-based electrospun nanofibers in medical biomaterials, *Nanomedicine Nanotechnol. Biol. Med.* 8 (2012) 1242–1262.
- [36] D.H. Reneker, A.L. Yarin, H. Fong, S. Koombhongse, Bending instability of electrically charged liquid jets of polymer solutions in electrospinning, *J. Appl. Phys.* 87 (2000) 4531–4547.

- [37] R. Asmatulu, M.B. Yildirim, W.S. Khan, A. Adeniji, H.L. Wamocha, Nanofiber fabrication and characterization for the engineering education, (2007).
- [38] A. Haghi, M. Akbari, Trends in electrospinning of natural nanofibers, *Phys. Status Solidi A*. 204 (2007) 1830–1834.
- [39] M. Ziabari, V. Mottaghitalab, A. Haghi, Application of direct tracking method for measuring electrospun nanofiber diameter, *Braz. J. Chem. Eng.* 26 (2009) 53–62.
- [40] A. Suthar, G. Chase, Nanofibres in filter media, *Chem. Eng. Lond.* (2001) 26–28.
- [41] F. Anton, Artificial thread and method of producing same, (1940).
- [42] V.G. Drozin, The electrical dispersion of liquids as aerosols, *J. Colloid Sci.* 10 (1955) 158–164.
- [43] G.I. Taylor, Disintegration of water drops in an electric field, *Proc. R. Soc. Lond. Ser. Math. Phys. Sci.* 280 (1964) 383–397.
- [44] K. Lee, H. Kim, H. Bang, Y. Jung, S. Lee, The change of bead morphology formed on electrospun polystyrene fibers, *Polymer*. 44 (2003) 4029–4034.
- [45] F. Anton, Process and apparatus for preparing artificial threads, (1934).
- [46] L. Larrondo, R. St. John Manley, Electrostatic fiber spinning from polymer melts. I. Experimental observations on fiber formation and properties, *J. Polym. Sci. Polym. Phys. Ed.* 19 (1981) 909–920.
- [47] L. Wannatong, A. Sirivat, P. Supaphol, Effects of solvents on electrospun polymeric fibers: preliminary study on polystyrene, *Polym. Int.* 53 (2004) 1851–1859.
- [48] A. Koski, K. Yim, S. Shivkumar, Effect of molecular weight on fibrous PVA produced by electrospinning, *Mater. Lett.* 58 (2004) 493–497.
- [49] S. Sukigara, M. Gandhi, J. Ayutsede, M. Micklus, F. Ko, Regeneration of Bombyx mori silk by electrospinning—part 1: processing parameters and geometric properties, *Polymer*. 44 (2003) 5721–5727.
- [50] H. Fong, D.H. Reneker, Elastomeric nanofibers of styrene–butadiene–styrene triblock copolymer, *J. Polym. Sci. Part B Polym. Phys.* 37 (1999) 3488–3493.
- [51] G. Eda, S. Shivkumar, Bead-to-fiber transition in electrospun polystyrene, *J. Appl. Polym. Sci.* 106 (2007) 475–487.
- [52] H. Fong, I. Chun, D.H. Reneker, Beaded nanofibers formed during electrospinning, *Polymer*. 40 (1999) 4585–4592.
- [53] Q. Yang, Z. Li, Y. Hong, Y. Zhao, S. Qiu, C. Wang, Y. Wei, Influence of solvents on the formation of ultrathin uniform poly (vinyl pyrrolidone) nanofibers with electrospinning, *J. Polym. Sci. Part B Polym. Phys.* 42 (2004) 3721–3726.
- [54] Z. Li, C. Wang, One-dimensional nanostructures: electrospinning technique and unique nanofibers, Springer, 2013.
- [55] J. Tao, S. Shivkumar, Molecular weight dependent structural regimes during the electrospinning of PVA, *Mater. Lett.* 61 (2007) 2325–2328.
- [56] X. Zong, K. Kim, D. Fang, S. Ran, B.S. Hsiao, B. Chu, Structure and process relationship of electrospun bioabsorbable nanofiber membranes, *Polymer*. 43 (2002) 4403–4412.
- [57] C. Huang, S. Chen, C. Lai, D.H. Reneker, H. Qiu, Y. Ye, H. Hou, Electrospun polymer nanofibers with small diameters, *Nanotechnology*. 17 (2006) 1558.
- [58] T. Subbiah, G. Bhat, R. Tock, S. Parameswaran, S. Ramkumar, Electrospinning of nanofibers, *J. Appl. Polym. Sci.* 96 (2005) 557–569.

- [59] P. Gupta, C. Elkins, T.E. Long, G.L. Wilkes, Electrospinning of linear homopolymers of poly (methyl methacrylate): exploring relationships between fiber formation, viscosity, molecular weight and concentration in a good solvent, *Polymer*. 46 (2005) 4799–4810.
- [60] S.-H. Tan, R. Inai, M. Kotaki, S. Ramakrishna, Systematic parameter study for ultra-fine fiber fabrication via electrospinning process, *Polymer*. 46 (2005) 6128–6134.
- [61] M.M. Hohman, M. Shin, G. Rutledge, M.P. Brenner, Electrospinning and electrically forced jets. II. Applications, *Phys. Fluids*. 13 (2001) 2221–2236.
- [62] A. GÖKTAŞ, Electrospinning of polystyrene/butyl rubber blends: a parametric study, (2008).
- [63] C. Mit-uppatham, M. Nithitanakul, P. Supaphol, Effects of Solution Concentration, Emitting Electrode Polarity, Solvent Type, and Salt Addition on Electrospun Polyamide-6 Fibers: A Preliminary Report, in: *Wiley Online Library*, 2004: pp. 293–300.
- [64] K. Lee, H. Kim, M. Khil, Y. Ra, D. Lee, Characterization of nano-structured poly ( $\epsilon$ -caprolactone) nonwoven mats via electrospinning, *Polymer*. 44 (2003) 1287–1294.
- [65] C. Hsu, S. Shivkumar, N. N-Dimethylformamide Additions to the Solution for the Electrospinning of Poly ( $\epsilon$ -caprolactone) Nanofibers, *Macromol. Mater. Eng.* 289 (2004) 334–340.
- [66] J.S. Lee, K.H. Choi, H.D. Ghim, S.S. Kim, D.H. Chun, H.Y. Kim, W.S. Lyoo, Role of molecular weight of atactic poly (vinyl alcohol)(PVA) in the structure and properties of PVA nanofabric prepared by electrospinning, *J. Appl. Polym. Sci.* 93 (2004) 1638–1646.
- [67] C.J. Buchko, L.C. Chen, Y. Shen, D.C. Martin, Processing and microstructural characterization of porous biocompatible protein polymer thin films, *Polymer*. 40 (1999) 7397–7407.
- [68] K. Pawlowski, H. Belvin, D. Raney, J. Su, J. Harrison, E. Siochi, Electrospinning of a micro-air vehicle wing skin, *Polymer*. 44 (2003) 1309–1314.
- [69] S. Zhao, X. Wu, L. Wang, Y. Huang, Electrospinning of ethyl–cyanoethyl cellulose/tetrahydrofuran solutions, *J. Appl. Polym. Sci.* 91 (2004) 242–246.
- [70] X. Yuan, Y. Zhang, C. Dong, J. Sheng, Morphology of ultrafine polysulfone fibers prepared by electrospinning, *Polym. Int.* 53 (2004) 1704–1710.
- [71] C. Zhang, X. Yuan, L. Wu, Y. Han, J. Sheng, Study on morphology of electrospun poly (vinyl alcohol) mats, *Eur. Polym. J.* 41 (2005) 423–432.
- [72] K.-H. Kim, L. Jeong, H.-N. Park, S.-Y. Shin, W.-H. Park, S.-C. Lee, T.-I. Kim, Y.-J. Park, Y.-J. Seol, Y.-M. Lee, Biological efficacy of silk fibroin nanofiber membranes for guided bone regeneration, *J. Biotechnol.* 120 (2005) 327–339.
- [73] S. Megelski, J.S. Stephens, D.B. Chase, J.F. Rabolt, Micro- and nanostructured surface morphology on electrospun polymer fibers, *Macromolecules*. 35 (2002) 8456–8466.
- [74] J.A. Matthews, G.E. Wnek, D.G. Simpson, G.L. Bowlin, Electrospinning of collagen nanofibers, *Biomacromolecules*. 3 (2002) 232–238.
- [75] D. Li, Y. Wang, Y. Xia, Electrospinning of polymeric and ceramic nanofibers as uniaxially aligned arrays, *Nano Lett.* 3 (2003) 1167–1171.

- [76] P. Katta, M. Alessandro, R. Ramsier, G. Chase, Continuous electrospinning of aligned polymer nanofibers onto a wire drum collector, *Nano Lett.* 4 (2004) 2215–2218.
- [77] N. Bhattarai, D. Edmondson, O. Veisoh, F.A. Matsen, M. Zhang, Electrospun chitosan-based nanofibers and their cellular compatibility, *Biomaterials.* 26 (2005) 6176–6184.
- [78] A. Theron, E. Zussman, A. Yarin, Electrostatic field-assisted alignment of electrospun nanofibres, *Nanotechnology.* 12 (2001) 384.
- [79] E. Smit, U. Büttner, R.D. Sanderson, Continuous yarns from electrospun fibers, *Polymer.* 46 (2005) 2419–2423.
- [80] W.E. Teo, S. Ramakrishna, A review on electrospinning design and nanofibre assemblies, *Nanotechnology.* 17 (2006) R89.
- [81] X. Wang, I.C. Um, D. Fang, A. Okamoto, B.S. Hsiao, B. Chu, Formation of water-resistant hyaluronic acid nanofibers by blowing-assisted electro-spinning and non-toxic post treatments, *Polymer.* 46 (2005) 4853–4867.
- [82] S.G. Kumbar, S.P. Nukavarapu, R. James, M. Hogan, C.T. Laurencin, Recent patents on electrospun biomedical nanostructures: an overview, *Recent Pat. Biomed. Eng.* 1 (2008) 68–78.
- [83] N. Li, J. Xiong, H. Xue, Effect of wheel rotating speed and LiCl additives on electrospun aligned polyacrylonitrile nanofiber, *Polym. Eng. Sci.* 51 (2011) 2178–2183.
- [84] B.M. Abunahel, N.Z.N. Azman, M. Jamil, Effect of Needle Diameter on the Morphological Structure of Electrospun n-Bi<sub>2</sub>O<sub>3</sub>/Epoxy-PVA Nanofiber Mats, (n.d.).
- [85] D. Li, Y. Xia, Electrospinning of nanofibers: reinventing the wheel?, *Adv. Mater.* 16 (2004) 1151–1170.
- [86] C. Mit-uppatham, M. Nithitanakul, P. Supaphol, Ultrafine electrospun polyamide-6 fibers: effect of solution conditions on morphology and average fiber diameter, *Macromol. Chem. Phys.* 205 (2004) 2327–2338.
- [87] C.S. Ki, J.W. Kim, J.H. Hyun, K.H. Lee, M. Hattori, D.K. Rah, Y.H. Park, Electrospun three-dimensional silk fibroin nanofibrous scaffold, *J. Appl. Polym. Sci.* 106 (2007) 3922–3928.
- [88] C.L. Casper, J.S. Stephens, N.G. Tassi, D.B. Chase, J.F. Rabolt, Controlling surface morphology of electrospun polystyrene fibers: effect of humidity and molecular weight in the electrospinning process, *Macromolecules.* 37 (2004) 573–578.
- [89] H.S. SalehHudin, E.N. Mohamad, W.N.L. Mahadi, A. Muhammad Afifi, Multiple-jet electrospinning methods for nanofiber processing: A review, *Mater. Manuf. Process.* 33 (2018) 479–498.
- [90] L. Persano, A. Camposeo, C. Tekmen, D. Pisignano, Industrial upscaling of electrospinning and applications of polymer nanofibers: a review, *Macromol. Mater. Eng.* 298 (2013) 504–520.
- [91] T. Krishnamoorthy, M.Z. Tang, A. Verma, A.S. Nair, D. Pliszka, S.G. Mhaisalkar, S. Ramakrishna, A facile route to vertically aligned electrospun SnO<sub>2</sub> nanowires on a transparent conducting oxide substrate for dye-sensitized solar cells, *J. Mater. Chem.* 22 (2012) 2166–2172.

- [92] S. Wang, Y. Yang, Y. Zhang, X. Fei, C. Zhou, Y. Zhang, Y. Li, Q. Yang, Y. Song, Fabrication of large-scale superhydrophobic composite films with enhanced tensile properties by multinozzle conveyor belt electrospinning, *J. Appl. Polym. Sci.* 131 (2014).
- [93] Y.-Y. Huang, D.-Y. Wang, L.-L. Chang, Y.-C. Yang, Fabricating microparticles/nanofibers composite and nanofiber scaffold with controllable pore size by rotating multichannel electrospinning, *J. Biomater. Sci. Polym. Ed.* 21 (2010) 1503–1514.
- [94] G. Müller, M. Möser, *Handbook of engineering acoustics*, Springer Science & Business Media, 2012.
- [95] L. Goines, L. Hagler, Noise pollution: a modern plague, *South Med J.* 100 (2007) 287–94.
- [96] M.J. Crocker, *Handbook of noise and vibration control*, John Wiley & Sons, 2007.
- [97] S.L. Lusk, B. Gillespie, B.M. Hagerty, R.A. Ziemba, Acute effects of noise on blood pressure and heart rate, *Arch. Environ. Health Int. J.* 59 (2004) 392–399.
- [98] K. Sachedina, A. Mohany, M. Hassan, Experimental study on damping acoustic pressure pulsations in pipeline systems using Helmholtz resonators, *J. Press. Vessel Technol.* 142 (2020).
- [99] T. Lato, A. Mohany, Passive damping of pressure pulsations in pipelines using Herschel-Quincke tubes, *J. Sound Vib.* 448 (2019) 160–177.
- [100] K. Sachedina, T. Lato, A. Mohany, M. Hassan, Effect of Incident Acoustic Pressure Amplitude on the Transmission Loss of Helmholtz Resonators, *Vibration.* 3 (2020) 34–41.
- [101] D. Parikh, N. Sachinvala, Y. Chen, L. Sun, G. Bhat, S. Ramkumar, Acoustic Properties of Environmentally Benign Automotive Natural Fiber Composites., *AATCC Rev.* 6 (2006).
- [102] V. Tarnow, Measurement of sound propagation in glass wool, *J. Acoust. Soc. Am.* 97 (1995) 2272–2281.
- [103] H. Kuttruff, *Room acoustics*, Crc Press, 2016.
- [104] H.V. Fuchs, *Applied Acoustics: Concepts, Absorbers, and Silencers for Acoustical Comfort and Noise Control: Alternative Solutions-Innovative Tools-Practical Examples*, Springer Science & Business Media, 2013.
- [105] G. Leventhall, P. Pelmear, S. Benton, A review of published research on low frequency noise and its effects, (2003).
- [106] T.L. Yang, D.-M. Chiang, R. Chen, Development of a novel porous laminated composite material for high sound absorption, *J. Vib. Control.* 7 (2001) 675–698.
- [107] S.-H. Park, Acoustic properties of micro-perforated panel absorbers backed by Helmholtz resonators for the improvement of low-frequency sound absorption, *J. Sound Vib.* 332 (2013) 4895–4911.
- [108] T.J. Cox, P. D'antonio, *Acoustic absorbers and diffusers: theory, design and application*, Crc Press, 2009.
- [109] W. Frommhold, H. Fuchs, S. Sheng, Acoustic performance of membrane absorbers, *J. Sound Vib.* 170 (1994) 621–636.
- [110] R. Chanaud, Effects of geometry on the resonance frequency of Helmholtz resonators, *J. Sound Vib.* 178 (1994) 337–348.

- [111] M.J. Kingan, J.R. Pearse, Sound absorption of porous material in combination with perforated facings, in: 2004: pp. 83–87.
- [112] D. Borelli, C. Schenone, I. Pittaluga, Analysis of sound absorption behaviour of polyester fibre material faced with perforated panels, in: Acoustical Society of America, 2013: p. 015045.
- [113] J.P. Arenas, M.J. Crocker, Recent trends in porous sound-absorbing materials, *Sound Vib.* 44 (2010) 12–18.
- [114] L. Abd AL-Rahman, R.I. Raja, R.A. Rahman, Attenuation of noise by using absorption materials and barriers: a review, *Int. J. Eng. Technol.* 2 (2012).
- [115] D.-Y. Maa, Theory and design of microperforated panel sound-absorbing constructions, *Sci. Sin.* 18 (1975) 55–71.
- [116] D.-Y. Maa, Potential of microperforated panel absorber, *J. Acoust. Soc. Am.* 104 (1998) 2861–2866.
- [117] K. Sakagami, M. Morimoto, M. Yairi, A. Minemura, A pilot study on improving the absorptivity of a thick microperforated panel absorber, *Appl. Acoust.* 69 (2008) 179–182.
- [118] H. Xiang, S. Tan, X. Yu, Y. Long, X. Zhang, N. Zhao, J. Xu, Sound absorption behavior of electrospun polyacrylonitrile nanofibrous membranes, *Chin. J. Polym. Sci.* 29 (2011) 650.
- [119] J. Mohrova, K. Kalinova, Different structures of PVA nanofibrous membrane for sound absorption application, *J. Nanomater.* 2012 (2012) 11.
- [120] H. Liu, D. Wang, N. Zhao, J. Ma, J. Gong, S. Yang, J. Xu, Application of electrospinning fibres on sound absorption in low and medium frequency range, *Mater. Res. Innov.* 18 (2014) S4-888.
- [121] C.M. Wu, M.H. Chou, Sound absorption of electrospun polyvinylidene fluoride/graphene membranes, *Eur. Polym. J.* 82 (2016) 35–45.
- [122] W.S. Khan, R. Asmatulu, M.B. Yildirim, Acoustical properties of electrospun fibers for aircraft interior noise reduction, *J. Aerosp. Eng.* 25 (2012) 376–382.
- [123] C.Y. Chen, Filtration of aerosols by fibrous media, *Chem. Rev.* 55 (1955) 595–623.
- [124] W.E. Ranz, J. Wong, Impaction of dust and smoke particles on surface and body collectors., *Ind. Eng. Chem.* 44 (1952) 1371–1381.
- [125] J. Pich, Theory of aerosol filtration by fibrous and membrane filters, *Aerosol Sci.* (1966).
- [126] N. Fuchs, *The Mechanics of Aerosols* Pergamon Oxford, (1964).
- [127] H.-S. Park, Y.O. Park, Filtration properties of electrospun ultrafine fiber webs, *Korean J. Chem. Eng.* 22 (2005) 165–172.
- [128] N. Ghochaghi, *Experimental Development of Advanced Air Filtration Media Based on Electrospun Polymer Fibers*, (2014).
- [129] W.C. Hinds, *Aerosol technology: properties, behavior, and measurement of airborne particles*, John Wiley & Sons, 1999.
- [130] D. Thomas, P. Contal, V. Renaudin, P. Penicot, D. Leclerc, J. Vendel, Modelling pressure drop in HEPA filters during dynamic filtration, *J. Aerosol Sci.* 30 (1999) 235–246.



- [131] B. Maze, H.V. Tafreshi, Q. Wang, B. Pourdeyhimi, A simulation of unsteady-state filtration via nanofiber media at reduced operating pressures, *J. Aerosol Sci.* 38 (2007) 550–571.
- [132] S. Jaganathan, H.V. Tafreshi, B. Pourdeyhimi, On the pressure drop prediction of filter media composed of fibers with bimodal diameter distributions, *Powder Technol.* 181 (2008) 89–95.
- [133] C. Zhu, C.-H. Lin, C.S. Cheung, Inertial impaction-dominated fibrous filtration with rectangular or cylindrical fibers, *Powder Technol.* 112 (2000) 149–162.
- [134] Y. Chuanfang, Aerosol filtration application using fibrous media—an industrial perspective, *Chin. J. Chem. Eng.* 20 (2012) 1–9.
- [135] M. Zhu, J. Han, F. Wang, W. Shao, R. Xiong, Q. Zhang, H. Pan, Y. Yang, S.K. Samal, F. Zhang, Electrospun nanofibers membranes for effective air filtration, *Macromol. Mater. Eng.* 302 (2017) 1600353.
- [136] A. Vanangamudi, S. Hamzah, G. Singh, Synthesis of hybrid hydrophobic composite air filtration membranes for antibacterial activity and chemical detoxification with high particulate filtration efficiency (PFE), *Chem. Eng. J.* 260 (2015) 801–808.
- [137] C. Hung, Experimental investigation and theoretical analysis on air filtration of sub-micron aerosols by nanofiber filter, (2010).
- [138] K.M. Yun, A.B. Suryamas, F. Iskandar, L. Bao, H. Niinuma, K. Okuyama, Morphology optimization of polymer nanofiber for applications in aerosol particle filtration, *Sep. Purif. Technol.* 75 (2010) 340–345.
- [139] R. Balgis, C.W. Kartikowati, T. Ogi, L. Gradon, L. Bao, K. Seki, K. Okuyama, Synthesis and evaluation of straight and bead-free nanofibers for improved aerosol filtration, *Chem. Eng. Sci.* 137 (2015) 947–954.
- [140] W.W.-F. Leung, C.-H. Hung, P.-T. Yuen, Effect of face velocity, nanofiber packing density and thickness on filtration performance of filters with nanofibers coated on a substrate, *Sep. Purif. Technol.* 71 (2010) 30–37.
- [141] Z. Wang, C. Zhao, Z. Pan, Porous bead-on-string poly (lactic acid) fibrous membranes for air filtration, *J. Colloid Interface Sci.* 441 (2015) 121–129.
- [142] X. Li, H. Kong, J. He, Study on highly filtration efficiency of electrospun polyvinyl alcohol micro-porous webs, *Indian J. Phys.* 89 (2015) 175–179.
- [143] P. Li, C. Wang, Y. Zhang, F. Wei, Air filtration in the free molecular flow regime: a review of high-efficiency particulate air filters based on carbon nanotubes, *Small.* 10 (2014) 4543–4561.
- [144] C.-H. Hung, W.W.-F. Leung, Filtration of nano-aerosol using nanofiber filter under low Peclet number and transitional flow regime, *Sep. Purif. Technol.* 79 (2011) 34–42.
- [145] K. Kim, C. Lee, I.W. Kim, J. Kim, Performance modification of a melt-blown filter medium via an additional nano-web layer prepared by electrospinning, *Fibers Polym.* 10 (2009) 60–64.
- [146] N. Zhu, D. Zhang, W. Wang, X. Li, B. Yang, J. Song, X. Zhao, B. Huang, W. Shi, R. Lu, A novel coronavirus from patients with pneumonia in China, 2019, *N. Engl. J. Med.* (2020).

- [147] C.S. Goldsmith, K.M. Tatti, T.G. Ksiazek, P.E. Rollin, J.A. Comer, W.W. Lee, P.A. Rota, B. Bankamp, W.J. Bellini, S.R. Zaki, Ultrastructural characterization of SARS coronavirus, *Emerg. Infect. Dis.* 10 (2004) 320.
- [148] S. Lin, C. Lee, S. Lee, C. Kao, C. Lin, A. Wang, S. Hsu, L. Huang, Surface ultrastructure of SARS coronavirus revealed by atomic force microscopy, *Cell. Microbiol.* 7 (2005) 1763–1770.
- [149] W.W.-F. Leung, Y.T. Chau, Experiments on filtering nano-aerosols from vehicular and atmospheric pollutants under dominant diffusion using nanofiber filter, *Sep. Purif. Technol.* 213 (2019) 186–198.
- [150] P.M. Mannucci, S. Harari, I. Martinelli, M. Franchini, Effects on health of air pollution: a narrative review, *Intern. Emerg. Med.* 10 (2015) 657–662.
- [151] R.J. Mentz, E.C. O'Brien, Air pollution in patients with heart failure: lessons from a mechanistic pilot study of a filter intervention, (2016).
- [152] R.D. Brook, S. Rajagopalan, C.A. Pope III, J.R. Brook, A. Bhatnagar, A.V. Diez-Roux, F. Holguin, Y. Hong, R.V. Luepker, M.A. Mittleman, Particulate matter air pollution and cardiovascular disease: an update to the scientific statement from the American Heart Association, *Circulation.* 121 (2010) 2331–2378.
- [153] K. Yoon, B.S. Hsiao, B. Chu, Functional nanofibers for environmental applications, *J. Mater. Chem.* 18 (2008) 5326–5334.
- [154] N. Wang, A. Raza, Y. Si, J. Yu, G. Sun, B. Ding, Tortuously structured polyvinyl chloride/polyurethane fibrous membranes for high-efficiency fine particulate filtration, *J. Colloid Interface Sci.* 398 (2013) 240–246.
- [155] H. Wan, N. Wang, J. Yang, Y. Si, K. Chen, B. Ding, G. Sun, M. El-Newehy, S.S. Al-Deyab, J. Yu, Hierarchically structured polysulfone/titania fibrous membranes with enhanced air filtration performance, *J. Colloid Interface Sci.* 417 (2014) 18–26.
- [156] Y. Yang, S. Zhang, X. Zhao, J. Yu, B. Ding, Sandwich structured polyamide-6/polyacrylonitrile nanonets/bead-on-string composite membrane for effective air filtration, *Sep. Purif. Technol.* 152 (2015) 14–22.
- [157] Q. Zhang, J. Welch, H. Park, C.-Y. Wu, W. Sigmund, J.C. Marijnissen, Improvement in nanofiber filtration by multiple thin layers of nanofiber mats, *J. Aerosol Sci.* 41 (2010) 230–236.
- [158] A.K. Selvam, G. Nallathambi, Polyacrylonitrile/silver nanoparticle electrospun nanocomposite matrix for bacterial filtration, *Fibers Polym.* 16 (2015) 1327–1335.
- [159] P.K. Stoimenov, R.L. Klinger, G.L. Marchin, K.J. Klabunde, Metal oxide nanoparticles as bactericidal agents, *Langmuir.* 18 (2002) 6679–6686.
- [160] L. Zhang, J. Luo, T.J. Menkhaus, H. Varadaraju, Y. Sun, H. Fong, Antimicrobial nano-fibrous membranes developed from electrospun polyacrylonitrile nanofibers, *J. Membr. Sci.* 369 (2011) 499–505.
- [161] C. Wang, S. Wu, M. Jian, J. Xie, L. Xu, X. Yang, Q. Zheng, Y. Zhang, Silk nanofibers as high efficient and lightweight air filter, *Nano Res.* 9 (2016) 2590–2597.
- [162] S. Chuangchote, T. Sagawa, S. Yoshikawa, Electrospinning of poly (vinyl pyrrolidone): Effects of solvents on electrospinnability for the fabrication of poly (p-phenylene vinylene) and TiO<sub>2</sub> nanofibers, *J. Appl. Polym. Sci.* 114 (2009) 2777–2791.

- [163] N. Soin, S. Anand, T. Shah, Energy harvesting and storage textiles, in: *Handb. Tech. Text.*, Elsevier, 2016: pp. 357–396.
- [164] C.M. Wu, M.H. Chou, Sound absorption of electrospun polyvinylidene fluoride/graphene membranes, *Eur. Polym. J.* 82 (2016) 35–45.
- [165] P. Cassagnau, Melt rheology of organoclay and fumed silica nanocomposites, *Polymer*. 49 (2008) 2183–2196.
- [166] P. Eriksson, A. Albertsson, P. Boydell, G. Prautzsch, J. Månson, Prediction of mechanical properties of recycled fiberglass reinforced polyamide 66, *Polym. Compos.* 17 (1996) 830–839.
- [167] U. Berardi, R. Ramakrishnan, Characterization of porous materials in compressed and uncompressed conditions using a three-microphones method, in: *ASA*, 2016: p. 040002.
- [168] G. Wang, D. Yu, A.D. Kelkar, L. Zhang, Electrospun nanofiber: Emerging reinforcing filler in polymer matrix composite materials, *Prog. Polym. Sci.* 75 (2017) 73–107.
- [169] S. Deshmukh, A. Rao, V. Gaval, P. Mahanwar, Mica-filled PVC composites: effect of particle size, filler concentration, and surface treatment of the filler, on mechanical and electrical properties of the composites, *J. Thermoplast. Compos. Mater.* 24 (2011) 583–599.
- [170] H.W. Tong, S.K.C. Kwok, H.C. Kwok, Protective masks with coating comprising different electrospun fibers interweaved with each other, formulations forming the same, and method of producing thereof, (2019).
- [171] Z. Zou, M. Yao, Airflow resistance and bio-filtering performance of carbon nanotube filters and current facepiece respirators, *J. Aerosol Sci.* 79 (2015) 61–71.
- [172] M. McGrory, D.C. Cirac, O. Gaussen, D. Cabrera, G. Engineers, Sound absorption coefficient measurement: Re-examining the relationship between impedance tube and reverberant room methods, in: 2012.
- [173] I. ISO, 10534-2: Acoustics-Determination of sound absorption coefficient and impedance in impedance tubes-Part 2: Transfer-function method, (2001).
- [174] E. ISO, 10534-1, Acoust. Sound Absorpt. Coeff. Impedance Tubes--Part. 1 (2001).
- [175] E. DIN, 354: Acoustics-Measurement of sound absorption in a reverberation room (ISO 354: 2003), Ger. Version EN ISO. 354 (2003) 2003.
- [176] G.C.C. da Silva, M.A. de Araújo Nunes, R.V. Lopes, A.B.A. Júnior, Design and construction of a low cost impedance tube for sound absorption coefficients measurements, in: 2013: pp. 105–115.
- [177] ASTM E-1050, Standard test method for impedance and absorption of acoustical materials using a tube, two microphones and a digital frequency analysis system, in: *American Society for Testing and Materials West Conshohocken, PA*, 1990.
- [178] M. Suhanek, K. Jambrosic, M. Horvat, A comparison of two methods for measuring the sound absorption coefficient using impedance tubes, in: *IEEE*, 2008: pp. 321–324.
- [179] J. Han, D. Herrin, A. Seybert, Accurate measurement of small absorption coefficients, *SAE Trans.* (2007) 1701–1705.
- [180] H. Levine, J. Schwinger, On the radiation of sound from an unflanged circular pipe, *Phys. Rev.* 73 (1948) 383.

- [181] J.C. Rubio-Romero, M. del Carmen Pardo-Ferreira, J.A. Torrecilla-García, S. Calero-Castro, Disposable masks: Disinfection and sterilization for reuse, and non-certified manufacturing, in the face of shortages during the COVID-19 pandemic, *Saf. Sci.* 129 (2020) 104830.
- [182] M. Elkasaby, H.A. Hegab, A. Mohany, G.M. Rizvi, Modeling and optimization of electrospinning of polyvinyl alcohol (PVA), *Adv. Polym. Technol.* 37 (2018) 2114–2122.
- [183] K. Magniez, C. De Lavigne, B. Fox, The effects of molecular weight and polymorphism on the fracture and thermo-mechanical properties of a carbon-fibre composite modified by electrospun poly (vinylidene fluoride) membranes, *Polymer*. 51 (2010) 2585–2596.
- [184] M.M. Hohman, M. Shin, G. Rutledge, M.P. Brenner, Electrospinning and electrically forced jets. I. Stability theory, *Phys. Fluids*. 13 (2001) 2201–2220.
- [185] X. Li, L. Lin, Y. Zhu, W. Liu, T. Yu, M. Ge, Preparation of ultrafine fast-dissolving cholecalciferol-loaded poly (vinyl pyrrolidone) fiber mats via electrospinning, *Polym. Compos.* 34 (2013) 282–287.
- [186] L. Mei, R. Han, Y. Gao, Y. Fu, Y. Liu, Effect of electric field intensity on the morphology of magnetic-field-assisted electrospinning PVP nanofibers, *J. Wuhan Univ. Technol.-Mater Sci Ed.* 28 (2013) 1107–1111.
- [187] C. Zhang, X. Yuan, L. Wu, Y. Han, J. Sheng, Study on morphology of electrospun poly (vinyl alcohol) mats, *Eur. Polym. J.* 41 (2005) 423–432.
- [188] D. Li, Y. Xia, Fabrication of titania nanofibers by electrospinning, *Nano Lett.* 3 (2003) 555–560.
- [189] Y. Xin, Z. Huang, E. Yan, W. Zhang, Q. Zhao, Controlling poly (p-phenylene vinylene)/poly (vinyl pyrrolidone) composite nanofibers in different morphologies by electrospinning, *Appl. Phys. Lett.* 89 (2006) 053101.
- [190] Y. Jin, X. Lu, C. Wang, Fabrication of discontinuous fibers of poly (N-vinylpyrrolidone) containing metalloporphyrin molecules, *J. Appl. Polym. Sci.* 102 (2006) 6017–6022.
- [191] M. Papila, Y. Menceloğlu, Effect of electrospinning parameters on polyacrylonitrile nanofiber diameter: An investigation by response surface methodology, *Mater. Des.* 29 (2008) 34–44.
- [192] G.R. Mitchell, *Electrospinning: principles, practice and possibilities*, Royal Society of Chemistry, 2015.
- [193] Q. Yang, Z. Li, Y. Hong, Y. Zhao, S. Qiu, C. Wang, Y. Wei, Influence of solvents on the formation of ultrathin uniform poly (vinyl pyrrolidone) nanofibers with electrospinning, *J. Polym. Sci. Part B Polym. Phys.* 42 (2004) 3721–3726.
- [194] S. Chuangchote, T. Sagawa, S. Yoshikawa, Electrospinning of poly (vinyl pyrrolidone): Effects of solvents on electrospinnability for the fabrication of poly (p-phenylene vinylene) and TiO<sub>2</sub> nanofibers, *J. Appl. Polym. Sci.* 114 (2009) 2777–2791.
- [195] M.M. Hohman, M. Shin, G. Rutledge, M.P. Brenner, Electrospinning and electrically forced jets. I. Stability theory, *Phys. Fluids*. 13 (2001) 2201–2220.
- [196] C. Zhang, X. Yuan, L. Wu, Y. Han, J. Sheng, Study on morphology of electrospun poly (vinyl alcohol) mats, *Eur. Polym. J.* 41 (2005) 423–432.

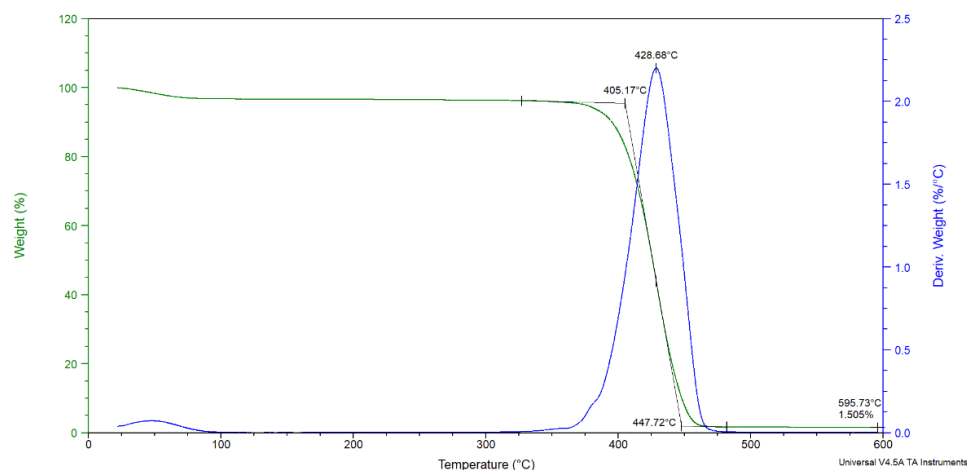
- [197] Utkarsh, H. Hegab, M. Tariq, N.A. Syed, G. Rizvi, R. Pop-Iliev, Towards Analysis and Optimization of Electrospun PVP (Polyvinylpyrrolidone) Nanofibers, *Adv. Polym. Technol.* 2020 (2020).
- [198] X. Zhang, Vibration sound absorption theory and acoustic design, Xi'an Jiaotong Univ. Press Xi'an. (2007) 15.
- [199] M.K. Ozturk, B. Nergis, C. Candan, K. Kalinova, THE INFLUENCE OF AIR GAP BETWEEN NANOFIBROUS LAYER AND RIGID WALL ON THE SOUND ABSORPTION BEHAVIOR, *Text. Sci. Econ.* 160 (n.d.) 37.
- [200] K. Kalinová, Nanofibrous resonant membrane for acoustic applications, *J. Nanomater.* 2011 (2011).
- [201] M. Ibrahim, R. Melik, Physical parameters affecting acoustic absorption characteristics of fibrous materials, *Proc. Math. Phys. Soc. Egypt.* 46 (1978) 17–25.
- [202] H. Qui, Y. Enhui, Effect of thickness, density and cavity depth on the sound absorption properties of wool boards, *AUTEX Res. J.* 18 (2018) 203–208.
- [203] C.M. Wu, M.H. Chou, Sound absorption of electrospun polyvinylidene fluoride/graphene membranes, *Eur. Polym. J.* 82 (2016) 35–45.
- [204] A.C. Canalli Bortolassi, V.G. Guerra, M.L. Aguiar, L. Soussan, D. Cornu, P. Miele, M. Bechelany, Composites based on nanoparticle and pan electrospun nanofiber membranes for air filtration and bacterial removal, *Nanomaterials.* 9 (2019) 1740.
- [205] B. Li, C. Huang, X. Yang, PREPARATION AND CHARACTERIZATION OF ELECTROSPUN WOOL KERATIN/POLYETHYLENE OXIDE NANOFIBERS FOR AIR FILTRATION APPLICATIONS., *Dig. J. Nanomater. Biostructures DJNB.* 12 (2017).
- [206] H.W. Tong, S.K.C. Kwok, H.C. Kwok, Protective masks with coating comprising different electrospun fibers interweaved with each other, formulations forming the same, and method of producing thereof, (2019).
- [207] H. Zhong, Z. Zhu, J. Lin, C.F. Cheung, V.L. Lu, F. Yan, C.-Y. Chan, G. Li, Reusable and recyclable graphene masks with outstanding superhydrophobic and photothermal performances, *ACS Nano.* 14 (2020) 6213–6221.
- [208] W. Jang, J. Yun, K. Jeon, H. Byun, PVdF/graphene oxide hybrid membranes via electrospinning for water treatment applications, *Rsc Adv.* 5 (2015) 46711–46717.
- [209] A. Yar, B. Haspulat, T. Üstün, V. Eskizeybek, A. Avcı, H. Kandaş, S. Achour, Electrospun TiO<sub>2</sub>/ZnO/PAN hybrid nanofiber membranes with efficient photocatalytic activity, *RSC Adv.* 7 (2017) 29806–29814.
- [210] F.A. Sheikh, M.A. Kanjwal, S. Saran, W.-J. Chung, H. Kim, Polyurethane nanofibers containing copper nanoparticles as future materials, *Appl. Surf. Sci.* 257 (2011) 3020–3026.
- [211] Utkarsh, H. Hegab, M. Tariq, N.A. Syed, G. Rizvi, R. Pop-Iliev, Towards Analysis and Optimization of Electrospun PVP (Polyvinylpyrrolidone) Nanofibers, *Adv. Polym. Technol.* 2020 (2020).
- [212] R. Jan, A. Habib, M.A. Akram, A.N. Khan, Uniaxial drawing of graphene-PVA nanocomposites: Improvement in mechanical characteristics via strain-induced exfoliation of graphene, *Nanoscale Res. Lett.* 11 (2016) 1–9.

- [213] Z. Wang, Z. Pan, J. Wang, R. Zhao, A novel hierarchical structured poly (lactic acid)/titania fibrous membrane with excellent antibacterial activity and air filtration performance, J. Nanomater. 2016 (2016).

## Appendices

### Appendix A

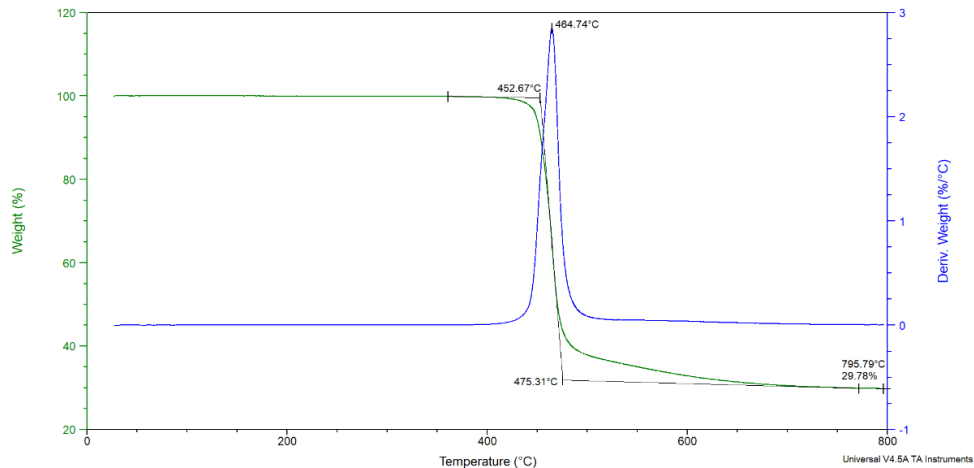
#### A1. TGA thermograph of pure PVP powders.



#### A2. TGA measurements of PVP-based specimens.

Polymer Sample	Onset of Degradation (°C)	Peak of $d(\text{weight})/d(\text{time})$ vs temp (°C)	Residue (%)
PVP	405.17	428.68	1.505
PVP 8	412.66	436.12	3.319
PVP 10	412.13	436.61	2.630
PVP 12	408.32	436.09	3.632
PVP 8 -- CNT 0.25	412.75	437.64	5.925
PVP 8 -- CNT 0.5	410.96	436.13	7.182
PVP 8 -- CNT 1	407.69	434.38	8.259
PVP 8 -- GN 0.25	411.63	434.93	3.910
PVP 8 -- GN 0.50	410.09	432.22	4.302
PVP 8 -- GN 1	408.95	432.79	5.433
PVP 8 -- FS 0.25	414.26	437.42	4.950
PVP 8 -- FS 0.5	414.46	438.43	6.570
PVP 8 -- FS 1	411.50	438.74	9.754
PVP 8 -- FG 0.25	413.68	435.71	2.912
PVP 8 -- FG 0.5	410.81	432.27	5.069
PVP 8 -- FG 1	413.55	435.64	2.947
PVP 8 -- MC 0.25	412.02	435.44	3.975
PVP 8 -- MC 0.5	412.72	434.98	7.387
PVP 8 -- MC 1	412.04	435.54	7.428

### A3. TGA thermograph of pure PVDF pellets.



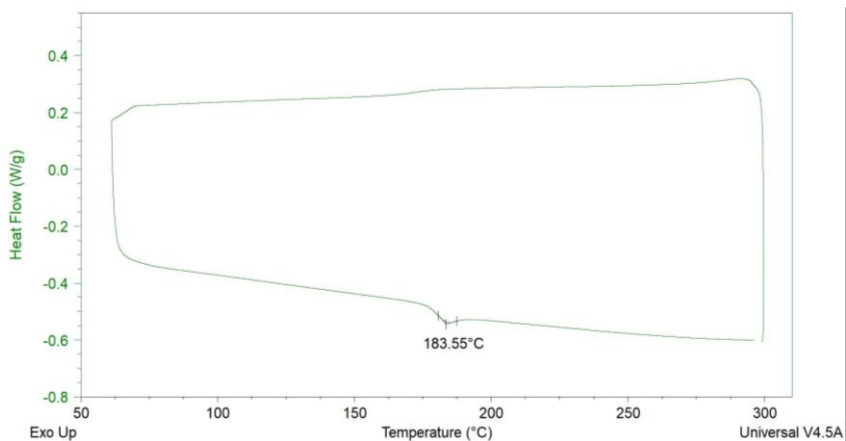
### A4. TGA measurements of PVDF-based specimens.

Polymer Sample	Onset of Degradation (°C)	Peak of $d(\text{weight})/d(\text{time})$ vs temp (°C)	Residue (%)
PVDF	452.67	464.74	29.780
PVDF 20	456.01	467.07	27.790
PVDF 22	454.40	466.82	28.450
PVDF 25	455.01	467.65	28.570
PVDF -- CNT 0.25	459.21	471.09	26.870
PVDF -- CNT 0.5	455.62	468.22	30.390
PVDF -- CNT 1	452.46	463.85	32.650
PVDF -- GN 0.25	458.46	470.20	28.090
PVDF -- GN 0.50	458.20	470.28	28.380
PVDF -- GN 1	457.48	469.91	29.140
PVDF -- FS 0.25	466.12	476.420	25.450
PVDF -- FS 0.5	464.81	474.600	26.400
PVDF -- FS 1	461.38	474.000	26.750
PVDF -- FG 0.25	460.53	470.640	27.500
PVDF -- FG 0.5	460.74	471.050	27.300
PVDF -- FG 1	457.34	469.720	25.650
PVDF -- MC 0.25	444.38	460.220	29.330
PVDF -- MC 0.5	439.07	454.710	29.220
PVDF -- MC 1	431.59	446.480	29.100



## Appendix B

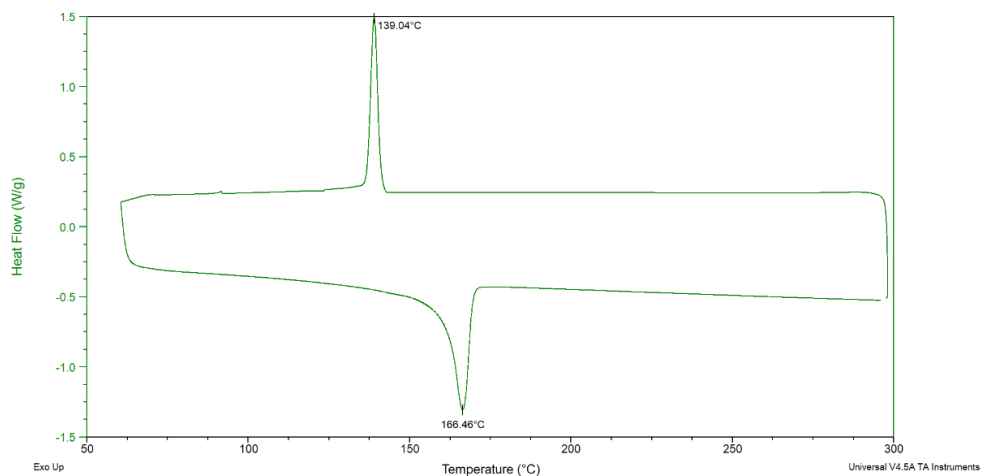
### B1. DSC thermograph of pure PVP powders.



### B2. DSC measurements of PVP-based specimens.

Polymer Sample	Glass Transition Temp. – Tg (°C)
PVP	183.55
PVP 8	142.22
PVP 10	142.75
PVP 12	145.41
PVP -- CNT 0.25	145.45
PVP -- CNT 0.5	145.23
PVP -- CNT 1	143.52
PVP -- GN 0.25	144.58
PVP -- GN 0.50	141.47
PVP -- GN 1	140.91
PVP -- FS 0.25	147.90
PVP -- FS 0.5	147.15
PVP -- FS 1	148.41
PVP -- FG 0.25	144.19
PVP -- FG 0.5	143.36
PVP -- FG 1	143.43
PVP -- MC 0.25	146.24
PVP -- MC 0.5	147.43
PVP -- MC 1	145.44

### B3. DSC thermograph of pure PVDF pellets.

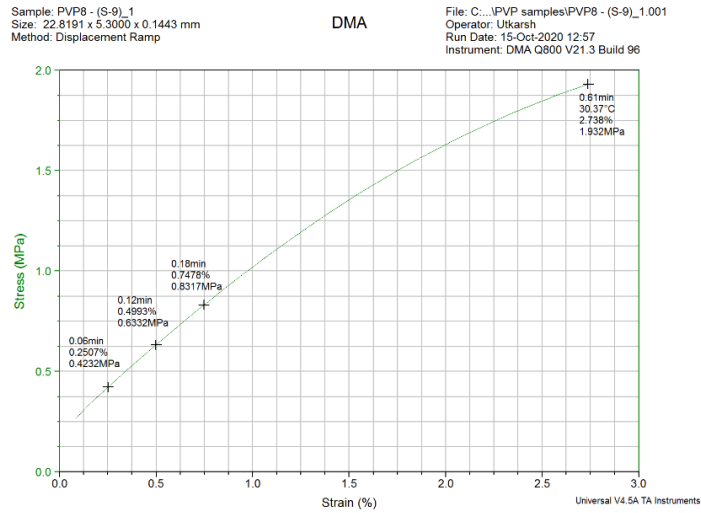


### B4. DSC measurements of PVDF-based specimens.

Polymer Sample	Melting Temp. – T <sub>m</sub> (°C)	Crystallization Temp. - T <sub>c</sub> (°C)
PVDF	166.46	139.04
PVDF 20	165.94	138.41
PVDF 22	166.24	138.06
PVDF 25	165.99	138.20
PVDF -- CNT 0.25	167.43	146.49
PVDF -- CNT 0.5	167.50	146.70
PVDF -- CNT 1	167.68	147.21
PVDF -- GN 0.25	166.64	141.29
PVDF -- GN 0.50	167.11	144.05
PVDF -- GN 1	167.25	145.73
PVDF -- FS 0.25	166.28	139.80
PVDF -- FS 0.5	166.20	140.54
PVDF -- FS 1	165.77	140.22
PVDF -- FG 0.25	166.49	140.37
PVDF -- FG 0.5	166.49	139.91
PVDF -- FG 1	166.35	138.60
PVDF -- MC 0.25	166.46	138.85
PVDF -- MC 0.5	166.23	139.09
PVDF -- MC 1	166.19	139.18

## Appendix C

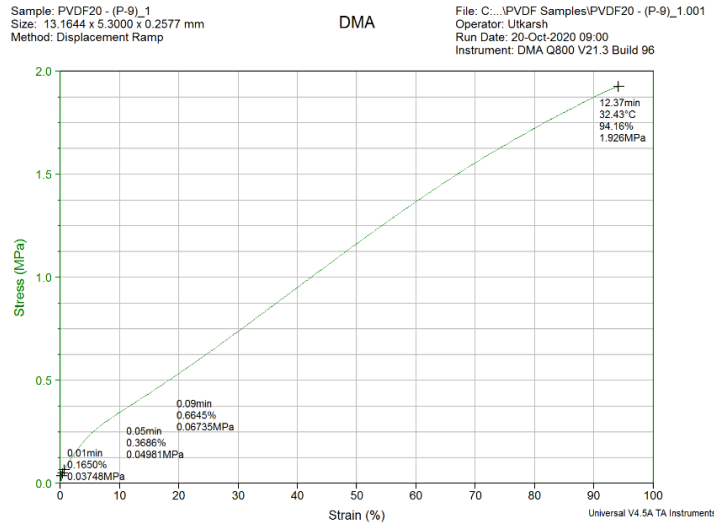
### C1. DMA of pure PVP nanofiber membrane.



### C2. DMA measurements of PVP-based specimens.

Polymer Sample	Tensile Strength (Mpa)		Elongation at break (%)		Young's Modulus (Mpa)	
	Avg.	Std.	Avg.	Std.	Avg.	Std.
PVP 8	1.91	0.03	2.35	0.38	0.93	0.076
PVP 10	1.70	0.18	5.37	0.26	0.63	0.012
PVP 12	0.59	0.02	4.35	0.27	0.17	0.008
PVP8 CNT 0.25	0.50	0.03	2.83	0.05	0.22	0.009
PVP8 CNT 0.5	0.32	0.00	1.41	0.02	0.21	0.003
PVP8 CNT 1	0.69	0.02	3.50	0.30	0.19	0.004
PVP8 GN 0.25	0.50	0.01	2.95	0.10	0.25	0.007
PVP8 GN 0.50	0.33	0.03	2.38	0.05	0.17	0.009
PVP8 GN 1	0.41	0.02	3.31	0.26	0.19	0.002
PVP8 FS 0.25	0.42	0.02	1.24	0.22	0.34	0.016
PVP8 FS 0.5	0.49	0.04	0.93	0.11	0.40	0.054
PVP8 FS 1	0.50	0.01	0.75	0.03	0.60	0.005
PVP8 FG 0.25	0.86	0.05	4.56	0.30	0.32	0.015
PVP8 FG 0.5	0.89	0.02	4.49	0.28	0.33	0.002
PVP8 FG 1	0.50	0.04	1.84	0.14	0.29	0.064
PVP8 MC 0.25	0.58	0.03	2.20	0.26	0.34	0.024
PVP8 MC 0.5	0.46	0.01	1.56	0.05	0.32	0.008
PVP8 MC 1	0.40	0.02	2.07	0.14	0.24	0.005

### C3. DMA of pure PVDF nanofiber membrane.

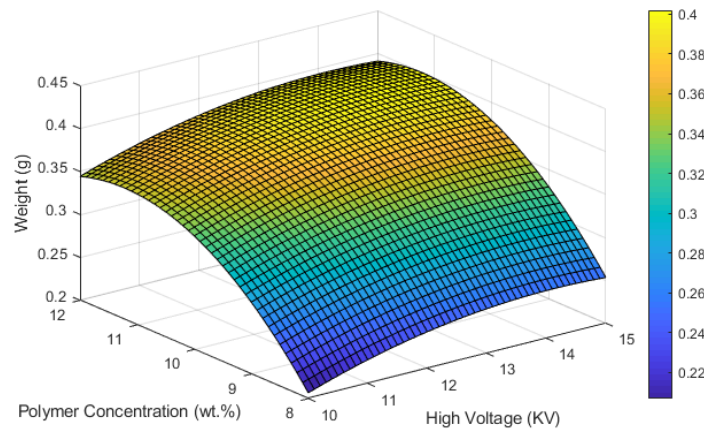
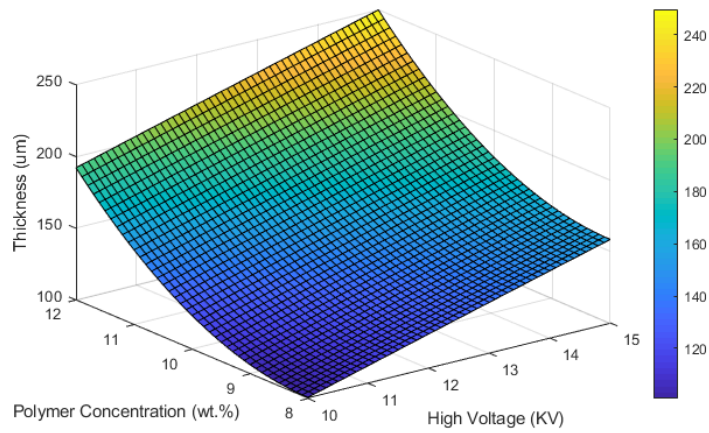
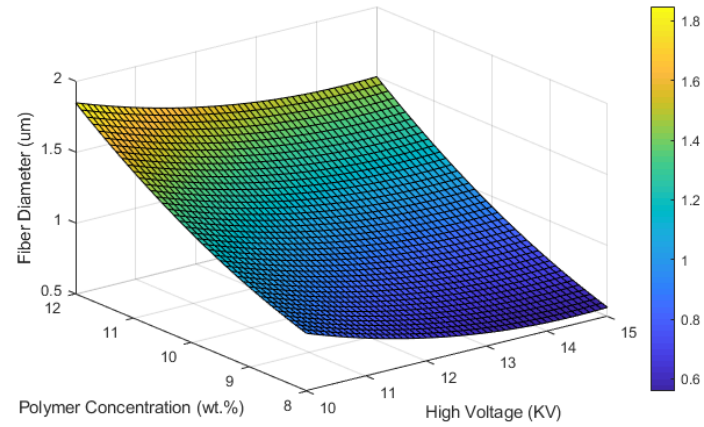


### C4. DMA measurements of PVDF-based specimens.

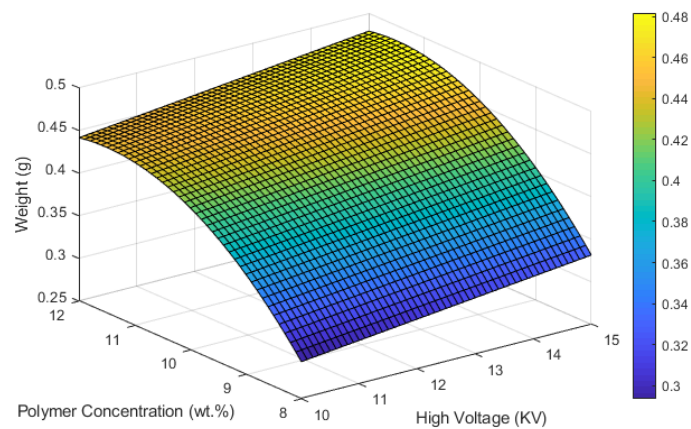
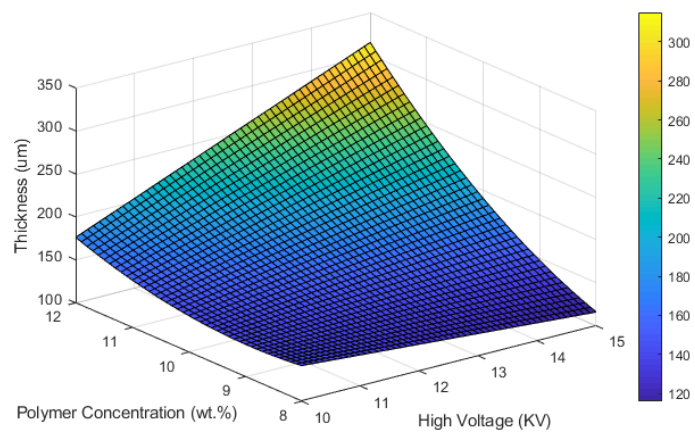
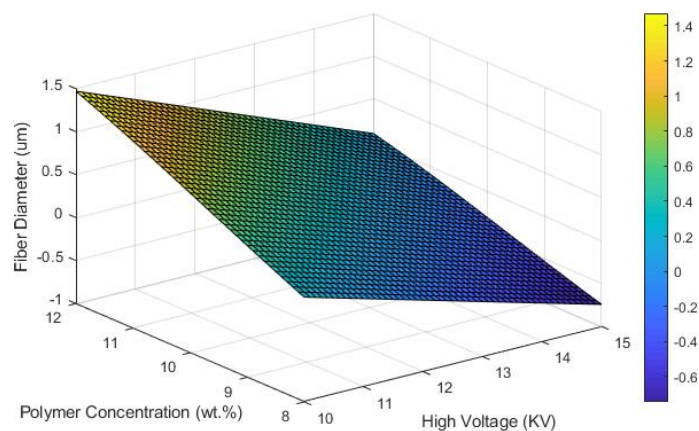
Polymer Sample	Tensile Strength (Mpa)		Elongation at break (%)		Young's Modulus (Mpa)	
	Avg.	Std.	Avg.	Std.	Avg.	Std.
PVDF 20	1.75	0.16	83.09	8.88	0.06	0.003
PVDF 22	1.83	0.41	65.79	6.30	0.04	0.007
PVDF 25	3.53	0.12	87.97	3.08	0.08	0.003
PVDF20CNT 0.25	1.20	0.04	94.62	2.21	0.03	0.001
PVDF20 CNT 0.5	1.02	0.01	76.96	5.26	0.05	0.002
PVDF20 CNT 1	0.57	0.02	36.84	1.45	0.05	0.002
PVDF20 GN 0.25	1.73	0.16	107.70	5.76	0.04	0.005
PVDF20 GN 0.50	1.52	0.15	97.01	10.79	0.04	0.004
PVDF20 GN 1	1.47	0.15	65.49	8.16	0.05	0.001
PVDF20 FS 0.25	1.85	0.00	99.15	3.25	0.04	0.001
PVDF20 FS 0.5	1.60	0.12	89.72	9.80	0.04	0.004
PVDF20 FS 1	1.42	0.05	86.96	4.18	0.04	0.002
PVDF20 FG 0.25	3.51	0.36	132.20	4.92	0.08	0.007
PVDF20 FG 0.5	2.84	0.23	116.77	2.03	0.05	0.004
PVDF20 FG 1	2.87	0.09	99.11	14.00	0.07	0.007
PVDF20 MC 0.25	2.41	0.11	102.23	2.14	0.06	0.006
PVDF20 MC 0.5	2.23	0.05	100.40	2.41	0.05	0.003
PVDF20 MC 1	1.87	0.21	68.29	9.96	0.05	0.018

## Appendix D

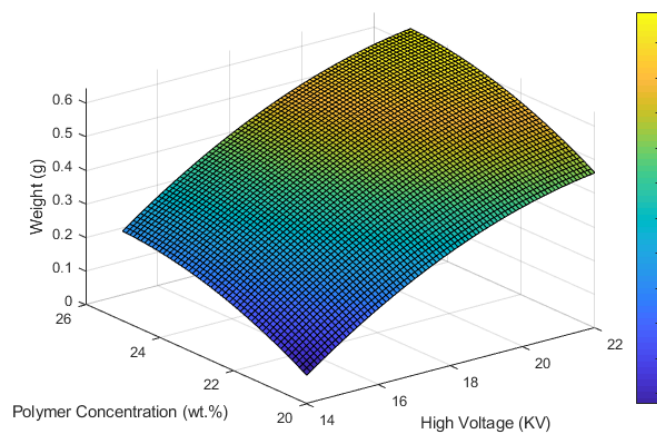
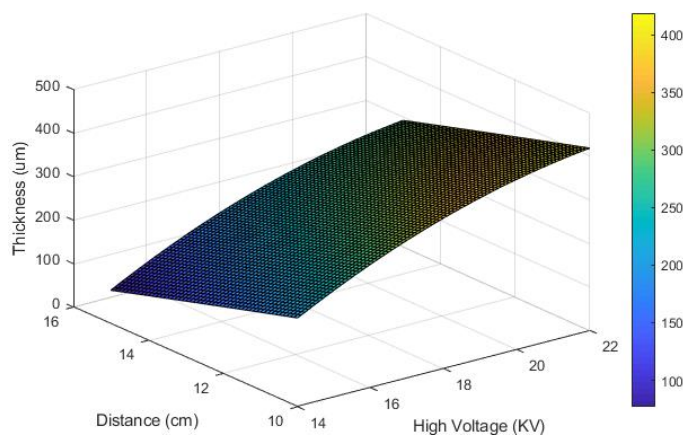
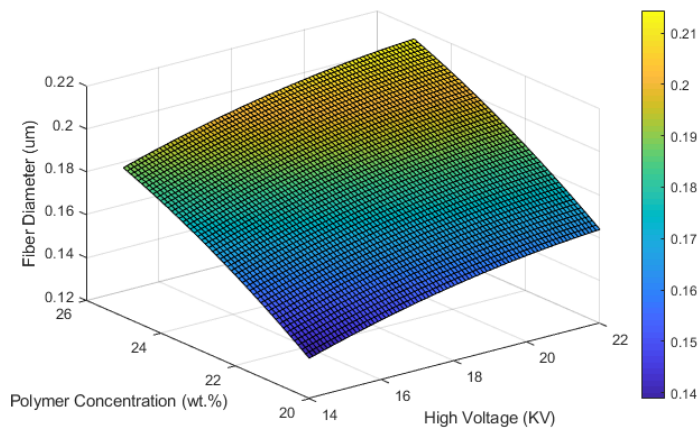
D1. Three-dimensional surface and contour plots demonstrating the effect of significant design parameters on fiber diameter, thickness, and weight of PVP nanofiber membranes using RSM models.



D2. Three-dimensional surface and contour plots demonstrating the effect of significant design parameters on fiber diameter, thickness, and weight of PVP nanofiber membranes using GP models.

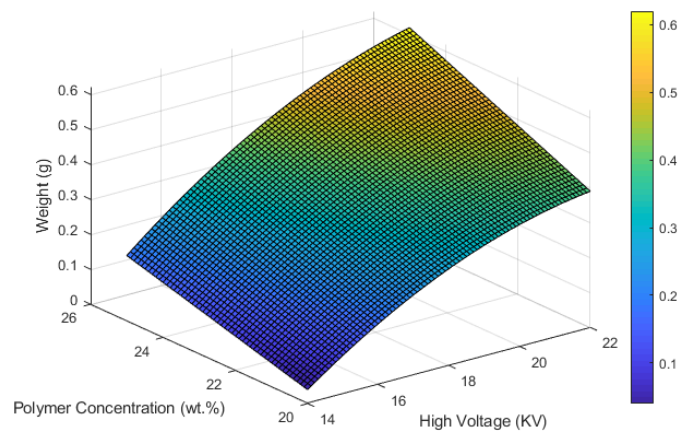
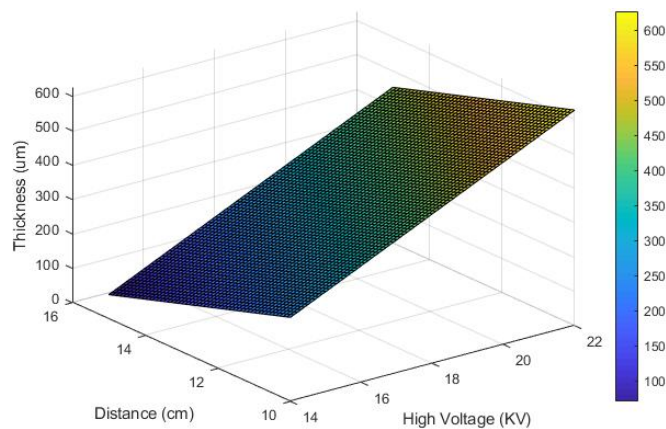
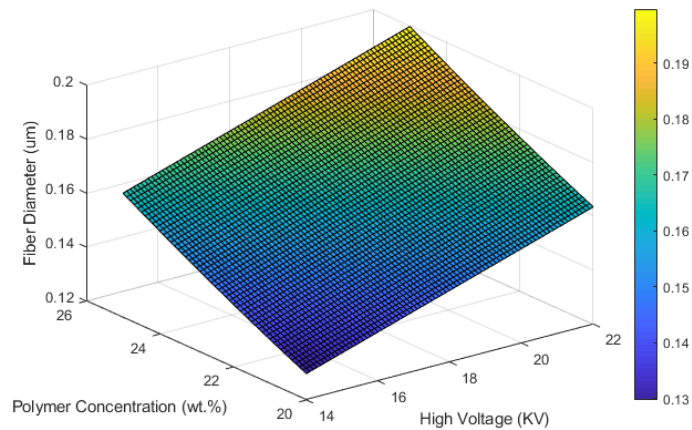


D3. Three-dimensional surface and contour plots demonstrating the effect of significant design parameters on fiber diameter, thickness, and weight of PVDF nanofiber membranes using RSM models.





D4. Three-dimensional surface and contour plots demonstrating the effect of significant design parameters on fiber diameter, thickness, and weight of PVDF nanofiber membranes using GP models.





## Appendix E

### E1. Modelling and Optimization Criteria for Electrospinning of Polymeric Materials Case 1: PVP

a) Objective Function:

<b>Fiber Diameter</b>	<b>RSM</b>	$5.6522 - 0.5087A - 0.2850B + 0.0008C - 0.5591D + 5.3488E + 0.0176A^2 + 0.0260B^2 - 4.6e^{-7}C^2 + 0.0228D^2 - 3.1333E^2$
	<b>GP</b>	$0.0517 * E * B^2 + 0.0006 * D * E * A^2 - 0.1846 - 0.03150 * A - 5.7462e^{-6} * D * B^4 - 0.0318 * A * B * E^2$
<b>Thickness</b>	<b>RSM</b>	$-250.5700 + 12.4507A - 91.8828B - 0.2048C + 81.8174D + 360.1778E - 0.0388A^2 + 5.7367B^2 + 0.0001C^2 - 3.1985D^2 - 168.3333E^2$
	<b>GP</b>	$1136.3181 + 668.0433 * E + -7185.6879 * E / D + 0.4108 * A * B^2 - 31.3939 * A - 34.4828 * D - 73.4696 * B$
<b>Weight</b>	<b>RSM</b>	$-0.8859 + 0.0818A + 0.3184B - 0.0003C - 0.1242D - 0.5238E - 0.0029A^2 - 0.0142B^2 + 1.8e^{-7}C^2 + 0.0049D^2 + 0.3934E^2$
	<b>GP</b>	$0.3853 * E + 0.2830 * B + 0.0405 * A + 0.0002 * C * E - 1.7256 - 7.3247e^{-6} * A * C - 0.0322 * A * E - 0.0123 * B^2$

b) Decision Variables and Constraints:

High Voltage (KV)	A	$\left\{ \begin{array}{l} 10 \leq A \leq 15 \\ 08 \leq B \leq 12 \\ 500 \leq C \leq 1500 \\ 10 \leq D \leq 15 \\ 0.6 \leq E \leq 1.0 \end{array} \right.$
Polymer Concentration (Wt.%)	B	
Collector Rotation (RPM)	C	
Distance (cm)	D	
Flow Rate (ml/hr)	E	

### Case 2: PVDF

a) Objective Function:

<b>Fiber Diameter</b>	<b>RSM</b>	$-0.72211 + 0.01211V + 0.03623C - 0.00002S + 0.03336D + 0.0825F - 0.00025V^2 - 0.00058C^2 - 0.00123D^2 - 0.0375F^2$
	<b>GP</b>	$0.2135 + 0.0411 * E + 0.0013 * A * D + -0.0499 * E / C + 1.6135e^{-7} * C * B^2 - 0.0101 * D - 0.0127 * A - 8.3543e^{-6} * C * D$
<b>Thickness</b>	<b>RSM</b>	$-8286.0415 + 104.4778V + 718.6601C - 0.3421S - 23.3675D - 411.6055F - 2.1571V^2 - 15.8999C^2 + 0.0001S^2 - 0.0831D^2 + 232.4444F^2$
	<b>GP</b>	$25297.7783 + 2591.1964 * A + 1.1508 * B^3 + -37584.5145 * A / B - 34.6556 * D - 1710.4827 * B - 1.7251 * A * B^2$
<b>Weight</b>	<b>RSM</b>	$-4.9069 + 0.1946V + 0.3156C + 0.00002S - 0.1261D + 0.5318F - 0.0041V^2 - 0.0062C^2 + 1e^{-8}S^2 + 0.00372D^2 - 0.32111F^2$
	<b>GP</b>	$0.1045 * A + 10.5551 / D + 0.0022 * A * D + 0.0021 * A * B + 8.9782e^{-6} * A * C - 2.3849 - 0.0002 * C - 0.0039 * A^2$

b) Decision Variables and Constraints:

High Voltage (KV)	A	}	$14 \leq A \leq 22$
Polymer Concentration (Wt.%)	B		$20 \leq B \leq 25$
Collector Rotation (RPM)	C		$500 \leq C \leq 1500$
Distance (cm)	D		$10 \leq D \leq 15$
Flow Rate (ml/hr)	E		$0.6 \leq E \leq 1.0$

E2. Signal-to-Noise (S/N) ratio

1) Nominal-the-Best

$$S/N = 10 \log_{10} [(\bar{Y}^2/S^2) - (1/n)]$$

Where,  $\bar{Y}$  = Average signal factors

$S^2$  = Variance or noise factors

n = Number of measurements

2) Smaller-the-Better

$$S/N = -10 \log_{10} [(\sum y^2)/n]$$

3) Larger-the-Better

$$S/N = -10 \log_{10} [(\sum 1/y^2)/n]$$

In the present study, it should be stated that all three output responses followed the Smaller-the-Better criteria.

E3. Signal-to-Noise (S/N) ratio and confirmation study for PVP

Run	FD (nm)	S/N <sub>FD</sub>	Thickness (μm)	S/N <sub>T</sub>	Weight (mg)	S/N <sub>w</sub>
1	662	-56.42	122.47	-41.76	228.7	-47.18
2	933	-59.39	145.97	-43.28	54.0	-34.65
3	744	-57.43	152.28	-43.65	354.4	-50.99
4	1253	-61.96	165.58	-44.38	360.4	-51.14
5	1243	-61.89	94.93	-39.54	311.9	-49.88
6	1527	-63.68	106.43	-40.54	425.8	-52.58
7	1865	-65.41	170.62	-44.64	413.0	-52.32
8	2540	-68.09	143.80	-43.15	449.6	-53.06
9	1507	-63.56	137.05	-42.73	371.4	-51.39
10	605	-55.64	112.26	-41.01	276.4	-48.84
11	819	-58.27	151.05	-43.58	255.8	-48.16
12	570	-55.12	154.04	-43.75	305.3	-49.695
13	1091	-60.76	224.77	-47.03	434.1	-52.75
14	1048	-60.41	94.12	-39.47	367.7	-51.31
15	879	-58.88	140.72	-42.96	432.0	-52.71
16	2075	-66.34	228.44	-47.17	403.9	-52.12
17	1290	-62.21	208.40	-46.37	470.9	-53.46
18	1120	-60.98	237.22	-47.51	405.3	-52.16
19	536	-54.58	92.86	-39.35	291.0	-49.28
20	598	-55.53	97.54	-39.78	316.4	-50.00
21	921	-59.28	144.26	-43.18	343.0	-50.71
22	668	-56.49	188.78	-45.51	423.1	-52.53
23	1074	-60.62	152.62	-43.67	402.8	-52.10
24	926	-59.33	209.57	-46.42	403.3	-52.11
25	1465	-63.32	305.26	-49.69	422.0	-52.50
26	1486	-63.44	276.61	-48.83	317.4	-50.03
27	1560	-63.86	287.95	-49.18	422.3	-52.51

Confirmation Experiments										
A	B	C	D	E	FD	S/N	T	S/N	W	S/N
15	8	500	10	0.6	536	-28.64	92.86	-21.08	291.0	-25.85
15	8	500	10	0.6	498		88.24		251.2	
Error%					7.0895		4.98		13.677	

E4. Signal-to-Noise (S/N) ratio and confirmation study for PVDF

Run	FD (nm)	S/N <sub>FD</sub>	Thickness (μm)	S/N <sub>T</sub>	Weight (mg)	S/N <sub>w</sub>
1	135	-42.61	356.84	-51.05	182.7	-45.23
2	138	-42.79	73.22	-37.29	126.8	-42.06
3	112	-40.98	40.39	-32.12	70.4	-36.95
4	202	-46.11	141.20	-42.99	138.9	-42.85
5	139	-42.86	94.77	-39.53	135.1	-42.61
6	139	-42.86	245.14	-47.78	295.6	-49.41
7	160	-44.08	125.50	-41.97	167.2	-44.46
8	178	-45.01	310.18	-49.83	381.3	-51.62
9	157	-43.92	200.58	-46.04	206.4	-46.29
10	132	-42.41	344.28	-50.73	511.1	-54.17
11	128	-42.14	213.80	-46.60	285.0	-49.09
12	137	-42.73	310.49	-49.84	199.2	-45.98
13	144	-43.17	289.56	-49.23	318.3	-50.05
14	198	-45.93	296.43	-49.43	298.0	-49.48
15	173	-44.76	405.76	-52.16	625.2	-55.92
16	211	-46.49	333.65	-50.46	467.2	-53.39
17	192	-45.67	340.37	-50.63	687.9	-56.75
18	193	-45.71	329.68	-50.36	502.1	-54.01
19	142	-43.05	353.67	-50.97	394.1	-51.91
20	176	-44.91	353.93	-50.97	396.0	-51.95
21	169	-44.56	257.72	-48.22	422.9	-52.52
22	204	-46.19	654.04	-56.31	623.6	-55.89
23	149	-43.46	452.45	-53.11	530.1	-54.48
24	128	-42.14	640.50	-56.13	636.7	-56.07
25	240	-47.60	209.65	-46.43	569.9	-55.11
26	182	-45.20	269.43	-48.61	644.1	-56.17
27	194	-45.76	327.58	-50.31	661.8	-56.41

Confirmation Experiments										
A	B	C	D	E	FD	S/N	T	S/N	W	S/N
14	20	1500	15	1	112	-22.13	40.39	-17.78	70.4	-20.22
14	20	1500	15	1	119		44.26		78.2	
Error%					-6.25		-9.581		-11.08	

## Appendix F

F1. Rights and permissions for the figures used in the thesis.



Order Number: 1135490

Order Date: 26 Jul 2021

### Payment Information

Utkarsh Utkarsh  
fnu.utkarsh@ontariotechu.net  
Payment method: Invoice

**Billing Address:**  
Mr. Utkarsh Utkarsh  
1820 Dalhousie Crescent  
Oshawa, ON L1G8C5  
Canada

+1 (289) 688-6599  
fnu.utkarsh@ontariotech  
u.net

**Customer Location:**  
Mr. Utkarsh Utkarsh  
1820 Dalhousie Crescent  
Oshawa, ON L1G8C5  
Canada

### Order Details

1. Angewandte Chemie. Ausgabe A, Wissenschaftlicher Teil

**Billing Status:**  
Open

Article: Super-Hydrophobic Surface of Aligned Polyacrylonitrile Nanofibers

Order License ID	1135490-1	Type of use	Republish in a thesis/dissertation
Order detail status	Completed	Publisher	ANGEWANDTE CHEMIE
ISSN	1521-3757	Portion	Image/photo/illustration
			0.00 CAD
			Republishing Permission

[Figure 2.4]

### LICENSED CONTENT

Publication Title	Angewandte Chemie. Ausgabe A, Wissenschaftlicher Teil	Rightsholder	John Wiley & Sons - Books
Article Title	Super-Hydrophobic Surface of Aligned Polyacrylonitrile Nanofibers	Publication Type	e-Journal
		Start Page	1269
		End Page	1271
		Issue	7
Author/Editor	Gesellschaft Deutscher Chemiker.	Volume	114
Date	01/01/1949		
Language	German		
Country	Germany		

### REQUEST DETAILS

Portion Type	Image/photo/illustration	Distribution	Worldwide
Number of images / photos / illustrations	3	Translation	Original language of publication
Format (select all that apply)	Print,Electronic	Copies for the disabled?	Yes
Who will republish the content?	Academic institution	Minor editing privileges?	No
Duration of Use	Life of current edition	Incidental promotional use?	No
Lifetime Unit Quantity	Up to 500,000	Currency	CAD
Rights Requested	Main product		

## NEW WORK DETAILS

Title	Development of Polymeric Nano-Composite Fiber Based Structures for Acoustics and Filtration Applications	Institution name	University of Ontario Institute of Technology (Ontario Tech University)
		Expected presentation date	2021-08-16
Instructor name	Dr. Ghaus Rizvi and Dr. Remon Pop-Iliev		

## ADDITIONAL DETAILS

The requesting person / organization to appear on the license

UTKARSH

## REUSE CONTENT DETAILS

Title, description or numeric reference of the portion(s)	Figure 1. SEM images of a) surface of the as-prepared anodic aluminum oxide membrane; b) surface of the PAN nanofibers; c) cross-sectional view of the as-synthesized PAN nanofibers	Title of the article/chapter the portion is from	Super-Hydrophobic Surface of Aligned Polyacrylonitrile Nanofibers
Editor of portion(s)	Feng, Lin, Dr.; Li, Shuhong, Dr.; Li, Huanjun, Dr.; Zhai, Jin, Dr.; Song, Yanlin, Prof.; Jiang, Lei, Prof.; Zhu, Daoben, Prof.	Author of portion(s)	Feng, Lin, Dr.; Li, Shuhong, Dr.; Li, Huanjun, Dr.; Zhai, Jin, Dr.; Song, Yanlin, Prof.; Jiang, Lei, Prof.; Zhu, Daoben, Prof.
Volume of serial or monograph	114	Publication date of portion	2002-04-02
Page or page range of portion	1269-1271		

## John Wiley & Sons - Books Terms and Conditions

No right, license or interest to any trademark, trade name, service mark or other branding ("Marks") of WILEY or its licensors is granted hereunder, and you agree that you shall not assert any such right, license or interest with respect thereto. You may not alter, remove or suppress in any manner any copyright, trademark or other notices displayed by the Wiley material. This Agreement will be void if the Type of Use, Format, Circulation, or Requestor Type was misrepresented during the licensing process. In no instance may the total amount of Wiley Materials used in any Main Product, Compilation or Collective work comprise more than 5% (if figures/tables) or 15% (if full articles/chapters) of the (entirety of the) Main Product, Compilation or Collective Work. Some titles may be available under an Open Access license. It is the Licensors' responsibility to identify the type of Open Access license on which the requested material was published, and comply fully with the terms of that license for the type of use specified. Further details can be found on Wiley Online Library <http://olabout.wiley.com/WileyCDA/Section/id-410895.html>.

### 2. Polymer engineering and science

**Billing Status:**  
Open

Article: Polybenzimidazole nanofiber produced by electrospinning

Order License ID	1135490-2	Type of use	Republish in a thesis/dissertation
Order detail status	Completed	Publisher	JOHN/WILEY & SONS, INC.
ISSN	0032-3888	Portion	Chart/graph/table/figure
			0.00 CAD
			Republishing Permission

[Figure 2.6]

### LICENSED CONTENT

Publication Title	Polymer engineering and science	Publication Type	Journal
Article Title	Polybenzimidazole nanofiber produced by electrospinning	Start Page	849
		End Page	854
		Issue	5
Author/Editor	PORTER, ROGER S., SOCIETY OF PLASTICS ENGINEERS.	Volume	39
		URL	<a href="http://onlinelibrary.wiley.com/journal/10.1002/(ISSN)1548-2634">http://onlinelibrary.wiley.com/journal/10.1002/(ISSN)1548-2634</a>
Date	01/01/1965		
Language	English		
Country	United States of America		
Rightsholder	John Wiley & Sons - Books		

### REQUEST DETAILS

Portion Type	Chart/graph/table/figure	Distribution	Worldwide
		Translation	Original language of publication
Number of charts / graphs / tables / figures requested	1	Copies for the disabled?	Yes
Format (select all that apply)	Print, Electronic	Minor editing privileges?	No

Who will republish the content?	Academic institution	Incidental promotional use?	No
Duration of Use	Life of current edition	Currency	CAD
Lifetime Unit Quantity	Up to 500,000		
Rights Requested	Main product		

## NEW WORK DETAILS

Title	Development of Polymeric Nano-Composite Fiber Based Structures for Acoustics and Filtration Applications	Institution name	University of Ontario Institute of Technology (Ontario Tech University)
		Expected presentation date	2021-08-16
Instructor name	Dr. Ghaus Rizvi and Dr. Remon Pop-Iliev		

## ADDITIONAL DETAILS

The requesting person / organization to appear on the license	Utkarsh
---	---------

## REUSE CONTENT DETAILS

Title, description or numeric reference of the portion(s)	Fig. 1. Schematic diagram of experimental set-up used for electrospinning.	Title of the article/chapter the portion is from	Polybenzimidazole nanofiber produced by electrospinning
Editor of portion(s)	Kim, Jong-Sang; Reneker, Darrell H.	Author of portion(s)	Kim, Jong-Sang; Reneker, Darrell H.
Volume of serial or monograph	39	Publication date of portion	2004-04-08
Page or page range of portion	849-854		

## John Wiley &amp; Sons - Books Terms and Conditions

No right, license or interest to any trademark, trade name, service mark or other branding ("Marks") of WILEY or its licensors is granted hereunder, and you agree that you shall not assert any such right, license or interest with respect thereto. You may not alter, remove or suppress in any manner any copyright, trademark or other notices displayed by the Wiley material. This Agreement will be void if the Type of Use, Format, Circulation, or Requestor Type was misrepresented during the licensing process. In no instance may the total amount of Wiley Materials used in any Main Product, Compilation or Collective work comprise more than 5% (if figures/tables) or 15% (if full articles/chapters) of the (entirety of the) Main Product, Compilation or Collective Work. Some titles may be available under an Open Access license. It is the Licensors' responsibility to identify the type of Open Access license on which the requested material was published, and comply fully with the terms of that license for the type of use specified Further details can be found on Wiley Online Library <http://olabout.wiley.com/WileyCDA/Section/id-410895.html>.

## 3. Physica status solidi : PSS. A, Applications and materials science

Article: Trends in electrospinning of natural nanofibers

Billing Status:  
Open



Order License ID	1135490-3	Type of use	Republish in a thesis/dissertation
Order detail status	Completed	Publisher	WILEY - VCH VERLAG GMBH & CO. KGAA
ISSN	1862-6300	Portion	Chart/graph/table/figure

0.00 CAD

Republishing Permission

[Figure 2.7]

## LICENSED CONTENT

Publication Title	Physica status solidi : PSS. A, Applications and materials science	Publication Type	Journal
Article Title	Trends in electrospinning of natural nanofibers	Start Page	1830
		End Page	1834
		Issue	6
		Volume	204
Date	01/01/2005		
Language	English		
Country	Germany		
Rightsholder	John Wiley & Sons - Books		

## REQUEST DETAILS

Portion Type	Chart/graph/table/figure	Distribution	Worldwide
Number of charts / graphs / tables / figures requested	1	Translation	Original language of publication
Format (select all that apply)	Print,Electronic	Copies for the disabled?	Yes
Who will republish the content?	Academic institution	Minor editing privileges?	Yes
Duration of Use	Life of current edition	Incidental promotional use?	No
Lifetime Unit Quantity	Up to 500,000	Currency	CAD
Rights Requested	Main product		

## NEW WORK DETAILS

Title	Development of Polymeric Nano-Composite Fiber Based Structures for Acoustics and Filtration Applications	Institution name	University of Ontario Institute of Technology (Ontario Tech University)
Instructor name	Dr. Ghaus Rizvi and Dr. Remon Pop-Iliev	Expected presentation date	2021-08-16

## ADDITIONAL DETAILS

The requesting person / organization to appear on the license

Utkarsh

## REUSE CONTENT DETAILS

Title, description or numeric reference of the portion(s)	Fig. 1 (online colour at: <a href="http://www.pss-a.com">www.pss-a.com</a> ) Schematic of electrospinning set up	Title of the article/chapter the portion is from	Trends in electrospinning of natural nanofibers
Editor of portion(s)	Haghi, A. K.; Akbari, M.	Author of portion(s)	Haghi, A. K.; Akbari, M.
Volume of serial or monograph	204	Publication date of portion	2007-06-01
Page or page range of portion	1830-1834		

## John Wiley & Sons - Books Terms and Conditions

No right, license or interest to any trademark, trade name, service mark or other branding ("Marks") of WILEY or its licensors is granted hereunder, and you agree that you shall not assert any such right, license or interest with respect thereto. You may not alter, remove or suppress in any manner any copyright, trademark or other notices displayed by the Wiley material. This Agreement will be void if the Type of Use, Format, Circulation, or Requestor Type was misrepresented during the licensing process. In no instance may the total amount of Wiley Materials used in any Main Product, Compilation or Collective work comprise more than 5% (if figures/tables) or 15% (if full articles/chapters) of the (entirety of the) Main Product, Compilation or Collective Work. Some titles may be available under an Open Access license. It is the Licensors' responsibility to identify the type of Open Access license on which the requested material was published, and comply fully with the terms of that license for the type of use specified Further details can be found on Wiley Online Library <http://olabout.wiley.com/WileyCDA/Section/id-410895.html>.

## 4. Applied Acoustics: Concepts, Absorbers, and Silencers for Acoustical Comfort and Noise Control : Alternative Solutions - Innovative Tools - Practical Examples

Billing Status:  
Open

Order License ID	1135490-4	Type of use	Republish in a thesis/dissertation
Order detail status	Completed	Publisher	Springer Berlin Heidelberg
ISBN-13	9783642293665	Portion	Chart/graph/table/figure

0.00 CAD

Republishing Permission

[Figure 2.11]

## LICENSED CONTENT

Publication Title	Applied Acoustics: Concepts, Absorbers, and Silencers for Acoustical Comfort and Noise Control : Alternative Solutions - Innovative Tools - Practical Examples	Country	Germany
		Rights holder	Springer
		Publication Type	Book
		URL	<a href="http://www.springerlink.com/index/pdf/10.1007/978-3-642-29367-2">http://www.springerlink.com/index/pdf/10.1007/978-3-642-29367-2</a>
Author/Editor	Fuchs, Helmut V.		

Date 08/31/2012

Language English

## REQUEST DETAILS

Portion Type	Chart/graph/table/figure	Distribution	Worldwide
Number of charts / graphs / tables / figures requested	1	Translation	Original language of publication
Format (select all that apply)	Print,Electronic	Copies for the disabled?	Yes
Who will republish the content?	Academic institution	Minor editing privileges?	Yes
Duration of Use	Life of current edition	Incidental promotional use?	No
Lifetime Unit Quantity	Up to 500,000	Currency	CAD
Rights Requested	Main product		

## NEW WORK DETAILS

Title	Development of Polymeric Nano-Composite Fiber Based Structures for Acoustics and Filtration Applications	Institution name	University of Ontario Institute of Technology (Ontario Tech University)
		Expected presentation date	2021-08-16
Instructor name	Dr. Ghaus Rizvi and Dr. Remon Pop-Iliev		

## ADDITIONAL DETAILS

The requesting person / organization to appear on the license

Utkarsh

## REUSE CONTENT DETAILS

Title, description or numeric reference of the portion(s)	Design characteristics of porous/fibrous absorbers: (a) with optimum matching ratio $\epsilon=2$ (dashed line) and $\epsilon=6$ (dotted line); (b) for random (solid line) and normal (dashed dotted line) sound incidence	Title of the article/chapter the portion is from	Passive Absorbers
		Author of portion(s)	Fuchs, Helmut V.
		Publication date of portion	2012-08-31
Editor of portion(s)	N/A		
Volume of serial or monograph	N/A		
Page or page range of portion	31-42		

## Springer Terms and Conditions

A maximum of 10% of the content may be licensed for republication. The user is responsible for identifying and seeking separate licenses for any third party materials that are identified anywhere in the work. Without a separate license, such third party materials may not be reused.

If you are placing a request on behalf of/for a corporate organization, please use RightsLink. For further information visit

<http://www.nature.com/reprints/permission-requests.html> and

<https://www.springer.com/gp/rights-permissions/obtaining-permissions/882>. If the content you are requesting to reuse is under a CC-BY 4.0 licence (or previous version), you do not need to seek permission from Springer

Nature for this reuse as long as you provide appropriate credit to the original publication.

<https://creativecommons.org/licenses/by/4.0/>

## 5. Applied acoustics : Acoustique appliqué. Angewandte Akustik

Billing Status:  
Open

Article: A pilot study on improving the absorptivity of a thick microperforated panel absorber

Order License ID	1135490-5	Type of use	Republish in a thesis/dissertation
Order detail status	Completed	Publisher	PERGAMON
ISSN	0003-682X	Portion	Chart/graph/table/figure

0.00 CAD

Republishing Permission

[Figure 2.14]

## LICENSED CONTENT

Publication Title	Applied acoustics : Acoustique appliqué. Angewandte Akustik	Publication Type	Journal
Article Title	A pilot study on improving the absorptivity of a thick microperforated panel absorber	Start Page	179
		End Page	182
		Issue	2
		Volume	69
Date	01/01/1968		
Language	English, French, German		
Country	United Kingdom of Great Britain and Northern Ireland		
Rightsholder	Elsevier Science & Technology Journals		

## REQUEST DETAILS

Portion Type	Chart/graph/table/figure	Distribution	Worldwide
Number of charts / graphs / tables / figures requested	2	Translation	Original language of publication
		Copies for the disabled?	Yes

Format (select all that apply)	Print,Electronic	Minor editing privileges?	Yes
Who will republish the content?	Academic institution	Incidental promotional use?	No
Duration of Use	Life of current edition	Currency	CAD
Lifetime Unit Quantity	Up to 44,999		
Rights Requested	Main product		

## NEW WORK DETAILS

Title	Development of Polymeric Nano-Composite Fiber Based Structures for Acoustics and Filtration Applications	Institution name	University of Ontario Institute of Technology (Ontario Tech University)
		Expected presentation date	2021-08-16
Instructor name	Dr. Ghaus Rizvi and Dr. Remon Pop-Iliev		

## ADDITIONAL DETAILS

The requesting person / organization to appear on the license	Utkarsh
---	---------

## REUSE CONTENT DETAILS

Title, description or numeric reference of the portion(s)	Figure 2 and Figure 3	Title of the article/chapter the portion is from	A pilot study on improving the absorptivity of a thick microperforated panel absorber
Editor of portion(s)	Sakagami, Kimihiro; Morimoto, Masayuki; Yairi, Motoki; Minemura, Atsuo	Author of portion(s)	Sakagami, Kimihiro; Morimoto, Masayuki; Yairi, Motoki; Minemura, Atsuo
Volume of serial or monograph	69		
Page or page range of portion	179-182	Issue, if republishing an article from a serial	2
		Publication date of portion	2008-02-01

## Elsevier Science &amp; Technology Journals Terms and Conditions

Elsevier publishes Open Access articles in both its Open Access journals and via its Open Access articles option in subscription journals, for which an author selects a user license permitting certain types of reuse without permission. Before proceeding please check if the article is Open Access on <http://www.sciencedirect.com> and refer to the user license for the individual article. Any reuse not included in the user license terms will require permission. You must always fully and appropriately credit the author and source. If any part of the material to be used (for example, figures) has appeared in the Elsevier publication for which you are seeking permission, with credit or acknowledgement to another source it is the responsibility of the user to ensure their reuse complies with the terms and conditions determined by the rights holder. Please contact [permissions@elsevier.com](mailto:permissions@elsevier.com) with any queries.

## 6. Chinese journal of polymer science

Billing Status:  
Open

Article: Sound absorption behavior of electrospun polyacrylonitrile nanofibrous membranes

Order License ID	1135490-6	Type of use	Republish in a thesis/dissertation
Order detail status	Completed	Publisher	Springer
ISSN	1439-6203	Portion	Chart/graph/table/figure

0.00 CAD

Republication Permission

[Figure 2.15, 2.16 and 2.17]

## LICENSED CONTENT

Publication Title	Chinese journal of polymer science	Publication Type	e-Journal
Article Title	Sound absorption behavior of electrospun polyacrylonitrile nanofibrous membranes	Start Page	650
		End Page	657
		Issue	6
		Volume	29
Date	01/01/2008		
Language	English		
Country	Germany		
Rightholder	Springer Nature BV		

## REQUEST DETAILS

Portion Type	Chart/graph/table/figure	Distribution	Worldwide
Number of charts / graphs / tables / figures requested	3	Translation	Original language of publication
Format (select all that apply)	Print,Electronic	Copies for the disabled?	Yes
Who will republish the content?	Academic institution	Minor editing privileges?	Yes
Duration of Use	Life of current edition	Incidental promotional use?	No
Lifetime Unit Quantity	Up to 500,000	Currency	CAD
Rights Requested	Main product		

## NEW WORK DETAILS

Title	Development of Polymeric Nano-Composite Fiber Based Structures for Acoustics and Filtration Applications	Institution name	University of Ontario Institute of Technology (Ontario Tech University)
Instructor name	Dr. Ghaus Rizvi and Dr. Remon Pop-Iliev	Expected presentation date	2021-08-16

## ADDITIONAL DETAILS

The requesting person / organization to appear on the license

Utkarsh

## REUSE CONTENT DETAILS

Title, description or numeric reference of the portion(s)	Figure 2, Figure 4, and Figure 5	Title of the article/chapter the portion is from	Sound absorption behavior of electrospun polyacrylonitrile nanofibrous membranes
Editor of portion(s)	Hai-fan, Xiang; Shuai-xia, Tan; Xiao-lan, Yu; Yu-hua, Long; Xiao-li, Zhang; Ning, Zhao; Jian, Xu	Author of portion(s)	Hai-fan, Xiang; Shuai-xia, Tan; Xiao-lan, Yu; Yu-hua, Long; Xiao-li, Zhang; Ning, Zhao; Jian, Xu
Volume of serial or monograph	29		
Page or page range of portion	650-657	Publication date of portion	2011-08-18

## Springer Nature BV Terms and Conditions

If you are placing a request on behalf of/for a corporate organization, please use RightsLink. For further information visit

<http://www.nature.com/reprints/permission-requests.html> and

<https://www.springer.com/gp/rights-permissions/obtaining-permissions/882>. If the content you are requesting to reuse is under a CC-BY 4.0 licence (or previous version), you do not need to seek permission from Springer Nature for this reuse as long as you provide appropriate credit to the original publication.

<https://creativecommons.org/licenses/by/4.0/>

## 7. European polymer journal

Article: Sound absorption of electrospun polyvinylidene fluoride/graphene membranes

Billing Status:  
Open

Order License ID	1135490-7	Type of use	Republish in a thesis/dissertation
Order detail status	Completed	Publisher	PERGAMON
ISSN	0014-3057	Portion	Chart/graph/table/figure

0.00 CAD

Republication Permission

[Figure 2.22 and 2.23]

## LICENSED CONTENT

Publication Title	European polymer journal	Rights holder	Elsevier Science & Technology Journals
Article Title	Sound absorption of electrospun polyvinylidene fluoride/graphene membranes	Publication Type	Journal
		Start Page	35
		End Page	45
		Volume	82
Date	01/01/1965		
Language	English, French, German, Italian		



Country United Kingdom of Great Britain and Northern Ireland

### REQUEST DETAILS

Portion Type	Chart/graph/table/figure	Distribution	Worldwide
Number of charts / graphs / tables / figures requested	4	Translation	Original language of publication
Format (select all that apply)	Print,Electronic	Copies for the disabled?	Yes
Who will republish the content?	Academic institution	Minor editing privileges?	Yes
Duration of Use	Life of current edition	Incidental promotional use?	No
Lifetime Unit Quantity	Up to 44,999	Currency	CAD
Rights Requested	Main product		

### NEW WORK DETAILS

Title	Development of Polymeric Nano-Composite Fiber Based Structures for Acoustics and Filtration Applications	Institution name	University of Ontario Institute of Technology (Ontario Tech University)
		Expected presentation date	2021-08-16
Instructor name	Dr. Ghaus Rizvi and Dr. Remon Pop-Iliev		

### ADDITIONAL DETAILS

The requesting person / organization to appear on the license Utkarsh

### REUSE CONTENT DETAILS

Title, description or numeric reference of the portion(s)	Figure 7, 8, 9, and 10	Title of the article/chapter the portion is from	Sound absorption of electrospun polyvinylidene fluoride/graphene membranes
Editor of portion(s)	Wu, Chang Mou; Chou, Min Hui	Author of portion(s)	Wu, Chang Mou; Chou, Min Hui
Volume of serial or monograph	82	Publication date of portion	2016-09-01
Page or page range of portion	35-45		



## Elsevier Science & Technology Journals Terms and Conditions

Elsevier publishes Open Access articles in both its Open Access journals and via its Open Access articles option in subscription journals, for which an author selects a user license permitting certain types of reuse without permission. Before proceeding please check if the article is Open Access on <http://www.sciencedirect.com> and refer to the user license for the individual article. Any reuse not included in the user license terms will require permission. You must always fully and appropriately credit the author and source. If any part of the material to be used (for example, figures) has appeared in the Elsevier publication for which you are seeking permission, with credit or acknowledgement to another source it is the responsibility of the user to ensure their reuse complies with the terms and conditions determined by the rights holder. Please contact [permissions@elsevier.com](mailto:permissions@elsevier.com) with any queries.

### 8. Separation and purification technology

**Billing Status:**  
Open

**Article:** Charged PVDF multilayer nanofiber filter in filtering simulated airborne novel coronavirus (COVID-19) using ambient nano-aerosols.

Order License ID	1135490-8	Type of use	Republish in a thesis/dissertation
Order detail status	Completed	Publisher	Elsevier Ltd
ISSN	1383-5866	Portion	Image/photo/illustration

0.00 CAD

Republication Permission

[Figure 2.28]

### LICENSED CONTENT

Publication Title	Separation and purification technology	Rights holder	Elsevier Science & Technology Journals
Article Title	Charged PVDF multilayer nanofiber filter in filtering simulated airborne novel coronavirus (COVID-19) using ambient nano-aerosols.	Publication Type	Journal
		Start Page	116887
		Volume	245
Date	01/01/1997		
Language	English		
Country	United Kingdom of Great Britain and Northern Ireland		

### REQUEST DETAILS

Portion Type	Image/photo/illustration	Distribution	Worldwide
Number of images / photos / illustrations	2	Translation	Original language of publication
Format (select all that apply)	Print, Electronic	Copies for the disabled?	Yes
Who will republish the content?	Academic institution	Minor editing privileges?	Yes
Duration of Use	Life of current edition	Incidental promotional use?	No

Lifetime Unit Quantity	Up to 44,999	Currency	CAD
Rights Requested	Main product		

## NEW WORK DETAILS

Title	Development of Polymeric Nano-Composite Fiber Based Structures for Acoustics and Filtration Applications	Institution name	University of Ontario Institute of Technology (Ontario Tech University)
		Expected presentation date	2021-08-16
Instructor name	Dr. Ghaus Rizvi and Dr. Remon Pop-Iliev		

## ADDITIONAL DETAILS

The requesting person / organization to appear on the license	Utkarsh
---	---------

## REUSE CONTENT DETAILS

Title, description or numeric reference of the portion(s)	Schematic 1a and Schematic 1b	Title of the article/chapter the portion is from	Charged PVDF multilayer nanofiber filter in filtering simulated airborne novel coronavirus (COVID-19) using ambient nano-aerosols.
Editor of portion(s)	Sun, Qiangqiang; Leung, Wallace Woon-Fong		
Volume of serial or monograph	245	Author of portion(s)	Sun, Qiangqiang; Leung, Wallace Woon-Fong
Page or page range of portion	116887	Publication date of portion	2020-08-15

## Elsevier Science &amp; Technology Journals Terms and Conditions

Elsevier publishes Open Access articles in both its Open Access journals and via its Open Access articles option in subscription journals, for which an author selects a user license permitting certain types of reuse without permission. Before proceeding please check if the article is Open Access on <http://www.sciencedirect.com> and refer to the user license for the individual article. Any reuse not included in the user license terms will require permission. You must always fully and appropriately credit the author and source. If any part of the material to be used (for example, figures) has appeared in the Elsevier publication for which you are seeking permission, with credit or acknowledgement to another source it is the responsibility of the user to ensure their reuse complies with the terms and conditions determined by the rights holder. Please contact [permissions@elsevier.com](mailto:permissions@elsevier.com) with any queries.

## 9. Journal of colloid and interface science

Billing Status:  
Open

Article: Tortuously structured polyvinyl chloride/polyurethane fibrous membranes for high-efficiency fine particulate filtration.

Order License ID	1135490-9	Type of use	Republish in a thesis/dissertation
Order detail status	Completed	Publisher	ACADEMIC PRESS
ISSN	0021-9797	Portion	Image/photo/illustration

**[Figure 2.29]****LICENSED CONTENT**

Publication Title	Journal of colloid and interface science	Rightholder	Elsevier Science & Technology Journals
Article Title	Tortuously structured polyvinyl chloride/polyurethane fibrous membranes for high-efficiency fine particulate filtration.	Publication Type	Journal
		Start Page	240
		End Page	246
		Volume	398
Author/Editor	KERKER, M		
Date	01/01/1966		
Language	English		
Country	United States of America		

**REQUEST DETAILS**

Portion Type	Image/photo/illustration	Distribution	Worldwide
Number of images / photos / illustrations	1	Translation	Original language of publication
Format (select all that apply)	Print,Electronic	Copies for the disabled?	Yes
Who will republish the content?	Academic institution	Minor editing privileges?	Yes
Duration of Use	Life of current edition	Incidental promotional use?	No
Lifetime Unit Quantity	Up to 44,999	Currency	CAD
Rights Requested	Main product		

**NEW WORK DETAILS**

Title	Development of Polymeric Nano-Composite Fiber Based Structures for Acoustics and Filtration Applications	Institution name	University of Ontario Institute of Technology (Ontario Tech University)
Instructor name	Dr. Ghaus Rizvi and Dr. Remon Pop-Iliev	Expected presentation date	2021-08-16

**ADDITIONAL DETAILS**

The requesting person / organization to appear on the license

Utkarsh

**REUSE CONTENT DETAILS**

Title, description or numeric reference of the portion(s)	Scheme 1. (a) The filtration process of PVC/PU membranes for 300–500 nm NaCl aerosol particles. (b) Cross-section of PVC/PU membranes with different flow channels.	Title of the article/chapter the portion is from	Tortuously structured polyvinyl chloride/polyurethane fibrous membranes for high-efficiency fine particulate filtration.
Editor of portion(s)	Wang, Na; Raza, Aikifa; Si, Yang; Yu, Jianyong; Sun, Gang; Ding, Bin	Author of portion(s)	Wang, Na; Raza, Aikifa; Si, Yang; Yu, Jianyong; Sun, Gang; Ding, Bin
Volume of serial or monograph	398	Publication date of portion	2013-05-15
Page or page range of portion	240-246		

### Elsevier Science & Technology Journals Terms and Conditions

Elsevier publishes Open Access articles in both its Open Access journals and via its Open Access articles option in subscription journals, for which an author selects a user license permitting certain types of reuse without permission. Before proceeding please check if the article is Open Access on <http://www.sciencedirect.com> and refer to the user license for the individual article. Any reuse not included in the user license terms will require permission. You must always fully and appropriately credit the author and source. If any part of the material to be used (for example, figures) has appeared in the Elsevier publication for which you are seeking permission, with credit or acknowledgement to another source it is the responsibility of the user to ensure their reuse complies with the terms and conditions determined by the rights holder. Please contact [permissions@elsevier.com](mailto:permissions@elsevier.com) with any queries.

### 10. Journal of colloid and interface science

Article: Hierarchically structured polysulfone/titania fibrous membranes with enhanced air filtration performance.

Billing Status:  
Open

Order License ID	1135490-10	Type of use	Republish in a thesis/dissertation
Order detail status	Completed	Publisher	ACADEMIC PRESS
ISSN	0021-9797	Portion	Chart/graph/table/figure

0.00 CAD  
Republication Permission

### LICENSED CONTENT

[Figure 2.30]

Publication Title	Journal of colloid and interface science	Rights holder	Elsevier Science & Technology Journals
Article Title	Hierarchically structured polysulfone/titania fibrous membranes with enhanced air filtration performance.	Publication Type	Journal
		Start Page	18
		End Page	26
		Volume	417
Author/Editor	KERKER, M		

Date 01/01/1966  
 Language English  
 Country United States of America

### REQUEST DETAILS

Portion Type	Chart/graph/table/figure	Distribution	Worldwide
Number of charts / graphs / tables / figures requested	1	Translation	Original language of publication
Format (select all that apply)	Print,Electronic	Copies for the disabled?	Yes
Who will republish the content?	Academic institution	Minor editing privileges?	Yes
Duration of Use	Life of current edition	Incidental promotional use?	No
Lifetime Unit Quantity	Up to 44,999	Currency	CAD
Rights Requested	Main product		

### NEW WORK DETAILS

Title	Development of Polymeric Nano-Composite Fiber Based Structures for Acoustics and Filtration Applications	Institution name	University of Ontario Institute of Technology (Ontario Tech University)
Instructor name	Dr. Ghaus Rizvi and Dr. Remon Pop-Iliev	Expected presentation date	2021-08-16

### ADDITIONAL DETAILS

The requesting person / organization to appear on the license Utkarsh

### REUSE CONTENT DETAILS

Title, description or numeric reference of the portion(s)	Fig. 5. FE-SEM images of (a) PSU/TiO2-2.5, (b) PSU/TiO2-5, (c) PSU/TiO2-7.5 and (d) PSU/TiO2-10 fibrous membranes.	Title of the article/chapter the portion is from	Hierarchically structured polysulfone/titania fibrous membranes with enhanced air filtration performance.
Editor of portion(s)	Wan, Huigao; Wang, Na; Yang, Jianmao; Si, Yinsong; Chen, Kun; Ding, Bin; Sun, Gang; El-Newehy, Mohamed; Al-Deyab, Salem S.; Yu, Jianyong	Author of portion(s)	Wan, Huigao; Wang, Na; Yang, Jianmao; Si, Yinsong; Chen, Kun; Ding, Bin; Sun, Gang; El-Newehy, Mohamed; Al-Deyab, Salem S.; Yu, Jianyong
Volume of serial or monograph	417	Publication date of portion	2014-03-01

Page or page range of  
portion 18-26

## Elsevier Science & Technology Journals Terms and Conditions

Elsevier publishes Open Access articles in both its Open Access journals and via its Open Access articles option in subscription journals, for which an author selects a user license permitting certain types of reuse without permission. Before proceeding please check if the article is Open Access on <http://www.sciencedirect.com> and refer to the user license for the individual article. Any reuse not included in the user license terms will require permission. You must always fully and appropriately credit the author and source. If any part of the material to be used (for example, figures) has appeared in the Elsevier publication for which you are seeking permission, with credit or acknowledgement to another source it is the responsibility of the user to ensure their reuse complies with the terms and conditions determined by the rights holder. Please contact [permissions@elsevier.com](mailto:permissions@elsevier.com) with any queries.

### 11. Separation and purification technology

Billing Status:  
Open

Article: Sandwich structured polyamide-6/polyacrylonitrile nanonets/bead-on-string composite membrane for effective air filtration

Order License ID	1135490-11	Type of use	Republish in a thesis/dissertation
Order detail status	Completed	Publisher	Elsevier Ltd
ISSN	1383-5866	Portion	Chart/graph/table/figure

0.00 CAD

Republication Permission

[Figure 2.31]

### LICENSED CONTENT

Publication Title	Separation and purification technology	Rightholder	Elsevier Science & Technology Journals
Article Title	Sandwich structured polyamide-6/polyacrylonitrile nanonets/bead-on-string composite membrane for effective air filtration	Publication Type	Journal
		Start Page	14
		End Page	22
		Volume	152
Date	01/01/1997		
Language	English		
Country	United Kingdom of Great Britain and Northern Ireland		

### REQUEST DETAILS

Portion Type	Chart/graph/table/figure	Distribution	Worldwide
		Translation	Original language of publication
Number of charts / graphs / tables / figures requested	1	Copies for the disabled?	Yes
Format (select all that apply)	Print,Electronic	Minor editing privileges?	Yes



Who will republish the content?	Academic institution	Incidental promotional use?	No
Duration of Use	Life of current edition	Currency	CAD
Lifetime Unit Quantity	Up to 44,999		
Rights Requested	Main product		

## NEW WORK DETAILS

Title	Development of Polymeric Nano-Composite Fiber Based Structures for Acoustics and Filtration Applications	Institution name	University of Ontario Institute of Technology (Ontario Tech University)
		Expected presentation date	2021-08-16
Instructor name	Dr. Ghaus Rizvi and Dr. Remon Pop-Iliev		

## ADDITIONAL DETAILS

The requesting person / organization to appear on the license	Utkarsh
---	---------

## REUSE CONTENT DETAILS

Title, description or numeric reference of the portion(s)	Figure 7 (a-b)	Title of the article/chapter the portion is from	Sandwich structured polyamide-6/polyacrylonitrile nanonets/bead-on-string composite membrane for effective air filtration
Editor of portion(s)	Yang, Yinjing; Zhang, Shichao; Zhao, Xinglei; Yu, Jianyong; Ding, Bin		
Volume of serial or monograph	152	Author of portion(s)	Yang, Yinjing; Zhang, Shichao; Zhao, Xinglei; Yu, Jianyong; Ding, Bin
Page or page range of portion	14-22	Publication date of portion	2015-09-01

## Elsevier Science &amp; Technology Journals Terms and Conditions

Elsevier publishes Open Access articles in both its Open Access journals and via its Open Access articles option in subscription journals, for which an author selects a user license permitting certain types of reuse without permission. Before proceeding please check if the article is Open Access on <http://www.sciencedirect.com> and refer to the user license for the individual article. Any reuse not included in the user license terms will require permission. You must always fully and appropriately credit the author and source. If any part of the material to be used (for example, figures) has appeared in the Elsevier publication for which you are seeking permission, with credit or acknowledgement to another source it is the responsibility of the user to ensure their reuse complies with the terms and conditions determined by the rights holder. Please contact [permissions@elsevier.com](mailto:permissions@elsevier.com) with any queries.

## 12. Nano research

Article: Silk nanofibers as high efficient and lightweight air filter

Billing Status:  
Open

Order License ID	1135490-12	Type of use	Republish in a thesis/dissertation
Order detail status	Completed		

ISSN	1998-0124	Publisher	Springer-Verlag Berlin/Heidelberg
		Portion	Chart/graph/table/figure
			0.00 CAD
			Republication Permission

[Figure 2.32]

## LICENSED CONTENT

Publication Title	Nano research	Rights holder	Springer Nature BV
Article Title	Silk nanofibers as high efficient and lightweight air filter	Publication Type	Journal
		Start Page	2597
		End Page	2597
Author/Editor	Qing hua da xue (Beijing, China)	Issue	9
Date	01/01/2008	Volume	9
Language	English		
Country	Germany		

## REQUEST DETAILS

Portion Type	Chart/graph/table/figure	Distribution	Worldwide
		Translation	Original language of publication
Number of charts / graphs / tables / figures requested	2	Copies for the disabled?	Yes
Format (select all that apply)	Print,Electronic	Minor editing privileges?	Yes
Who will republish the content?	Academic institution	Incidental promotional use?	No
Duration of Use	Life of current edition	Currency	CAD
Lifetime Unit Quantity	Up to 500,000		
Rights Requested	Main product		

## NEW WORK DETAILS

Title	Development of Polymeric Nano-Composite Fiber Based Structures for Acoustics and Filtration Applications	Institution name	University of Ontario Institute of Technology (Ontario Tech University)
		Expected presentation date	2021-08-16
Instructor name	Dr. Ghaus Rizvi and Dr. Remon Pop-Iliev		

## ADDITIONAL DETAILS

The requesting person / organization to appear on the license

## REUSE CONTENT DETAILS



Title, description or numeric reference of the portion(s)	Figure 2a and Figure 4a	Title of the article/chapter the portion is from	Silk nanofibers as high efficient and lightweight air filter
Editor of portion(s)	Xie, Jiarong; Zheng, Quanshui; Yang, Xudong; Jian, Muqiang; Zhang, Yingying; Wang, Chunya; Wu, Shuyi; Xu, Luping	Author of portion(s)	Xie, Jiarong; Zheng, Quanshui; Yang, Xudong; Jian, Muqiang; Zhang, Yingying; Wang, Chunya; Wu, Shuyi; Xu, Luping
Volume of serial or monograph	9	Publication date of portion	2008-01-01
Page or page range of portion	2597-2597		

### Springer Nature BV Terms and Conditions

If you are placing a request on behalf of/for a corporate organization, please use RightsLink. For further information visit

<http://www.nature.com/reprints/permission-requests.html> and

<https://www.springer.com/gp/rights-permissions/obtaining-permissions/882>. If the content you are requesting to reuse is under a CC-BY 4.0 licence (or previous version), you do not need to seek permission from Springer Nature for this reuse as long as you provide appropriate credit to the original publication.

<https://creativecommons.org/licenses/by/4.0/>

### 13. Macromolecular materials and engineering

Article: Electrospun Nanofibers Membranes for Effective Air Filtration

Billing Status:  
Open

Order License ID	1135490-13	Type of use	Republish in a thesis/dissertation
Order detail status	Completed	Publisher	WILEY - V C H VERLAG GMBH & CO. KGAA
ISSN	1438-7492	Portion	Chart/graph/table/figure
			0.00 CAD
			Republication Permission

### LICENSED CONTENT

[Figure 2.29 – 2.32]

Publication Title	Macromolecular materials and engineering	Rightsholder	John Wiley & Sons - Books
Article Title	Electrospun Nanofibers Membranes for Effective Air Filtration	Publication Type	Journal
Date	01/01/2000	Start Page	1600353
Language	English, French, German	Issue	1
Country	Germany	Volume	302

### REQUEST DETAILS

Portion Type	Chart/graph/table/figure	Distribution	Worldwide
--------------	--------------------------	--------------	-----------

Number of charts / graphs / tables / figures requested	10	Translation	Original language of publication
Format (select all that apply)	Print,Electronic	Copies for the disabled?	Yes
Who will republish the content?	Academic institution	Minor editing privileges?	Yes
Duration of Use	Life of current edition	Incidental promotional use?	No
Lifetime Unit Quantity	Up to 500,000	Currency	CAD
Rights Requested	Main product		

## NEW WORK DETAILS

Title	Development of Polymeric Nano-Composite Fiber Based Structures for Acoustics and Filtration Applications	Institution name	University of Ontario Institute of Technology (Ontario Tech University)
		Expected presentation date	2021-08-16
Instructor name	Dr. Ghaus Rizvi and Dr. Remon Pop-Iliev		

## ADDITIONAL DETAILS

The requesting person / organization to appear on the license	Utkarsh
---	---------

## REUSE CONTENT DETAILS

Title, description or numeric reference of the portion(s)	Figure 6b, 7(a-d), 8a, and 10(a-c)	Title of the article/chapter the portion is from	Electrospun Nanofibers Membranes for Effective Air Filtration
Editor of portion(s)	Zhu, Miaomiao; Han, Jingquan; Wang, Fang; Shao, Wei; Xiong, Ranhua; Zhang, Qilu; Pan, Hui; Yang, Yong; Samal, Sangram Keshari; Zhang, Feng; Huang, Chaobo	Author of portion(s)	Zhu, Miaomiao; Han, Jingquan; Wang, Fang; Shao, Wei; Xiong, Ranhua; Zhang, Qilu; Pan, Hui; Yang, Yong; Samal, Sangram Keshari; Zhang, Feng; Huang, Chaobo
Volume of serial or monograph	302	Publication date of portion	2017-01-01
Page or page range of portion	1600353		

### John Wiley & Sons - Books Terms and Conditions

No right, license or interest to any trademark, trade name, service mark or other branding ("Marks") of WILEY or its licensors is granted hereunder, and you agree that you shall not assert any such right, license or interest with respect thereto. You may not alter, remove or suppress in any manner any copyright, trademark or other notices displayed by the Wiley material. This Agreement will be void if the Type of Use, Format, Circulation, or Requestor Type was misrepresented during the licensing process. In no instance may the total amount of Wiley Materials used in any Main Product, Compilation or Collective work comprise more than 5% (if figures/tables) or 15% (if full articles/chapters) of the (entirety of the) Main Product, Compilation or Collective Work. Some titles may be available under an Open Access license. It is the Licensors' responsibility to identify the type of Open Access license on which the requested material was published, and comply fully with the terms of that license for the type of use specified Further details can be found on Wiley Online Library <http://olabout.wiley.com/WileyCDA/Section/id-410895.html>.

---

**Total Items: 13**

Subtotal: 0.00 CAD  
**Order Total: 0.00 CAD**



FNU Utkarsh &lt;fnu.utkarsh@ontariotechu.net&gt;

**[Figure 2.7]****Request to procure rights and permission to republish one figure in my PhD thesis**

2 messages

FNU Utkarsh <fnu.utkarsh@ontariotechu.net>  
To: susan.matveyeva@wichita.edu

Tue, Aug 17, 2021 at 8:59 PM

Dear Sir/Madam,

I hope this email finds you well

I am sending this email as a kind request for procuring rights and permission to republish one figure from "R. Asmatulu, M.B. Yildirim, W.S. Khan, A. Adeniji, H.L. Wamocha, Nanofiber fabrication and characterization for the engineering education, (2007)" for my PhD thesis submission to the School of Graduate and Postdoctoral Studies at the University of Ontario Institute of Technology (Ontario Tech) in Oshawa, Ontario, Canada.

I would really appreciate it if I can get a response sooner as I have to submit the thesis before the deadline.

Thanks

Best regards,  
Utkarsh

—

Best Regards,  
Utkarsh  
PhD Candidate  
AMME - Ontario Tech University  
2000, Simcoe Street North, Oshawa,  
Ontario, L1G0C5, Canada

Matveyeva, Susan <Susan.Matveyeva@wichita.edu>  
To: "fnu.utkarsh@ontariotechu.net" <fnu.utkarsh@ontariotechu.net>

Wed, Aug 18, 2021 at 10:10 AM

Dear Utkarsh,

The authors granted you permission to republish one figure from their conference paper in your PhD thesis.

Regards

Dr. Susan Matveyeva

---

Susan J. Matveyeva, PhD, MLIS, B.Mus

Associate Professor, Catalog &amp;

Institutional Repository Librarian

Wichita State University Libraries

<https://mail.google.com/mail/u/0/?ik=f9a496483a&view=pt&search=all&permthid=thread-a%3Ar-3718054976724285887&simpl=msg-a%3Ar25370291...> 1/3

Order Number: 1136298

Order Date: 27 Jul 2021

### Payment Information

Utkarsh Utkarsh  
fnu.utkarsh@ontariotechu.net  
Payment method: Invoice

**Billing Address:**  
Mr. Utkarsh Utkarsh  
1820 Dalhousie Crescent  
Oshawa, ON L1G8C5  
Canada

+1 (289) 688-6599  
fnu.utkarsh@ontariotech  
u.net

**Customer Location:**  
Mr. Utkarsh Utkarsh  
1820 Dalhousie Crescent  
Oshawa, ON L1G8C5  
Canada

### Order Details

1. Acoustic absorbers and diffusers : theory, design and application

**Billing Status:**  
Open

Order License ID	1136298-1	Type of use	Republish in a thesis/dissertation
Order detail status	Completed	Publisher	Taylor & Francis
ISBN-13	9780203893050	Portion	Chart/graph/table/figure

0.00 CAD

Republication Permission

[Figure 2.13]

### LICENSED CONTENT

Publication Title	Acoustic absorbers and diffusers : theory, design and application	Country	United Kingdom of Great Britain and Northern Ireland
Author/Editor	Cox, Trevor J., D'Antonio, Peter.	Rightholder	Taylor & Francis Informa UK Ltd - Books
Date	01/01/2009	Publication Type	Book
Language	English		

### REQUEST DETAILS

Portion Type	Chart/graph/table/figure	Distribution	Worldwide
Number of charts / graphs / tables / figures requested	3	Translation	Original language of publication
Format (select all that apply)	Print, Electronic	Copies for the disabled?	Yes
		Minor editing privileges?	Yes

Who will republish the content?	Academic institution	Incidental promotional use?	No
Duration of Use	Life of current edition	Currency	CAD
Lifetime Unit Quantity	Up to 44,999		
Rights Requested	Main product		

## NEW WORK DETAILS

Title	Development of Polymeric Nano-Composite Fiber Based Structures for Acoustics and Filtration Applications	Institution name	University of Ontario Institute of Technology (Ontario Tech University)
		Expected presentation date	2021-08-16
Instructor name	Dr. Ghaus Rizvi and Dr. Remon Pop-Iliev		

## ADDITIONAL DETAILS

The requesting person / organization to appear on the license	Utkarsh
---	---------

## REUSE CONTENT DETAILS

Title, description or numeric reference of the portion(s)	Description of resonant absorber; (a) Helmholtz and (b) Membrane or panel-based, and (c) Acoustic performance of porous mineral wool absorber and perforated sheet covered mineral wool layer	Title of the article/chapter the portion is from	Resonant Absorbers
		Author of portion(s)	Cox, Trevor J.; D'Antonio, Peter.
		Publication date of portion	2009-01-01
Editor of portion(s)	N/A		
Volume of serial or monograph	N/A		
Page or page range of portion	157-185		

## Taylor &amp; Francis Informa UK Ltd - Books Special Terms and Conditions

THIS PERMISSION DOES NOT COVER ANY THIRD PARTY COPYRIGHTED WORK WHICH MAY APPEAR IN THE MATERIAL REQUESTED. USER IS RESPONSIBLE FOR OBTAINING PERMISSION FOR SUCH MATERIAL SEPARATELY FROM THIS GRANT. Please make sure the appropriate source is credited. Insert information as appropriate. Each copy containing our material must bear a credit line in the following format: Copyright (Insert © Year) From (Insert Title) by (Insert Author/Editor Name). Reproduced by permission of Taylor and Francis Group, LLC, a division of Informa plc.

Total Items: 1

Subtotal: 0.00 CAD  
Order Total: 0.00 CAD

Order Number: 1141326

Order Date: 17 Aug 2021

### Payment Information

Utkarsh Utkarsh  
fnu.utkarsh@ontariotechu.net  
Payment method: Invoice

**Billing Address:**  
Mr. Utkarsh Utkarsh  
1820 Dalhousie Crescent  
Oshawa, ON L1G8C5  
Canada  
  
+1 (289) 688-6599  
fnu.utkarsh@ontariotech  
u.net

**Customer Location:**  
Mr. Utkarsh Utkarsh  
1820 Dalhousie Crescent  
Oshawa, ON L1G8C5  
Canada

### Order Details

#### 1. Handbook of Engineering Acoustics

**Billing Status:**  
Open

Order License ID	1141326-1	Type of use	Republish in a thesis/dissertation
Order detail status	Completed	Publisher	Springer Berlin Heidelberg, Springer Berlin Heidelberg
ISBN-13	9783642435508	Portion	Image/photo/illustration
			0.00 CAD
			Republication Permission

#### LICENSED CONTENT

Publication Title	Handbook of Engineering Acoustics	Country	Germany
Date	12/14/2014	Rightsholder	Springer
Language	English	Publication Type	Book

#### REQUEST DETAILS

Portion Type	Image/photo/illustration	Distribution	Worldwide
Number of images / photos / illustrations	1	Translation	Original language of publication
Format (select all that apply)	Print, Electronic	Copies for the disabled?	Yes
Who will republish the content?	Academic institution	Minor editing privileges?	Yes
Duration of Use	Life of current edition	Incidental promotional use?	No

[Figure 2.8]

Lifetime Unit Quantity	Up to 500,000	Currency	CAD
Rights Requested	Main product		

### NEW WORK DETAILS

Title	Development of Polymeric Nano-Composite Fiber Based Structures for Acoustics and Filtration Applications	Institution name	University of Ontario Institute of Technology (Ontario Tech University)
		Expected presentation date	2021-08-20
Instructor name	Dr. Ghaus Rizvi and Dr. Remon Pop-Iliev		

### ADDITIONAL DETAILS

The requesting person / organization to appear on the license	Utkarsh
---	---------

### REUSE CONTENT DETAILS

Title, description or numeric reference of the portion(s)	Extra aural reaction lines	Title of the article/chapter the portion is from	The effect of sound on humans
Editor of portion(s)	Dr. Gerhard M€uller and Dr. Michael M€oser	Author of portion(s)	C. Maschke and U. Widmann
Volume of serial or monograph	N/A	Publication date of portion	2014-12-14
Page or page range of portion	76		

### Springer Terms and Conditions

A maximum of 10% of the content may be licensed for republication. The user is responsible for identifying and seeking separate licenses for any third party materials that are identified anywhere in the work. Without a separate license, such third party materials may not be reused.

If you are placing a request on behalf of/for a corporate organization, please use RightsLink. For further information visit

<http://www.nature.com/reprints/permission-requests.html> and

<https://www.springer.com/gp/rights-permissions/obtaining-permissions/882>. If the content you are requesting to reuse is under a CC-BY 4.0 licence (or previous version), you do not need to seek permission from Springer Nature for this reuse as long as you provide appropriate credit to the original publication.

<https://creativecommons.org/licenses/by/4.0/>

Total Items: 1

Subtotal: 0.00 CAD  
Order Total: 0.00 CAD